Modelling the effects of forest regeneration on streamflow using forest growth models

PhD dissertation

Dominik Jaskierniak, BSc GradDipSIS (Honours)

September, 2011

(University of Tasmania)

A thesis submitted in partial fulfilment of the requirements for a PhD Degree at the School of Geography and Environmental Studies, University of Tasmania.

Declaration

This thesis contains no material which has been accepted for the award of any other degree or diploma in any tertiary institution, and to the best of my knowledge and belief, contains no material previously published or written by another person, except where due reference is made in the text of the thesis.

Signed

Yours Dominik Jaskierniak

Authority of Access

This thesis may be made available for loan and limited copying and communication in accordance with the Copyright Act 1968.

Signed

Yours Dominik Jaskierniak

Publications

The publisher of the paper comprising chapter 5 hold the copyright for that content, and access to the material may be sought from the respective journal. The published paper is titled:

Jaskierniak, D., Lane, P.N.J., Robinson, A. & Lucieer, A., 2011. Extracting LiDAR indices to characterise multilayered forest structure using mixture distribution functions. *Remote Sensing of Environment*, **115** (2), 573-585.

Abstract

Forest regeneration is a dynamic process that affects forest hydrology through changes in structure and density of natural forests. In Victoria and Tasmania, forest hydrology models that manage the potential impacts of land cover disturbance on the water resource are not data-driven with information on vegetation dynamics that affect forest water use. Current models underutilise forest inventory databases for managing the forested water resources, even though available evidence suggests an inverse relationship between forest growth rates and long-term changes in streamflow. This dissertation is the first published study that uses forest inventory data to produce spatiotemporal forest growth models to explain vegetation-induced streamflow trends. The study was undertaken in nine small catchments (7.4 to 52.8 ha) located in Melbourne's Maroondah water catchment.

The hydrology model runs on an annual time step and partitions streamflow data into climate-induced noise using a climate filter, and vegetation-induced trend using an ellipse and gamma ("Kuczera curve") function. A simulation exercise demonstrates how well the model structure isolates the vegetation-induced trend from climatic variability in streamflow using a range of synthesised scenario cases. The model framework allows for comparison of streamflow trends against a detailed forest growth model by using the same gamma function to quantify forest growth and vegetation-induced streamflow trends.

To spatially extrapolate forest growth, field measured stand characteristics were empirically analysed against LiDAR indices. The indices were produced with mixture models, which used 11 distribution functions to summarise complex canopy attributes with bimodal distributions. The LiDAR indices were used to predict overstorey stand volumes and basal area, and understorey basal area of 18-, 37-, and 70-year old Mountain Ash forest with variable density classes and treatment effects. Observed versus predicted values of eucalyptus basal area and stand volume were highly correlated, with bootstrap r^2 ranging from 0.61 to 0.89 and 0.67 to 0.88 respectively. Non-eucalyptus basal area r^2 ranged from 0.5 to 0.91.

To temporally extrapolate stand volumes and basal area, LiDAR indices and permanent plot data were used in mixed effects models to capture the spatial heterogeneity in, and temporally polymorphic nature of forest growth. The spatiotemporal models of forest growth were then lumped to the catchment-scale to represent changes in growth rates over the stream gauging period. The relationship between catchment-scale gamma parameters of forest growth and forest water use were explored, and results demonstrate that forest growth provides useful information for explaining streamflow trends published in the literature and quantified in this study.

Acknowledgements

I would like to thank many people for assistance and guidance during this research. First of all, I thank my supervisors Arko Lucieer and Richard Doyle for their encouragement, patience, and overwhelming support throughout the project. Their diligence in overseeing the thesis is appreciated. My special thanks is also extended to my research advisors Patrick Lane and George Kuczera for their contribution in proof reading, editing, and providing specialist advice. Their forest hydrology expertise was invaluable at directing the project. I would also like to acknowledge with gratitude the office space and resources provided by Melbourne University and Newcastle University. Both opportunities provided ideal conditions for my science to progress with the support of colleagues from all over Australia. In the Forest and Water Group (Melbourne University) I am indebted to Richard Benyon, Patrick Mitchell, Paul Feikema, Chris Sherwin, Gary Sheridan, Phil Noske, and Huge Smith for their insight into forest hydrological systems. At the School of Civil Engineering (Newcastle University), I am grateful for the contribution Mark Thyre, Dmitri Kavetski, and Tom Micevski made in overseeing the statistical computing challenges I faced.

I am also thankful for the forest inventory modelling insight Andrew Robinson and Owen Jones at the Mathematics Department (Melbourne University) provided. My gratitude is also extended to Rob Musk from Forestry Tasmania and Fiona Hamilton from Department of Sustainability of Environment for their support during the forest growth modelling exercises. For overseeing challenging statistical programming exercises I would also like to thank Simon Wotherspoon from the Mathematics Department (University of Tasmania).

A big thanks needs to go to Ian Watson for unearthing original field sheets of permanent growth plot data measured by Melbourne Water. The discovery became a central component of my PhD. I am also grateful to Melbourne Water for providing the LiDAR data and hydrological time series. Thanks also goes out to CRC for Forestry and the Forest and Water Group (Melbourne University) for financing the field work. I am also indebted to the following field support: Ben Hargreaves, Shane

Schmidt, Stan Jaskierniak, Sam Hoffman, Amy Rayner, and Michael Jaskierniak. For resolving computer issues I am indebted to Darren Turner.

And my deepest gratitude is reserved for my loved ones. Firstly Samya Jabour for her support during the most difficult times of my PhD. You are a champion and I will forever thank you for your efforts. My parents Stanislaw and Czeslawa have been my corner stone throughout my life and the love they provide has been my biggest motivation. As has been the loving encouragement received from my dearest partner Suzy Bates, numerous friends, and extended family. Thank you.

Contents

List of Figures

List of Tables

List of Symbols, Variables, and Units

Age	Age of the forest	years
BA	Basal area	m^2 ha^{-1}
CAI	Current annual increment	m^2 ha^{-1} yr^{-1}
DBH	diameter at breast height	cm
ET_p	Pasture evapotranspiration	m yr^{-1}
ET_f	Forest evapotranspiration	m yr^{-1}
ET	Evapotranspiration	m yr^{-1}
E_o	annual potential evapotranspiration	m yr^{-1}
ε	light-use efficiency	g MJ^{-1}
$g_{s\ max}$	maximum stomatal conductance	cm s^{-1}
g_s	stomatal conductance	cm sec-1
g_c	canopy conductance	cm sec-1
G	Above ground productivity	m^3 $ha^{-1}yr^{-1}$
k	Sapwood hydraulic conductivity	m^3 $m^{-2}sec^{-1}$
L_{max}	maximum reduction in average streamflow yield	mm
LA	Leaf area	m^2
LAI	Leaf area index	m^2(leaf) m^2(ground)
MAI	Mean annual increment	m^2 ha^{-1} yr^{-1}
P	Precipitation	mm
Pmax	Maximum forest growth increment	m^3 $ha^{-1}yr^{-1}$
Q	Solar Radiation	μ mol m^{-2} sec^{-1}
Q_a	Canopy absorbed radiation	μ mol m^{-2} sec^{-1}
Q_t	Observed runoff	m^3 day^{-1}
q	Sap flux density	mL cm^{-2} hr^{-1}
R_n	net radiation	W m^{-2}
R_j	Stem resistance	Pa hr-1 kg^{-1}
$\overline{r_s}$	stomatal resistance	sec^{-1} cm^{-1}
ΔS	changes in soil water storage	J m^{-2} day^{-1}
SA	Sapwood area	m^2
SA_{BH}	Sapwood area at breast height	m^2
SA_{CB}	Sapwood area at crown base	m^2

t	Temperature	^{o}C
T	Transpiration	m yr^{-1}
$Tmax_{sf}$	time of maximum yield reduction	years
$Tmax_{sf}$	time of maximum forest growth rates	years
VPD	Vapour Pressure Deficit	Pa
w	plant available water capacity	-
w_f	forest available water capacity	-
w_p	pasture available water capacity	-
W	Soil moisture	mm
ΔW	Soil water deficit	mm
WUE	Water use efficiency	m^3 (stem) m^{-3} (water)
ψ_{max}	Pre-dawn leaf water potential	Pa
ψ_l	Leaf water potential	Pa
z	Height of LiDAR hit	m

Chapter 1: Introduction

1.1. Context and background of the water resource issue

Forest disturbance caused by timber harvesting or bushfire processes leads to changes in structure and density of natural forests, which causes changes in evapotranspiration (*ET*) and hence streamflow over the regeneration period. After the 1939 bushfires in mountain ash forest (*E.regnans*) of Melbourne's water catchments, a relationship between forest age and streamflow yield was found to suggest that regenerating forests use more water than mature forest (Langford, 1976). Experimental studies of these findings have been confirmed with a large body of research identifying the causal processes (Kuczera, 1987; Vertessy *et al*., 1993; Vertessy *et al*., 1996; Watson, 1999; Watson *et al*., 1999a; Vertessy *et al*., 2001; Watson *et al*., 2001; Feikema *et al*., 2006; Pfautsch *et al*., 2010).

Forested catchments of south-eastern Australia are very dynamic ecosystems regularly subject to land cover disturbance. In recent history, Victoria has had 1.12 million ha burn in 2002/03; 1.15 million ha burn in 2006/07; and an area 30% of Melbourne's water catchments burn in 2008/09. In 1939, an area of almost 2 million ha burnt in Victoria, whereas in Tasmania only 265,000 ha burnt in 1967. The intensity of the burns over these regions has been highly variable, which effectively resulted in highly variable regeneration processes and hence post-disturbance *ET* rates. As well as bushfire disturbances, management of State Forests in both Tasmania and Victoria involves a range of silvicultural practices that harvest vast regions of timber-producing land with 60 to 100 years logging rotations. The scale of natural and anthropogenic land cover disturbance in forested catchments is having a significant effect on future streamflow trends.

In Australia, important water supply catchments are often largely forested, particularly in the mountainous terrain of the high yielding catchments supplying our large cities and the Murray Darling Basin. For example, the extensively forested north east of Victoria occupies only 2% of the Murray Darling Basin but produces 38% of its inflows (North East Catchment Management Authority, 2004), and almost all of Melbourne's water is supplied from forested catchments (Vertessy *et al*. 2001).

Despite this, no study has developed a generalised approach for accurate assessment of how broad-scale changes in forest structure influence *ET*. This substantial knowledge gap imposes serious limitations on our ability to predict future water availability from forested catchments.

1.2. Managing regenerating forest water use

Kuczera (1987) generalised the relationship between forest age and streamflow using rainfall and runoff data from eight forested catchments subject to the 1939 bushfire, and the resulting model is cited as the well-known "Kuczera Curve" shown in figure 1.1. The Kuczera Curve shows that two years after an old-growth forest disturbance, annual streamflow average begins to decrease and reaches its lowest value for forests 27 years of age, before a gradual recovery to pre-disturbance streamflow levels when the forest reaches maturity. In the 1990s, Victorian forest management agencies predicted the effects of planned forestry operations in Ash type forests of Melbourne's water catchments using the Kuczera curve and forest age data, without accounting for forest water use variation due to other environmental influences (Watson, 1999).

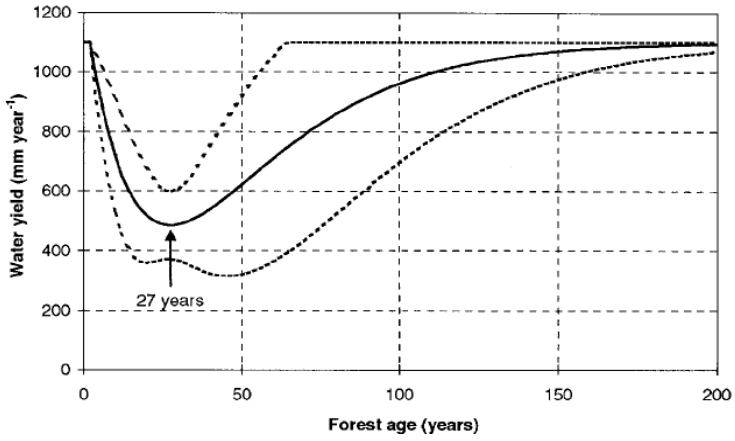

Figure 1.1: The Kuczera Curve (with 90% confidence limits) predicting water yield decline from forest age in Mountain ash forests. Minimum yield is predicted to occur when the forest is 27 years old

In recognising the inaccuracies in streamflow predictions that assume spatial invariance of the forest water use versus age relationship, Watson (1999) developed a process-based model call Macaque to represent the *ET* process with spatially variable parameters. Over the past decade, Macaque has been applied to manage the forested

water resource subject to planned forestry operations and bushfire disturbance in Victoria (Feikema *et al*., 2006). Macaque consists of more than 70 parameters, and quantifies spatiotemporal changes in *ET* using data from *E.regnans* forest to empirically derive a canopy Leaf Area Index (*LAI*) versus age relationship, and stomatal conductivity (g_s) versus age relationship.

For Macaque's *ET* estimates to be data-driven with site-specific information, extensive measurements of *LAI* and g_s within and above the canopy are required. Unfortunately, quantifying g_s of *E.regnans* is difficult due to their great heights (>65m), and calculations of *LAI* is complicated by the vertical orientation of *E.regnans* leaves (England & Attiwill, 2006) and line-of-site obstruction by understorey vegetation. There are also challenges in measuring seasonal and inter-annual variability of *LAI* due to site-specific effects of water deficit on leaf production rates, expansion rates, size, senescence and shedding. For these reasons, spatiotemporal estimates of *LAI* and g_s are highly uncertain and strongly influenced by the site-specific conditions during and prior to data collection.

Applying Macaque to forest types other than *E.regnans* is also inaccurate as the model does not empirically quantify forest water use in non-ash and mixed-species forest. Even though there is evidence that similar, although subdued, responses to land-cover disturbance occur in such forests (Cornish, 1993; Cornish & Vertessy, 2001; Lane & Mackay, 2001; Roberts *et al*., 2001; Bren *et al*., 2010; Macfarlane *et al*., 2010), Macaque assumes non-ash forest types have a constant water use equivalent to old-growth conditions. The challenges in measuring spatiotemporal changes in *LAI* and g_s has meant Macaque has been applied across vast regions of Victoria and Tasmania with empirical data for *E.regnans* forest from small site-specific experiments, and assumptions for non-ash forest types known to be unreliable. As Macaque also requires site-specific information on catchment level understorey *LAI* and g_s, similar challenges also exist in quantifying spatiotemporal changes in understorey *ET* rates.

Dynamic forested catchments that supply water for downstream communities consist of a range of forest types and age classes, transpiring at different rates and contributing variable amounts of water depending on site-specific conditions. For this

reason, it is necessary to quantify the impact of vegetation dynamics on the water resource so that decision makers, planners, and managers of the forested water resource optimise drought security with appropriate restrictions, allocations, and deliveries of water resource.

1.3. The need for a data-driven model framework

Forest hydrology models in south-eastern Australia would benefit greatly from a data-driven methodology that quantifies hydrologically related plant physiological processes to explain spatiotemporal forest water use with site- and species-specific information. This dissertation aims to address this significant limitation in forest hydrology by developing forest growth models that quantify hydrologically relevant forest regeneration processes. It is argued that present forest hydrology models, used for policy applications in south-eastern Australia, undermine the importance of existing forest inventory and forest mensuration databases for managing the forested water resource. Detailed forest inventory data exists for most catchments in south-eastern Australia, and this information needs to be used more effectively to manage future streamflow trends.

Using typical forest inventory data, this dissertation quantifies spatiotemporal stand volumes and stand basal area (*BA*) for a set of stream gauged catchments, as both of these forest characteristics represent hydrologically relevant changes in regeneration processes. For example, Kuczera (1987) chose the gamma equation to represent decadal streamflow trends as the non-linear curve was considered to reflect changes in forest growth rates. Generally speaking, eucalyptus growth rates are the inverse of the Kuczera curve along the time axis as forest growth curves have an initial rapid increase in growth rates followed by a gradual reduction in growth rates after a maximum growth rate is reached. The present dissertation is the first published study that uses forest inventory data to produce forest growth models to explain streamflow trends in hydrological time series.

The relationship between forest productivity and forest water use is an important concept in forest hydrology and its recognition has been largely omitted in Tasmania's and Victoria's forest management systems. The timber industry optimises its timber resource yield by harvesting trees at an age when sawlog timber growth rates are slow, as it

becomes more economically viable to harvest the timber and regenerate a faster growing forest. Tasmania's and Victoria's sustainable timber yield calculations determine the harvesting rotations, and hence forest age and water use over State forests, with no explicit scientific evaluation (except for Melbourne's water catchments) to determine appropriate restrictive measures on the rate of disturbance in order to account for catchment-specific water resource demand (Forestry Tasmania, 2007; Vanclay & Brack, 2008). Using forest inventory data in forest hydrology models allows for water use to be integrated into forest agency data management systems. Such an approach would allow for relevant policy makers to create integrated catchment management policies with data-driven models that are able to quantify streamflow for environmental and societal needs once the effects of bushfire disturbance or timber harvesting is accounted for.

Over the past two decades, a large body of forest hydrology research has scaled up tree-level water use to the catchment-level using sap flow measurements (Dunn & Connor, 1993; Vertessy *et al*., 1995; Haydon *et al*., 1996; Vertessy *et al*., 1997; Forrester *et al*., 2009; Macfarlane *et al*., 2010; Pfautsch *et al*., 2010). The research suggests differences in *ET* with age are overwhelmingly a result of differences in stand sapwood conducting area (*SA*). As *BA* is a good predictor of *SA* (Vertessy *et al*., 1997), accurate spatiotemporal *BA* estimates over forested catchments provides site- and species-specific information for explaining spatiotemporal forest water use. For this purpose, the present study produces a novel methodology for generating high resolution spatiotemporal *BA* estimates across large regional landscapes.

1.3. Research questions

The following research questions are addressed in this dissertation:

1. In Victoria and Tasmania, are existing forest hydrology models data-driven with vegetation dynamics that affect forest water use?
2. Does plant physiological theory support the use forest growth models to explain forest water use?
3. Can forest inventory data be used to generate spatially variable forest characteristics that are hydrologically relevant and at a resolution useful for forest hydrology research?

4. Can climate filters be used to remove the climatic variability in streamflow in order to quantify a decadal streamflow trend attributed to forest regeneration processes?
5. Can forest inventory data be used to generate spatiotemporal forest growth models to explain streamflow trends in hydrological time series during the regeneration period of a timber producing forest?

1.4. Aims

The overarching aims of this dissertation are to:

- Use readily available forest inventory data to quantify the forest regeneration process with forest characteristics useful for forest hydrology research.
- Develop a climate filter that removes climatic variability in streamflow, and undertake a simulation exercise that determines how parameter inference is affected by data availability of the hydrological time series and the extent of the land-cover disturbance.
- Demonstrate that spatiotemporal forest growth models may be used to explain catchment-level trends in forest water use over the forest regeneration period.

1.5. Thesis outline

Chapter two reviews Tasmania's and Victoria's forest hydrology models used to inform policy makers of the potential impacts of land cover disturbance on the water resource. The review provides a critique on how existing models represent the forest regeneration processes that influence forest water use.

Chapter three reviews plant physiological characteristics that regulate the soil-to-atmosphere water flow pathway of timber yielding forest types and plantations, with the overall objective to identify the processes that affect spatiotemporal variability in forest water use. The review also explores the relationship between plant physiological regulators of forest productivity and water use, to provide scientific reasoning for using forest inventory data to explain decadal streamflow trends.

Chapter four provides a detailed overview of the forest hydrology model structure used in this dissertation to explain streamflow trends in hydrological time series. A

description of the study site, field measurements, forest inventory data, and hydrological time series is also presented.

Chapter five uses Light Detection and Ranging (LiDAR) data to produce a generalised approach for stratifying and characterising the structure of specific vegetation layers of a multilayered eucalyptus forest over a catchment. The methodology produces canopy profile indices of understorey and overstorey vegetation using mixture models with a wide range of theoretical distribution functions. The methodology is applied to permanent plot data to predict overstorey stand volumes and basal area, and understorey basal area of mountain ash forest.

Chapter six applies permanent plot data to mixed effects models to estimate the spatial heterogeneity and temporally polymorphic nature in forest growth over the catchments. Using both the logistic and gamma equations, parameter estimates of the forest growth models were determined for each catchment.

Chapter seven applies aggregated rainfall data to the climate filter sub-model of the overall model structure to explain the climatic variation in the hydrological time-series data. A simulation exercise is undertaken to determine: how the climate filter parameter inference is affected by the extent and duration of the hydrological time series; and how substantial a post-disturbance decadal streamflow trend needs to be for the model structure to accurately identify it.

Chapter eight spatially distributes the forest growth models to generate lumped to the catchment forest growth curves for evaluation against the modelled trends in streamflow data. The limitations of the present study are also discussed and recommendations for future research are presented.

Chapter nine provides a summary of the dissertation as well as specific conclusions found in the study

Chapter 2: Review of Tasmania's and Victoria's forest hydrology models

2.1. Introduction

This chapter provides a review of forest hydrology models, Macaque and TasLUCaS; both of which are designed to quantify impacts of land cover disturbance on streamflow in Victoria and Tasmania respectively. A review of model applications that address State level policy obligations is also undertaken to determine whether forest and water resource managers are provided with an accurate assessment of how forest harvesting and other land cover disturbances affect community water supply. First, an overview of the Kuczera curve is presented, as the Kuczera curve has contributed significantly to the development of both models, and hence overall management of forested water resource in both States.

2.2. Kuczera curve

In 1939 a bushfire burnt a large portion of Melbourne's water-supply catchments resulting in significantly reduced streamflow during the following decades. Approximately 53% of Melbourne's water supply catchments are fire sensitive ash-type species (i.e. *E.regnans, E.delegatensis and E.nitens)* that were extensively and irreversibly damaged by the fires. The rest comprise of fire resistant drier mixed-species (i.e. *E.obliqua* and *E.viminalis)* that survived the fires with thick fire-resistant bark and epicormic shoots to replace the scorched crown. Kuczera (1985) analysed data from eight catchments affected by the 1939 bush fire to develop a model that estimated reductions in average catchment streamflow below old-growth forest streamflow levels. In the study, Kuczera (1985) assumed there was no impact of burnt mixed species forest on long-term streamflow trends as mixed species survive fire.

The effect of natural variations in climate poses a fundamental problem in detecting long-term streamflow trends during regeneration, and to describe this variation Kuczera (1987) used Langford's (1976) climate-index model. This involved generating climate indices to represent the climatic variation with rainfall records and

pre-disturbance streamflow records; and by subtracting the effects of climate indices from post-fire streamflow records the residuals represent streamflow changes due to forest regeneration. Langford's (1976) methodology required three assumptions: (1) a moderate to long term pre-fire streamflow record (ten or more years) to calibrate the climate-index model; (2) the pre-fire streamflow data needed to represent old-growth forest unaffected by earlier fires; and (3) pre-fire vegetation needed to be killed and regenerating over most of the catchment to identify a trend.

Kuczera (1987) was able to relax the first two assumptions by replacing Langford's linear regression technique with a non-linear curve that was consistent with available evidence on long-term streamflow recovery. The assumed recovery recognised streamflow reductions are largely explained by post-disturbance forest growth rates, and as growth rates of mature or old-growth ash are very small, pre-disturbance streamflow in old-growth catchments is almost stationary with a quasi hydrologic equilibrium. Figure 2.1 shows the general shape of the long-term streamflow trend curve, which is consistent with available evidence on stand growth rates (West & Mattay, 1993). The exact shape of the post-disturbance streamflow trend curve was *a priori* unknown and regression theory, with least squares error assumptions, was used on streamflow data to infer posterior distributions and confidence limits of hydrologic parameters. These parameters included maximum reduction in average yield (L_{max}) and time to maximum yield reduction ($1/K$) following bushfire.

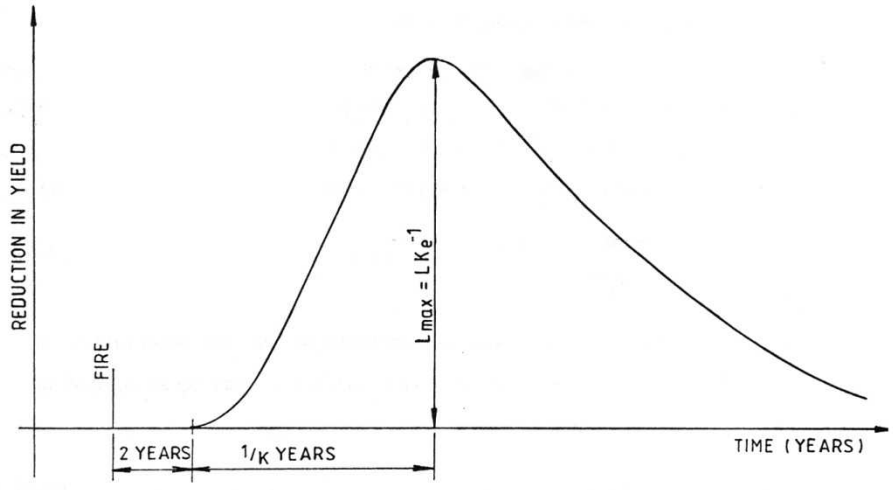

Figure 2.1: The Gamma curve used by Kuczera (1985) to represent vegetation-induced reduction in streamflow

The results found that all eight catchments attained their maximum streamflow reduction relative to old growth forest about 20-30 years after disturbance. No significant streamflow increases were evident immediately after the disturbance. The resulting fits were satisfactory with goodness of fit criteria R^2 ranging between 0.77 and 0.9. Kuczera (1987) regionalised the model outcomes using an empirical Bayes approach to relate the estimated hydrologic parameters to measured catchment characteristics such as forest composition. It was concluded that for a catchment with 100% regenerating ash forest with pre-disturbance annual streamflow of 1100 mm, the regional model estimated a maximum yield reduction of 615 mm approximately 27 years after disturbance, as shown in the Kuczera curve of figure 1.1.

2.3. Macaque: Victoria's forest hydrology model

The Kuczera curve is a useful representation of the potential impacts of land cover disturbance on the water resource but the challenge lies in extrapolating the curve so that it is useful for a broader range of environmental conditions. For this purpose, Watson (1999) developed a process based model that evaluates the effects of land cover disturbance on streamflow with adjustable parameters based on site specific conditions. The Macaque model (Watson 1999) simulates temporal streamflow predictions quantified by Kuczera (1985) by hypothesising catchment water yield changes could be explained by changes in Leaf Area Index (*LAI*) and stomatal conductance (g_s). The model operates at a daily time-step to simulate predictions over 100 years and focuses on large-scale forest hydrological processes.

Macaque contains over 70 parameters and although there are dozens of parameters to calibrate, in practice most are given default values and calibration involves two parameters; the precipitation scalar to adjust the rainfall surface (water input), and the ratio of hydraulic gradient to the surface gradient to control the internal drainage rate (transfer function). The present critique of Macaque focuses on three modelling components that quantify changes in *ET* with forest age. These are: (1) canopy *LAI* versus age relationship (*LAI:Age* curve), (2) the spatial distribution of *LAI* over the catchment, and (3) the g_s versus age relationship.

2.3.1. Ash eucalypt canopy LAI versus age relationship

The central component in Macaque is the representation of the canopy LAI versus age relationship (*LAI:Age* curve), which was produced with a set of allometric relationships illustrated in the flow chart of figure 2.2. The first step involved an allometric model relating destructive measurements of *LA* of 78 individual *E.regnans* trees from four stands, with measured tree diameter at breast height (*DBH*) and mean *DBH* for the trees in the stand to which the tree belonged too. In the second step, the allometric model was applied to a database of 2079 *DBH* measurements from 17 *E.regnans* stands in order to derived *LAI* predictions for each stand. Thirdly, the 17 stand LAI predictions where plotted against stand age and adjusted for variations in stocking rates to produce the *LAI:Age* curve. An evaluation of the regressions used to construct the *LAI:Age* curve is presented in the next section.

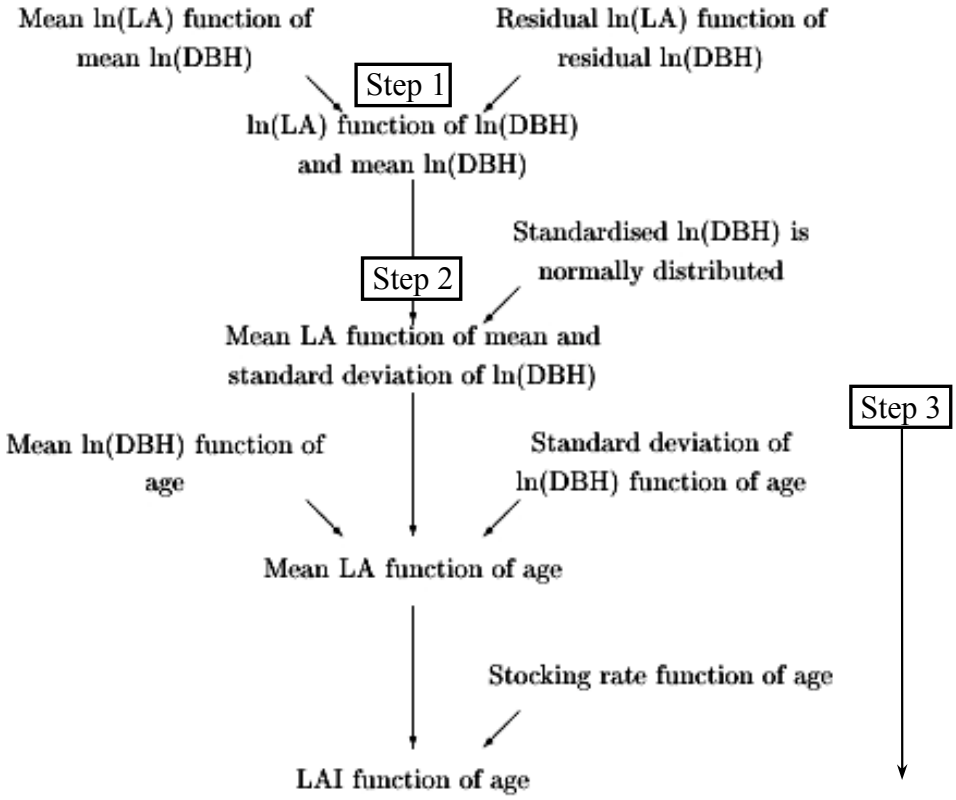

Figure 2.2: Flow chart summarising the steps taken to establish the relationship between *LAI* and age (from Watson, 1999)

2.3.1.1. Calculation of ln(LA) versus ln (DBH) and mean ln(DBH) (Step 1)

Data from four single aged stands, aged 5, 16, 56, and 225 years old were used to predict *LA* from *DBH* and mean *DBH* of an *E.regnans* forest stand. Figure 2.3 plots tree *LA* versus *DBH* along the log-log axis showing clustering of data for each stand as well as the sample mean (white circle) of each stand (Watson *et al*., 1999a). The linear regression lines for the 5, 16, 56, and 225 year old stands in figure 2.3 have an R^2 of 0.898, 0.929, 0.836, and 0.085 respectively.

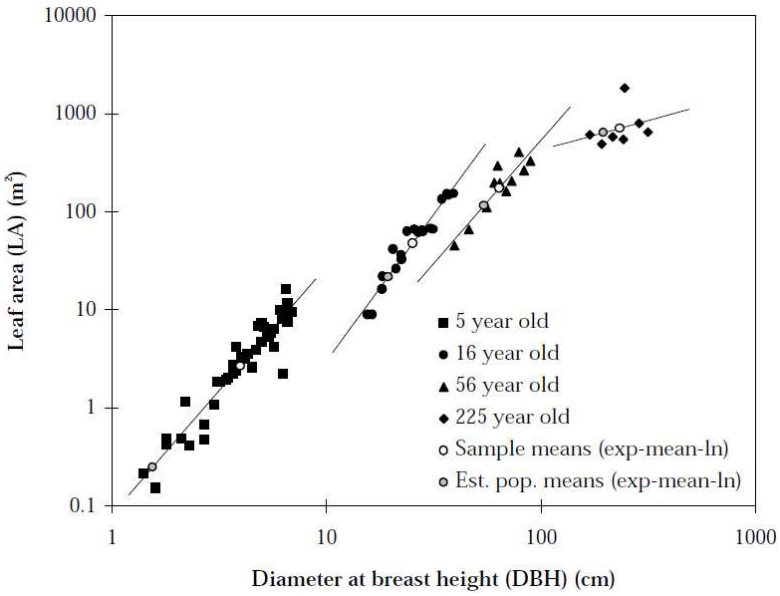

Figure 2.3: Sample *LA* versus *DBH* for four stands plotted on the log axis, which also provides; regression lines, sample means (white circles) and population means (grey circles) estimated from simple regression equations outlined below (from Watson, 1999).

2.3.1.2. Calculation of mean stand LA versus mean and standard deviation of ln(DBH) (Step 2)

In order to predict stand *LA* with the tree-level relationship in figure 2.3, each stand's sample mean and population mean of *DBH* was required. This complicated the situation as the *LA* data was not always measured in conjunction with the *DBH* measurements of all trees in the stand population. For this reason, population mean *ln(DBH)* was approximated from a *DBH* versus age relationship derived from a 17 stand database consisting of 2,079 *DBH* measurements, as shown in Figure 2.4 (a). The youngest two stands in figure 2.4 (a) were corrected in 2.4 (b) by hypothesising

that regeneration does not take place until sometime after age zero. In maximising R^2, the calibrated adjustment of 5.04 was higher than expected for the hypothesised delay in forest development. Thus, Watson (1999a) acknowledges the model is not reliable at predicting mean *DBH* for forests younger than or close to five years of age.

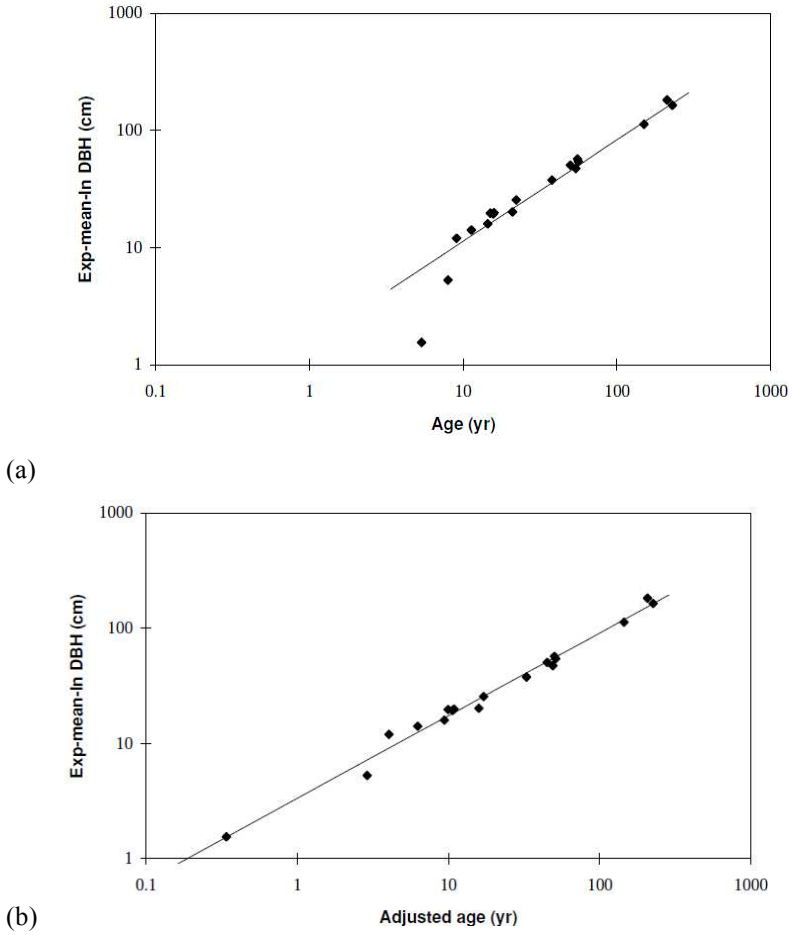

Figure 2.4: Logarithmic plot with the line of best fit for (a) *exp-mean-In DBH* versus ages, and (b) *exp-mean-In DBH* versus adjusted ages (from Watson, 1999).

As the regression in figure 2.4(b) uses a dataset different to the one used to construct the *LAI* versus *DBH* relationship in figure 2.3, it was necessary to assume the sampled values of *ln(DBH)* from the 17 stands were uniformly distributed in order to allow for *LAI* estimates of these stands. Figure 2.5 provides standardised *ln(DBH)* data plotted against the standard probability distribution function to show the distributions were irregular, multi-modelled, and peaked (Watson *et al*., 1999a).

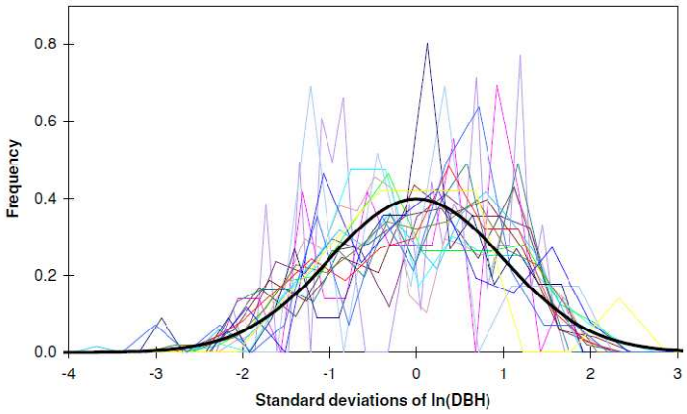

Figure 2.5: Histograms (using lines instead of bars) of *ln(DBH)* values within each stand; standardised and scaled to have zero mean, unit standard deviation, and unit area. A standard normal probability distribution function is provided for reference (from Watson, 1999).

To derive stand *ln(LA)*, the population means of *ln(DBH)* at age 5, 16, 56, and 225 was used even though figure 2.3 shows a clear offset between each stand's sample (white circle) and population mean (grey dot); indicating the *LA* samples were not representative of the stand populations with a bias towards sampling larger trees (Watson *et al*., 1999a). Using this estimated population mean of *ln(DBH)*, figure 2.6(a) shows the linear regression between mean stand *ln(LA)* and mean stand *ln(DBH)*. In figure 2.6(a), the 225 year old stand represents a population mean derived from a *LA* sample with R^2 of 0.085, whereas the five year old stand with *BA* estimates was considered dubious as a result of the required adjustment undertaken in figure 2.4. Using the relationship in figure 2.6(a), the final model for predicting *LA* of any tree in a stand given its *DBH* and mean *DBH* of an *E.regnans* forest stand was obtained. Figure 2.6(b) applies the model to *LA* data and shows the 95% confidence limits.

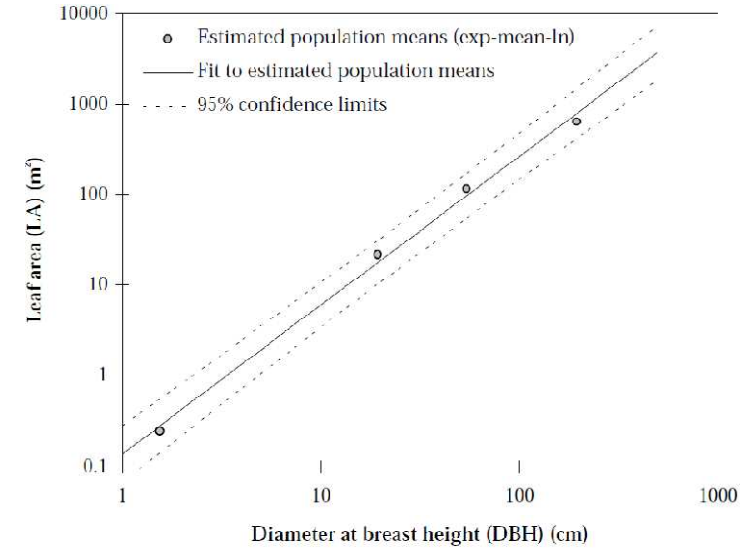

(a)

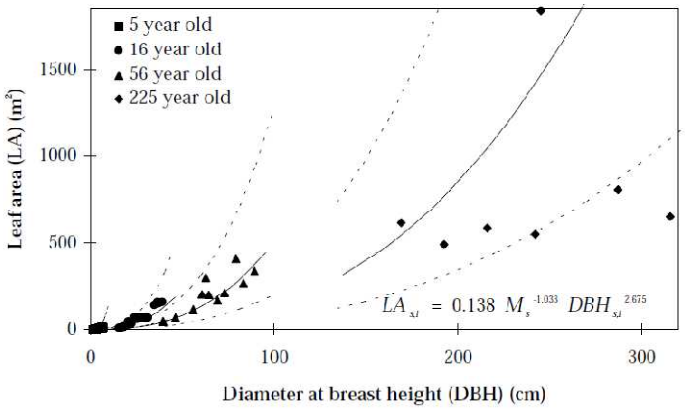

(b)

Figure 2.6 (a) Estimated variation in (estimated) population mean between stands *ln(LA)* and *ln(DBH)* and; **(b)** *LA* versus *DBH* for the four stands with 95% confidence limits (dashed lines) (from Watson, 1999).

2.3.1.3. Constructing the LAI versus age relationship (Step 3)

The *LAI*:*Age* relationship was constructed using the 17 stands with *DBH* measurements and the model predicting *LA,* which meant mean *LA* for trees within each stand needed to be derived. As shown in the flow chart of figure 2.2, the procedure required an estimation of the variance of *ln(DBH)* with the assumption that the distribution of *DBH* for all stands had a normal distribution. However, figure 2.5 shows the distributions were actually irregular, multimodal, and peaked. Figure 2.7 shows the line of best fit for variance of *ln(DBH)* versus adjusted age; with an R^2=0.504 suggesting the variance of *ln(DBH)* on age did not fit the data well.

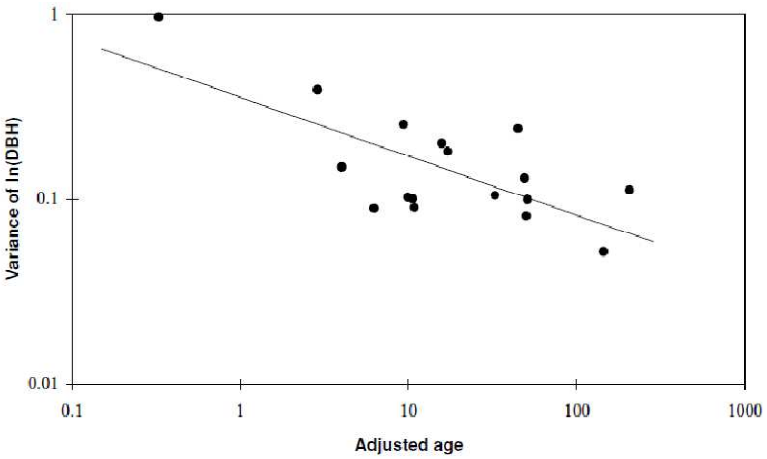

Figure 2.7: Line of best fit for variance of *In(DBH)* versus age for each stand (from Watson, 1999).

The above assumptions and regression equations were then used to construct the *LAI:Age* curve for the 17 forest stands. Results in figure 2.8(a) show a great deal of scatter, which was improved in Figure 2.8 (b), by correcting the relationship based on each stand's deviation in stocking rates; even though the 17 stands were meant to represent healthy fully stocked single-aged *E.regnans* stands. The data used in the relationship represents fully stocked stands, which are rare in native forests and for this reason more scatter would be expected for typical forest stands found in catchments requiring forest hydrology management. The final *E.regnans LAI:Age* curve is provided in figure 2.8 (b).

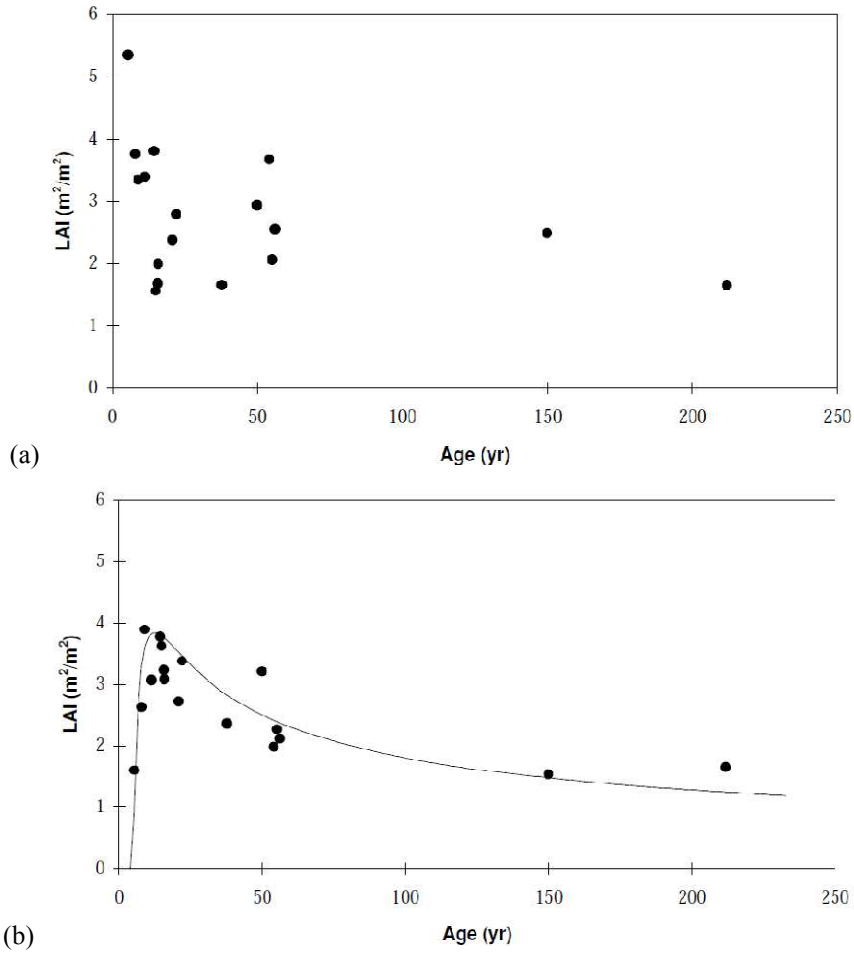

Figure 2.8: Predicted *LAI* versus age for healthy, fully stocked single-aged stands (a) uncorrected, and (b) corrected for variability in stocking rate and the final model is superimposed (from Watson, 1999).

It is important to recognise that the *LAI:Age* relationship relied on *LA* measurements of 78 individual trees from four stands. The methodology fails to recognise the seasonal and inter-annual variability of *LAI* due to site-specific effects of water deficit on leaf production rates, expansion rates, size, senescence, and shedding. For this reason, extrapolating the *LAI* model in space and time is full of uncertainty as measurements at one point in time were strongly influenced by the site-specific conditions during and prior to data collection.

2.3.2. Non-ash eucalypt and non eucalypt LAI versus age relationship

A large portion of Melbourne's water catchments consist of non-ash eucalypts and less data is available for empirically quantifying long-term trends in *LAI* for these species. For this reason, Macaque assumes such species have an initial rapid increase

in *LAI* for the first 5 to 10 years followed by a constant species-specific *LAI,* as shown in figure 2.9. The species-specific constant in table 2.1 was derived from areal average remotely sensed *LAI* values using the methodology described in section 2.3.3. For all non-ash species listed in table 2.1, the curve in figure 2.9 results in streamflow increase for the first 5-10 years after disturbance of old-growth, followed by a recovery to constant old-growth streamflow levels. These estimates are known to be incorrect as non-ash species follow a similar streamflow trend to ash-species (Cornish, 1993; Cornish & Vertessy, 2001; Lane & Mackay, 2001; Roberts *et al*., 2001; Macfarlane *et al*., 2010).

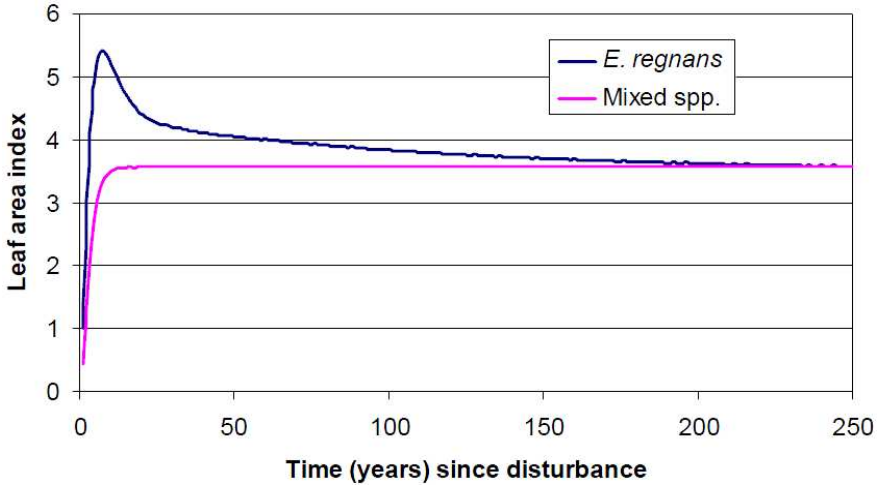

Figure 2.9: *LAI:Age* curve for *E.regnans* and mixed species (from Feikema *et al*., 2006)

Table 2.1: *LAI:Age* curve types and long-term trends in *LAI* for main vegetation types in Melbourne's water catchments (from Feikema *et al*., 2006).

Forest type	*LAI* curve type	Maximum *LAI*	Long term *LAI*
Acacia dealbata	Constant*	3.91	3.91
E. delegatensis	Watson (1999)$_2$	5.7	3.2
E. nitens	Watson (1999)$_1$	6.0	3.5
E. pauciflora	Constant*	2.5	2.5
E. regnans	Watson (1999)$_1$	6.0	3.5
E. sieberi	Constant*	2.94	2.94
Mixed spp.	Constant*	3.56	3.56
Rainforest	Constant*	3.77	3.77
Heath	Constant*	2.50	2.50
Leptospermum spp.	Constant*	3.35	3.35
Grassland	Constant*	1.50	1.50
Not vegetated	Constant*	3.15	3.15

* Constant after first 5 to 10 years after establishment derived from remote sensed images; 1 Watson (1999), Equation 8.45; 2 Watson (1999), Equation 8.45. Same as 1 but with *LAI* lower by 0.3

2.3.3. Spatial distribution of LAI over the catchment

With the use of Landsat TM images from four different years, two attempts were made by Watson (1999) to extrapolate the *LAI:Age* curves and develop spatial maps of total *LAI*. Shade corrections where performed on the images to remove the effects of illumination and viewing angles. The shade-corrected images were used to calculate the normalised difference vegetation index (*NDVI*), which recognises the positive correlation between vegetation amount and near infra-red reflectance, and the negative correlation between vegetation amount and red reflectance. The shade-corrected *NDVI* data were used to produce transformed *NDVI (TNDVI)* values, which did not improve results but converts the values into *LAI* estimates.

In the first attempt, Watson (1999) plotted shade-corrected *NDVI* against a dataset of ground measured *LAI* (using Li-Cor PCA instrumentation) to find no correlation, as shown in figure 2.10. A second attempt involved using a forest age dataset from logging coupes and fire affected regions in the imagery to formulate a relationship between shade-corrected *NDVI* (averaged over region/coupe) and age (figure 2.11). As there were four images for each coupe/region, figure 2.11 shows four values for each area linked by a line. The most notable feature in figure 2.11 is that *NDVI* does

not vary greatly for vegetation between 20 and 240 years of age, raising uncertainty for *LAI* estimates using age specific *NDVI* maps.

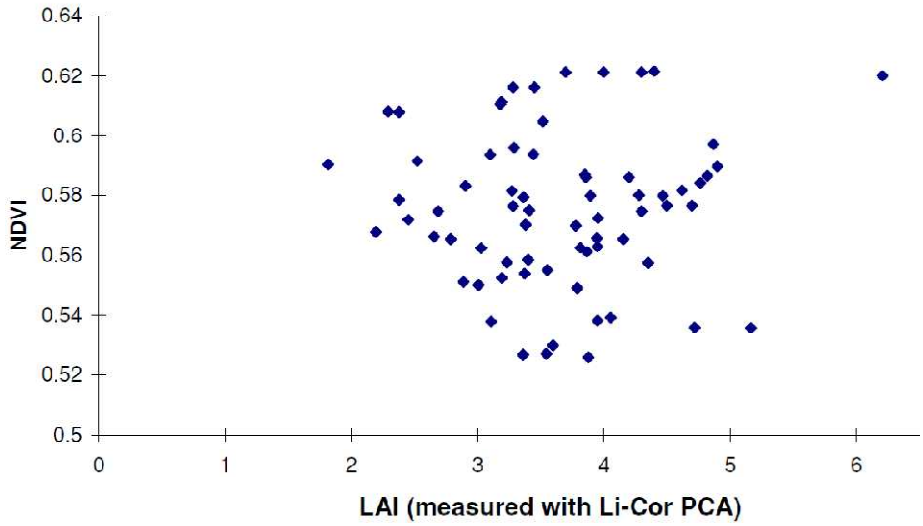

Figure 2.10: 50 m radius-averaged *NDVI* derived from shade corrected imagery plotted against ground measured *LAI* using a Li-Cor PCA (from Feikema *et al*., 2006).

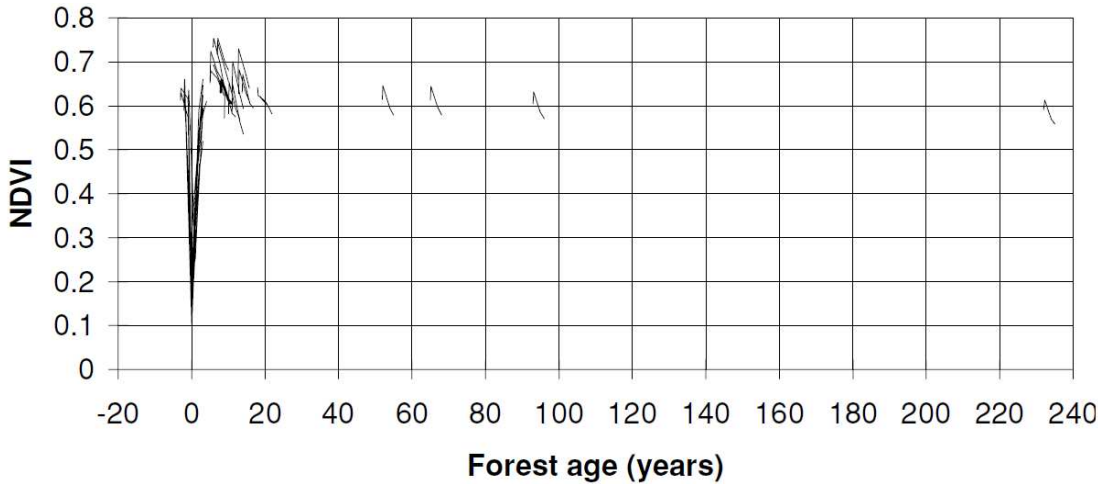

Figure 2.11: The relation between shade-corrected *NDVI* and forest age for *E.regnans* (from Feikema *et al*., 2006).

Watson (1999) examined whether total *LAI* (Li-Cor PCA) and *NDVI* have the same relationship with forest age. This involved grouping the Li-Cor PCA data of figure 2.10 into forest age averages, and superimposing the results over the *NDVI* versus age plot, as shown in figure 2.12. For a given forest age, the average Li-Cor PCA values (circles in figure 2.12) were derived from data with a high variance, as shown in figure 2.10. The dark line in figure 2.12 represents the *E.regnans Total LAI*:*Age*

equation, where one parameter was set as a default theoretical maximum value, and the other two parameters were adjusted subjectively by eye to give the best visual match between estimate (*TNDVI*) and measured *LAI*. Note in figure 2.12, that although average Li-Cor PCA values were used to fit the model by eye, the average Li-Cor PCA values for 50-60 year old forests are highly variable and within the same range as 10-30 and 200 year old forests.

Even though age was not well correlated with *TNDVI* or Li-Cor PCA values, the *E.regnans Total LAI*:*Age* model only uses forest age data to extrapolate the model. The model is also used to estimate understorey *LAI* by subtracting *Canopy LAI* in figure 2.8(b) from *Total LAI* in figure 2.12.

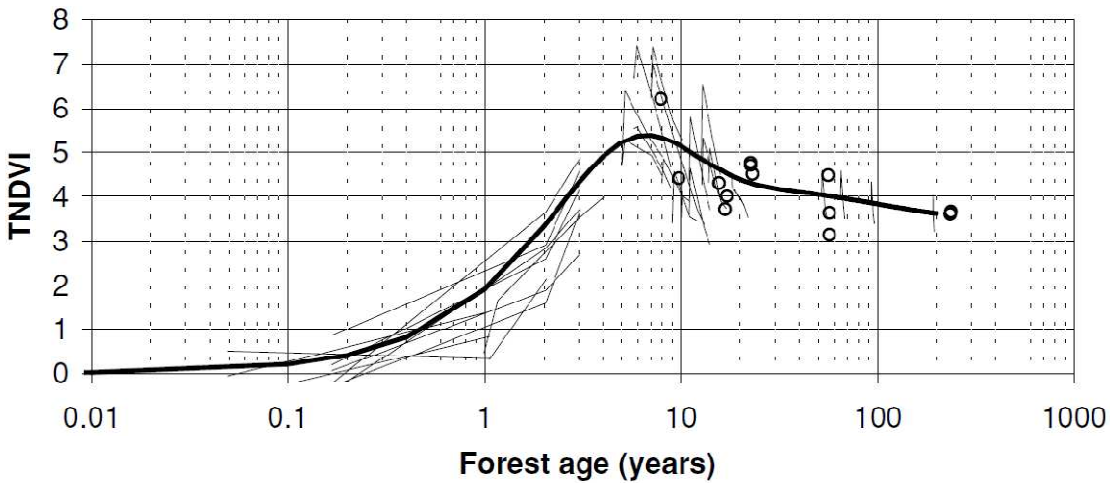

Figure 2.12: Total *LAI* of *E.regnans* forest. The circles are ground measurements of *LAI* made using a Li-Cor PCA. The short thin lines are *LAI* values estimated using (shade-corrected) *TNDVI* derived from Landsat TM imagery. The long curved line is the predictive model (from Feikema *et al*., 2006).

2.3.4. Stomatal conductance versus age relationship

The Macaque model requires maximum stomatal conductance ($g_{s\,max}$) for canopy and understorey vegetation. However, these values vary with species, leaf age, and forest age (White, 1996). Watson (1999) integrated a $g_{s\,max}$ sub-model into Macaque to have $g_{s\,max}$ decline with age for both canopy and understorey vegetation. The conceptual sub-model assumes that mean daily sapwood velocity is constant with age (Dunn & Connor, 1993; Vertessy *et al*., 1997), therefore changes in $g_{s\,max}$ with age may be determined with a relationship between *SA/LAI* and forest age. Such a relationship, shown in figure 2.13, was formulated by scaling *E.regnans SA*

measurements from 13 sites to a stand level using a *SA/DBH* relationship (Watson, 1999). For this relationship to be applied, corresponding *LAI* values were required using equations that related *LA* to *DBH* in section 3.3.1.3*;* hence were subject to the same uncertainty outlined above. The resulting $g_{s\ max}$*:Age* relationship is assumed to represent all forest types of both canopy and understorey vegetation without further evidence to suggest this is actually the case.

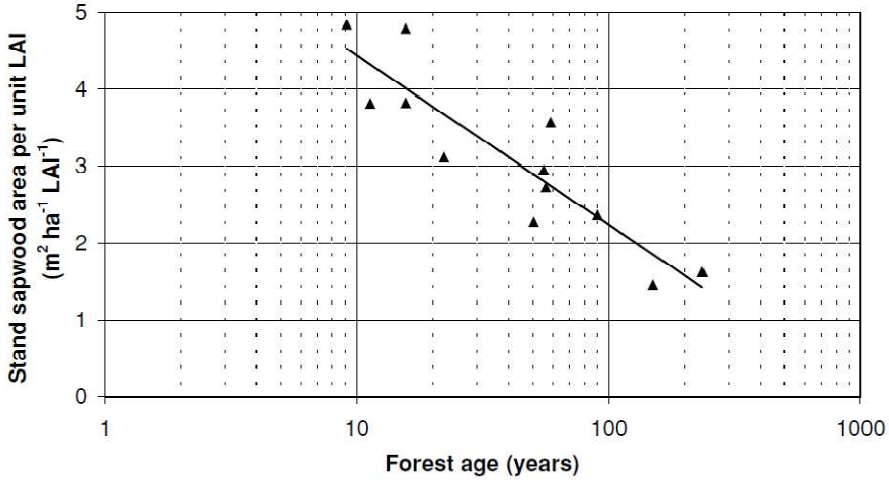

Figure 2.13: Stand sapwood area per unit leaf area, with power function fitted by linear regression (from Feikema *et al*., 2006).

2.3.5. Final model results

With the use of the relationships outlined above, the "simulated Kuczera" curve in figure 2.14 is Macaque's forest water use curve evaluated against the Kuczera curve by simulating streamflow trends using synthetic, noiseless climate data (Watson, 1999). It is evident Watson's curve is different to the Kuczera curve in many ways but most pronounced in the first several years after treatment. Figure 2.8 shows the *LAI:Age* curve included no data for forest stands less than five years of age and the three LAI estimates for 5-10 year old forests were highly variable. For these reasons, Vertessy (2001) recognised that the equations used to derive *LAI* values were not reliable for the first ten years. There are also differences in the curves after the initial peak, as the "Watson curve" was affected by uncertainly in the regression equations representing stands older than 56 years of age.

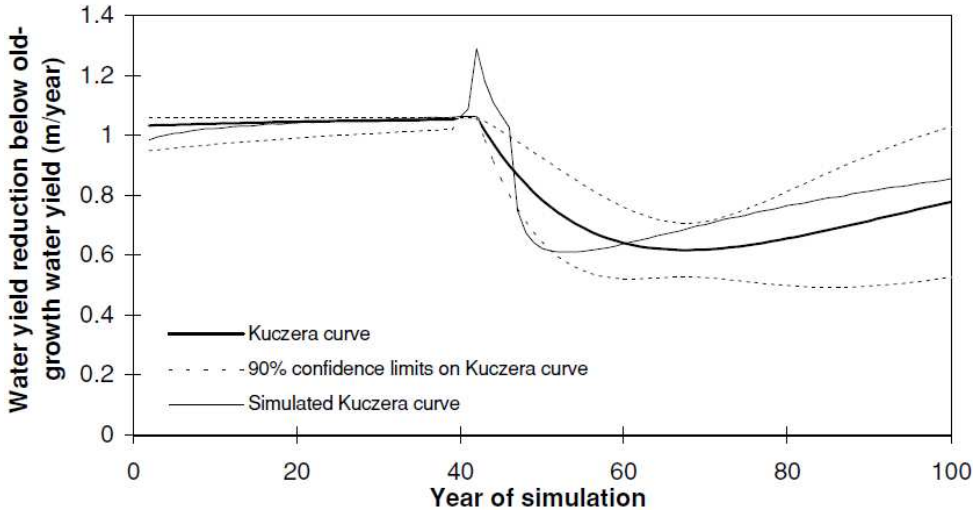

Figure 2.14: Simulation of the Kuczera curve using Macaque supplied with synthetic, noiseless climate data (from Watson, 1999).

2.4. Forest hydrology model applications in Victoria

Victoria has experience a long history of debate about the relative costs and benefits of timber and water production in State forests of Melbourne's water catchment. The Melbourne Water Resources Strategy, *21st Century Melbourne; a WaterSmart City, 2002,* again raised the issue of the impacts of forest harvesting activities on Melbourne's water supply, which resulted in the Government's White Paper, *Securing Our Water Future Together* ("the White Paper"). The White Paper stated (in Action 2.21) that the Government will, among other initiatives, undertake hydrological studies on the impact of logging on streamflow in State forests supplying water to Melbourne. Feikema *et al.* (2006) undertook the study with Macaque, and generated vegetation specific water yield curves for Department of Sustainability and Environment's (DSE) Integrated Forest Planning System (IFPS) to inform the forest industry of the impacts of various timber harvesting options on both timber and water yields. Below is a review of the work undertaken by Feikema *et al.* (2006) to determine whether Macaque can be data-driven and used to address the Government initiatives.

2.4.1. Melbourne's water supply (Macaque application)

Feikema *et al.* (2006) applied Macaque to the following eight catchments predominantly covered by State forests; Thomson, Armstrong Creek (Main and East), Cement Creek, McMahons Creek, Starvation Creek, Tarago and Bunyip. For

each catchment, changes in streamflow were modelled using vegetation type and age data. Vegetation data was amalgamated into eleven vegetation types: *E. delegatensis*, *E. regnans*, *E. nitens*, Rainforest, *Leptospermum* species, *E. pauciflora*, *A.dealbata*, Grassland, Heath, *E. sieberi*, and mixed species; and uneven-aged forests were assigned a single age class determined by the dominant age class. To apply Macaque using this data the below limitations and assumptions where identified.

2.4.1.1. Canopy and understorey LAI versus age curves

Section 2.3.1 outlined the methodology used to construct the *E.regnans* canopy *LAI:Age* relationship, focusing on applied assumptions that introduced uncertainty in the final result. Feikema *et al.* (2006) used the *LAI:Age* relationship to represent all ash eucalypts, even though they recognise that *LA* is likely to differ between ash species. Table 2.2 shows that ash eucalypts represent 41.5% of the study site, and as outlined in section 2.3.2 the rest of the vegetation is represented with a model where *LAI* rapidly increases for the first 5 to 10 years before becoming constant right through to old-growth (figure 2.9). This is a significant assumption known to be incorrect (Cornish, 1993; Cornish & Vertessy, 2001; Lane & Mackay, 2001; Roberts *et al*., 2001; Macfarlane *et al*., 2010). It is important to note that when Kuczera (1987) made the assumption there was no impact of burnt mixed species forest on long-term streamflow trends (as mixed species survive fires), this does not mean the assumption should be extended to logging of mixed species, which is the focus of this report. Based on table 2.1 and figure 2.9, Macaque erroneously assumes 58.5% of the study area has an initial increase in streamflow for the first 5-10 years followed by a constant pre-disturbance (old-growth) streamflow.

Table 2.2: Summary of catchment area and percentage of ash vegetation in the study areas

Catchment	Catchment Area (km2)	Ash Vegetation (%)
Thomson	476.52	37.8
Armstrong Creek	39.28	65.2
Armstrong Creek East	14.49	24.9
Cement Creek	14.25	91.2
McMahons Creek	39.52	49.7
Starvation Creek	31.31	51.2
Tarago	191	37.6
Bunyip	39.44	53.2
Total	845.81	41.5

Understorey *LAI* for ash eucalypts was determined by subtracting *Canopy LAI* (figure 2.8(b)) from *Total LAI* (figure 2.12). For non-ash forest types, understorey *LAI* was assumed to be half of *Total LAI* value estimated from the non-ash forest type curve in figure 2.9 and the remaining other half was assumed to be *Canopy LAI*. There is no empirical evidence to suggest this is the case and is likely to be unreliable considering the varied "non-ash forest types" in table 2.1 include both dry eucalypts and rainforest vegetation.

2.4.1.2. Spatial distribution of LAI curves

Forest type and age data were used to spatially distribute ash forest *LAI* values using table 2.1 and figure 2.9. As ash forest *LAI* curves in figure 2.8(b) and 2.12 were constructed in the Maroondah catchment, Feikema *et al.* (2006) undertook an adjustment to the spatially distributed *LAI* values over the study catchments based on each catchment's "wetness index" (Ellis *et al*., 1999); defined as *P/E*, where *P* was average annual rainfall and *E* was annual pan evaporation. Table 2.3 was constructed to determine the relative wetness index for each catchment, and "where appropriate" the *LAI* values were scaled. Accordingly, it was assumed the *LAI* value for Tarago catchment needed to be scaled down by 80% whereas all other catchments required no adjustments for reasons unexplained. Considering *LAI* estimates largely influence the final *ET* results, the made assumptions and reasoning were unjustified.

Table 2.3: Weighted average long term rainfall and pan evaporation, calculated wetness index, and relative wetness index of the study catchment relative to the Maroondah catchments (from Feikema *et al*., 2006).

Catchment	Rainfall (P)	Evaporation (E)	Wetness index (P/E)	Relative wetness index
Maroondah	1469	927	1.59	1.00
Thomson	1379	795	1.73	1.09
Armstrong (Main)	1545	866	1.78	1.12
Armstrong (East)	1417	920	1.54	0.97
Cement	1611	963	1.67	1.05
McMahons	1486	881	1.69	1.06
Starvation	1583	857	1.85	1.16
Tarago	1261	981	1.29	0.80
Bunyip	1449	932	1.55	0.97

The resulting *LAI* maps were compared to raw *NDVI* images without correcting the images for shading, terrain, and atmospheric factors. For example, Feikema *et al.* (2006) used figure 2.15 to subjectively compare the *NDVI* image with the *LAI* map (Macaque input), and suggested they had similar patterns without recognising that terrain shading in the *NDVI* images confounded any attempt to make clear visual comparisons.

For non-ash eucalypts, constant *LAI* values for each species (table 2.1) where derived by Watson (1999) with areal averaged *TNDVI* values across the Maroondah catchment. As Feikema *et al.* (2006) did not use *NDVI* images to create spatially distributed *TNDVI* maps over their study catchments, all non-ash eucalypt species were assigned the constant generated by Watson (1999a).

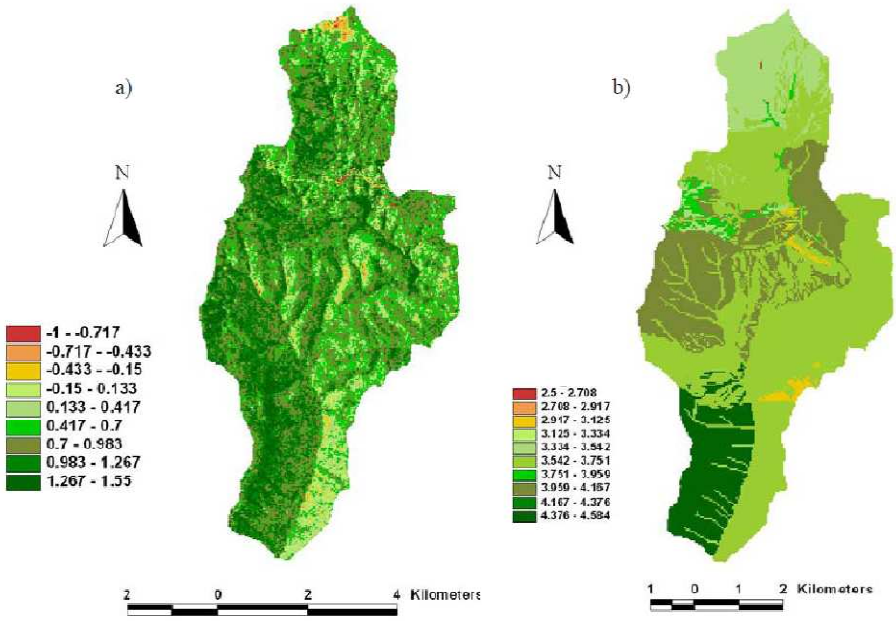

Figure 2.15: Example of how comparison between (a) raw NDVI maps were made with (b) LAI map used in Macaque (from Feikema *et al*., 2006).

2.4.1.3. Canopy and understorey maximum stomatal conductance curve

Changes in *E.regnans* $g_{s\ max}$ with age (figure 2.13) were assumed to hold for all eucalypts, non-eucalypt overstorey, and understorey forest types without empirical evidence. Considering the differences in *VPD* for overstorey and understorey vegetation, this assumption is known to be unreliable.

2.4.1.4. Sensitivity analysis

A sensitivity analysis was conducted on the Thomson catchment to investigate effects of uncertainty in *LAI* and $g_{s\ max}$ on streamflow. Feikema (2006) used a long-term simulation dataset with no inter-annual climatic variability to increase and decrease *LAI* by 10% and found streamflow changes of -9.57 to +10.63% respectively. It is highly likely the *LAI* maps outlined above include errors much greater than 10%, which will strongly influence streamflow changes. Watson (1999a) used the Maroondah catchment to undertake a sensitivity analysis of streamflow response to maximum stomatal conductance values using *E.regnans* literature values 0.0025 and 0.0065 m day $^{-1}$ (Feikema *et al* 2006) arbitrarily chose 0.005 m day $^{-1}$), to show respective streamflow changes of:

- +50% to -33% for canopy maximum stomatal conductance, and

- +33% to -24% for understorey maximum stomatal conductance.

Environmental controls on stomatal conductance, such as humidity and temperature are also sensitive at affecting streamflow estimates, and yet temperature inputs (also used to estimate humidity) involved a single base station generally not in the catchment (Feikema *et al*., 2006). Watson (1999a) found other parameters to be sensitive, such as the nominal soil evaporation depth parameter that was given the value of 3 cm; but realistically varying the value by a factor of two (1.5 to 6 cm) resulted in changes in streamflow of -27% to +28%. Feikema *et al.* (2006) did not use any soil data in the modelling exercise and made the assumption that soil is uniform for all catchments, knowing this is not the case for such large catchments. Watson (1999a) recognised that Macaque is sensitive to both the overall water holding capacity and water transmissivity of the soil.

2.4.1.5. Model calibration procedure

A number of Macaque parameters are able to completely alter the scale of the predicted hydrograph when varied within their respective bounds of certainty (Watson, 1999). For this reason, the calibration procedure undertaken by Feikema *et al.* (2006) kept almost all unknown parameters constant. It thus focused on calibrating two parameters; *precipitation scalar*, and the *ratio of the hydraulic to the surface gradient* parameter. This calibration procedure successfully reduces the difference between predicted and observed streamflow, and improves the coefficient of efficiency, which was the objective function used in the calibration process.

The *precipitation scalar* parameter allows the incoming rainfall to be increased or decreased uniformly. The *ratio of the hydraulic to the surface gradient* parameter has a large influence over the rate of rainfall transfer into streamflow. With the calibration of these two parameters alone, "satisfactory" hydrograph fits were possible with quite strong coefficient of efficiency values, but this does not imply *ET* estimates are accurate. It is possible to get very similar results with a wide range of *LAI* maps, $g_{s\,max}$ parameters, and other *ET* related inputs by calibrating the two chosen parameters. Macaque has no way of separating the uncertainty in the parameter calibration process from uncertainty in *ET* measurements as it adjusts the *precipitation scalar* parameter so rainfall suits mean daily streamflow. For this

reason, Feikema *et al.'s* (2006) evaluation of the eight study catchments was not data driven, and results provide poor estimates of streamflow changes due to logging disturbances.

2.4.1.6. Species-specific water yield curves

The second main objective of the Feikema *et al.* (2006) report involved developing species-specific water yield curves for DSE's IFPS, to allow for forestry practices within Melbourne's water catchments to account for the water resource. In doing so, Feikema *et al.* (2006) followed the methodology described by Peel *et al.* (2002b) who applied Macaque using data on species type, stand age, and mean annual rainfall to generated a set of equations estimating species-specific annual water yields.

Macaque discretises hillslopes into elementary spatial units (ESU), and each ESU was modelled separately using synthetic climate and forest age data, as well as real vegetation type data. Feikema *et al.* (2006) averaged the streamflow sequences of all species-specific ESU's to produce species-specific water yield curves. Figure 2.16(a) shows an example of a species specific curve, where the water yield trend is interpreted as being species-specific even though modelling of hydrologically relevant vegetation characteristics was not undertaken.

As observed in figure 2.16(b), some of the ESU's exhibited random oscillations thought to be due to numerical instability in Macaque (Feikema *et al*., 2006). For this reason, a procedure identified and removed all unacceptable ESU's; defined as ESU with >0.9m difference in water-yield from one year to the next. As shown in figure 2.16(c), many ESU's also had zero water-yield for several years (over 100 years in some cases), followed by a sudden increase once yield became positive. A subjective decision was made to remove ESU's with water yield equalling zero for more than 15 years from the analysis. It was considered unlikely for annual water yield to ever equal zero (Feikema *et al*., 2006), but ESU's with water yield equalling zero for less than 15 years were accepted in the analysis.

Table 2.4 provides a summary of results to show that only 59% of all ESU's were considered acceptable based on the two criteria above. The numerical instability meant an *LAI:Age* curve needed to be subjectively fitted by eye through the averaged

species-specific ESU's whilst preserving the average magnitude in water loss in order to derive species-specific water use parameter values. The present dissertation aims to improve on this particular method used to estimate species-specific water use as it is evident in section 2.3 and 2.4 that Macaque's modelling framework produces erroneous results that are not data driven.

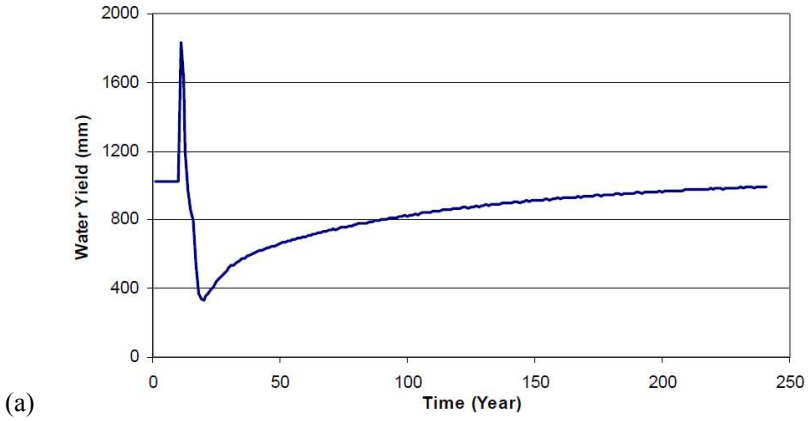

(a)

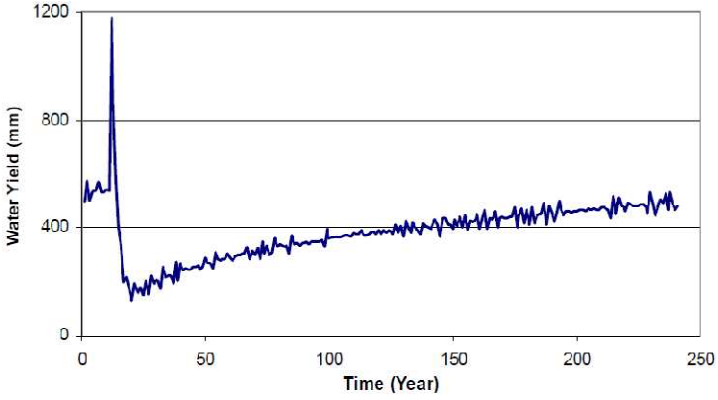

(b)

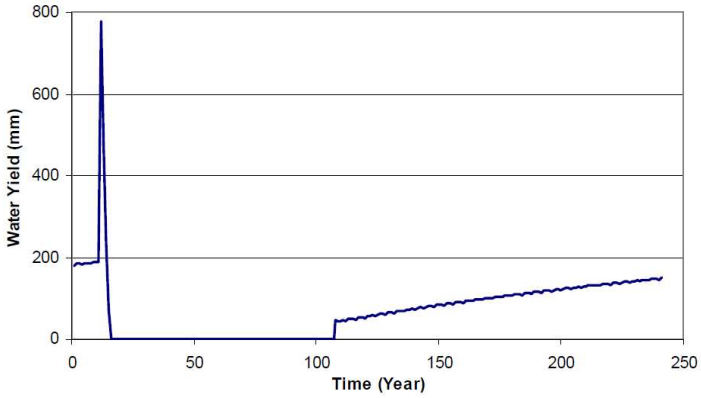

(c)

Figure 2.16: An example of an ESU with an (a) acceptable annual water yield, (b) unacceptable annual water yield due to unexplained oscillations, and (c) unacceptable annual water yield due to prolonged zero water yield (from Feikema *et al*., 2006).

Table 2.4: Summary of the percentage of acceptable EUS's for each catchment (from Feikema *et al*., 2006)

Catchment	Number of vegetated ESU's	Number of acceptable ESU's	% acceptable ESU's
Thomson	1129	373	33
Armstrong Creek (Main)	309	164	53
Armstrong Creek (East)	124	15	12
McMahons Creek	398	219	55
Starvation Creek	308	161	52
Tarago	1027	919	89
Bunyip	401	335	83
Total	3696	2186	59

2.5. TasLUCaS- Tasmania's forest hydrology model

TasLUCaS predicts streamflow changes after land cover disturbance of gauged and ungauged catchments. To assume pre-disturbance streamflow at ungauged sites TasLUCaS implements the Zhang curves, which are based on the Budyko framework (Brown *et al*., 2006). An overview of Budyko framework is first presented, followed by an evaluation of the Zhang curves in order to provide an informed critique of the TasLUCaS model structure.

2.5.1. Budyko framework

Water balance studies in vegetated catchments demonstrate a good relationship between long-term average annual *ET* and average annual precipitation (*P*) (Budyko, 1974). It has also been recognised that *ET* is a complex process strongly related to local net radiation, and the interaction of vegetation with available water. Figure 2.17 demonstrates how the average annual *ET* component in a catchment's water balance is restricted by available water (*P*) and atmospheric demand in the form of average annual potential evapotranspiration (E_o). Lines A and B define the maximum possible *ET* for a catchment due to the limiting factors E_o and *P* respectively.

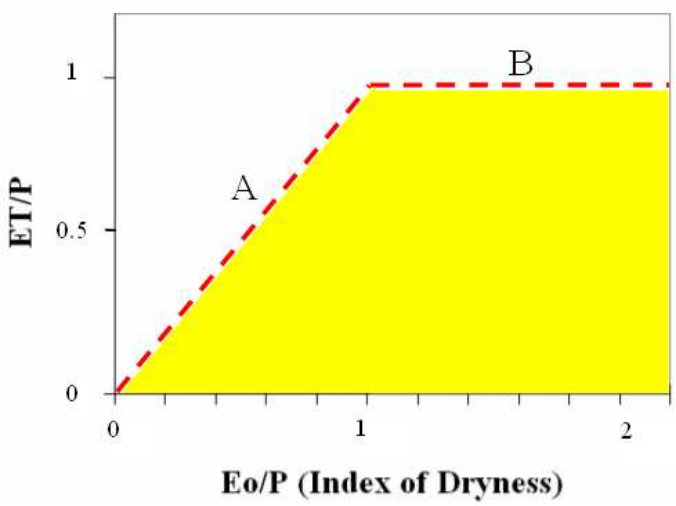

Figure 2.17: Maximum possible *ET* from a catchment using the ratio of mean annual *ET* to *P* as a function of the index of dryness (*Eo/P*)

Humid regions have conditions where $P>E_o$, $ET = E_o$, and $E_o/P<1$. Under humid conditions, *ET* is limited by available energy, which is the dotted line A, such that (Zhang *et al*., 1999):

$$ET \rightarrow R_n \quad \text{when} \quad R_n/P \rightarrow 0 \qquad [2.1]$$

where R_n is net radiation. In Arid regions, $ET = P$ when $ET/P=1$ and $Eo>P$. Under arid conditions, *ET* is limited by water availability (*P*), which is the dotted line B, such that (Zhang *et al*., 1999):

$$R/P \rightarrow 0 \quad \text{or} \quad ET/P \rightarrow 1 \quad \text{when} \quad R_n/P \rightarrow \infty \qquad [2.2]$$

where R is runoff.

To represent relationships [2.1] and [2.2], Budyko (1974) used a simple bucket model with a supply-demand framework that assumed a catchment's inter-annual net drainage is negligible because soil water storage (ΔS) and groundwater flow are at steady state. The assumption that changes in ΔS are zero is only valid for long term averages much greater than one year, and over a period when the interaction between vegetation and soil moisture is at equilibrium; otherwise ΔS can be larger than *ET* or streamflow over a single year. Budyko (1974) reasoned that inter-annual fluctuations

in groundwater flow may only be negligible if the framework is applied to large catchments (>10,000 km^2). With these conditions met, the macroclimate becomes the principle determinant of a catchment's streamflow and *ET*, which may be represented with the Budyko curve (figure 2.18).

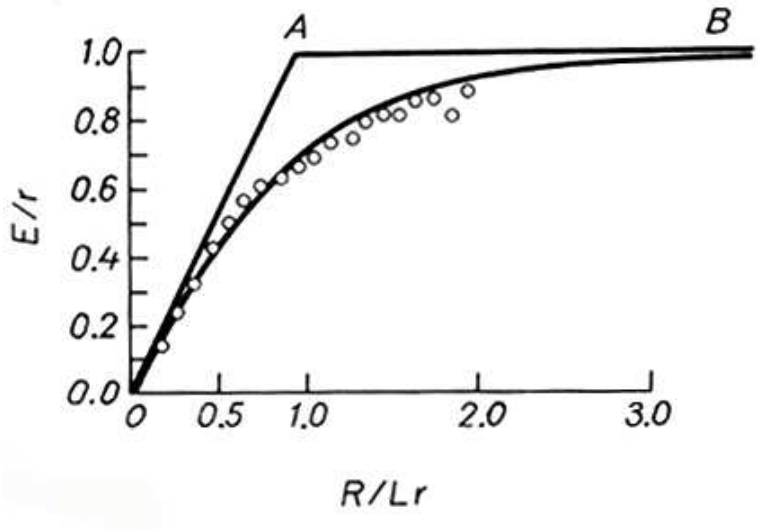

Figure 2.18: Dependence of the ratio of evaporation (E) to precipitation (r) upon the radiative index of dryness (R/Lr) (from Budyko,1974)

2.5.2. Zhang curves

Zhang *et al.* (1999) applied the Budyko framework using equation 4, where the dimensionless function (*F*) satisfied [2.1] and [2.2] and figure 2.17, such that:

$$\frac{E\ T}{P} = F\left(\frac{E_o}{P}\right) \qquad [2.3]$$

As [2.3] is principally based on the effects of macroclimatic conditions on *ET*, Zhang *et al.* (1999) introduced a dimensionless parameter, plant available water capacity (*w*), to account for the effects of vegetation change on *ET*, such that:

$$\frac{E\ T}{P} = F\left(\frac{E_o}{P}, w\right) \qquad [2.4]$$

Zhang *et al.* (1999) formulated an interpolator with [2.4] to predict average annual *ET* using measured *P*, estimated E_o, and calibrated *w*, such that:

$$\frac{E\,T}{P} = \frac{1 + w\,\frac{E_o}{P}}{1 + w\,\frac{E_o}{P} + \left(\frac{E_o}{P}\right)^{-1}} \qquad [2.5]$$

To calibrate *w,* Zhang *et al.* (1999) used catchment rainfall and streamflow data for more than 250 catchments from around the world. The catchment sizes varied from less than 1km^2 to 6 X 10^5 km^2, geographic locations and environmental conditions included; climatic conditions that varied from dry deserts of Yemen to rainforests of Brazil, soils that varied from sands through to clays, and annual rainfall with a whole range of seasonal distributions that varied from 35 mm to 2980 mm.

To calibrate separate *w* values for distinct vegetation classes, catchments were grouped into forest, mixed forest, and pasture where: "pasture" included crops, pasture, shrubs, and herbaceous plants; "forest" included a range of plantations, open forests, eucalyptus forest, rainforests forests and bamboo forests; and "mixed forest" included catchments not clearly classed into "pasture" or "forest". The various ecosystems, species, ages, and structurally different types of vegetation were ignored, as were differences in; advection, turbulent transport, canopy resistance, rainfall interception, leaf area, root system, and other highly variable plant physiological processes that affect *ET*.

Using [2.5] to calibrate *w*, *ET* is assumed to be the difference between rainfall and stream flow, each vegetation type is assumed to represent 100% of its catchment, and groundwater and ΔS are assumed to be inter-annually constant (Zhang *et al*., 1999). Figure 2.19 shows the resulting outcome where *w* was set to 2.0 for forest, 1.0 for mixed vegetation, and 0.5 for pasture. For each vegetation class, results show a large amount of variation when *ET* is not limited by water (i.e. $E_o/P > 1$) or energy (i.e. $E_o/P < 3.5$), and is strongly a function of vegetation cover. The results are most commonly depicted in what is called the Zhang curves (figure 2.20), which shows the relationship between annual ET and annual rainfall for both pasture and forest.

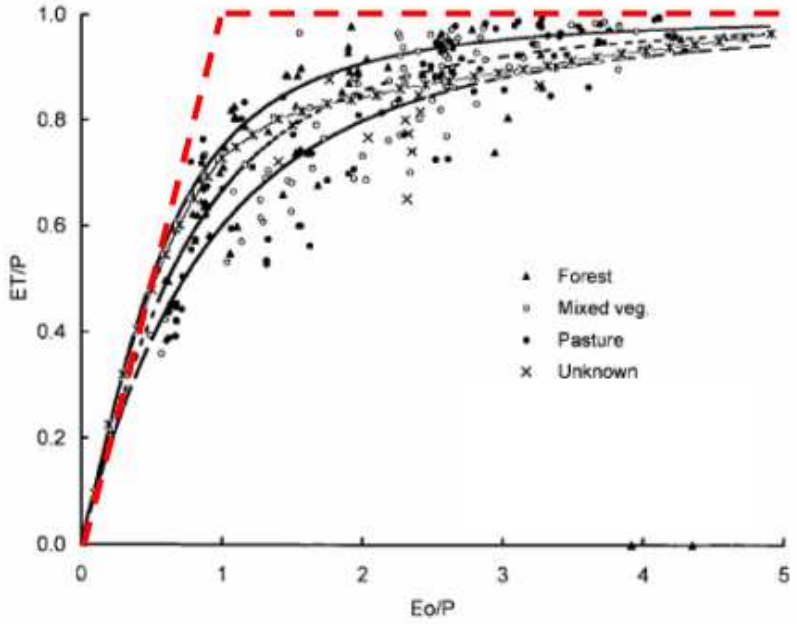

Figure 2.19: Ratio of mean annual evapotranspiration to rainfall as a function of the index of dryness (*Eo/P*) (from Zhang *et al*., 1999)

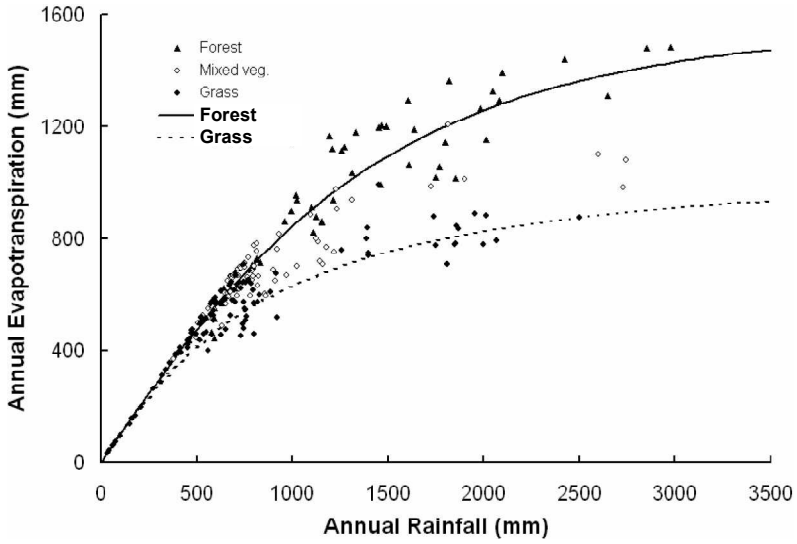

Figure 2.20: Zhang curves predicting the relationship between annual *ET* and *P* for both forest and pasture (from Brown *et al.,* 2006)

The Zhang curves have been generalised to make [2.5] applicable to catchments with varying proportions of forest and pasture by using a proportionality equation to weigh vegetation classes linearly according to fraction of forest cover (*f*) such that (Zhang *et al*., 2001a):

$$ET = fET_f + (1\text{-}f)ET_p \qquad [2.6]$$

where ET_p and ET_f are annual *ET* for pasture and forest respectively. By substituting [2.5] into [2.6], the generalised equation becomes:

$$ET = \left[\frac{1 + w_f \frac{E_{zf}}{P}}{1 + w_f \frac{E_{zf}}{P} + \frac{P}{E_{zf}}} + (1 - f) \frac{1 + w_p \frac{E_{zp}}{P}}{1 + w_p \frac{E_{zp}}{P} + \frac{P}{E_{zp}}} \right] \qquad [2.7]$$

where w_f and w_p are plant available water capacity of forest and pasture respectively, and E_{zf} and E_{zp} are constants that "cannot be interpreted as E_o in the traditional sense" (Zhang, 2001). Note that [2.7] was derived by substituting [2.5] into [2.6] and therefore E_{zf} and E_{xp} should mathematically represent E_o for forest and pasture but this is not the case.

2.5.2.1. Addressing problems with the Budyko/Zhang framework

The Budyko curve represents macroclimatic systems and assumes groundwater fluctuations are negligible if the catchment is larger than 10,000 km^2, and ΔS is zero when averaged over a long term period much greater than one year. Past studies have recognised deviation around the Budyko relationship and attributed the deviation to seasonality in climate (Milly, 1994; Koster & Suarez, 1999; Potter *et al*., 2005), soil hydraulics (Milly, 1994; Zhang *et al*., 1999; Porporato *et al*., 2004), vegetation classification (Donohue *et al*., 2006), and catchment size (Choudhury, 1999). Tall forested regions of south-eastern Australia have intra-annual variability in ΔS due to late winter/early spring rainfall patterns being coupled with summer low flow periods exacerbated by high evapotranspiration rates. Inter-annual variability in groundwater and ΔS is also evident when the El Nino Southern Oscillation (ENSO) cycle causes

episodic periods of low soil water availability and heavy groundwater uptake by eucalypts (Pook *et al*., 1966).

Management of the forested water resource is often at a spatial and temporal scale that violates the assumptions of the Budyko framework. To develop the framework beyond the representation of macro-climatic processes it is necessary to account for interaction of vegetation dynamics with soil water storage changes (Donohue *et al*., 2006) and local seasonal and inter-annual climatic conditions (Hickel & Zhang, 2006). In the case of regenerating forests, the age of the forest will affect ΔS, as is shown in figure 2.21. The figure uses data from a paired catchment study to show a regenerating forest dries up the soil profile more rapidly than the neighbouring old-growth forest (Howard & O'Shaughnessy, 1971). A linear trend of declining soil moisture is evident, which effectively reduces groundwater recharge, as well as discharge into the regenerating catchment's stream. The Kuczera curve also suggests regenerating forests deplete available soil water at different rates depending on forest age, and therefore long-term ΔS are not zero.

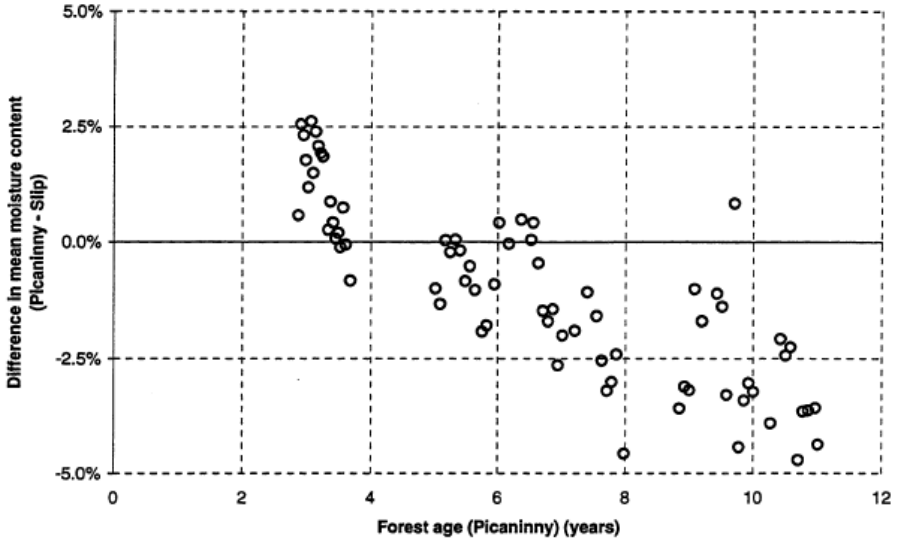

Figure 2.21: Effects of regeneration on soil moisture over time: represented as difference between a treated (Picaninny) and control (Slip) catchment (from Watson *et al.,* 1999b).

Considering forest age influences soil moisture and *ET* rates, for a given dryness index (E_o/P) old-growth or mature forests plot lower on the Budyko curve than regenerating vegetation with a higher soil moisture and groundwater uptake rate. Figure 2.22 shows that catchments experiencing a net annual increase in vegetation

growth rates are likely to experience an increase in *ET* and for this reason incrementally plot higher on the Budyko curve (Donohue *et al*., 2006). When a catchment transpires more than the annual rainfall by depleting the groundwater then it may potentially be above the Budyko asymptote (i.e. where the evaporative index is greater than 1).

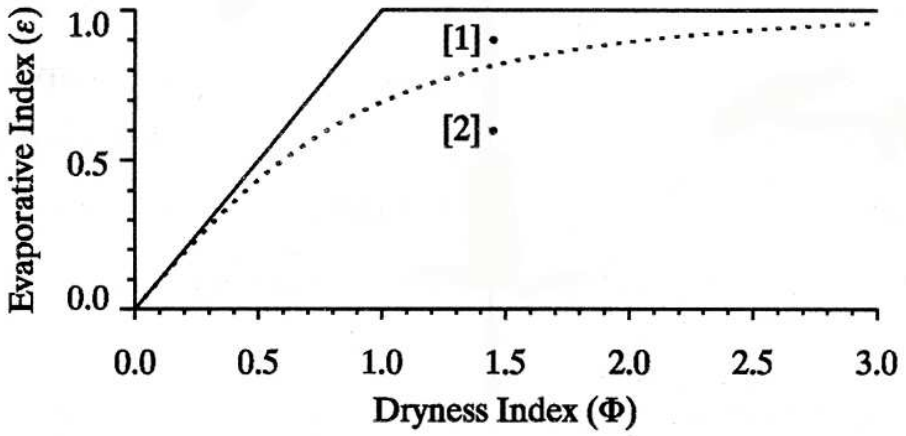

Figure 2.22: Response of Budyko curve to regenerating forest where; [1] represents an fast growing regenerating forest whereas [2] represents an old growth forest (from Donohue *et al.,* 2006).

Finally, the Zhang framework consists of a rudimentary classification system of "vegetation types", as figure 2.20 assumes each vegetation type exists over the whole spectrum of climatic conditions. Rather than having "forest" consist of very humid (ET/P<0.4) as well as very dry (E_o/P>4) vegetation types, a more constructive classification system is illustrated in figure 2.23. Figure 2.23 shows that vegetation A exists in humid regions where the limiting factor is energy, and water use only becomes a function of the vegetation when E_o/P>0.5. Vegetation C almost always exists in drier climates where rainfall is the limiting factor for quantifying *ET*, as $ET=P$, and water use becomes a function of vegetation only for conditions with lower E_o/P. Finally vegetation B exists in temperate conditions, where E_o is more or less *P*, and the vegetation's interaction with plant available water determines *ET* rate.

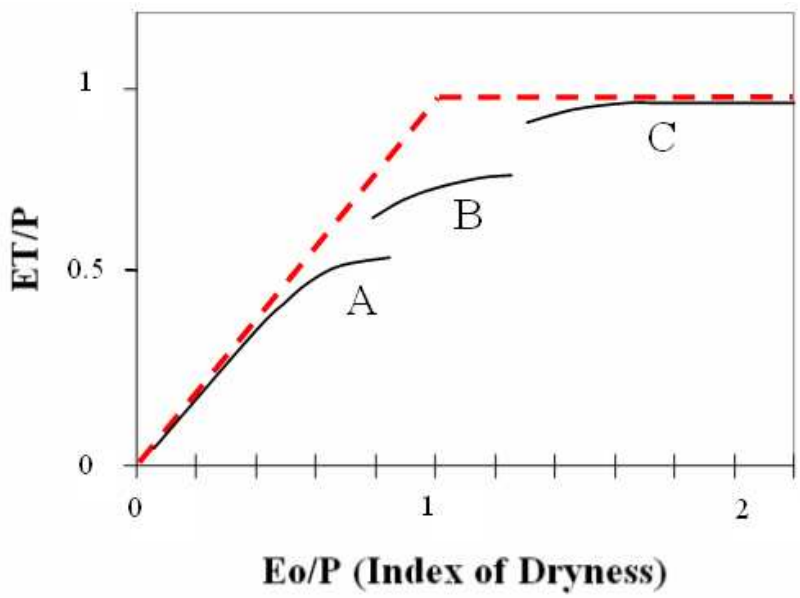

Figure 2.23: Examples of how vegetation specific curves may be generated within the natural limit of the vegetation specific ecosystem with: A representing a tropical forest type, B represents a temperate vegetation type limited by the vegetations interaction with plant available water, and C representing an arid vegetation type.

2.5.3. TasLUCaS model structure

TasLUCaS is a forest hydrology management tool designed to investigate the impacts of forest growth on the water resource in small ungauged catchments (<100 km^2) of Tasmania (Brown *et al*., 2006). Figure 2.24 shows a typical TasLUCaS output, where the impacts of converting a whole catchment from pasture into plantation is illustrated by the size of B, and determined by subtracting pre-treated annual streamflow (full line) from simulated changes in annual streamflow (dotted line). TasLUCaS uses Zhang curves to predict pre-disturbance streamflow at ungauged catchments. It assumes catchment size is not relevant in the model structure, which has been shown to be erroneous (Choudhury, 1999).

As is evident in figure 2.24, TasLUCaS does not account for variability in streamflow due to climatic variability. Instead, it uses a constant mean annual streamflow as the baseline from which streamflow trends begin from (Brown *et al*., 2006). TasLUCaS recognises two forms of land cover disturbance: (1) forest converted into plantations or regenerating forest, and (2) grassland converted into plantations. The model makes an erroneous assumption that forests converted into

plantation or regenerating forest will have the same hydrological impact on the water resource for a given age.

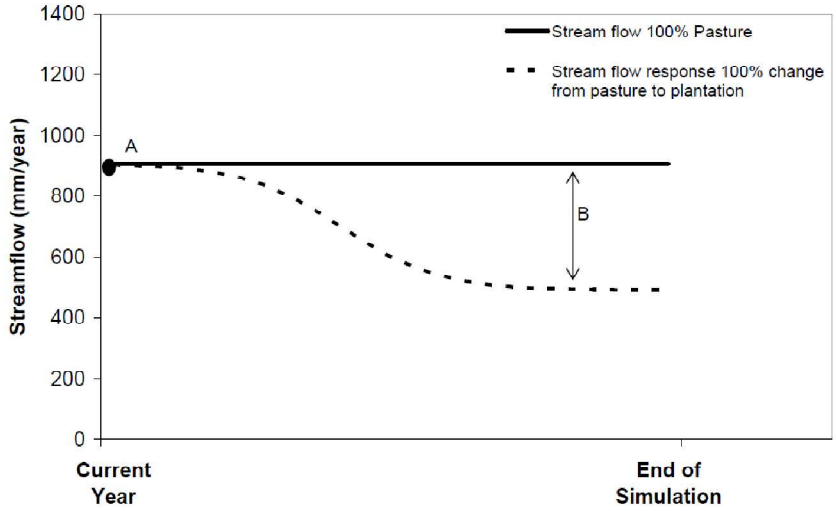

Figure 2.24: Conceptual diagram of how current mean annual streamflow (A), derived using the Zhang curves at ungauged catchments, responds to land cover disturbance with streamflow reduction (B) (from Brown *et al.,* 2006).

2.5.3.1. Predicting streamflow for pasture converted into plantation

To analyse streamflow changes due to pasture converted to plantations in gauged catchments, TasLUCaS results are driven by the nature of flow duration curves (FDC) at five South African catchments, one Australian catchment, and one New Zealand catchment. The FDC curves were adapted to TasLUCaS by formulating a generalised equation that explains changes in streamflow as:

$$\Delta SF = aP\left[\frac{1}{1+\exp\left(\frac{Age-T}{n}\right)}-1\right] \qquad [2.8]$$

where ΔSF is change in stream flow, Age is the age of the plantation, P is the annual rainfall, and parameters a, T, and n were calibrated to fit a generalised curve to the seven catchments. The generalised curve was scaled to represent the effects of 100% of an area treated by assuming a linear streamflow response to percent area treated. The generalised curve estimates streamflow changes with plantation age using only rainfall data.

Figure 2.25 shows predicted versus observed changes in streamflow after a plantation conversion for the seven catchments used to calibrate the generalised curve. Clearly the calibrated model fails to predict streamflow increases, and systematically produces erroneous results (i.e. overestimates) when streamflow reductions of more than 400 mm occur. A great deal of variation also exists for the rest of the predictions as streamflow predictions are simply driven by the average response of seven catchments used to calibrate the model.

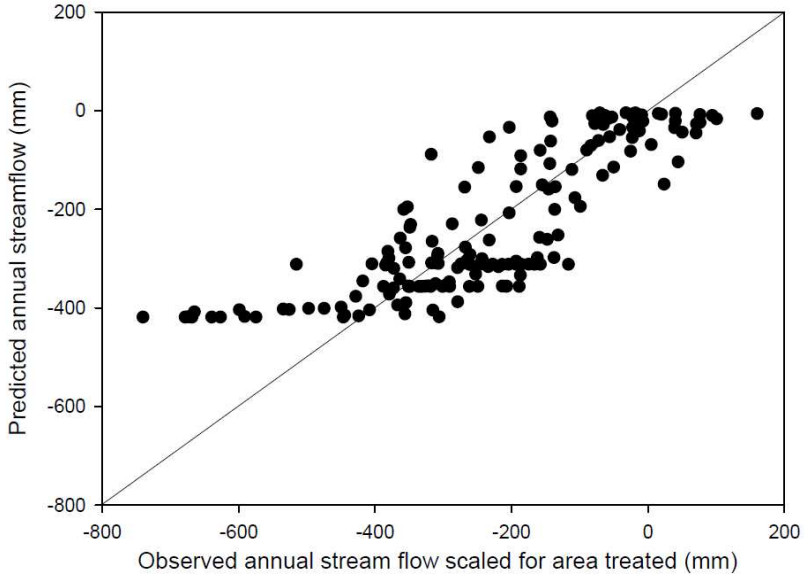

Figure 2.25: Observed versus predicted change in streamflow for all years using the seven catchments (from Brown *et al.,* 2006).

The size of the seven catchments ranged from 18-320 ha, whereas TasLUCaS was designed for catchments as large as 10,000 ha (Brown *et al*., 2006). Flow duration curves are sensitive to catchment size because smaller catchments are more likely to be ephemeral and have variable streamflow levels but this discrepancy in catchment size was disregarded.

2.5.3.2. Predicting streamflow for tree cover disturbance

When forest disturbance is followed by forest regeneration or plantation conversion, TasLUCaS applies the Macaque *LAI:Age* curve (section 3.3.1.3.). The *LAI:Age* curve was produced for ash forest types and Brown (2006) assumes with no empirical evidence it is applicable to plantations. Brown (2006) calibrated the *LAI:Age* curve with eight paired catchments, which included five structurally diverse regenerated

forest and three pine plantations. Figure 2.26 provide TasLUCaS predictions of streamflow for the eight catchments used to calibrate the model to show a systematic error once observed changes in streamflow drop below -150 mm and a great deal of variation for all other observations.

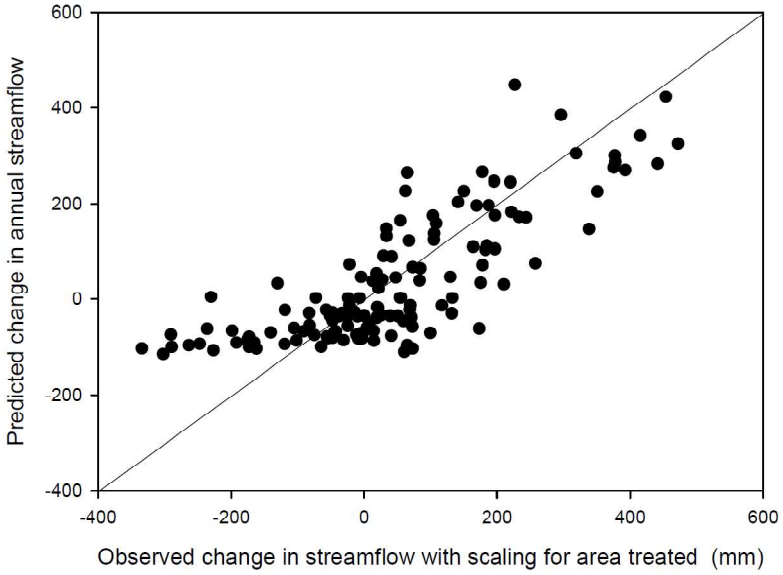

Figure 2.26: Observed versus the predicted changes in streamflow for all years using the eight paired catchments (from Brown *et al.,* 2006).

Figure 2.27 applies the model to regions with rainfall ranging from 800 mm to 2100 mm to find reductions in streamflow never dropping below -150 mm, whereas the Kuczera curve predicts water losses as high as 615 mm for catchments with 1100 mm of rainfall.

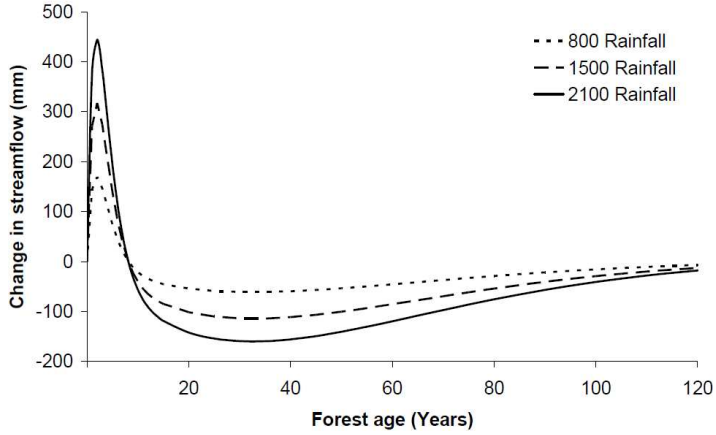

Figure 2.27: Predicted change in streamflow for disturbance of mature forest using TasLUCaS. Note the data used to fit these curves is limited to forest ages of 35 years and less (from Brown *et al.,* 2006).

2.5.3.3. Generating results with TasLUCaS

When pre-treatment stream gauged data exists, TasLUCaS only improves post-treatment streamflow predictions by using the observed pre-treatment mean annual streamflow value as the baseline from which the streamflow trend begins. It is important to note that post-disturbance streamflow data makes no improvement to the nature of the streamflow trend. The post-disturbance streamflow trend is determined with the calibration of equation 2.8 using seven external catchments discussed in section 2.5.3.1, or the calibration of the *LAI:Age* curve using eight external catchments discussed in section 2.5.3.2. As shown in figure 2.28, the pre-disturbance mean streamflow determines the streamflow base line (line), post-disturbance trend is estimated using the calibrated equations (dashed line), and post-disturbance streamflow data are not used in the model

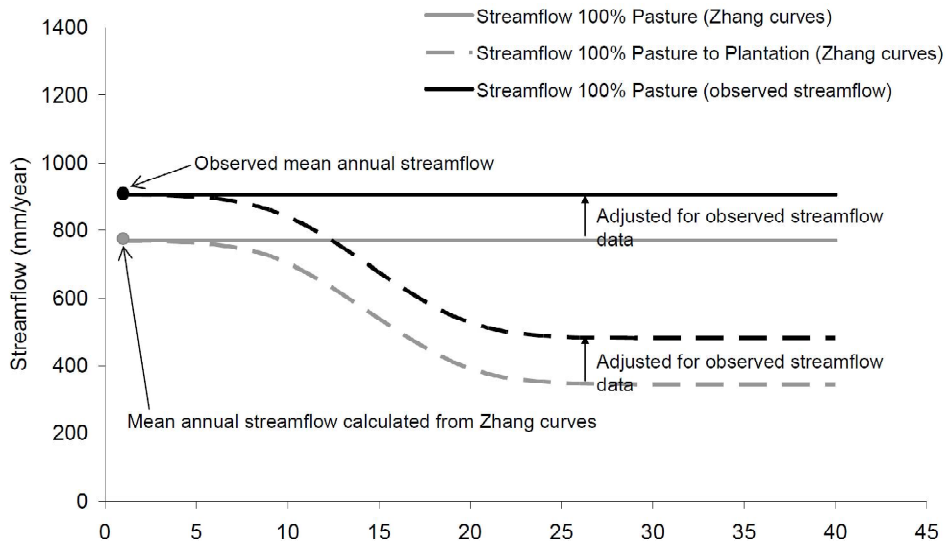

Figure 2.28: Example of how TasLUCaS predicts streamflow for ungauged catchment response (grey) and gauged catchment response (black) (from Brown *et al.,* 2006).

When predicting streamflow at ungauged catchments, TasLUCaS estimates pre-treatment streamflow using the Zhang curves (2001a), and then calculates streamflow changes relative to pre-treatment estimates using the calibrated equations and rainfall data. In figure 2.29, Brown *et al.* (2006) used a set of Tasmanian catchments less than 100 km^2 in size to evaluate the appropriateness of equation (2.8) at estimating pre-treatment streamflow, and found the Zhang curves introduce significant uncertainty in estimating pre-treatment streamflow.

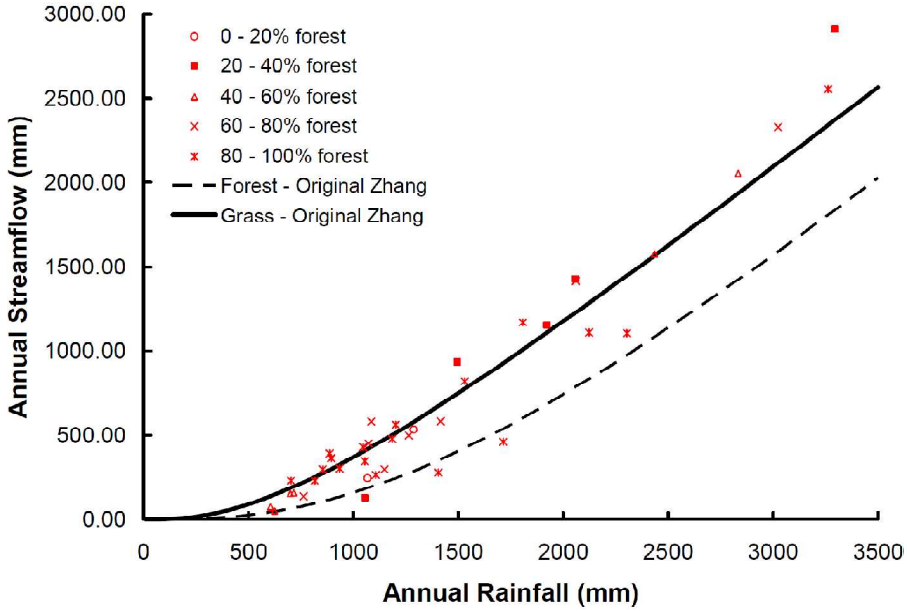

Figure 2.29: Tasmanian data shown in relation to the Zhang curves, grouped by percentage of forest cover (from Brown *et al.,* 2006).

Figure 2.30 shows output examples of TasLUCaS streamflow predictions due to repeated land cover disturbances caused by successive timber harvesting rotations. The rotation length is defined as the age of the forest before it is harvested, whereas the uptake phase is defined as the amount of time it takes for the whole catchment to be harvested. It is evident TasLUCaS predicts recovery in streamflow in a repetitive fashion after each successive disturbance as it erroneously assumes ΔS and changes in groundwater levels are zero for small catchments exposed to short rotation plantations. In reality, a cumulative reduction in streamflow after each rotation would be expected if soil and groundwater storage is depleted more rapidly than it is able to be recharged by rainfall. This is often the case for short plantation rotations that have been shown to deplete the landscape's water storages (Honeysett *et al*., 1996).

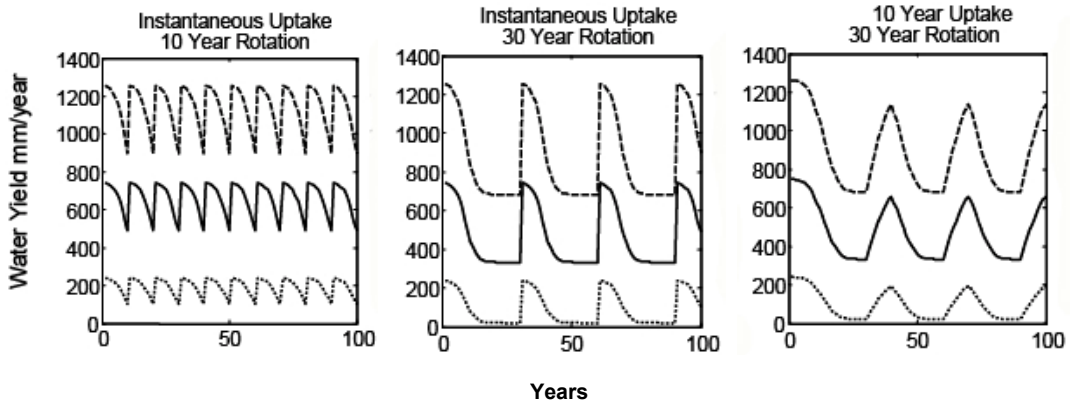

Figure 2.30: Impact of different rotation lengths and periods of uptake on predicted stream flow (from Brown *et al.,* 2006).

2.6. Forest hydrology model applications in Tasmania

Both Macaque and TasLUCaS have been applied in Tasmania with the following results.

2.6.1. Launceston's water supply (Macaque application)

Macaque has been used in Tasmania to model low flows in Launceston's water catchment (Peel *et al*., 2002a). Water is supplied to Launceston directly from the North Esk and St Patricks River without the use of water storage structures, making the level of summer flows critically important for Launceston's water supply. For this reason, Macaque was applied to simulate historic streamflow records with emphasis on accurate predictions of low flows. The vegetation in Launceston's water catchments consist of a mixture of ash eucalypt species (*E.regnans* and *E.delegatensis*) and pasture. Forestry development has involved harvesting native forests followed by regeneration, and replacing both *E.regnans* forest and low productivity farmland with *E.nitens* plantations.

The study's greatest limitation was the inaccessibility of the site specific vegetation age data. The forest has been logged over time, but precise records were not available from Forestry Tasmanian even though vegetation age was the hydrologically significant variable under scrutiny for its impact on the water resource (Peel, 2001). For this reason, the State Forests where classed as follows;

"Regrowth that is older than 20 years is assumed to be the result of logging activity that is assumed to have occurred in 1945. Regrowth that is younger than 20 years is also assumed to be due to logging activity and is assumed to have occurred in 1985." Peel et al. (2001)

As all regrowth older than 20 years was assumed to be 57 year old and all regrowth younger than 20 years was assumed to be 17 year old, water use of both vegetation ages was similar if plotted on the Kuczera curve (figure 1.1). Clearly, the lack of available data gave the results little merit so no further evaluation will be made of the report. Forestry practices continue in Launceston's water catchment with little accurate assessment of the likely future repercussions on the Launceston's water supply.

2.6.2. Tasmania's forest land-use planning tool (TasLUCaS application)

As part of the Inter Governmental Agreement on a National Water Initiative (NWI), the "Water Availability and Forest Land-use Planning Tool" (WAFLPT) was developed by the Tasmanian Government to assess the potential impact of water interception by plantation forests. The WAFLPT is comprised of four major components, two of which include TasLUCaS functions to quantify changes in; (1) water availability as a result of future plantation forestry development, and (2) surface water hydrology model that incorporates the outputs from TasLUCaS functions into a water balance model (DPIW, 2008). The first application of the WAFLPT was on the Ringarooma catchment, as the *Ringarooma Water Management Plan* (WMP) required increases in environmental water flow for ecosystem management. Increases in streamflow were proposed with a 58% seasonal reduction of water allocations for irrigators, but irrigators expressed concerns that plantation forestry is largely contributing to the reduced streamflow situation (Armstrong Agricultural Services & National Strategic Services, 2001). The modelled WAFLPT results found minimal impact of large increases in plantation conversions on water yields (DPIW, 2008), which could be attributed to the erroneous TasLUCaS model structure outlined above.

TasLUCaS has also been used extensively by Natural Resources Management (NRM) in Tasmania to provide policy recommendations on the management of

Tasmania's water resource without recognising the significant errors in the model structure highlighted in this review.

2.7. Conclusion

A thorough review has been undertaken of the two main forest hydrology models used to inform policy makers of the potential impacts of land cover disturbance on the water resource in both Tasmania and Victoria. It is evident that both models have a great deal of uncertainty in quantifying streamflow trends after land cover disturbance, as the models are not data-driven and largely influenced by incorrect assumptions. Macaque is a highly parameterised model that is only able to successfully make use of site-specific forest age data, whereas forest type data is used with highly erroneous assumptions. TasLUCaS makes use of site-specific forest age data to determine streamflow trends, and makes poor use of site-specific streamflow data as streamflow trends are derived by parameters derived from external catchments. TasLUCaS makes no attempt to make use of forest type data as it classifies all forest types and plantations with the same hydrological response.

In order to produce accurate estimates of streamflow response after a land cover disturbance, the present dissertation argues it is necessary to accurately quantify catchment-specific forest growth processes during regeneration. The next chapter provides a review of plant physiological characteristics that regulate the soil-to-atmosphere water flow pathway of forests to develop a hydrology model that predicts forest water use with site-specific data on forest regeneration processes.

Chapter 3: Plant physiological regulators of forest productivity and water use

3.1. Introduction

Plant physiological processes are strongly regulated by external environmental conditions. The physical and physiological characteristics of trees respond to water availability and climate factors to regulate the water flow pathway from soil to atmosphere. The climate determines the maximum potential evaporation rates through conditions relating to humidity, solar radiation, rainfall, temperature and wind. Plant available soil water sets a limit on uptake of water from the soil profile, with soil texture and structure determining the storage capacity and hydraulic conductivity of the soil. The plant root architecture determines the accessibility of deep groundwater reserves for plant water uptake.

This review chapter will outline the physical and physiological characteristics that regulate the water flow pathways of timber yielding forest types and plantations. The overall objective is to determine how water use efficiency over a life time of a timber stand influences the relationship between forest productivity and forest water use. In this thesis, water use efficiency (*WUE*) is defined as the stem growth increment per unit of water used. It is important to know *WUE* when predicting forest water use with forest inventory data in order to account for variability in forest water use per growth increment. For site specific conditions, forests regulate productivity and water use with mechanisms that function over a range of time scales. As would be expected the short- and medium-term regulators of *WUE* contribute to the long term responses (Morris & Benyon, 2005). A summary of the different time-scales is provided below, followed by an overview that explicitly links the different levels of physical and plant physiological responses that regulate forest productivity and water use:

- Short time-scale responses involve regulating water use through stomatal closure and xylem cavitation. These responses are strongly influenced by the

diurnal climatic conditions that affect soil water potential and the atmospheric vapour pressure deficit.

- Medium time-scale responses involve shifts of resource allocation from one component of the plant to another; such as leaf senescence and root mortality due to drought, and seasonal climatic variability in rainfall, potential evapotranspiration, and plant available soil water.
- Long time-scale responses involve the regulation of forest productivity and water use due to changes in site specific constraints imposed by the finite resources over a life time of the stand. Decadal changes in stand level competition result in forest structural changes in leaf area (*LA*), sapwood area (*SA*), and root biomass as a means to regulate the hydrological equilibrium of a catchment.

3.2. Short time-scale responses that regulate forest productivity and water use

Diurnal climatic patterns represented in solar radiation, humidity and temperature measurements, as well as the stochastic spatiotemporal patterns represented in rainfall and wind conditions require plants to constantly adjust transpiration *(T)* rates to optimise their WUE. For this purpose, stomatal conductance (g_s) varies on a time-scale that is seconds to hours, and provides the fine tuning of stand water use driven by the environment (Morris & Benyon, 2005). Stomatal conductance is the rate at which water vapour transpires through stomata, and relates to the relative size of the stomatal aperture.

3.2.1. Role of atmospheric and soil moisture conditions on stomatal regulation

In a broad sense, g_s regulate a negative feedback mechanism that responds to a plant's water potential gradient from soil to atmosphere. The atmospheric conditions are represented by the measure of vapour pressure deficit (*VPD*), which is the atmospheric capacity to absorb moisture due to the relative humidity and temperature. An increase in *VPD* in the middle of the day results in changes to the water potential gradient, which a plant responds to by regulating g_s with stomatal closure to reduce *T* rates. Figure 3.1 shows that sap flux, a surrogate for *T*, is closely related to *VPD*. In coniferous canopies, Whitehead (1985) found that *VPD* can

account for 75% of variation in g_s. This is because T is strongly regulated by g_s on both hourly and daily time-scales.

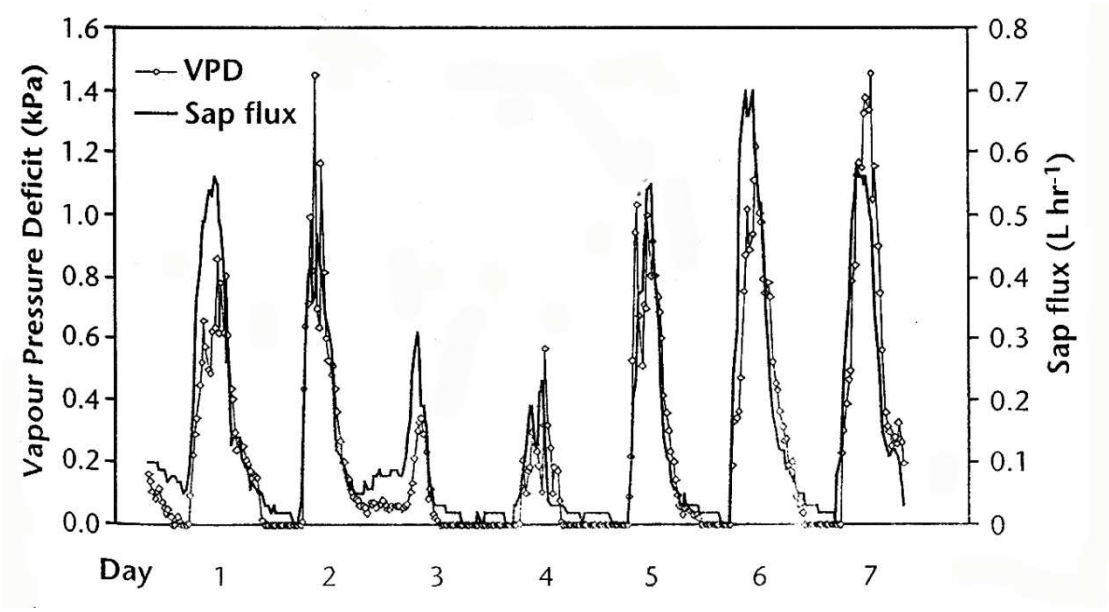

Figure 3.1: Diurnal variation in vapour pressure deficit and sap flux (T) by a 3-year-old *E.globulus* tree (from Morris & Benyon, 2005).

As g_s responds to the gradient between leaf water potential and soil water potential, the ability of the soil profile to store water will also influence g_s (Whitehead, 1985). If a plant shows signs of drought stress due to dry soil conditions, stomatal closure prevents xylem cavitation. For example, figure 3.2 shows the canopy conductance (g_c), which is the product of g_s and leaf area density integrated over the canopy depth, varies for two stands of *E.camaldulensis* in similar climates but different soils (Morris & Benyon, 2005). The leaf area density is defined as the total one-sided leaf area per unit canopy volume. Figure 3.2 shows g_c was less responsive to VPD at the sandy loam site than the medium clayey soils, as the sandy loam soils contained a soil texture with better conditions for water availability.

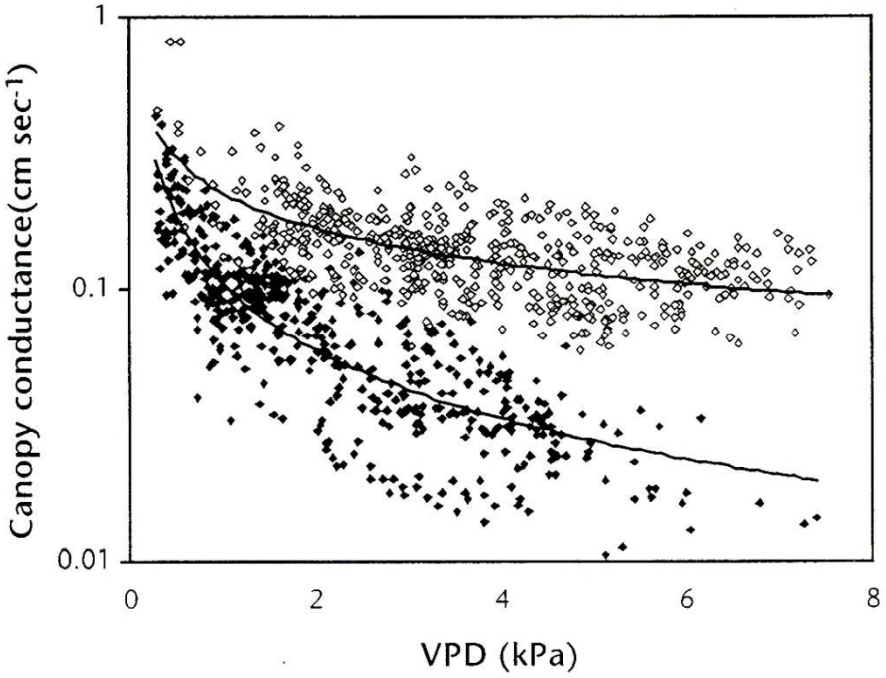

Figure 3.2: Reduction in g_c with increasing *VPD* in two stands of *E.camaldulensis* in similar climate but contrasting soil texture. Open symbols – 3 year old plantation on coarse sandy loam, north Pakistan; closed symbol – 6 year old plantation on medium clay, Victoria, Australia (from Morris & Benyon, 2005).

3.2.2. Role of stomata in optimising water use efficiency in plants

There is evidence in agricultural plants that stomata optimise *WUE* by maintaining a constant ratio of water transpired to carbon gain (Whitehead, 1985). The constant ratio implies that the water use may be determined from the productivity of the crop. Figure 3.3 shows that this relationship is also evident in some native vegetation, as exemplified in *Rhagodia baccata,* a coastal shrub found on the west coast of Australia (Hellmuth, 1968). It is notable that the rate of transpiration and rate of assimilation are related for both the summer and winter months of the year. Stomatal closure reduces water loss for trees but this comes at an expense, as the rate at which CO_2 enters leaves is also reduced, which in turn reduces photosynthesis for biomass production. For a given plant species, if biomass productivity is closely linked to water use then this implies the actual temporal variation in productivity optimises *WUE* (Cowan, 1981).

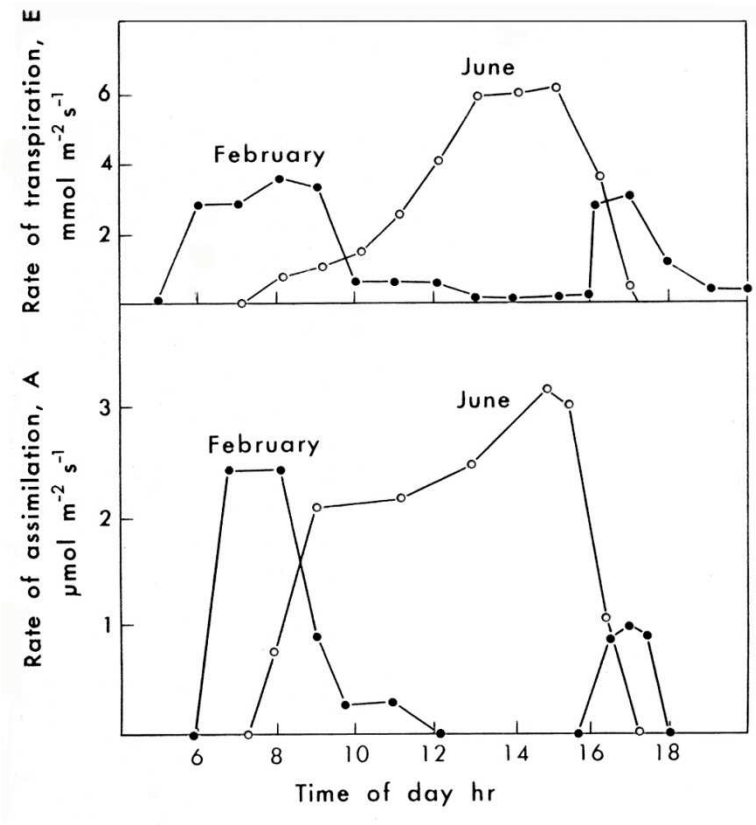

Figure 3.3: Rate of transpiration and assimilation in *Rhagodia baccata* during a winter and summer day near Mt Magnet, Western Australia. (from Hellmuth, 1968)

3.2.3. Variation in stomatal regulation between eucalypt species

Eucalypt species have adapted to a range of climatic conditions, which has resulted in different levels of drought tolerance. The variability in drought tolerance between species has allowed for appropriate plantation species to be selected for particular environmental site conditions. For example, *E.nitens* is less drought tolerant than *E.globulus* and strongly favours mid to high elevation, fertile soils and high-rainfall sites. Stomatal conductance (g_s) of *E.nitens* seedlings has been found to be consistently above that of *E.globulus* on irrigated plots and the reverse was found on rain fed plots over a drought cycle (White *et al*., 1986). The stomatal regulation is strongly reflected in the tree growth of the two species at different locations, with *E.nitens* growing fastest on wetter sites, whereas *E.globulus* performing best on drier sites (Florence, 1996). This suggests that under drought conditions, *E.globulus* is better at regulating the response to available water than *E.nitens,* which may be attributed to either differences in the root systems capacity at exploiting the soil moisture and groundwater, or differences in *WUE*.

Plant available water strongly influences eucalyptus growth and physiology. Pre-dawn leaf water potential (ψ_{max}) may be used to estimate a plant's susceptibility to water stress (White *et al*., 1999). The leaf water potential (ψ_l) becomes more negative with soil drying, and the slower recovery of ψ_{max} in *E.nitens* indicates that the effect of water stress is prolonged, which results in a slower recovery of g_s following an increase in turgor. Generally, g_s is strongly associated with rates of carbon assimilation, and *E.nitens* have reduced productivity on drier sites as a result of slower g_s recovery after a rainfall event (Whitehead & Beadle, 2004).

Sinclair (1980) performed a study of drought tolerance of two eucalypt species; *E.obliqua* (subgenus: *Monocalyptus*), and *E.laucoxylon* (*Symphyomyrtus*) to exemplify how eucalypts from different evolutionary origins have different regulations of ψ_l and g_s. The results in figure 3.4 show that the diurnal ψ_l and g_s values in the winter time where similar for both species whereas in the summer time the reduction in *E.obliqua* stomatal opening restricted transpiration, and hence limited diurnal variation in ψ_l. Florence (1980) also recognised that subgenus *Monocalyptus* has a lower tolerance of prolonged water stress than other *Eucalyptus* subgenera.

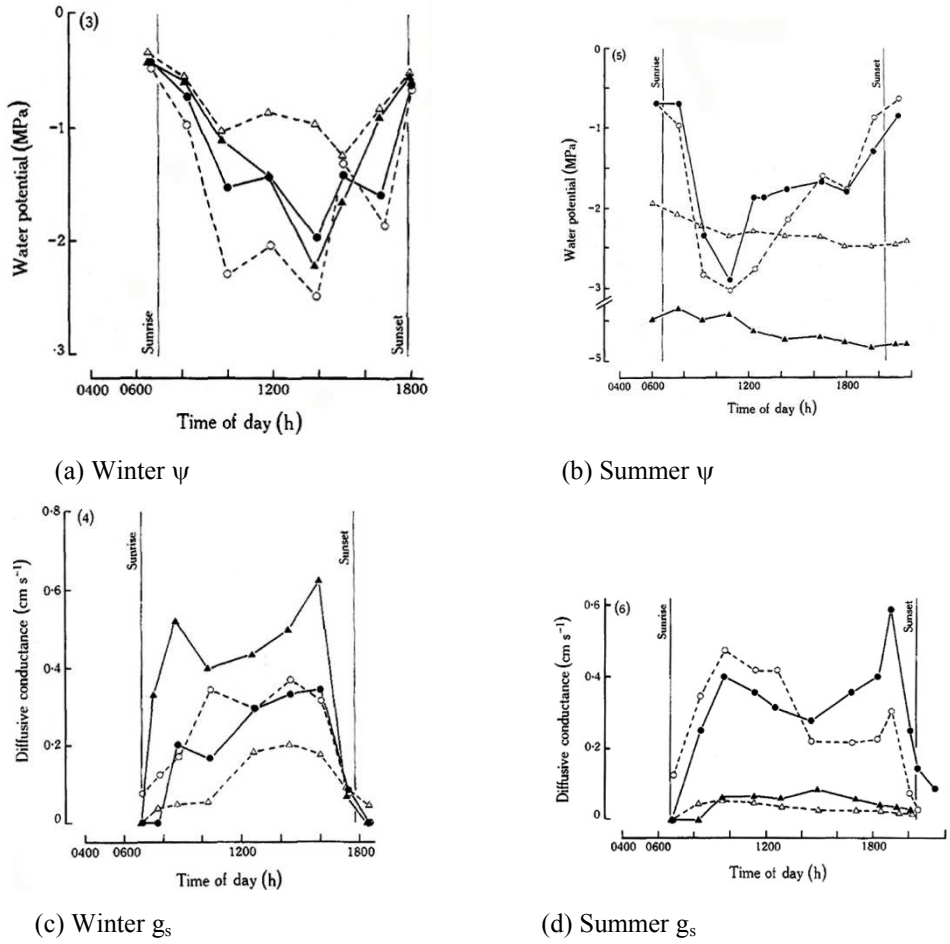

(a) Winter ψ (b) Summer ψ

(c) Winter g_s (d) Summer g_s

Figure 3.4: Water potentials (ψ) of two *E.obliqua* (triangle) and *E.fasciculosa* (circle) trees in; (a) winter, and (b) summer. Diffusive conductance (g_s) of two *E.obliqua* (triangle) and *E.fasciculosa* (circle) trees in; (c) winter, and (d) summer (from Sinclair, 1980).

Generally speaking the most productive plant species are those that maintain the highest g_s, as an increase in g_s increases carbon assimilation rates at the expense of water loss. Duncan *et al.* (2000) analysed plantation growth data collected in Gippsland, Victoria for 140 seedlots from 36 eucalypt species. They identified seven species considered most successful. The best performing species across the range of sites were *E.globulus*, *E.nitens* and *E.viminalis,* which are all from series *Viminales*, sub-genus *Symphyomyrtus,* and are the favoured plantation species in Australia. The other four species included *E.regnans* (series *Obliquae*, sub-genus *Monocalyptus)* and *E.botryoides*, *E.saligna* and *E.grandis* (series *Salignae*, sub-genus *Symphyomyrtus*). It is interesting to note that six of the seven most productive species are *Symphyomyrtus*, which are known to actively transpire at a time of soil moisture deficit. This may be attributed to *Symphyomyrtus* having a better root system to exploit groundwater or faster recovery of ψ_{max}.

3.2.4. Uncertainties in quantifying stomatal processes

Stomatal conductance is arguably the most difficult parameter to measure in any process based *T* model and hence is often calibrated. To exemplify the level of intrinsic variability in $g_{s,}$ figure 3.2 above shows g_c (product of g_s and leaf area density) plotted on the log axis. The high variance reflects the uncertainty in parametarising g_s. This is also illustrated in figure 3.5, which show g_s variability for *E.globulus* and *E.nitens* as a function of solar radiation, air temperature, and vapour pressure deficit (White *et al*., 1999).

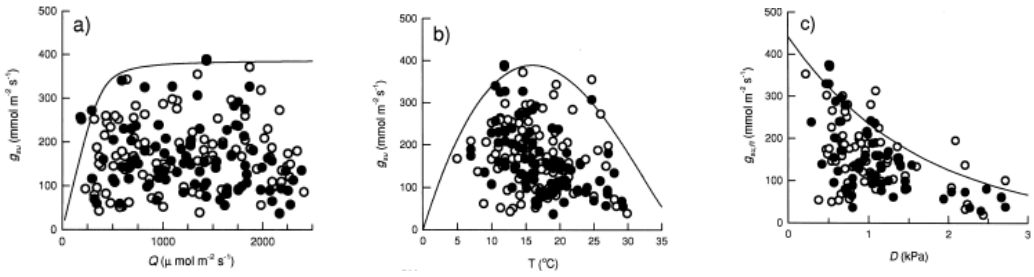

Figure 3.5: Stomatal conductance of the upper canopy of *E.globulus* (open circle) and *E.nitens* (closed circle) as a function of (a) solar radiation, (b) temperature and (c) vapour pressure deficit (from White *et al.,* 1999).

The existing challenges in quantifying g_s leads one to believe that it seems more appropriate to analyse forest *WUE* at a spatiotemporal scale more representative of a forested catchment (Denmead, 1984; Meinzer, 1993). Otherwise the level of uncertainty becomes further compounded with the task of scaling stomatal measurements to a more useful catchment scale. Despite these challenges, the role g_s has in regulating the plant's water potential gradient is crucial for understanding forest *WUE* at the medium time-scale.

3.3. Medium time-scale responses that regulate forest productivity and water use

A forest's seasonal and inter-annual above-ground biomass productivity is strongly dependent on the canopy's ability to intercept light, and the root system's ability to access available water. Plant physiological processes respond to seasonal changes in climatic variables by shifting resource allocation from one component of the plant to another. Structural changes in the morphology of a plant regulate forest productivity and water use in a way that optimises *WUE* over a seasonal time-scale. This section

will address the role tree canopies and root systems have in regulating forest productivity and water use.

3.3.1. Role of tree canopies in regulating forest productivity and water use

In native forests of Australia, potential productivity due to maximum rates of photosynthesis is high but maximum rates are rarely achieved because of limitations in water and nutrient availability (Whitehead & Beadle, 2004). The relationship between the sum of canopy absorbed radiation, Q_a, and productivity, G, over a period of time is linear, such that:

$$G = \varepsilon \Sigma Q_a \qquad [3.1]$$

where the slope is the light-use efficiency, ε (Whitehead & Beadle, 2004). For a given stand, ε decreases as productivity becomes limited by climatic factors such as rainfall and temperature or site variables such as nutrient availability.

There is a strong dependency of productivity on photosynthesis, which in turn depends on the rate of development of leaf area (*LA*) as the stand matures. There is evidence to show that addition of water and nutrient to eucalyptus plantations results in higher values of *LA* and hence productivity (Whitehead & Beadle, 2004). Cromer and Williams (1982) performed a fertiliser trial experiment where *E.globulus* was harvested at ages 2, 4, and 9.5 years to calculate annual above-ground productivity for each time interval. The average *LA* was also calculated and used to estimate the intercepted radiation for the different age groups. As shown in figure 3.6, they found a very strong linear relationship between intercepted radiation and total above-ground production (r^2:0.99). The fertiliser response increased *LA* to result in higher intercepted light levels for timber production. Most differences in annual production could be explained by differences in accumulated annual light interception (Lindser, 1984).

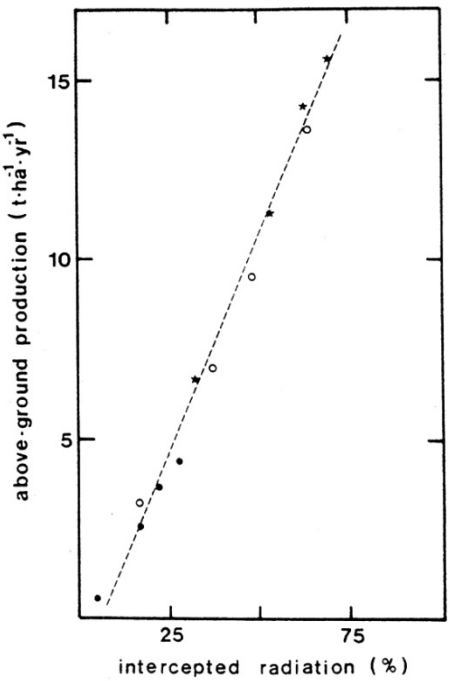

Figure 3.6: The relationship between above ground biomass productivity and intercepted radiation in a fertiliser trial of E.globulus at age: 2 years (filled circles), 4 years (open circles) and 9.5 (filled stars) (from Cromer and Williams, 1982)

The effects of water deficit on leaf production rates, expansion rates, size, senescence and shedding are well documented (Specht, 1972; Grier & Running, 1977; Eagleson, 1982; Eagleson & Tellers, 1982; Gholz, 1982; Kozlowski, 1982; Eagleson & Segarra, 1985; Nemani & Running, 1989). Pook *et al.* (1997) showed that over any given year, large seasonal variability exists in eucalypt *LA* due to soil moisture conditions. As the trees' ability to intercept radiation is strongly dependent on the seasonal timing of leaf development, expansion and death throughout the year, soil moisture conditions will affect above ground biomass production.

Cromer *et al.* (1984) performed an irrigation experiment with *Pinus radiata,* to show how water limitations influence the relationship between forest productivity and incident solar radiation. By measuring *LA* each month over a two year period for a control and irrigated stand, they were able to quantify the extent by which water limitations affected the relationship between accumulated intercepted radiation and diameter increments (figure 3.7). At the start of the experiment both treatments had a Leaf Area Index (*LAI*) of 4.5, whereas after two years the irrigated and control plots had *LAI* of 6.5 and 3.6 respectively. The decrease in growth rates for the control plots

was due to the decreased conversion efficiency of radiation caused by water limitations (Lindser, 1984). For both stands, the results show a linear relationship between accumulated intercepted radiation and diameter increments once both stands adjusted to the water regime (i.e. approximately 6 months into experiment).

Seasonal water stress can affect forest productivity by reducing *LAI* as well as affect the energy conversion efficiency of photosynthesis through stomatal closure. The final *LAI* measurements in Cromer *et al.* (1984) indicate that leaf production and shedding was the stand's response to water availability. In figure 3.7, the change in slope suggests stomatal regulation may have also reduced growth in the control plot by reducing the energy conversion efficiency.

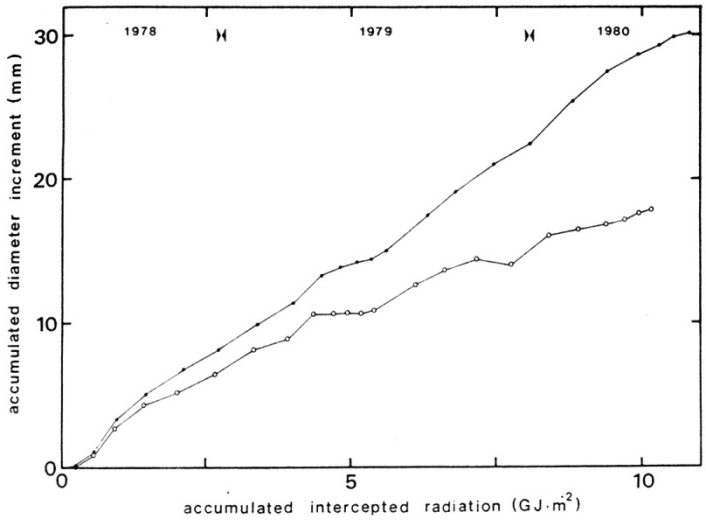

Figure 3.7: The relationship between accumulated diameter increment and intercepted radiation for a *Pinus radiata* control plot (open circle) and irrigated plot (filled circle) over a two years period (from Cromer *et al.,* 1984)

There is some evidence to show that in a plant's attempt to optimise *WUE* with adjustments to *LA* and stomatal regulation, *WUE* varies seasonally. Figure 3.8 shows a linear relationship between seasonal variability of *VPD* and *WUE*, where each point represents one calendar month averaged from observations over two years in five *E.globulus* plantations. The relationship suggests eucalypts grown in different climatic regions would be expected to have different *WUE* as a result of different climatic pressures on *LA* and stomatal regulation (Morris & Benyon, 2005). For example, annual *WUE* of a plantation in an arid region will be lower than that of a plantation in a temperate region.

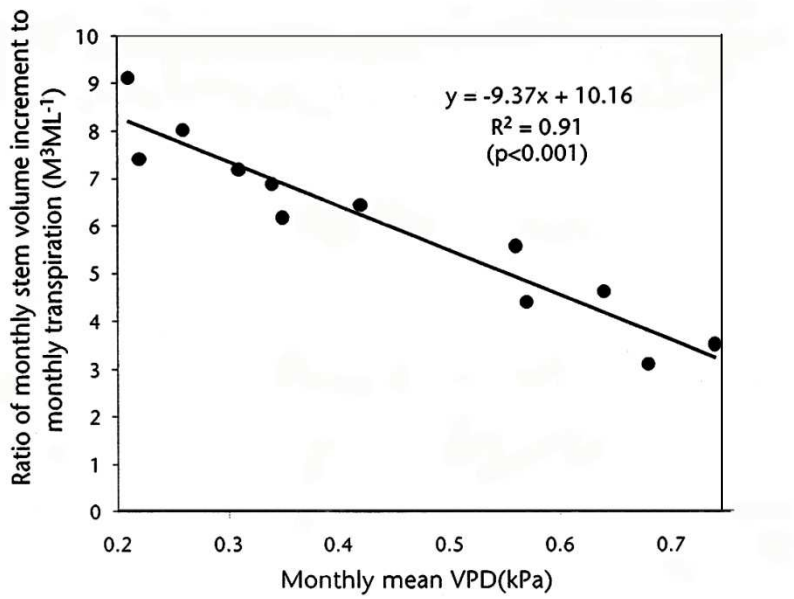

Figure 3.8: Relationship between monthly *WUE* and monthly *VPD* in five *E.globulus* plantations in south-east South Australia (from Morris & Benyon, 2005).

Within a region of relatively uniform climatic conditions, *WUE* for a particular eucalypt species on contrasting soil conditions is less variable. Benyon *et al*. (1999) performed a salinity experiment that measured tree growth and quantified water use per unit leaf area (*WU:LA*) for 6-year old *E.camaldulensis* plantations on two sites with variable soil and groundwater salinity levels. Although salinity reduced growth rates and leaf area development as a result of the reduced tree water uptake, figure 3.9 shows that the *WU:LA* remained the same for the non-saline and moderately saline site. Lindser (1984) also shows that *WU:LA* remains relatively constant, while changes in *LA* occur due to water availability. Finally, Mahmood *et al.* (2001) also reported similar results for *E.camaldulensis* plantations in Pakistan to support the argument that for a particular species, *WU:LA* is regionally constant over a uniform climate. This section has demonstrated that both productivity and water use are strongly related to *LA*.

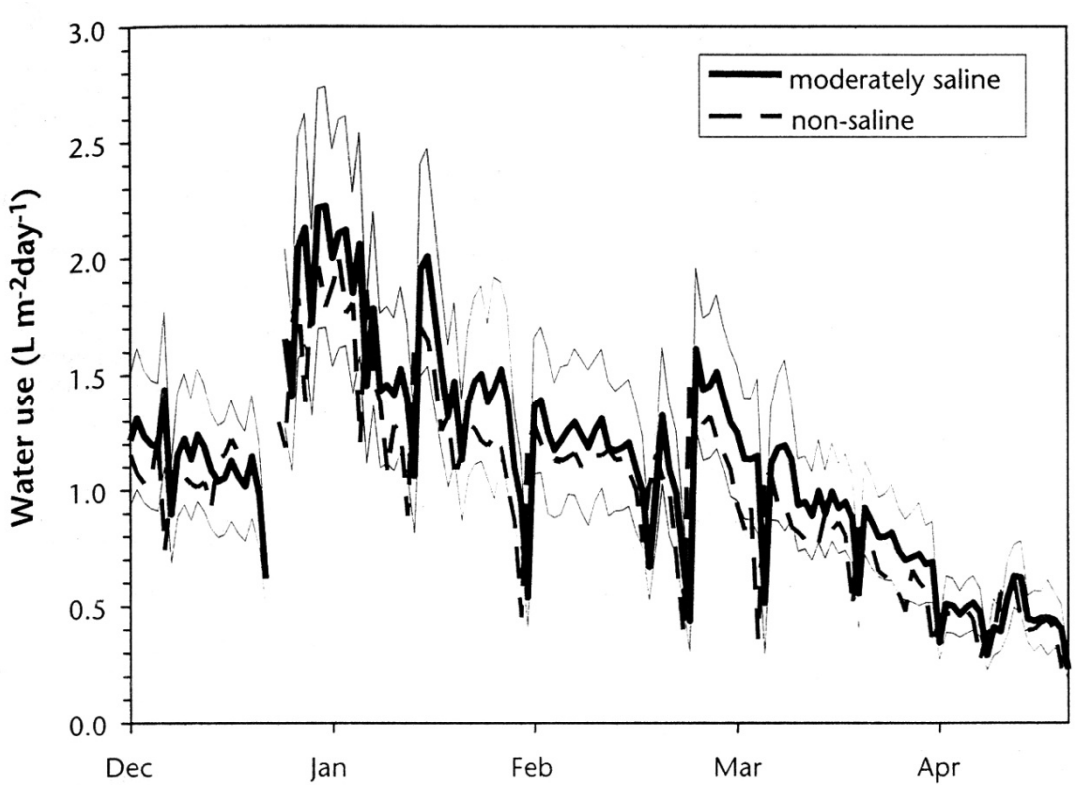

Figure 3.9: Water use per unit leaf area for 6-year-old *E.camaldulensis* trees on non-saline and moderately saline soils with thin lines providing the upper the lower 95% confidence limits for the moderately saline trees (from Benyon *et al*., 1999)

3.3.2. The inter-specific variability in tree water use per unit leaf area

Hatton *et al.* (1998) showed strong evidence that *WU:LA* is independent of plant species. The study included multi-species stands from; wet-dry season tropical woodlands of Northern Territory (three eucalypt and two other species), Mediterranean climate forests of Western Australia (two eucalypt species), woodland system with evenly distributed annual rainfall in southern New South Wales (three eucalypt species), and a plantation on saline conditions (three eucalypt species). For each site, tree water use was measured with a heat pulse method, and *LA* was measured by the Adelaide technique described by Andrew *et al.* (1979). In Western Australia, measurements were taken in both spring (wet) and autumn (dry) whereas the woodland in NSW had measurements taken in both summer and autumn. Over the climatically contrasting sites, results found a strong site specific linear relationship between *LA* and mean daily water use (i.e. constant *WU:LA*) that was independent of tree species. A single factor (species) analysis of variance did not

detect significant differences between species *WU:LA*. Although the study lacked replications for each site, the study's strength was in the similar *WU:LA* for different species across the climatically contrasting sites.

To support figure 3.8, which suggests seasonal variability in *WUE*, Hatton *et al.* (1998) showed that the slope representing the relationship between *LA* and tree water use was seasonally variable with higher *WU:LA* during months with higher *VPD*. Hatton *et al.* (1998) found no inter-specific variability in *WU:LA* as differences in water use between sites was climatically driven and reflected differences in the water potential gradient that affects the plant's water flow pathway from soil to atmosphere.

To further support the argument that *WU:LA* is similar between species, a simple model of canopy conductance proposed by Sziecz and Long (1969) is presented:

$$g_c = \overline{r_s}//LAI \qquad [3.2]$$

where $\overline{r_s}$ is mean stomatal resistance. For a canopy to regulate water use, $\overline{r_s}$ or *LAI* may be adjusted. When soil moisture levels are low, adjusting the numerator by increasing $\overline{r_s}$ results in higher leaf-air vapour pressure gradients, lower net carbon assimilation per unit leaf area, and potentially fatal leaf temperature (Pook, 1986). Adjusting the dominator, by decreasing LAI allows for the remaining leaves to maintain stomatal conductance more efficiently and the leaf shedding accelerates the nutrient cycle, which is particularly important in much of Australia's nutrient deficient environment. For this reason, g_c varies between species due to the variation in *LAI*, whereas $\overline{r_s}$ is more constant for a given *LA,* which is determined by site conditions to result in a site specific *WU:LA*.

3.3.3. Role of root systems in regulating forest productivity and water use

Plant-available water-holding capacity of soil may vary from around 50 to 400 mm per metre of soil depth (Morris & Benyon, 2005). The depth of the root zone and water storage properties of soils is therefore crucial in determining water availability. As shown in figure 3.10, water supply (rainfall, groundwater and irrigation)

explained 94% of the variation in transpiration for five south-eastern Australian plantations (Morris & Benyon, 2005).

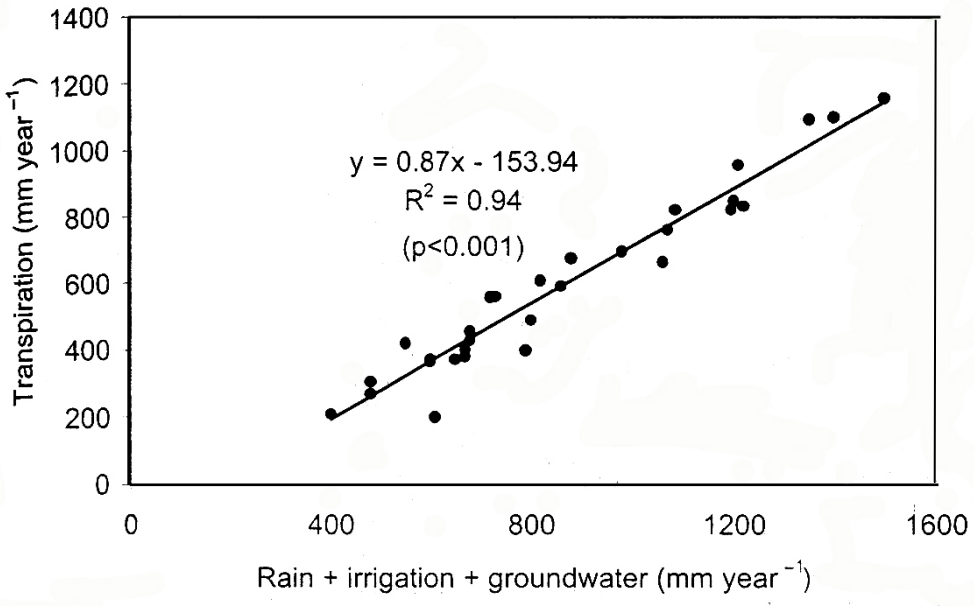

Figure 3.10: Relationship between annual available water and annual transpiration for plantations in south-eastern Australia (from Morris and Benyon, 2005)

Many studies have identified that eucalyptus transpiration demand, particularly in the drier months, may be met from water obtained from the saturated zone in the lower depths of the soil profile (Talsma & Gardner, 1986; Dye, 1996; Knight, 1999; O'Grady *et al*., 1999; White *et al*., 2002). The position of the plantation in the landscape has a large influence on the plantation's *T* because topography and catchment hydrogeology have an effect on the depth of the watertable and hence water availability. The rate of groundwater extraction by roots depends on the saturated hydraulic conductivity of the soil, depth of the watertable, and density of roots in the groundwater system. In Deniliquin, groundwater use for 3-5 year old *E.grandis* varied due to differences in soil properties rather than depth to the water (Polglase *et al*., 2002). If there are no chemical and physical barriers to limit root penetration to groundwater, during periods when trees do not receive an adequate supply of rainfall and irrigation, groundwater uptake will dominate the tree's water supply (Morris & Benyon, 2005). Groundwater can be sourced from a very early age of a plantation, as Dye (1997) has demonstrated that 3-year old *E.grandis* trees use sub-soil water reserves 8 m below the surface.

Differences in root architecture between species are important in determining water use as there is a great deal of inter-specific variability in root systems that exploit the soil profile. Falkiner *et al.* (2006) made comparisons between root systems of *Corymbia maculate* and *E.grandis* and found significant differences, with *C.maculate* roots being more developed around the capillary fringe just above the groundwater table. Due to differences in root systems, *C. maculata* had a groundwater uptake of 733 mm year^{-1} (72% of the annual water use) whereas at the same site *E.grandis* of the same age used only 377 mm year^{-1} (56% of the annual total water use) (Morris & Benyon, 2005).

In south-eastern Tasmania, Honeysett *et al.* (1992) analysed plantation water use and growth of two contrasting species *E.nitens* and *E.delegatensis* during their fourth and fifth year of growth. Experiments involved measuring stand volumes, soil water deficit ΔW up to the depth of 1 m for soils assumed to be at least 1.5 metres deep, and *LA*. Soil water deficit (ΔW) represented the water content of the root zone defined as difference between water content at field capacity and measured water content. The results found that *LA* and growth rates for *E.nitens* were approximately twice that of *E.delegatensis* over the experiment period. This meant both species had similar stand volume per unit leaf area over the experiment period, supporting figure 3.6, which suggests productivity is proportional to the light absorbed.

In assuming *ET* was simply gross rainfall (*P*) minus ΔW over the study period, Honeysett *et al.* (1992) did not include groundwater uptake when calculating WUE of each species. Using the definition, $ET = P - \Delta W$, Honeysett *et al.* (1992) calculated *E.nitens* to have a much higher WUE, and attributed it to the reduction in stomatal conductance of *E.nitens* rather than the unaccounted groundwater uptake. Honeysett *et al.* (1992) results are contrary to Sinclair (Sinclair, 1980; Florence, 1996), who found that *Symphyomyrtus* species (*E.nitens*) are known to actively transpire at a time of water stress by accessing ground water, whereas *Monocalyptus* (*E.delegatensis*) are more sensitive to drought stress and respond with rapid stomatal closure to preserve water at the expense of productivity.

In figure 3.11, a fortnightly break-down of *WUE* by Honeysett *et al.* (1992) shows *WUE* for both species was similar when soil was close to field capacity (week 170-

174), and most different when soil moisture dropped towards wilting point (week 232-246). As Honeysett *et al* (1992) do not account for groundwater use in their model, the WUE estimates are likely to be higher when the plants rely on groundwater. Considering Sinclair (1980), this was likely to be the case for *E.nitens* in figure 3.11 when soil moisture dropped during weeks 188 to 190, and after week 232. Root systems are very opportunistic and are capable of penetrating below fractures in bedrock and rock floaters to access deep groundwater many metres below the assumed and highly uncertain soil depth level. Effective root depths represented by the depth of a hand held augur penetrated into soil are unlikely to correlate well with the maximum amount of water available for deep rooted eucalyptus trees (Dye, 2000).

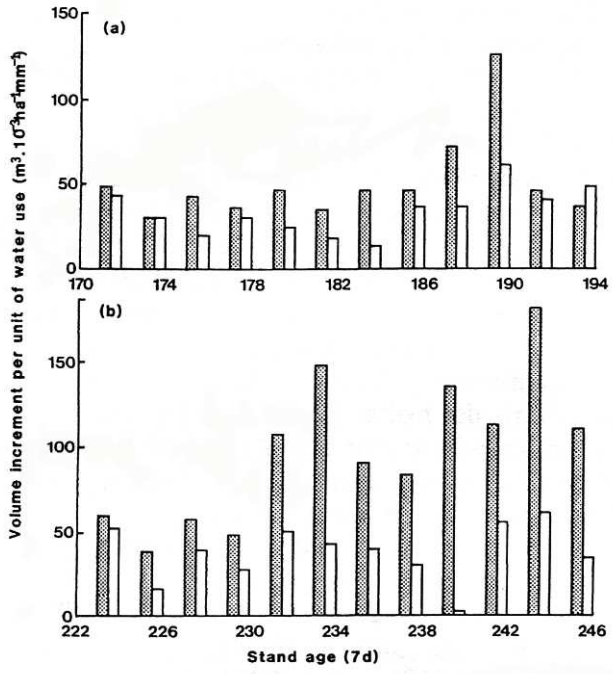

Figure 3.11: Water use efficiency of stands of E.nitens (shaded) and E.delegatensis (clear) as a function of stand age (in weeks) (from Honeysett *et al.,* 1992)

In follow up experiments undertaken by Honeysett *et al.* (1996) on a site with a mean soil depth to bedrock or rock floater of 0.6 m, groundwater was measured using an oversized hole mechanically drilled into the rock base to a total depth of 3 m. The experiment involved soil moisture, and groundwater measurements in *E.globulus* and *E.nitens* plantations over the first four years of growth. The results showed that

plantations began to source water from the groundwater near the end of the second year of growth, and this coincided with the time when the soil profile had a moisture deficit close to wilting point conditions. These experiments highlight that inter-specific variation in growth rates was due to differences in the root system's ability to exploit groundwater and not due to differences in *WUE*.

3.3.4. Effects of soil type and root architecture on WUE

Theivaeyanathan *et al.* (2001) demonstrated that *WUE* in plantations can be variable when comparing sites with contrasting soil hydraulic descriptors and/or plants that have contrasting root architecture. Theivaeyanathan *et al.* (2001) devised an experiment that analysed the amount of soil water depleted at different depths for *E.grandis* and *C.maculata* plantations established on two contrasting soils in the Murray Riverina regions, south-eastern Australia. On one site in Norwood Park the soils were alkaline, saline, sodic, and massive clay, whereas the other site, Karawatha, had sandy loam soils with neutral chemical and physical properties. Figure 3.12 shows that *E.grandis* roots were predominantly confined to the upper 1 m whereas the *C.maculata* had roots extending 2.8 m through the sandy soil to the watertable (Theivaeyanathan & Polglase, 2005).

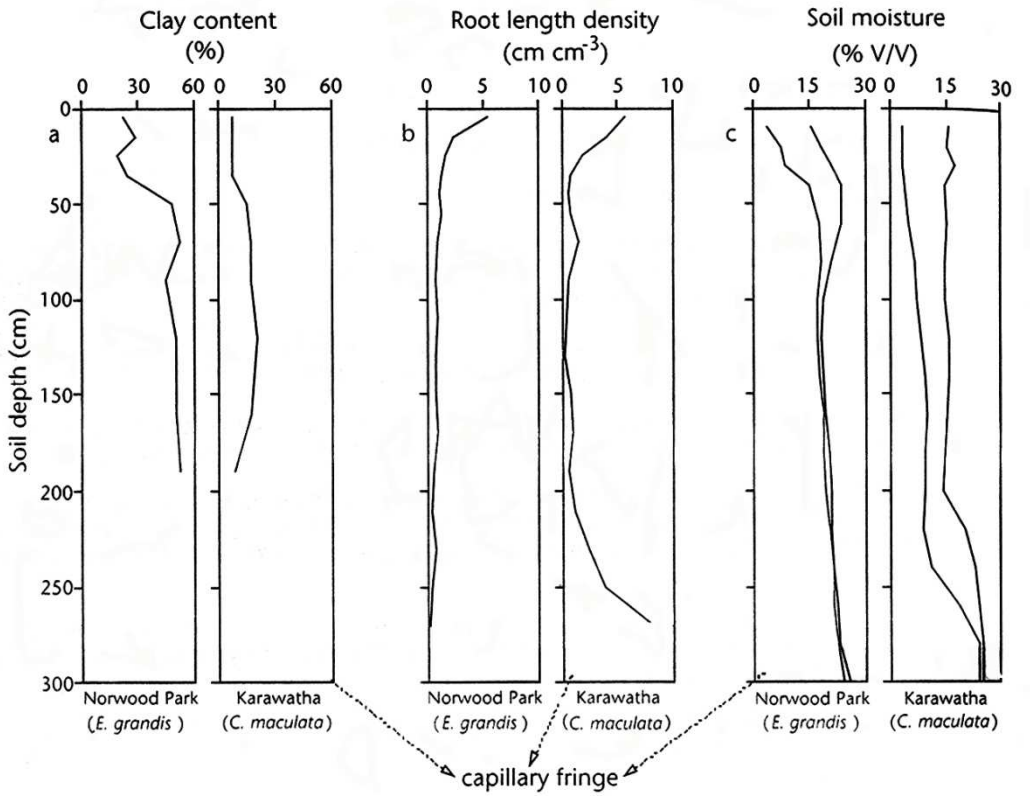

Figure 3.12: Comparison of (a) clay content of soil, (b) root distribution, and (c) highest and lowest soil water content at 4-year old *E.grandis* and *C.maculata* sites near Deniliquin, NSW (from Theivaeyanathan *et al.,* 2001)

For both sites, total water use was calculated using sap flow measurements. On the sandy soils, *ET* far exceeded the amount of water available in the soil profile and water was sourced from the groundwater table, whereas the clayey site had no evidence of groundwater depletion. Theiveyanathan *et al.* (2001) also measured stem volume growth to show a much higher growth rate on the sandy soils (16 m^3 ha^{-1} $year^{-1}$) compared to the reduced stem volume sizes on the saline clayey soils (5.8 m^3 ha^{-1} $year^{-1}$). For *E.grandis*, it was found that *WUE* of trees on sandy and clayey soils was 42.2 and 72 m^3/mm respectively. This demonstrates that for extremely contrasting soil types the distribution of biomass is distinctly different and energy is invested into different plant processes for the survival of the plant.

Figure 3.12 shows the two species have markedly different root systems due to the soil structure, with the sandy soils allowing a more efficient water up-taking root system to be developed at the depth of the groundwater reservoir. It should be expected that for the same root length density, the almost impenetrable clayey soils

required the plant to invest a lot more energy into soil penetration, root elongation, and fine root development only to result in a less rewarding water resource. For this reason, soil texture may have a significant impact on *WUE* efficiency, groundwater use, and water uptake per unit of root length (Theivaeyanathan & Polglase, 2005; Falkiner *et al*., 2006). Root architecture that develops more effective means to source large bodies of water reservoirs in the subsurface zone will effectively allow (Honeysett *et al*., 1996) for more energy to be invested into the above-ground stand volume growth. Under such conditions, it may be assumed that *WUE* may be higher.

3.4. Long time-scale responses that regulate forest productivity and water use

Changes in water use over a lifetime of a forest and at a spatial scale of a catchment are of interest for managing forested catchments. Focusing on hydrological processes that operate at the appropriate spatial and temporal scale eliminates the uncertainty and plethora of assumptions otherwise associated with scaling issues. This section reviews how a forested catchment optimises *WUE* with plant physiological processes that respond to forest stand level competition over finite resources. The aim of this section is to determine whether forest productivity of tall eucalypt forested catchments may be used to quantify catchment level forest water use once consideration are made for the causal plant physiological processes and environmental variables that influence *WUE*.

3.4.1. Equilibrium in the hydraulic flow path of a tree

After a land cover disturbance, forest regrowth slowly restores an equilibrium that exists between all the hydrological components of a forest system (Jarvis, 1975; Kuczera, 1985; Whitehead, 1985; Morikawa *et al*., 1986; Cruiziat *et al*., 2002). Jarvis (1975) pioneered a hypothesis that after a forest disturbance, the conducting components of the hydraulic flow pathways in trees regulate the water potential gradient from soil to atmosphere so that the forested system becomes balanced in relation to the finite available resource.

Jarvis (1975) observed that for vascular plants, the water flow pathway through a tree has a well confined leaf water potential (ψ_l) that is within the limits of about -0.5 to -2.5 MPa. ψ_l is a physiological measurement that represents the general water status

of the plant, with increasingly negative values depicting an increase in water stress. As water transpires from a leaf, the water potential in the cell walls drop and because of the hydraulic nature of the pathway, the reduced ψ_l affects the plants hydraulic gradient between the soil and air. A ψ_l <-3.0 generally leads to leaf shedding followed by death of the tree. Jarvis (1975) demonstrated that the ψ_l is kept within limits for a tree by regulating the ratio of leaf area and sapwood area (*LA:SA*). It has been demonstrated that the more *LA* a tree has the more surface area is exposed to the climatic elements that drive *T*. This coincides with a proportional increase in *SA* to conduct the hydraulic pathways from soil to atmosphere and hence regulate ψ_l . The end result is that the *LA:SA* ratio reflects the strong relationship between *T* and timber volume increments.

Consider figure 3.13, which illustrates the hydrological response of a forest to selective removal of a portion of trees (Jarvis, 1975). The forest initially had *n* stems per hectare, each with sapwood area *SA*, leaf area *LA*, average leaf water potential ψ_l, and stem resistance R_j. R_j determines the rate of water flow (sap flux density) *q* through a given *SA*. The total hydraulic resistance of the pathway between soil and leaves is R_p *(=*R_j*/n)*. When half the trees (*n/2)* are removed to result in the thinned section of the illustration, R_p doubles. Initially stand *T* falls (E_t'<E_t) as there are half the initial stems (*n/2*) and basal area (*BA/2*). The increase in solar radiation and available soil water for the remaining trees results with an increase in the water flow through the sapwood (*q'>q*), which results in rapid growth to restore the hydraulic equilibrium. The resulting outcome after a given time is that the new stand with half the stems has the same *T*, as each stem doubles in *SA*, *LA* and *q*, whereas the R_j is reduced to half of its original value.

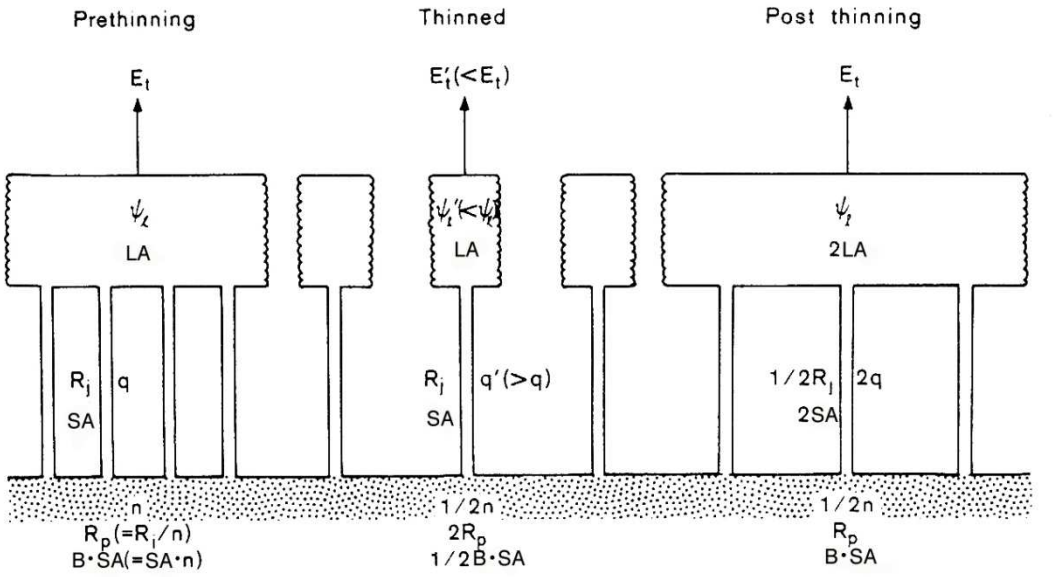

Figure 3.13: The relationships between lead water potential, sapwood cross sectional area, leaf area, transpiration rates, and flow resistance in a stand before and after thinning (from Jarvis, 1975)

3.4.2. Adjustments of stand form in response to environment under hydrological constraints

The parameter values described in figure 3.13 will adjust to environmental variables such as temperature, air humidity and available soil water. Lowering the temperature will increase R_p (i.e. sap flux density will decrease) in the stand's hydraulic soil to air flow pathway as the viscosity of water is higher for lower temperatures purely for physical reasons (Cochard *et al*., 2000). It may be expected that catchments exposed to regular frost and low temperatures will have trees with increased R_p, which results in a hydraulic adjustment that reduces *SA* and *LA*.

Magnani *et al.* (2002) used the Jarvis (1975) hydraulic equilibrium framework to demonstrate mathematically that R_p will decrease asymptotically with increases in VPD, where maximum stomatal conductance sets the asymptotic limit for R_p. It would be expected that dry climatic conditions with high *VPD* will result in a large water potential gradient in the stand's hydraulic flow pathway. As a result, the high VPD will reduce the R_p. To avoid excessive *T*, the high water potential gradient adjusts diurnally with stomatal closure or seasonally by reducing the *LA*:*SA* ratio with leaf shedding. If dry conditions persist, catastrophic xylem cavitation reduces stem basal area to equilibrate the *LA*:*SA* ratio toward its initial state.

In response to soil dryness, there is a marked increase in R_p due to the reduced water potential gradient in the stand's hydraulic flow pathway (Magnani *et al*., 2002). This would lead to extreme leaf water potentials without the onset of stomatal close or leaf shedding (Breda *et al*., 1993; Irvine *et al*., 1998). Stomata regulate leaf water potential above the level in which catastrophic xylem cavitation occurs. Furthermore because soil dryness also coincides with increases in hydraulic resistivity within the soil itself, there is a shift in plant resource distribution from foliage to conductive tissues in the fine root systems to reduce the R_p (Magnani 2002). Drought conditions increase plant resource allocation to fine roots, which results in reduced above ground growth rates. In relation to figure 3.13, increasing available soil water increases *LA*:*SA*, *q* increases, R_p decreases, and *T* increases.

3.4.3. Allometric relationship between leaf area and sapwood area at different growth stages of a forest stand

Allometry is an empirically based description of one plant descriptor in relation to another and is often used to research the *LA:SA* relationships. Medhurst *et al.* (1999) investigated the allometric relationships between *LA:SA* for *E.nitens* at different growth stages using 81 tree samples from 13 post-canopy closure sites and 34 tree samples from six pre-canopy closure sites. The study sites, located in Tasmania, consisted of a range of site qualities from; low to high nutrient status, 900 to 1400 mm rainfall, stand age from 2 to 13 years, fertiliser treatments (*N:P:K*) from 0:0:0 to 200:400:0 kg ha^{-1}, and stand densities from 1000 to 1430 stems ha^{-1}. To demonstrate the sheer contrast in the site quality for growth, post-canopy closure sites had a sapwood area range of 7 to 340 cm^2.

Results show that $LA:SA_{BH}$ (where SA_{BH} is sapwood area at 1.3m) varied with age until the age of four years in the pre-canopy closure sites (Medhurst *et al*., 1999). As shown in figure 3.14, there was a decrease in the leaf area per unit sapwood area until the $LA:SA_{BH}$ ratio became similar to the post-canopy closure sites soon after age four years. Similar observations were recognized in Beadle and Mummery (1989) and Beadle and Inions (1990) who found that the period leading to canopy closure had changes in *LA:SA*. Medhurst *et al.* (1999) suggests that this is induced by rapid

changes in light conditions in the developing early-aged crowns, which leads to changes in carbon allocation from leaf mass to stem wood.

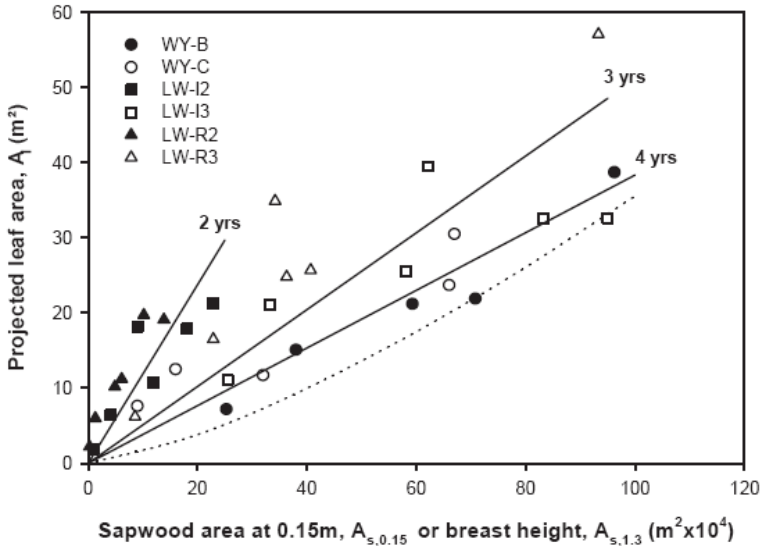

Figure 3.14: The relationship between sapwood area at breast height and leaf area for pre-canopy closure sites. Separate plots are shown for each site. Solid lines show change in relationship with age and dotted lines show non-linear relationship for post-canopy closure trees (from Medhurst *et al.,* 1999)

In figure 3.15, Medhurst *et al.* (1999) pooled the data for the post-canopy closure sites to show a strong non-linear relationship between projected leaf area *LA* and both SA_{BH} and $SA_{.CB}$ (where SA_{CB} is sapwood area at crown base). It is important to recognize that after the age of four years, the relationship was stable across all sites with markedly different silvicultural and environmental conditions, as reflected in the sapwood area range of 7 to 340 cm^2. The non-linearity in the relationship indicates that for larger trees; the *LA*:*SA* ratio was larger, and the sapwood hydraulic conductivity (*k*) also needed to be higher (Pothier *et al*., 1989). This is supported by Medhurst *et al.* (2002), who also demonstrated that resource capture, and hence growth rate influences *k.*

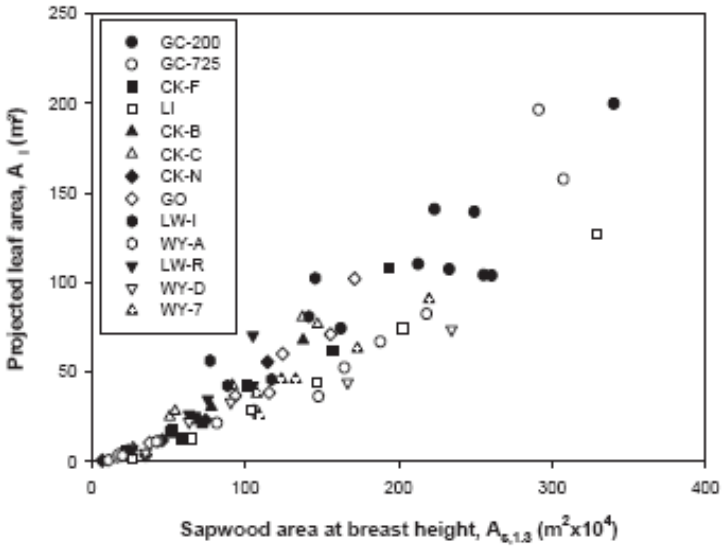

(a)

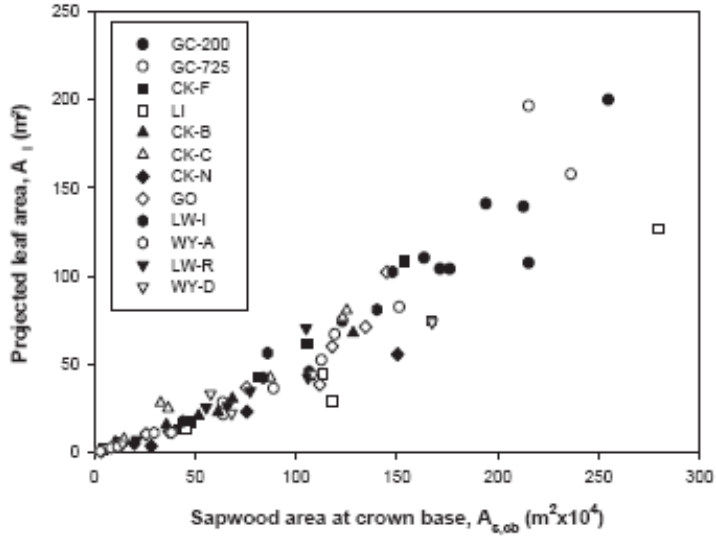

(b)

Figure 3.15: The relationship between (a) leaf area and sapwood area at breast height (n=81) and (b) leaf area and sapwood area at crown base (n=75) for post canopy closure sites (from Medhurst *et al.,* 1999)

Medhurst *et al.* (2002) measured *k* at crown base and at breast height to make comparisons. It was found that *k* increased by approximately 100% at crown base and this coincided with a decrease in sapwood area of 19%. This represented an increase in sap flux density of 60%, which was strongly correlated with almost 60% more leaves for the given sap wood area at crown height. This supports the argument that greater *k* allows for higher *T* rates through the leaf area (Medhurst & Beadle, 2002). Medhurst *et al.* (2002) also found that measurements of *k* at crown base were positively correlated with *LA:SA*, as a higher *LA:SA* has a larger transpiring leaf area

that sources water from a smaller sapwood area and can only do so if *k* increases to meet the demand for *T*. Similar results were found by Whitehead *et al.* (1984).

3.4.4. Effects of site condition on the relationship between leaf area and sapwood area

Whitehead (1978) and Binkley (1984) both identified a positive correlation between *LA:SA* and site quality. Considering a positive correlation also exists between *LA:SA* and *k* (Medhurst & Beadle, 2002), higher quality sites are likely to have higher *k*. Increases in *LA:SA* and *k* with site quality suggests higher T rates per SA occur with increases in water availability. As SA is an indication of recent forest growth, less water limited sites are likely to be less WUE, which could be explained by the fact that water limited sites (with reduced *LA:SA* and *k*) use water more sparingly in the summer period when most T occurs.

In Medhurst *et al.* (1999), changes in *LA:SA* over the first few years are in effect a result of site quality per stem being effectively reduced with increased competition for available water and intercepted light. In the first couple of years, the lack of spatial interaction for finite resources amongst the individual stems results in the site quality being more favorable per stem. With water not being limited, *k* and *LA:SA* are high and *WUE* is not adjusted upwards for an optimal resource capture that considers competition. Competition defines how finite the resource is by enforcing an optimal *WUE* that equilibrates the *LA*:*SA* ratio in order to consider the rate of stand productivity for the given water allocation. A positive correlation between *LA:SA* and site quality, the changing *LA:SA* over the initial years of growth, and the non-linearity of the *LA:SA* relationship suggest old forests on high quality sites and young forests without limited resources have a lower *WUE* than sites with restricted resources due to competition.

As water availability and climate factors influence the plant's water flow pathway from soil to air, drier atmospheric conditions would be expected to influence *LA:SA*. Magnani *et al.* (2002) used experiments on *Pinus sylvestris, Pinus contorta* and *Pinus ponderosa* to show that an increase in *VPD* affects the plant's hydraulic flow path in such a way that the finite water resource becomes more limited. Figure 3.16

provides a relationship between *LA:SA* and *VPD*, to demonstrate that *LA:SA*decreases as the demand for water increases.

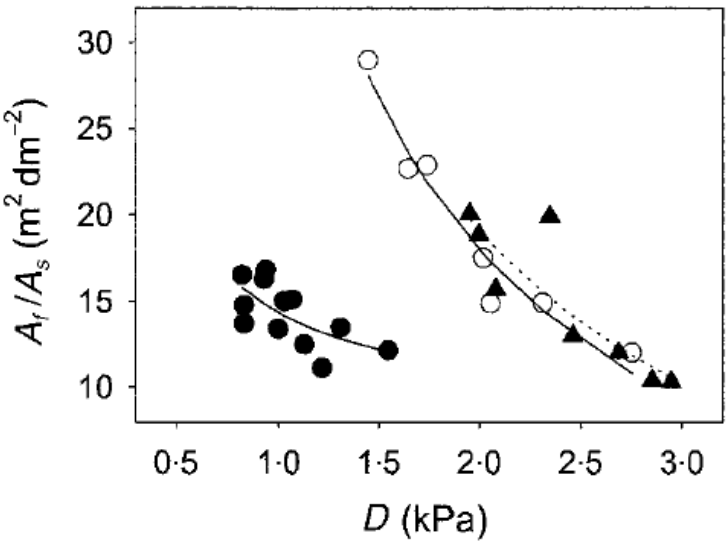

Figure 3.16: Effects of vapour pressure deficit (*D*) on the leaf-to-sapwood area ratio (*LA/SA*) of mature stand of *Pinus sylvestris* (•; Mencuccini, 2001*, Pinus contorta* (open circles) and *Pinus ponderosa* (o and Δ, respectively; DeLucia *et al*., 2000).

3.4.5. Effects of competition on forest productivity and water use

When a plantation is established, there is initially no competition between the individual stems for finite resources. This rapidly changes as the plantation develops and competition for resources affects stand productivity and water use. Morris and Benyon (2005) found that the stocking rates of three year old *E.globulus* and *E.grandis* plantations affects the *WUE* because of different levels of competition. In the study, each species was planted out with a stocking rate of 1333 trees ha^{-1} and 2666 trees ha^{-1} to show that the denser stand had a higher *WUE*. The denser stand's higher stand water use was not proportional to the increase in sap wood area as competition induced resistances to the water flow pathway between the soil and canopy boundary layer, which reduced sap flux density and in effect increased *WUE*.

Figure 3.17 represents the same two stands for the first six years of growth to show that the *LA:SA* ratio declined strongly during early years of growth, and after a few years both stands resulted in a consistently uniform *LA:SA* ratio (Morris & Benyon, 2005). Figure 3.14 also showed changes in *LA:SA* until age four years followed by

uniform ratio being established (Medhurst *et al*., 1999).

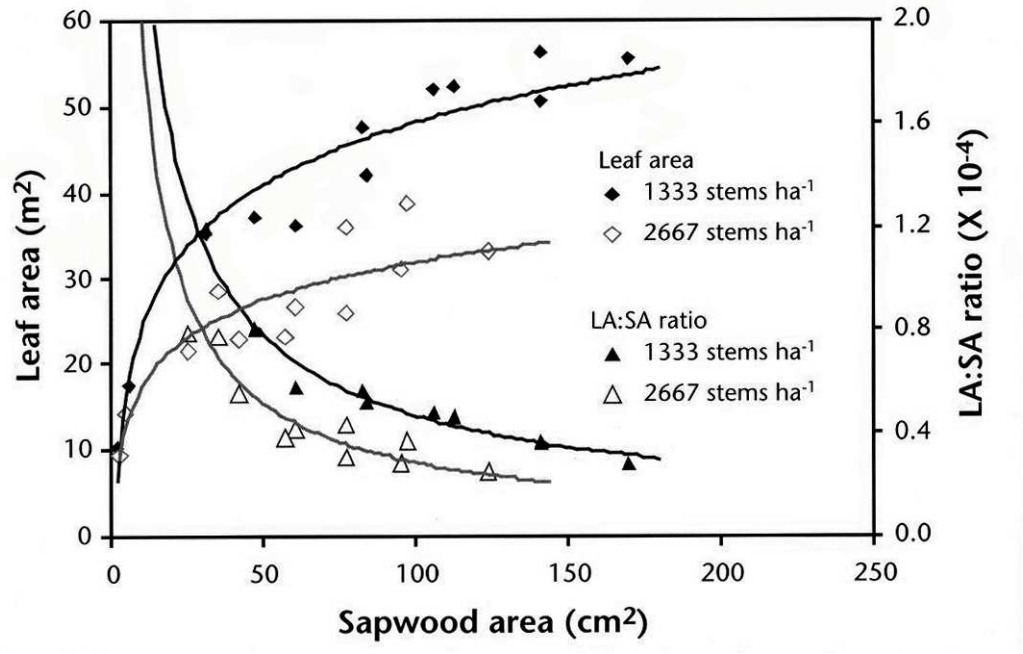

Figure 3.17: Leaf area and sapwood area of single trees of *E.globulus* and *E.grandis* in irrigated one to six year old stands with high and low stocking at Shepparton, Victoria (from Morris & Benyon, 2005)

The lack of competition for available soil water in the less stocked three year old plantation resulted in a higher soil conductance and hence less resistance of water flow through the soil-plant-atmosphere continuum pathway. The less stocked stand also had a lower *LA,* which resulted in lower atmospheric vapour pressure due to reduced crown shading (i.e. more solar radiation penetrating canopy to create drier atmosphere), reduced transpiration volume (i.e. less water vapour entering the atmosphere), and increased air movement (i.e. transpired water vapour is carried away more readily).The water potential gradient in the less stocked stand induced greater hydraulic conductance, which resulted in the trees using water less sparingly for the given growth rate. The contrasting *WUE* observed in the early years of the two stands became diminished once both plantations developed a closed canopy, and the limiting water resource became dictated by the same site condition and not by differences in competition (Morris & Benyon, 2005).

3.4.6. Effects of thinning on forest productivity and water use

Plantations reach a peak in their growth at a relatively early age so thinning often takes place at more than one occasion to optimise productivity. Thinning forest stands when volume increments reach their highest growth rate further accelerates the growth of crown and basal area of remaining trees, to result in a delayed higher peak in volume production (Florence, 1996). In Tasmania, Goodwin (1990) showed that for a 16 year-old *E.obliqua* regrowth thinned from 1650 stems/ha to 500 stems/ha, the net basal area growth was the same a year before and after the thinning despite the discrepancy in stems per hectare. Competition within unthinned stands results in relatively weak crowned trees with low *LA*, particularly on lower quality sites, which results in a slower growing timber resource (Florence, 1996).

In south-eastern South Australia at a low rainfall (500 mm yr^{-1}) and high rainfall (650 mm yr^{-1}) plantation site, transpiration was measured before and after a five year-old *E.globulus* stand was thinned (Fife *et al*., 2002). The drier site was thinned from 1100 to 400 stems ha^{-1}, whereas the wetter site was thinned from 700 to 400 stems ha^{-1}. The effect of thinning on the stand transpiration was short lived as the sap flux densities increased after thinning at both sites. Within 6 -12 months both sites had no statistically significant difference in transpiration rates between the thinned and unthinned treatments. The increase in sap flux density in thinning studies is common (Morris & Collopy, 1999; 2000; Medhurst *et al*., 2002). Thinning plantations increases the available solar radiation and soil water for the retained trees, which results in a physiological response in the stand to restore the balance in water supply and demand. The physiological response involves increasing the rate of sap flux to increase *WU:LA*, which increases growth rates of retained trees and over time the processes restore the *LA:SA* relationship (Morikawa *et al*., 1986).

This is demonstrated in figure 3.18, which shows a response of thinning *P.radiata* from a basal area of 30 m^2ha^{-1} to 15 m^2ha^{-1} (Lindser, 1984). The results show that the *LA:SA* adjusted by increasing the leaf area per stem area, which accelerated the growth of the stem area. The increase in growth was inevitably met with an increase in water use to balance out the supply and demand of available water until the hydraulic equilibrium was restored. Obviously if a stand is reduced to a size that far

exceeds its ability to re-allocate the water supply amongst retained trees then water use will not be completely restored. A consistent *LA:SA* relationship before and after thinning is supported with similar findings for a range of tree species (Grier & Waring, 1974; Rogers & T.M., 1979; Kaufmann & Troendle, 1981; Albrektson, 1984 Espinosa-Bancalari M.A. *et al*., 1987; Coyea & Margolis, 1992; White, 1996; Penner & G., 1996 Medhurst *et al*., 2002).

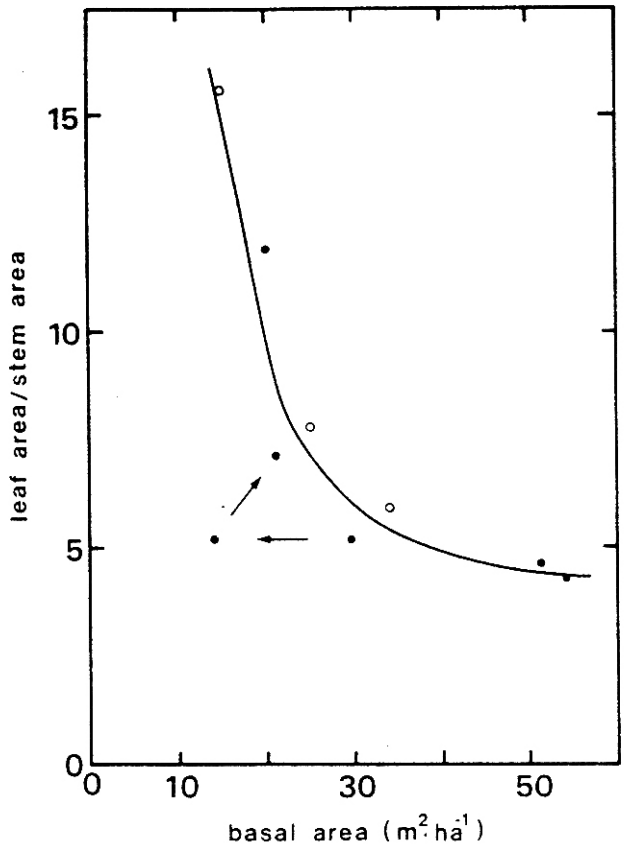

Figure 3.18: The ratio between leaf area and stem surface area (m^2/m^2) in relation to basal area in two age series of *Pinus radiata* plantations. The arrows indicate the change induced by thinning and the subsequent recovery after two years (from Lindser (1984)

This section has shown that thinning increases the available water resource which increases growth of the transpiring crown and timber producing basal area. This results in an increase in sap flux density and *LA:SA* until the water resource becomes limited by site conditions, which adjusts the *LA:SA* ratio to pre-thinning conditions. This provides strong evidence that forest productivity is strongly related to forest water use.

3.4.7. Effects of intensive forest management on forest productivity and water use

In the past decade it has become increasingly evident that timber plantations need to be managed with the water resource in mind (Nambiar & Ferguson, 2005). Plantation management often involves soil cultivation, weed control, optimised tree spacing, fertilisation, thinning, pruning, and planting of genetically selected vigorous strains of eucalypts. Chemical weed control and annual applications of nitrogen and phosphorus for the first few years of growth are usually closely interdependent in achieving an optimum growth response (Florence, 1996). Raison *et al.* (1982) has demonstrated that fertilisation is capable of producing a three-fold increase in wood production for a 9.5 year old *E.globulus* plantation. Intensive cultivation promotes effective root accessibility to soil water storages, which increases growth rates of plantations on soils that would naturally impede rapid colonisation of root systems and suppress above ground growth rates (Florence, 1996; Falkiner *et al*., 2006). The initial spacing of plantation stands optimises the stand density with a predetermined thinning and pruning regimes that provide the most efficient solar radiation uptake without imposing undue competition between trees (Florence, 1996). Plantation management improves stand vigour for carbon assimilation by optimising resource capture with increased transpiring leaf area and improved root systems to draw the required water.

Genetic selection methods, such as breeding inter-specific eucalyptus hybrids, are advancing rapidly to escalate plantation productivity. For example, *E.grandis* is limited with its potential plantation sites because of its need for more fertile soils and high rainfall (>800 mm year^{-1}) but its fast growth rates are favourable for breeding inter-specific eucalyptus hybrids that are suitable for a broader range of sites (Arnold *et al*., 2005). Improvements of *E.globulus* through genetic variation has provided stem volume gains of more than 15% and wood density gains of 10% (McRae, 2004).

The contrasting growth rate of native forests and plantations is best exemplified with an experiment undertaken by Turnbull *et al.* (1988) in South-East Tasmania. The study involved measuring timber volumes for intensively managed *E.globulus,*

E.nitens, *E.regnans* and *E.delegatensis* plantations that received uniform treatments of fertiliser, weed and pest control. Figure 3.19 compares the current annual increments (*CAI*) for the most successful gum species *E.nitens,* and ash species *E.delegatensis,* against *CAI* of regenerating forests derived from local native forest yield tables. A stand's *CAI* is simply the increase in timber volume over the current year. The results show maximum growth rates of regenerating forests, with a *CAI* of approximately 28 m^3/ha/yr at age 34, were exceeded by the *E.nitens* stand with a *CAI* of 31.7 m^3/ha/yr at age four years. *E.globulus* (not shown in figure 3.19) also exceeded the regenerated forest at age four years with a *CAI* of 30.3 m^3/ha/yr.

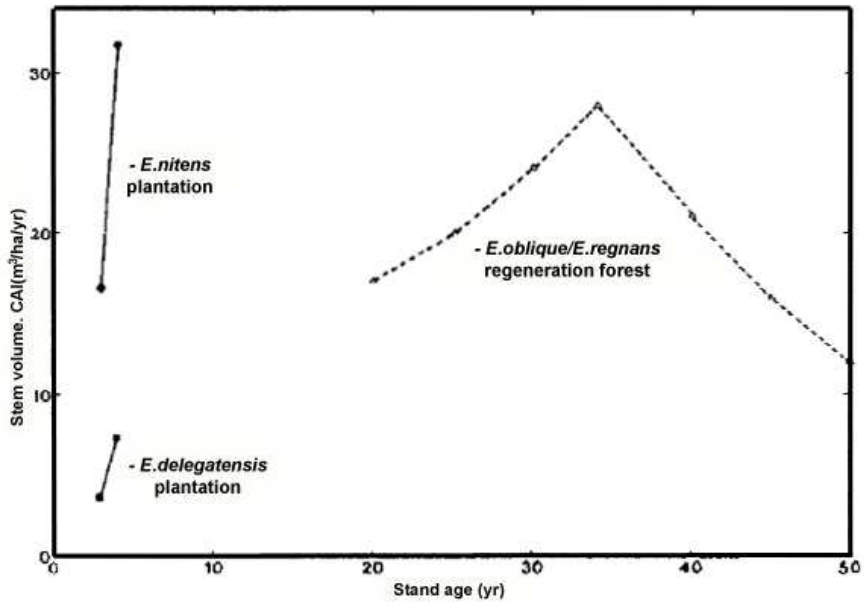

Figure 3.19: A comparison of current annual increment of intensively managed plantation and extensively managed regeneration forest (from Turnbull *et al.,* 19888)

It is evident that native forests exploit environmental resources rather conservatively, sacrificing rapid growth in order to ensure survival over an evolutionary time scale with long-term stress tolerance (Cannell 1979). Reducing the hydrological conductance at any section of a plant that transports water from soil to atmosphere reduces *T*. Native forests reduce water use by adopting a mechanism that reduces forest productivity through reducing *SA*. The astoundingly high growth rates of *E.nitens* and *E.globulus* were attributed to *LA* differences between species (Turnbull *et al*., 1988). Turnbull *et al.* (1988) recognised the faster volume growth in *Symphyomyrtus* [*E.nitens* and *E.globulus*] compared to the *Monocalyptus* [*E.obliqua* and *E.delegatensis*] species is due to the size of the photosynthetic canopy rather

than any difference in the efficiency of the photosynthetic process. It is possible to increase the total conductance of a catchment's vegetation by planting faster growing trees that have higher *LA* to result in greater SA (Morris & Benyon, 2005).

3.4.8. Catchment level forest productivity and water use

Kuczera (1987) developed an empirical relationship between streamflow and forest age to suggest a regenerating forest's water use is related to the forest's growth rate. Figure 1.1, which is commonly referred to as the Kuczera curve, shows that after a land cover disturbance of a *E.regnans* forest, the annual stream flow trend rapidly declines to age 27 before a gradual recovery in streamflow by about age 200. The results have lead to extensive research efforts that have explained similar streamflow trends with forest age for a range of forest types (Langford, 1976; Cornish & Vertessy, 2001; Lane & Mackay, 2001; Roberts *et al*., 2001; Vertessy *et al*., 2001; Watson *et al*., 2001; Bren *et al*., 2010; Macfarlane *et al*., 2010; Pfautsch *et al*., 2010).

There are no studies that have explicitly evaluated the Kuczera curve by relating a spatiotemporal model of a catchment's forest productivity with the catchment's streamflow trends. Interestingly, the general shape of the long-term stream flow trend in the Kuczera curve has a similar shape (but is inversely related) to the general shape of eucalyptus Mean Annual Increment (*MAI*) and *CAI* curves. The *MAI* is the average annual forest growth rate that corresponds to a given age of a forest stand and is calculated by dividing the timber yield value of a forest stand by its corresponding age. This provides strong evidence that forest productivity is closely related to forest water use on a catchment level.

West (1993) constructed growth curves, in the form of stand stem volume yield prediction models, for six eucalypt species. Figure 3.20 shows *CAI* and *MAI* curves for three south eastern Australia's main native timber resource species; *E.regnans*, *E.obliqua*, and *E. delegatensis*. Intrinsic growth rates of the three species did not differ greatly and the capacity of a site to supply resources for growth was the determining factor for growth rate. Interestingly, the peak *MAI* was approximately at the forest age of 27, which reflects the time when the predicted streamflow in the Kuczera curve in figure 1.1 reaches the lowest levels after a land cover disturbance. Considering the plant physiological theory presented, similar growth rates on similar

site conditions would suggest the *WUE* would be the same for all three species. Morris (2005) recognised that within a region of relatively uniform climate conditions, forests with the same productivity will have the same *WUE*, whereas over larger areas it is possible that *WUE* may vary.

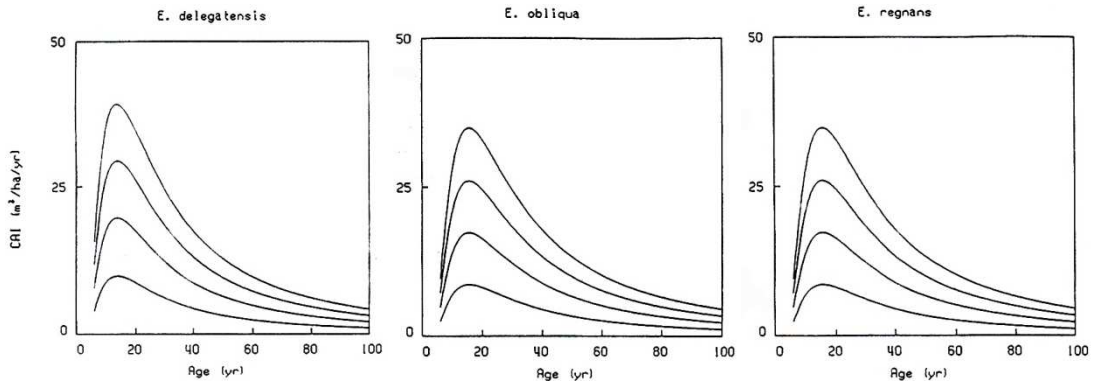

(a) Current Annual Increments of the three species

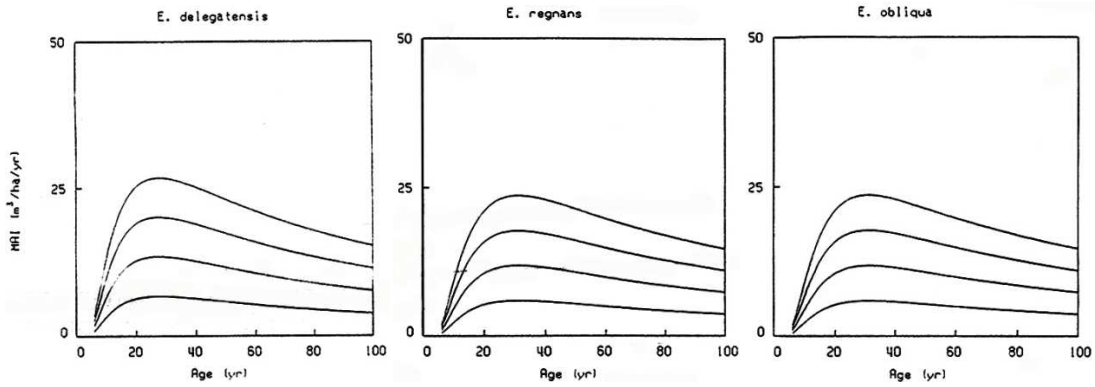

(b) Mean Annual Increments of the three species

Figure 3.20: The (a) CAI and (b) MAI curves for *E.regnans*, *E.obliqua*, and *E. delegatensis* (from West, 1993)

Variable *MAI* of eucalypts at different sites around Australia is due to the intrinsic growth characteristics of a species at different stages of development, as well as the sites innate capacity for growth (West & Mattay, 1993). For example, West (1981) compared growth rates for 13 mixed-species stands with naturally occurring even aged *E.regnans*, *E.obliqua* and *E.globulus* forests aged 20-79 in south-eastern Tasmania. The results showed that *E.globulus* had higher diameter increment than the other two species at about 20 years of age but lower increments after about 40 years. It is possible that *E.globulus* is more productive at an early age due to an increase in intercepted radiation by juvenile leaves with much higher leaf area. Plant physiological theory would also suggest that the early phase of productivity in

E.globulus (*Symphyomyrtus*) is a result of the root system being more effective at exploiting the groundwater system from an earlier age to allow for a higher water use. This is supported by Davidson and Reid (1980) and Zimmer and Grose (1958) who both found that *Monocalyptus* species have a lower root:shoot ratio in the seedling stages than *Symphyomyrtus* species. It is evident that forest growth increments during the life time of a forest are reflected in the development of plant physiological mechanisms that determine rates of forest water use (Noble, 1989).

3.5. Synthesis of plant physiological theory for generating forest growth models that explain streamflow trends

To explain streamflow trends with forest growth models it is necessary to account for the causal plant physiological processes and environmental variables that influence *WUE*. Figure 3.21 shows a relationship between annual transpiration and annual stem volume increment for 22 plantations at five sites located in South Australia, southern New South Wales (NSW), and northern NSW (Morris & Benyon, 2005). The plantations had highly variable management strategies and variable age classes consisting of four species; *E.grandis* (age 5 to 6), *E.globulus* (age 5 to 9), *P.radiata* (ages 5 to 30 years), and *C.maculata* (age 4). The sites' soil types are highly variable and include sands, loamy sands, heavy clays, saline soils and sodic massive clays. The *WUE* of the sites has considerable variation about the mean regression line, which may be attributed to a range of causal plant physiological processes and environmental variables. Below is a concise synthesis of the plant physiological theory addressed in the review that may explain the variable deviation in the mean regression line.

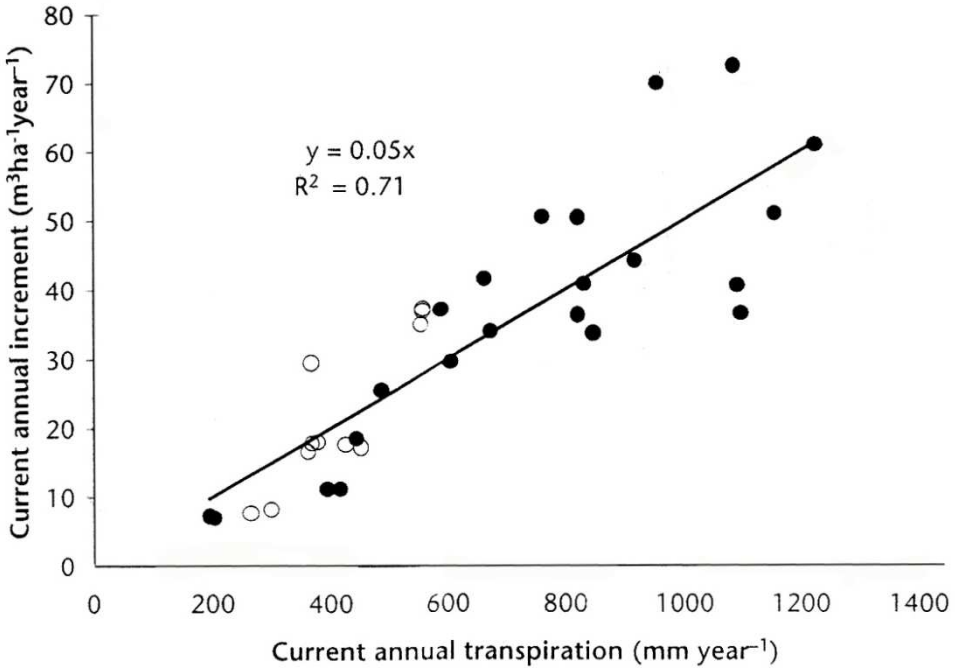

Figure 3.21: Relationship between current annual stem volume increment and current annual transpiration from a range of plantations in south-eastern Australia. Open circle are plantations with rainfall only. Closed circles represent plantations accessing additional water from the water table (from Morris & Benyon, 2005)

Stomata optimise *WUE* with g_s by responding to diurnal conditions in *VPD* and soil moisture (Morris & Benyon, 2005) in order to maintain a relatively constant ratio of water transpired to carbon gain (Farquhar & Sharkey, 1982; Whitehead, 1985; Hubbard *et al*., 2010). For this reason, regulation of g_s is strongly reflected in tree water use and growth (Hellmuth, 1968). Different species regulate g_s differently in response to high *VPD* due to differences in the root system's interaction with soil moisture and groundwater, as demonstrated between the *Symphyomyrtus* and *Monocalyptus* species (Sinclair, 1980). Literature provides little evidence that inter-specific variation in *WUE* is innately regulated by g_s for Australia's main timber producing species, as g_s variation is a function of environmental variables and the plant's ability to access soil moisture. Importantly, the uncertainty associated with quantifying and scaling g_s for catchment-scale studies means *WUE* should be quantified at a spatiotemporal scale of a forested catchment (Denmead, 1984; Meinzer, 1993; White *et al*., 1999).

Differences in annual forest production are highly correlated with differences in accumulated annual light intercepted by *LA* (Cromer & Williams, 1982). Cromer *et al.* (1982) demonstrated that fertiliser increases *LA*, and hence increases intercepted light, which linearly increases forest diameter increments. Large seasonal variability in soil moisture conditions coincide with fluctuations in *LA* (Pook *et al*., 1997), and irrigation experiments have shown that changes in *LA* due to soil moisture conditions are also linearly related to forest productivity (Cromer *et al*., 1984). *LA* is central to the relationship between forest productivity and water use as it also represents the transpiring surface that largely explains *T* rates (Watson *et al*., 1999a). The relationship is not completely explained by *LA* as eucalypts grown in different climatic regions may have different *WUE* as a result of different climatic pressures on *LA* and g_s. For this reason, regionalising a forest growth and water use relationship needs to consider the negative linear relationship between seasonal variability of *VPD* and *WUE* (Morris & Benyon, 2005). This may be done by developing a separate forest *WUE* relationship for broadly uniform climatic conditions represented by temperate, sub-tropical, and arid climatic regions.

Changes in *LA* with changes to water availability cause *WU:LA* to be relatively constant (Mahmood *et al*., 2001). Within relatively uniform climatic regions, *WU:LA* of a particular species is similar on contrasting soil types as g_s is similar, whereas g_c increases as a result of denser LA on soils that store plant available soil moisture more effectively (Benyon *et al*., 1999). Seasonally, plants regulate g_c by adjusting *LA* rather than g_s because with water shortages, decreasing g_s results in higher leaf-air vapour pressure gradients, lower net carbon assimilation per unit leaf area, and potentially fatal leaf temperature. Alternatively decreasing *LA* allows for the remaining leaves to maintain g_s more efficiently and the leaf shedding accelerates the nutrient cycle (Hatton *et al*., 1998). For this reason, the light intercepting and water transpiring *LA* strongly influences tree diameter increments through its response to plant available soil moisture.

The rate of groundwater extraction by roots depends on the saturated hydraulic conductivity of the soil (Polglase *et al*., 2002), depth of the watertable (Dye *et al*., 1997), and differences in root architecture between species (Noble, 1989). *WUE* of plants can be variable when comparing sites with contrasting soil hydraulic

descriptors and/or plants that have contrasting root architecture (Theivaeyanathan *et al*., 2001). Soil dryness increases soil hydraulic resistivity, which shifts plant resource distribution from foliage to fine root systems, reducing *WUE* of above-ground growth. Impenetrable soils require the plant to invest a lot more energy into soil penetration, root elongation, and fine root development for a less rewarding water resource, which reduces *WUE* due to water uptake per unit of root length (Falkiner *et al*., 2006). For these reasons, regionalising a relationship between forest growth and water use needs to consider the effects of contrasting soil types on *WUE* as a result of contrasting ratios of root:above-ground biomass development.

Equilibrium between all hydrological components of a forest system provides the most compelling evidence of a strong relationship between forest productivity and water use. As high *VPD* increases and soil dryness decreases a plant's water potential gradient, the plant physiology responds to the water potential gradient to make forested systems balanced in relation to the finite available resource (Jarvis, 1975). To avoid catastrophic xylem cavitation when a tree's ψ_l becomes too negative, the *LA:SA* ratio regulates the tree's hydraulic flow pathway. A strong relationship between *T* and growth is reflected in how *LA* and *SA* interact, as increasing *LA* increases *T* and growth (i.e. *SA* production).

Over the period of pre-canopy closure, soil moisture and light conditions become successively more limited, which results in a decrease in *LA:SA* ratio (Medhurst *et al*., 1999). Competition increases after canopy closure and *LA:SA* ratio becomes more constant and non-linear, with larger trees having higher *LA*:*SA* ratio and *k*, and hence higher *WU:LA* (Medhurst & Beadle, 2002). Increases in *LA:SA* and *k* means higher T rates per SA, which may suggest reduced *WUE* as there is less new growth (*SA*) for the given *T*. For the same reasons, a positive correlation between site quality and *LA:SA,* as well as site quality and *k*, also suggests reduced *WUE* at sites with less water limitations (Binkley, 1984). Finally, a negative relationship between *LA:SA* and *VPD* exists, which suggests that eucalypts grown in different climatic regions may have different *WUE* as a result of different climatic pressures on *LA* and g_s (Magnani *et al*., 2002).

Thinning in effect increases site quality for retained trees, which may reduce *WUE* by increasing *k* and *WU:LA*. Over time there is a restoration in pre-thinned *LA:SA* to restore the stand's optimal *WUE,* which is determined by site conditions when water resource is limited by competition (Morikawa *et al*., 1986). Thinning delays peak in *CAI* as net basal area growth increments may be same before and immediately after thinning due to higher growth rates and resource capture of retained trees (Goodwin, 1990). Prior to recovery of pre-thinned *LA:SA , WUE* is reduced as a result of reduced competition increasing water availability (Fife *et al*., 2002). For this reason, the regional model needs to recognise that understocked forests with unlimited water resource may be less *WUE*.

Replacing natural vegetation with forest management regimes not reflective of the natural environment will result in changes to the landscape's hydrology. Intensive forest management of plantations has been coined precision forestry (Battaglia *et al*., 2004) for its exhaustive use of the limited water resource with; soil cultivation (Falkiner *et al*., 2006), weed control (Florence, 1996), optimised tree spacing (Florence, 1996), fertilisation (Raison *et al*., 1982), thinning (Goodwin, 1990), pruning, and planting of genetically selected vigorous strains (McRae, 2004). Contrast to this management system, water use by native forests consists of many mechanisms that make certain that available water is not used excessively. Within the natural environment, site factors exert strong control on the vegetation's water up-take through species composition, natural stocking densities, natural stand structure, and natural disturbance periods. Considering the plant physiological theory presented, a regional model needs to recognise that plantations optimise competition for resource capture, which effectively increases water use per unit area greatly but imposes pressures on the system to become more *WUE*.

3.6. Conclusion

Forest growth models of tall eucalypt forested catchments may be used to quantify catchment level forest water use once considerations are made for the causal plant physiological processes and environmental variables that influence *WUE*. Presently, forest hydrology models in Australia underutilise existing forest inventory and forest mensuration databases for managing the forested water resource. Detailed forest

inventory data exists for most forested catchments in south eastern Australia and this information should be used to generate hydrologically relevant forest growth models that are capable of explaining streamflow trends. This chapter has demonstrated that forest inventory data, which is commonly used to model forest growth, may provide significantly more information to explain streamflow trends than the forest hydrology modelling methodologies described in chapter two.

The hydrological equilibrium in forested systems is driven by the response of *LA:SA* and sap flux density to environmental conditions and stand competition for the limited water resource. To improve on the already strong relationship between forest productivity and water use in figure 3.21, considerations need to be made for the:

- negative linear relationship between *VPD* and *WUE*, as inter-regional variability in *VPD* affect *LA* and g_s,
- effects of contrasting soil types, as increases in ease of soil root penetration and soil moisture holding capacity increase *WUE* by reducing root:above-ground biomass ratio,
- differences in inter-specific root system architecture between *Symphyomyrtus* and *Monocalyptus* species, as effective subsurface water exploitation results in an increase in *WUE* by reducing root:above-ground biomass ratio, and,
- extent of limitations of water resource due to competition and environmental pressures as; pre-canopy closure forests, understocked forests without water limitations, and forest sites with less water limitations are less *WUE*, whereas intensive systems such as plantations and water limited forests are more *WUE*.

Chapter 4: Overview of model structure

4.1 Introduction

4.1.1 Rationale behind proposed model structure

Hydrological modelling is often concerned with the processes of runoff generation to determine the proportion of the total rainfall that becomes runoff. Paired-catchment studies and water balance models have become the two most commonly used hydrological modelling methods for assessing the impact of forestry practices on water yield (Watson 2001). Using the paired catchment approach, hydrological time series from a "control" catchment are calibrated against pre-treatment data from a treated catchment to develop a regression relationship between the two. The resulting regression is applied to post-treatment streamflow data to produce residuals assumed to represent the treatment effect. Water balance models on the other hand calibrate pre-treatment streamflow with a simplified mathematical representation of forest hydrological processes to quantify the residuals of the post-treatment predictions as the assumed treatment effect.

Regionalising forest water use with either of these methods is problematic as paired catchment studies are dependent on "control" catchments for calibration purposes, and water balance models have governing equations with unresolved parameter uncertainty and scaling issues during the calibration procedure (Sivapalan, 2009). Both methods focus on hydrograph fitting to test the adequacy of the model, which forces an undue fixation on the idiosyncrasies of individual study catchments (Sivapalan, 2009). As a result, the predictive estimates for regional-scale applications run the risk of being less data-driven with site specific information and more influenced by the calibration of the hydrograph fitting procedure that couples control catchments with unresolved parameter uncertainties.

The present study explores a methodology with an alternative approach to modelling trends in hydrological time series. It is argued that to quantify changes in forest water use over a regeneration period of a forest, it is necessary to develop a model structure with a detailed account of hydrologically relevant vegetation dynamics

extracted from regionally available forest inventory data. Building on existing Australian forest hydrology models that only use forest age and broad forest type information to estimate an ungauged catchment's forest water use (i.e. Kuczera (1987), Watson (2001), and Brown (2006)), the present study explicitly quantifies hydrologically relevant changes in the spatiotemporal forest structure as a means to explain streamflow trends.

Kuczera (1985) developed a general climate-bushfire yield response model to implicitly suggest that changes in decadal streamflow trend during the regeneration of a forest are caused by changes in forest growth rates. Although the Kuczera curve is arguably the most regarded empirical equation in Australian forest hydrology research, no research to date has explicitly demonstrated how forest growth models may be used to identify the Kuczera curve in streamflow data. For this purpose, the proposed model structure evaluates changes in forest water use after a land-cover disturbance with a detailed account of hydrologically relevant vegetation dynamics extracted from regionally available forest inventory data.

4.2. Study site description

The study site is a part of Melbourne's water supply catchments located in the North Maroondah experimental area on the southern slopes of the Great Dividing Range, about 10 km north-east of Healesville. The study consists of six small catchments (7.4 - 33 ha) located at an elevation of approximately 600-800 m, with mean annual rainfall approximately 1700 mm. The mountainous region has a pattern of increasing rainfall and decreasing temperature with elevation. The seasonal oscillations of rainfall consist of the wettest seasons in winter and spring, whereas high evaporation is characteristic over the dry summers. The principle basement bedrocks of the region are igneous, mainly dacitic, which are medium to basic fine ground extrusive volcanics. The soils are red gradational well structured clayey soils, classified as red ferrosols krasnozems, up to 15 m deep with high permeability and water-holding capacity.

The North Maroondah area is predominantly occupied by mountain ash (*E.regnans*) forest of two age classes; old growth forest that survived 1939 bush fire and 1939

regrowth stands on sites that burnt during the fire. The understorey is mesophytic and dominated by woody species up to 15 m in height. Typical understorey species include: *Acacia dealbata, A.melanoxylon, A.obliquinerva, Bedfordia salicina, Olearia argophylla, O.lirata,* and *Pomaderris aspera* (Langford & O'Shaughnessy, 1977). The gully communities comprise of moisture depended vegetation normally confined to stream banks (within 20 to 200 m) and soakage areas feeding the stream, and include: *Atherosperma moschatum, Nothofagus cunninghamii, Blechnum procerum, B.nudum,* and *Dicksonia Antarctica* (Langford & O'Shaughnessy, 1977).

The field site consists of six experimental catchments within the North Maroondah Experimental Area located in figure 4.1. The experiments were established in 1968 to investigate the impacts of different forest densities and ages on forest water use. The forest structure of each catchment was altered by silvicultural treatments that involved: thinning of the eucalypt layer with two distinct retention rates, removal of the understorey, clear felling of 1939 re-growth patches that now consist of 37 year-old regenerating forest, and clearing of old-growth that can consist of 25 year-old forest. The variation in forest density and structural properties over the study site provide optimal conditions to investigate how forest regeneration impacts on forest water use.

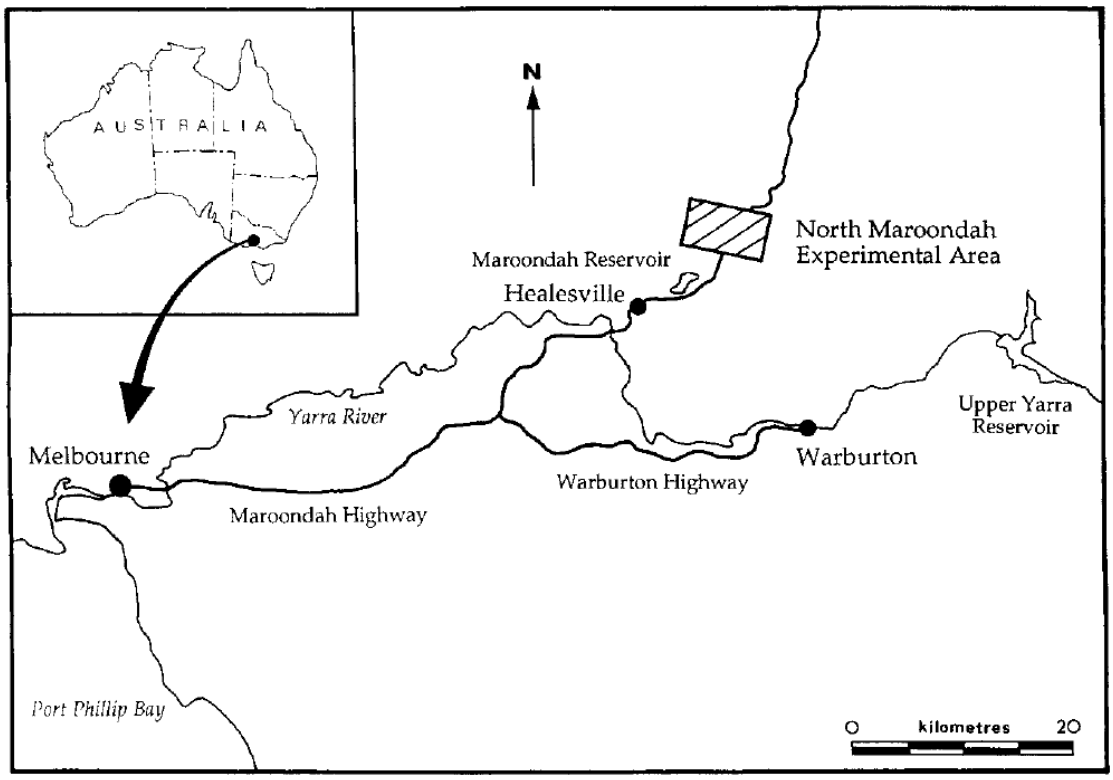

Figure 4.1: Location of the north Maroondah experimental area (from Vertessy *et al*. 1995)

4.3. Overview of model structure

Chapter two reviewed the Tasmanian and Victorian models used to manage the impacts of regenerating forests on the water resource. It was found that the models are not data-driven with site-specific information on vegetation dynamics that influence forest water use. Chapter three found there is a strong relationship between forest productivity and forest water use. As the environment within the North Maroondah Experimental Area consists of relatively uniform climatic and soil conditions, plant physiological theory in chapter three suggests all sites have the same pressures on water use efficiency. The dominant vegetation at the study site consists of *Monocalyptus* species and the forest was treated to result in different aged forests and vegetation densities. As all sites represent high quality and well stocked sites without water limitations, it is likely that water use efficiency may only be slightly variable when comparing pre- and post- canopy closure forests. For these reasons, the relationship between forest productivity and forest water use would be very similar for all catchments and provide a useful framework for developing a hydrology model.

To regionalise a hydrology model developed in gauged catchments, independent variables used to explain streamflow trends need to be available in ungauged catchments with runoff generating processes driven by the same independent variables. For this reason, the model structure uses stand basal area (*BA*) measurements and Discrete Light Detection and Ranging (LiDAR) data to formulate independent variables, as this data is typically available over vast regions needing accountability of the forested water resource.

The model structure runs on an annual time step and largely builds on the climate-bushfire yield response model produced by Kuczera (1985). The present study extends on the work undertaken by Kuczera (1985) by:

- formulating a generalised linear model (a climate filter) to represent the climatic variability in streamflow using a procedure that identifies the most effective independent variables with aggregated monthly rainfall data;
- relaxing the assumption that there is no immediate increase in streamflow after a land-cover disturbance using a linear equation; and,
- quantifying the decadal decrease in streamflow trend with a non-linear equation and then using forest growth models to explain the magnitude and duration of the reduced streamflow.

An overview of the mathematical form is presented in the following sections.

4.3.1. Climate filter

To identify decadal streamflow trends, a climate filter needs to distinguish random climatic fluctuations that lie within the natural variability range of streamflow from decadal trends as a result of vegetation disturbance and subsequent growth. Filtering out the effects of natural variation in climate on streamflow is a fundamental problem in detecting long-term trends in streamflow (Kuczera, 1985). For example, Langford (1976) used streamflow records of Melbourne's water catchments subject to the 1939 fire to perform a regression against climatic indices derived from neighbouring catchment streamflow data and rainfall records. The regression procedure involved formulating a climate filter by calibrating the pre-disturbance catchment conditions and then applying it to the post-disturbance data to quantify the residual assumed to be a result of the post-fire vegetation dynamic. For the climate filter to be effective,

the methodology required the assumption that the pre-disturbed catchment was in a state of quasi-hydrological equilibrium, hence consisted of mature or over-mature forest with negligible vegetation growth. This requirement meant that significant pre-1939 bush fire events at the O'Shannassy catchment confounded the results and hence erroneously showed there was no significant streamflow trend. The methodology was also limited in that, to reduce the uncertainty in the parameter estimates during calibration, the climate filter required the pre-disturbance runoff record to be at least 15 years long, which is rarely available, as is the case in this study.

To relax these restrictive assumptions, Kuczera (1985) developed a general climate-bushfire yield response model that simultaneously estimated the parameters for both the annual climate filter and forest water use trend response function. The climate filter used Langford's (1976) generalised linear model to define the mean residence time of seasonal rainfall from the source area to the outlet, and hence implicitly represents the rainfall-runoff transformation with the following equation:

$$Q_t = a + \sum_{i=1}^{3} b_i P_{i,t} + \varepsilon_t \qquad [4.1]$$

where Q_t is observed runoff for a May-April water year, $P_{1,t}$ is May-December rainfall for water year t, $P_{2,t}$ isDecember-April rainfall of antecedent water year $t-1$, $P_{3,t}$ is January-April rainfall for water year t, ε_t is a random error and a, b_1, b_2, b_3 are parameters to be estimated from pre-1939 data (Kuczera, 1987).

In theory, the climate filter aimed to capture the fast and slow flowing runoff processes in the transfer function. This study builds on the climate filter presented by Kuczera (1985) by not assuming that the rainfall data is aggregated in the same way as Langford (1976). Instead, a large array of independent variables derived from aggregated rainfall data are used to identify the most effective linear regression for explaining the rainfall induced streamflow variance. The overall objective is to reduce the residual standard error of the model in order to extract the streamflow trend with the greatest level of confidence.

In the proposed climate filter, the water year was not assumed to begin in May, as suggested by Langford (1976), and instead the optimal water year was identified by

evaluating each month as a potential starting month for a water year. For each water year, *T*, explanatory variables were constructed by aggregating monthly rainfall records for water year, *T*, as well as the antecedent water year, *T-1*. Rainfall records for water year *T* were aggregated to represent either two or three explanatory variables, with each explanatory variable having a minimum of two months of data. This is illustrated in figure 4.2(a) with each of the bars representing a candidate method for aggregating the monthly rainfall data. Figure 4.2(b) shows that the antecedent year was aggregated into either one or two explanatory variables where each explanatory variable had a minimum of two months, and some of the candidate methods had only a portion of the antecedent year with explanatory power. Each of the 37 possible combinations of explanatory variables developed using water year *T* were separately coupled to each of the 55 combinations of explanatory variables developed using the antecedent water year, *T-1*. In mathematical form, the proposed climate filter may be defined as:

$$Q_T = a + \sum_{i=1}^{m} B_i P_{i,T} + \sum_{j=1}^{n} Ant_j P_{j,T} + \varepsilon_T \qquad [4.2]$$

where Q_T is observed runoff in year *T*, $P_{i,T}$ is rainfall for water year *T* aggregated into *m* explanatory variables, $P_{j,T}$ is rainfall of antecedent water year *T-1* aggregated into *n* explanatory variables, ε_T is a random error and a, B_i, Ant_j, are parameters to be estimated from streamflow data.

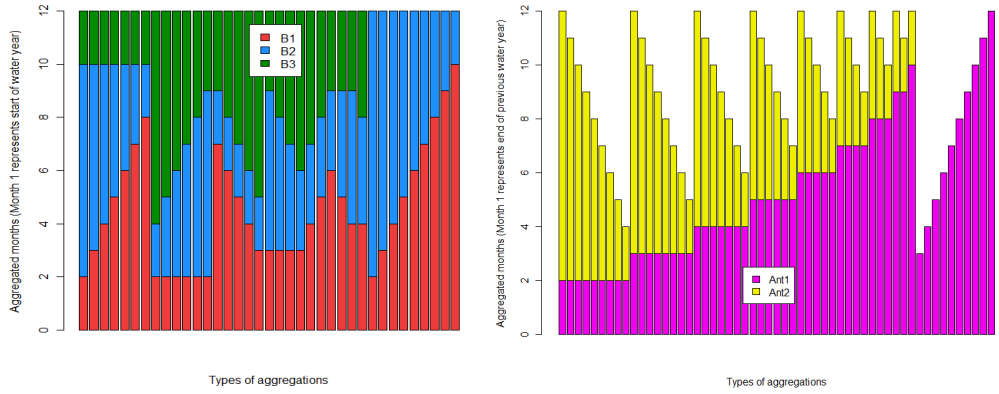

Figure 4.2: (a) Aggregation of monthly rainfall data for water year, *T*, where *B1*, *B2*, and *B3,* are explanatory variables, and month 1 and 12 respectively represent the first and last month of water year, *T*, **(b)** Aggregation of monthly rainfall data for antecedent water year, *T-1,* where *Ant1* and *Ant2* are explanatory variables, and month 1 and 12 respectively represent the last and first month of the antecedent year.

4.3.2. Post-disturbance trend

4.3.2.1. Ellipse curve to represent initial streamflow increase

There are discrepancies in the literature regarding the extent and duration of streamflow yield increase after a disturbance (Bosch & Hewlett, 1982; Kuczera, 1987), which may be attributed to differences in pre- and post-disturbance vegetation structure (Watson *et al*., 1999b). For example, Watson *et al.* (2001) found that after a disturbance of Picaninny catchment's old-growth forest, the failed regeneration in the following years resulted in a streamflow increase. In the case of Kuczera (1987), the study sites experienced disturbance to old growth forest, and successful natural regeneration resulted in no significant initial increase in post-disturbance yields. In cases where disturbance takes place in young high water using forests it is necessary to have a function representing the increase in streamflow immediately after a land-cover disturbance. For this purpose, the following ellipse equation was used:

$$\sqrt{\left|\frac{(C*p)^2 - Age^2*(C*p)^2}{(D*p)^2}\right|} \qquad [4.3]$$

where C is the magnitude of yield increase, D is the time it takes for streamflow to return to old-growth conditions, and p is the portion of catchment area disturbed. The choice of the ellipse function is somewhat arbitrary with the final justification dependent on how well the model explains the data. This is the same justification Kuczera (1987) made when selecting the gamma function, now commonly referred to as the Kuczera curve. As illustrated in the next section, the properties of the ellipse function are favourable considering regrowth increases water use incrementally after disturbance, and when streamflow reduces to old-growth levels the Kuczera curve couples well with the ellipse function. Importantly the ellipse function consists of only two parameters, both of which are physically interpretable.

4.3.2.2. Gamma curve to represent decadal streamflow trend

Following any immediate streamflow increase after a land-cover disturbance, a decreasing decadal streamflow trend needs to be represented with a response function that reflects the annual increments of BA over the duration of the

regeneration process (Kuczera, 1987). For this purpose, the present model structure adopts a gamma function, first proposed by Kuczera (1987) and defined as:

$$g(t) = L_{\max} K(Age - D)\exp[1 - K(Age - D], \qquad \text{if } Age \geq D$$

$$= \sqrt{\left| \frac{(C*p)^2 - Age^2 * (C*p)^2}{(D*p)^2} \right|}, \qquad \text{otherwise} \qquad [4.4]$$

where *g(t)* is the reduction in average annual yield (mm) at age *t* (years), following the 1939 fire, L_{max} is the maximum post-fire yield reduction (mm), *1/K* is the time (years) when the yield reduction is at a maximum and *D* is the same as [4.3].

By combining the climate filter, ellipse function and gamma function in [4.2] to [4.4], the overall model structure is used to make simultaneous parameter estimates for the climate variance and forest water use trends. The resulting multiple non-linear regression allows for a standard error of estimations to provide an expression of the uncertainty associated with the predictions. Figure 4.3 provides two hypothetical examples to illustrate the general behaviour of streamflow trends as a result of two successive disturbances. In figure 4.3(a) the two successive disturbances both take place in old-growth forest, whereas in figure 4.3(b) the second disturbance is partially in old growth forest (30%) and partially in regenerating forest (30%). The contributing streamflow losses from different parts of the catchment areas are also provided to interpret the overall catchment streamflow changes.

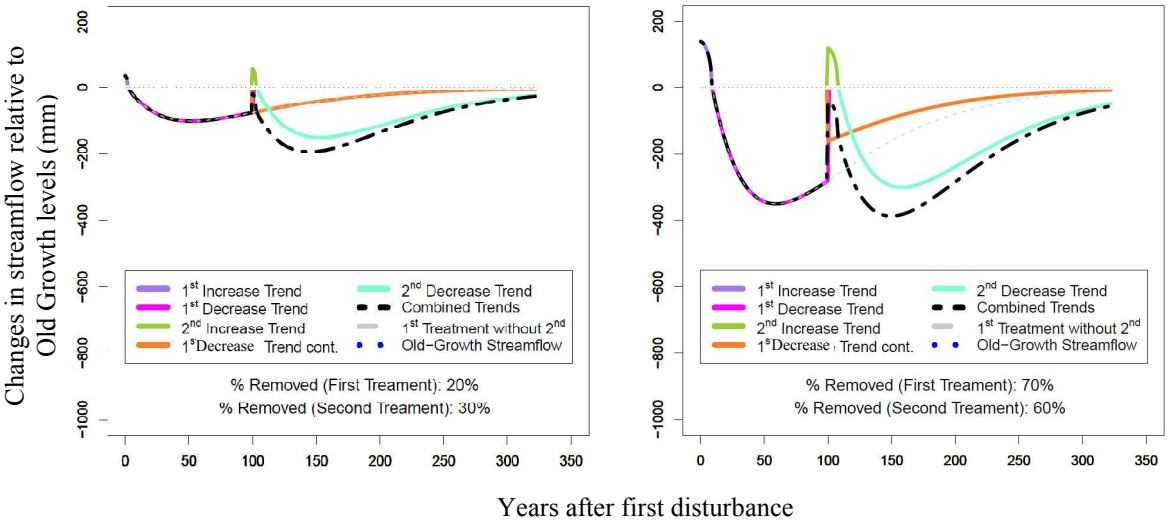

Figure 4.3: Two hypothetical examples with the first disturbance at year zero taking place when the whole catchment is old-growth. The second disturbance in (a) takes place in an old-growth part of a catchment whereas in (b) 30% of the second disturbance was in regenerating forest. The graphs provide separate measures of forest water use for different parts of the catchment, as well as an overall combined catchment streamflow trend.

4.3.3 Spatiotemporal forest growth modelling

Parameter estimates that represent the magnitude (L_{max}) and duration ($1/K$) of the streamflow trend function outlined above will be compared to parameter estimates representing changes in forest growth rates. This will involve producing lumped catchment-scale forest growth curves using permanent plot data. The procedure is developed in Chapter five and six and for the sake of continuity is summarised here:

Mixed effects models will be applied to permanent plot data to break down the growth curve's regression coefficients into a fixed component common to the population and a random component reflective of the individual plot's departure from the population. To spatially distribute the mixed effects model over the catchment, the random effects are plotted against LiDAR indices to explain the heterogeneity of forest growth over the catchment by prediction of random coefficients at unsampled locations. The spatiotemporal models of forest growth are then lumped to the catchment-scale by calculating for each growth year the average stand volume per hectare for each catchment.

LiDAR indices are produced by stratifying the multilayered eucalyptus forest with LiDAR data and characterising the structure of specific vegetation layers using a

mixture modelling procedure. The mixture modelling methodology produces canopy profile indices of understorey and overstorey vegetation with a wide range of theoretical distribution functions to summarise complex canopy attributes into a short list of parameters that are to be empirically analysed against eucalyptus stand volume and eucalyptus and non-eucalypt basal area measurements.

4.4. Description of field measurements

Table 4.1 provides a summary of the treatments applied to each of the catchments. As part of the original experiment design, permanent plots were established to measure stand basal area and heights. Table 4.1 provides information on the number of plots and measurement years made at each of the plots. The data was provided by Melbourne Water in the form of original field sheets as the data was not available electronically. Compared to typical forest inventory data used for timber accounting purposes, the dataset has measurements that are temporally more regular and spatially much denser for a given area.

Table 4.1: Summary statistics of permanent plots exposed to a range of silvicultural treatments

Catchment	Size (ha)	Treatment (year)	Plot Size (m)	Number of plots	Forest age	Number of measurements
Black Spur 1	17.66	Patch cut 40% (1972)	10X20	36	38-69	13
Black Spur 2	9.60	Thinned 40% (1972)	40X40	7	38-69	13
Black Spur 3	7.42	Thinned 60% (1972)	40X40	7	38-69	13
Ettercon 2	9.50	Understorey Removed (1972)	10X40	18	42-70	12
Ettercon 3	14.84	No Treatment	10X40	38	42-70	12
Myrtle 2	33.47	Clear fell (1984)	5X20 & 10X20	21	7-23	10

As part of this study, the permanent plots were revisited in the summer of 2008/09 for measurements of diameter at breast height over bark (*DBHOB*) of all eucalyptus trees, as well as all non-eucalyptus trees greater than 10 cm in *DBHOB*. Field measurements were taken for the original plots as well as 'extended' plots, which were increased in plot size (table 4.2) to account for changing forest conditions since the plots were established. Each plot was divided into subplots of 5 x 5 m grids in order to preserve the spatial arrangement of the trees for data analysis involving LiDAR data. Table 4.2 uses the 2008-09 field measured *DBHOB* data to provide summary statistics of the contrasting vegetation conditions for each of the catchments.

Table 4.2: Summary statistics of the extended plots located in six 1939 regenerating forest catchments exposed to a range of silvicultural treatments. Measurements made in the summer of 2009/10.

Catchment	Original Plot Size (m)	2009 Extended Plot Size (m)	Number of plots	Eucalyptus tree count per hectare			Eucalyptus basal area her hectare			Non-Eucalyptus basal area per hectare		
				Min	Mean	Max	Min	Mean	Max	Min	Mean	Max
Black Spur 1	10X20	15X20	76	0	118	266	0	36	123	0	9.1	51.4
Black Spur 2	40X40	40X40	7	75	96	131	34	48	59	1.9	4.7	10.9
Black Spur 3	40X40	40X40	7	50	76	112	36	48	63	0.7	3.1	5.6
Ettercon 2	10X40	15X40	21	0	133	217	0	43	67	0	2.9	28.1
Ettercon 3	10X40	15X40	40	17	140	317	15	51	84	1.9	7.6	18
Myrtle 2	5X20 & 10X20	15X20	21	167	458	969	16	36	63	0	4.1	14

Differential GPS measurements were collected at permanent pegs located at each plot using a dual frequency surveying grade Leica GPS1200 receiver. The DGPS accuracy was compromised by dense forest conditions and steep terrain, and for this

reason the plot locations were visually adjusted in a GIS by 0-5 m to manually correspond the pattern of tree tops in LiDAR data with field measured tree locations. Individual trees were allocated into 5 by 5 m sub-plots as shown in figure 4.4. In 2007, LiDAR data acquisition took place from a fixed wing aircraft, and table 4.3 provides the flight details and sensor configurations.

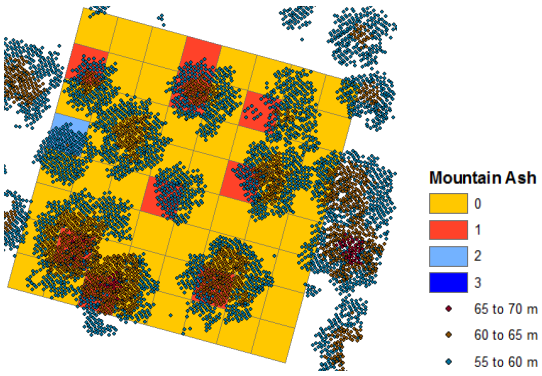

Figure 4.4: Example plot illustrating GIS procedure used to undertake manual pattern recognition between sub-plot tree locations and LiDAR hits representing tops of trees.

Table 4.3: Flight details and sensor configurations for the LiDAR data acquisition

LiDAR System Configurations	
Date of flight	August 26th 2007
Sensor Type	Optech ALTM3100
Flight Altitude (m)	800
Airspeed (km/hr)	220
Wavelength (Hz)	69
Pulse repetition rate (kHz)	100
Laser beam divergence (mrad)	0.3
Scan angle (degrees)	28
Mean footprint size (m)	0.16
Pulses per square metre	4
Maximum returned signals	4

4.5. Description of hydrological time series

The spatiotemporal forest growth models are coupled with hydrological time series to identify decadal trends in streamflow. Table 4.4 provides a summary of the stream gauged data used in this study, as well as information on the age of the forest at the time of treatment and over the duration of the stream gauging period. The Picaninny and Slip catchments were not involved in the forest growth modelling aspect of this study as the LiDAR data was not made available until a late stage of the project. For this reason, Picaninny and Slip where only used to evaluate the effectiveness of the climate filter at explaining climatic variance in streamflow, and identifying the decadal streamflow trend during regeneration.

Table 4.4: List of stream gauges used in the study and the forest age over the duration of the hydrological time series

Catchment	Stream gauge period	1939 Regeneration	Treatment year	Number of data years	Treatment forest age	Forest age at start and end of data*
Black Spur 1 (NM)	1971-1995 & 2008	Yes	1977	25	38	32-56 & 32-0-18
Black Spur 2 (NM)	1972- 1991 & 2008	Yes	1977	20	38	33-52
Black Spur 3 (NM)	1971-1995	Yes	1977	24	38	32-56
Ettercon 2 (NM)	1972- 1995 & 2008	Yes	1979	24	40	33-56
Ettercon 3 (NM)	1972- 2007	Yes	Control	35	-	33-68
Myrtle 2 (NM)	1972- 2007	No	1985	29	185	172-185 & 0-22
Myrtle 1 (NM)	1972- 2007	No	Control	35	-	Old Growth
Picaninny (CO)	1956-2008	No	1972	52	185	184-200 & 0-22
Slip (CO)	1968-2008	No	Control	38	-	Old Growth

Note: NM is North Maroondah and CO is Coranderrk

Although section 4.4 outlines that the forest inventory for the North Maroondah study sites is highly developed and adequate for forest growth modelling, it is evident that the hydrological time series has limitations as four catchments were decommissioned in the early- to mid-1990's. The study also raises the challenge of identifying trends in streamflow data under circumstances where two disturbances affect the streamflow yield instantaneously, as is the case for treated catchments regenerating after the 1939 fire. The effects of thinning, patch cuts, or the removal of understorey results in retained trees having an increase in water availability, which potentially increases water use per tree and counteracts streamflow gains due to reduced stocking densities (Jarvis, 1975). These vegetation dynamics raise challenges in identifying changes in streamflow trends due to treatment effects. Keeping these challenges in mind, the dissertation largely focuses attention on developing high resolution forest growth models for capturing spatiotemporal changes in hydrologically significant forest characteristics. Catchment level forest growth models of this kind may then provide insight into anticipated future streamflow trends given the influence of treatment effects on forest growth as well as the phase of the forest regeneration process.

To identify decadal trends in streamflow data, the climatic fluctuations in control catchments Myrtle 1 and Slip were filtered out using explanatory variables generated from rainfall data summarised in table 4.5 (a) and (b) respectively. As figure 4.5 (a) and (b) illustrate, the catchments in this study are very small relative to the very dense array of rain stations in close proximity and therefore the climate filter did not

require the rainfall data to be extrapolated over the catchments. As the overriding aim of the study was to use high resolution forest growth models to improve the way existing hydrology model represent hydrologically significant vegetation dynamics, the study resorted to using point location rain gauge data in the development of the climate filter. This involved using the methodology in section 4.3.1 to couple each of the rain gauges to respective control catchment datasets in order to formulate a set of independent variables that best explain climatic variance in an old-growth stream gauged catchments. The resulting climate model was then coupled to the ellipse and gamma function, and applied to the treated catchments to infer parameter values for the streamflow trend.

To better understand the limitations of the hydrological time series, a thorough simulation exercise was undertaken to determine how parameter inference is affected by data availability (chapter seven). To complement this analysis, the simulation also determined how substantial a post-disturbance decadal streamflow trend needs to be for the model structure to accurately identify it.

Table 4.5: List of (a) North Maroondah and (b) Coranderrk rain stations used in the study, and the elevation of each station as well as the duration and length of each dataset

(a) North Maroondah Rain Stations			
Rain Station	Elevation	Months of Data	Period
NM Rain Stn 1	892	352	1972-1998
NM Rain Stn 2	784	351	1972-1998
NM Rain Stn 3	896	155	1972 - 1984
NM Rain Stn 4	805	438	1972 - 2009
NM Rain Stn 5	765	441	1972 - 2009
NM Rain Stn 7	749	440	1972 - 2009
NM Rain Stn 8	596	155	1972 - 1984
NM Rain Stn 9	578	304	1972- 1996
NM Rain Stn 10	526	446	1972 - 2006
NM Rain Stn 11	496	151	1972 - 1984
NM Rain Stn 12	567	148	1972 - 1984
NM Rain Stn 13	597	131	1974 - 1984
NM Rain Stn 14	467	417	1974 - 2009
NM Rain Stn 15	579	278	1973 - 2009
NM Rain Stn 16	660	368	1974 – 2004
(b) Coranderrk Rain Stations			
Rain Station	Elevation	Months of Data	Period
CO Rain Stn1	212	192	1969-1984
CO Rain Stn 2	363	333	1969-2009
CO Rain Stn 3	521	192	1969-1984
CO Rain Stn 4	823	192	1969-1984
CO Rain Stn 5	611	474	1969-2009
CO Rain Stn 6	464	345	1969-1997
CO Rain Stn 7	398	192	1969-1984
CO Rain Stn 8	708	192	1969-1984
CO Rain Stn 9	443	344	1969-1997
CO Rain Stn 10	240	479	1969-2009
CO Rain Stn 11	658	474	1969-2009
CO Rain Stn 12	354	168	1971-1984
CO Rain Stn 13	410	415	1973-2009

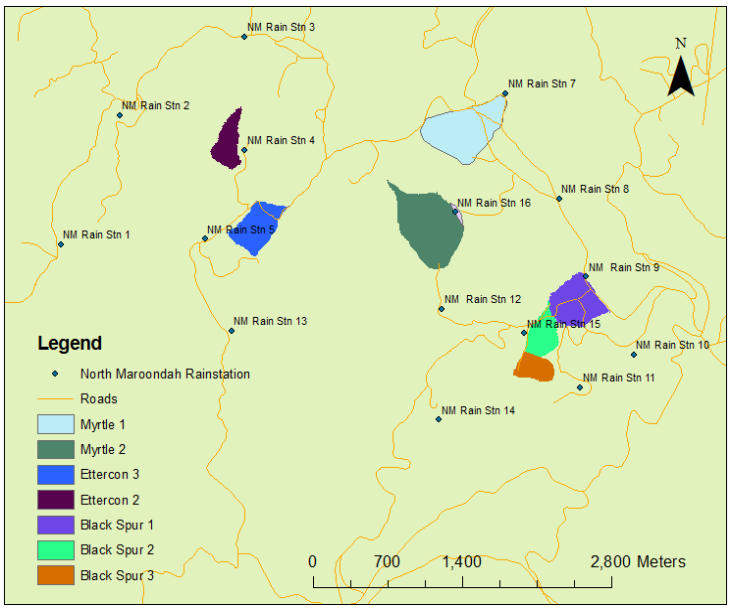

(a)

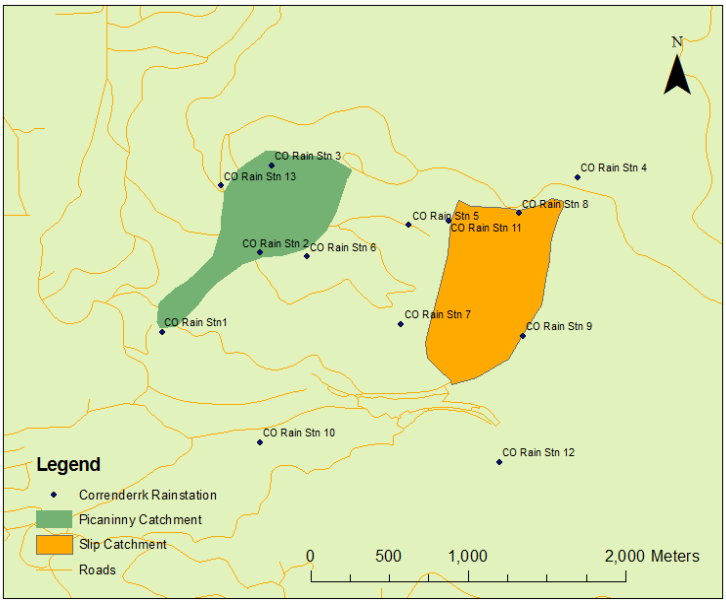

(b)

Figure 4.5: Delineated catchments and location of the rain stations used in the analysis for the (a) North Maroondah, and (b) Coranderrk catchments.

In the data analysis chapters that follow, a detailed evaluation of the spatiotemporal forest growth modelling is presented in Chapters five and six; the development of the climate filter and simulation exercise that explores limitations of the model structure are presented in Chapter seven; and the use of the forest growth models to explain the streamflow trends is presented in Chapter eight.

Chapter 5: Deriving LiDAR indices to characterise forest structure using mixture distribution functions

5.1. Introduction

5.1.1. Characterising multilayered forests with LiDAR data

Light Detection and Ranging (LiDAR) data are facilitating extraordinary advances in improving our understanding of the Earth's biomass by directly measuring the three-dimensional biophysical properties of the vegetation profile. The resulting representation of vertical structure of vegetation and topographic features over the terrain provides insight into the functional characteristics and processes of the land surface. Most LiDAR systems have a multi-echo capability and may capture between two and five returns for every laser pulse by penetrating beyond the first reflective surfaces of the canopy. The ability of discrete return sensors to capture a few echoes per pulse is particularly useful for forest industry applications, which require broad-area information on stand characteristics for timber inventory evaluation and forest growth modelling. For this particular purpose, mean tree height, basal area, and stand volume have been the most important forest mensuration parameters of interest (Naesset *et al*., 2004).

As well as characterising dominant forest stand attributes, LiDAR data may be used to categorise single-storey and multi-storey forest types, which has proven useful for mapping understorey fire behaviour (Zimble *et al*., 2003). Quantiles of height distribution in LiDAR forest data can be used to predict the vertical structure of forests (Naesset, 1997b; 1997a; Magnussen & Boudewyn, 1998; Naesset *et al*., 2004; Maltamo *et al*., 2005). Also, Canopy Height Models (CHM), such as mean canopy height, when derived from LiDAR data, are very accurate at characterising stand attributes because they are directly measured rather than indirectly calculated.

However, LiDAR indices based on discrete statistics such as percentiles and CHM may be improved further by classifying the LiDAR data into vegetation layers to determine vegetation specific statistics. In particular, in vertically heterogeneous multilayered forests it is necessary to stratify the vegetation to address the problem of

inter-stand variation in the ratio of LiDAR hits represented in the dominant canopy and the hits in the understorey.

A range of methods has been used to stratify the vegetation profile and develop layer-specific indices. Zimble *et al*. (2003) used height variance in LiDAR data to determine differences between single-storey and multi-storey forest types, but the method did not stratify each layer. Riano *et al*. (2003) on the other hand discriminated over-storey and under-storey vegetation hits using a cluster analysis technique based on a minimum Euclidean distance method. The crown base of the over-storey was then defined as the 1st percentile of the overstorey layer.

A canopy volume method using volumetric pixels (voxels) was adapted by Holmgren and Persson (2004) to separate the vegetation profile into overstorey and understorey layers. With the horizontal extent of each voxel being the sample plot size, and each voxel element being 0.5 m tall, they were able to assign a value of 0 or 1 to each element according to the relative frequency of *z* values occurring within the corresponding voxel. By assigning zero to each element that contained less than 1% of the total returns in a given voxel, the authors were able to define the base of the crown as the highest voxel element with a value of zero in a given column.

Barilotti *et al.* (2008) use polynomial regression functions applied to frequency histograms of vegetation profile data to identify base of the crown of dominant trees, by interpreting the local frequency minimum of the linear regression function as the vegetation layer threshold. Maltamo *et al*. (2005) determined the existence and number of understorey trees by examining the cumulative distributions of the canopy height density, computed as the proportion of hits above different height quantiles. The authors applied a histogram threshold method, developed by Lloyd (1982), to the cumulative distributions to cluster similar data vectors into groups as a means to define a threshold of the dominant tree layer and understorey trees. Although the procedure determined whether the height distribution of hits is multimodal, the accuracy of the results was largely dependent on the density of the dominant tree layer.

Donoghue *et al*. (2007) used near-infrared intensity of LiDAR hits to differentiate forest species common to different forest layers, as some species reflect light more intensely than others. Distinguishing vegetation layers based on intensity of hits is complicated because intensity values are dependent on variation in laser path length, orientation of the target relative to sensor, laser beam divergence, which alters the footprint size and the attenuation of the signal by the atmosphere. As a result, this approach needs calibration of the intensity values with configurations of the LiDAR system.

A promising method for separating LiDAR hits of different vegetation layers involves fitting of probability distribution models to the density profile of LiDAR data. To date, only unimodal distributions of the Weibull distribution function have been applied to derive LiDAR indices (Maltamo *et al*., 2004; Coops *et al*., 2007; Dean *et al*., 2009).

Coops *et al.* (2007) recognised that distribution functions provide a mechanism to summarise complex canopy attributes into a short list of parameters that can be empirically analysed against stand characteristics. Figure 5.1 describes the Weibull distribution function used by those authors to estimate the canopy structure of Douglas-fir forest stands. They found Weibull parameter β, which varies the spread of the distribution, was significantly correlated ($P<0.05$) to mean tree diameter at breast height (DBH), DBH, and stem density ($r^2 = 0.92$, $r^2 = 0.77$, $r^2 = 0.65$). The authors empirically identified a relationship between crown depth and Weibull parameter α, which provides for the scaling and positioning of the distribution.

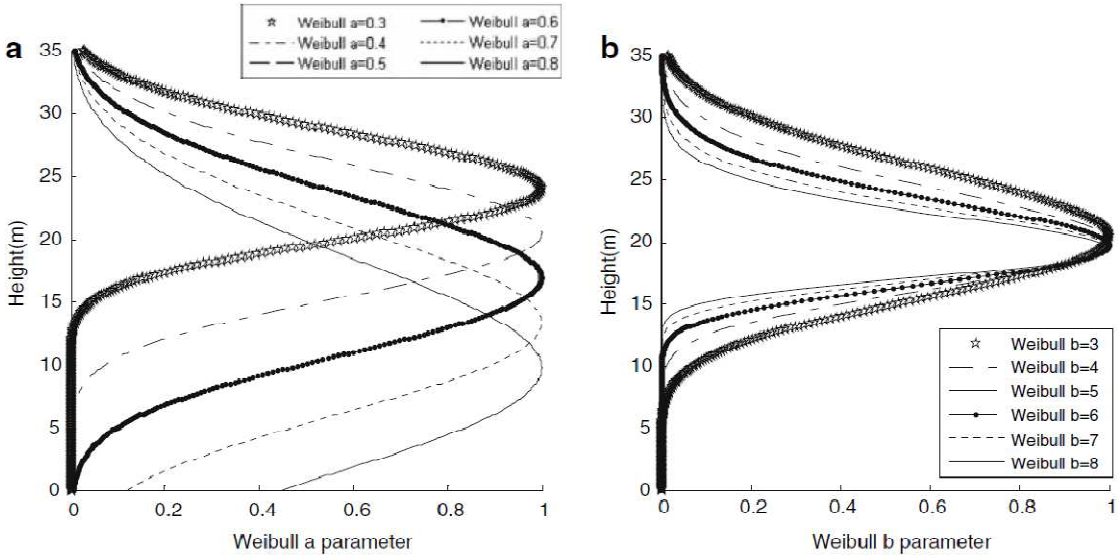

Figure 5.1 Effects of variation in the Weibull distribution parameters **(a)** α, which scales the distribution, and **(b)** β, which allows for an increase or decrease in the breadth of the distribution (from Coops *et al* 2007).

Dean *et al.* (2009) estimated height to the base of crown and the height to the median of canopy using truncated Weibull functions. The height to the canopy median was defined as height at the median of the distribution, whereas the height to the base of the live crown was defined as the height where the upper tail asymptotes to zero. Ground-based estimates and LiDAR-based indices of crown median and crown base differed by 0.3 m and 0.6 m respectively. Maltamo *et al*. (2004) found parameters from the Weibull distribution function may be used to identify suppressed trees in multi-layered spruce forests. By applying Weibull distribution functions to estimated tree height distributions obtained from LiDAR data, the authors used Weibull parameters to predict heights of small suppressed trees not identified in the point cloud data. The use of the method reduced RMSE values from 25% to 16% for stand volume estimates, and 75% to 49.2% for the number of stems.

5.1.2. LiDAR indices using mixture distribution functions

A mixture model is a probabilistic model for density estimation using a mixture distribution. Mixture models are often used in forest management to quantify merchantable timber by characterising the irregular diameter frequency distributions of mixed-species or uneven-aged forest stands (Zhang *et al*., 2001b; Liu *et al*., 2002; Zhang & Liu, 2006). The present study distinguishes itself from this typical use of mixture models in forest inventory analysis by applying mixture models to LiDAR

height distributions in order to estimate plot-level stand characteristics. This study generalises the unimodal distribution approach applied by Coops (2007), Dean (2009), and Maltamo (2004) by using mixture models with a range of theoretical distribution functions to develop LiDAR indices that are useful for a broad range of forest management purposes, including forest hydrological research. Forest structure regulates evapotranspiration rates through its influence on the wind profile, which partially determines the vapour pressure deficit at the transpiring leaf surface (Monteith, 1965). For this reason, LiDAR indices relating to crown height, density, depth, and closure of both under-storey and over-storey layers, are of interest for quantifying forest aerodynamic properties that influence evapotranspiration rates. Canopy profile attributes such as crown density, depth, and closure are also strongly related to Leaf Area Index (LAI), which is an important predictor of evapotranspiration (Vertessy *et al*., 2001). LiDAR indices that can predict forest productivity are important for forest hydrological research as forest growth rates may be used to predict forest water use (Raison *et al*., 2001).

In order to produce hydrologically related canopy profile indices, the two main objectives are:

- to develop a methodology that uses mixture models with a wide range of theoretical distribution functions as a means to provide a generalised approach for characterising the structure of specific layers of multilayered forests from LiDAR data, and
- to empirically evaluate the LiDAR derived canopy profile indices of understorey and overstorey vegetation for their capacity to predict vegetation specific plot level basal area and stand volumes in multilayered forests.

5.2. Methodology

5.2.1. Study site and field measurement description

To investigate the impacts of forest density and age on forest water use, permanent growth plots were established in a set of treated catchments in the early 1970s in Melbourne's water catchment. In the summer of 2008/09, the permanent plots were revisited for measurements of *DBHOB* of all eucalyptus trees, and non-eucalyptus trees greater than 10 cm in *DBHOB*. Refer to table 4.1 and 4.2 for a descriptive summary of the plots. In 2007, LiDAR data acquisition took place from a fixed wing

aircraft, and table 4.3 provides the flight details and sensor configurations. Section 4.4 provides a detailed description of the field work undertaken.

5.2.2. Generation of height above the ground

The height of the point cloud at an intercepted surface was measured relative to sea level, which consequently needed to be converted into a height above a ground surface to result in point clouds that represent vegetation height. The procedure involved producing an accurate digital terrain model (*DTM*) to subtract the ground elevation from the point clouds altitude. For this purpose, a DTM for each catchment was produced with a thin-plate spline interpolation using Topo to Raster, an ArcGIS interpolation tool based on ANUDEM (Hutchinson, 1989 Hutchinson, 2005).

The *DTM* interpolation procedure involved using classified ground hits separated from vegetation hits by the LiDAR contractor using Terrascan Software. The ground-classification procedure used an iterative procedure to build a triangulated model of the ground surface (Axelsson, 1999; Kraus & Pfeifer, 1999). The process involved producing grids over the study site using a grid size that was larger than any object in the study site and triangulating all points that represent the smallest height value within each grid. Using the triangulated points, an iterative process determined whether each point within its corresponding triangle may be classified as ground conditional on set of parameters that restrict the horizontal distance and vertical angle of the potentially ground-classified point from the already ground-classified points. All classified ground points were then triangulated before the process was repeated until all ground points were identified. Results were assumed to be correct and used to develop the *DTM*.

5.2.3. Preparing the LiDAR data for plot-based analysis

To use probability distributions to capture density of LiDAR points across the vertical profile, it was necessary to ensure that overlapping flight paths did not distort the density of the vegetation point cloud. The density of the vertical profile is otherwise distorted for all plots and grids partially represented by one flight path and partially by overlapping flight paths. As shown in figure 5.2, a point density map was generated to identify strips that had overlapping flight paths, which were delineated and intersected down the middle to define the boundary used to adjoin adjacent flight

paths. The GPS timestamp of the dataset was then used to group the point cloud into representative flight paths and the overlapping edges were removed.

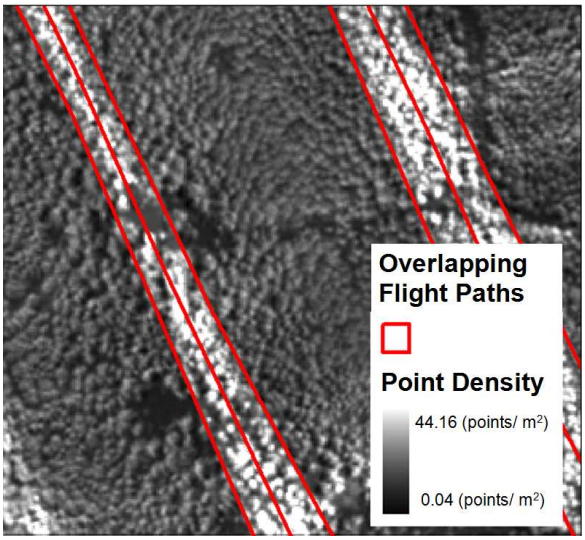

Figure 5.2: Point density layer showing the location of overlapping flight paths and the red lines delineate and intersect the overlapping areas to remove overlapping edges.

The resulting point cloud consisted of all four LiDAR returns and represented the vegetation density from the ground level up. The vegetation at the field sites predominantly consisted of a ground, understorey, and overstorey layer. As field measurements did not include the ground layer shrubs, all points with a height value less than 3 m were removed. The removal of these points was necessary as the methodology that follows only implements bimodal distributions, which do not fit the complete vegetation profile adequately. Alternatively, a multimodal mixture modelling exercise would be necessary. Such an extension is beyond the scope of this study, due to challenges addressed in the discussion.

5.2.4. Generation of mixture models to estimate vertical profile density

To process the computationally intensive technique outlined below, the University of Melbourne's servers running Red Hat Enterprise Linux 5.3 (64bit) with open source software R, version 2.8.1 was available (R Development Core Team, 2009). Four SunFire X4600M2 servers were used, each of which had 64 GB of memory and 8 CPUs x 4 cores (32 cores) with a CPU speed of 2.3GHz.

Using plot-based LiDAR data for each of the plot sizes, mixture distributions were applied to estimate the density of LiDAR points across the vertical profile of the vegetation structure as a means to develop a robust predictor of basal area and stand volume. In a complex native forest ecosystem, the form of the distribution of LiDAR points may be highly variable between forest types and age classes. To accommodate for such complexity in the density distributions, Generalized Additive Models for Location, Scale and Shape (GAMLSS) are used. GAMLSS are semi-parametric regression type models fitted with a parametric distribution assumption for the response variable, and may include non-parametric smoothing functions, hence "semi-parametric", to model the parameters of the distribution (Stasinopoulos *et al* 2008). The GAMLSS framework has been implemented using a series of packages available as part of the R software (R Development Core Team, 2009).

The GAMLSS R packages are suitable at handling complexity in the forest structure as there are 44 different continuous distribution functions available to capture the variability in the vertical profile. Table 5.1 provides a list of continuous distributions evaluated in this study using plot-based LiDAR data.

Table 5.1: Continuous distribution functions implemented using the GAMLSS package (from Stasinopoulos *et al*., 2008)

Distributions	**R Name**	**μ**	**σ**	**ν**	**τ**
Beta	BE()	logit	logit	-	-
Beta inflated (at 0)	BEOI()	logit	log	logit	-
Beta inflated (at 1)	BEZI()	logit	log	logit	-
Beta inflated (at 0 and 1)	BEINF()	logit	logit	log	log
Box-Cox Cole and Green	BCCG()	identity	log	identity	-
Box-Cox power exponential	BCPE()	identity	log	identity	log
Box-Cox-t	BCT()	identity	log	identity	log
Exponential	EXP()	log	-	-	-
Exponential Gaussian	exGAUS()	identity	log	log	-
Exponential gen. beta type 2	EGB2()	identity	identity	log	log
Gamma	GA()	log	log	-	-
Generalized beta type 1	GB1()	logit	logit	log	log
Generalized beta type 2	GB2()	log	identity	log	log
Generalized gamma	GG()	log	log	identity	-
Generalized inverse Gaussian	GIG()	log	log	identity	-
Generalize t	GT()	identity	log	log	log
Gumbel	GU()	identity	log	-	-
Inverse Gaussian	IG()	log	log	-	-
Johnson's SU (μ the mean)	JSU()	identity	log	identity	log
Johnson's original SU	JSUo()	identity	log	identity	log
Logistic	LO()	identity	log	-	-
Log normal	LOGNO()	log	log	-	-
Log normal (Box-Cox)	LNO()	log	log	fixed	-
NET	NET()	identity	log	fixed	fixed
Normal	NO()	identity	log	-	-
Normal family	NOF()	identity	log	identity	-
Power exponential	PE()	identity	log	log	-
Power exponential	PE2()	identity	log	log	-
Reverse Gumbel	RG()	identity	log	-	-
Skew exponential power type 1	SEP1()	identity	log	identity	log
Skew exponential power type 2	SEP2()	identity	log	identity	log
Skew exponential power type 3	SEP3()	identity	log	log	log
Skew exponential power type 4	SEP4()	identity	log	log	log
Sinh-arcsinh	SHASH()	identity	log	log	log
Skew t type 1	ST1()	identity	log	identity	log
Skew t type 2	ST2()	identity	log	identity	Log

Distributions	R Name	μ	σ	ν	τ
Skew t type 3	ST3()	identity	log	log	log
Skew t type 4	ST4()	identity	log	log	log
Skew t type 5	ST5()	identity	log	identity	log
T Family	TF()	identity	log	log	-
Weibull	WEI()	log	log	-	-
Weibull (PH)	WEI2()	log	log	-	-
Weibull (μ the mean)	WEI3()	log	log	-	-
Zero adjusted IG	ZAIG()	log	log	logit	-

The number of parameters used in the GAMLSS distributions varies from one to four, with almost all distributions represented by a location and scale parameter (except the exponential distribution) and some distributions represented by one or two shape parameters (υ and τ) to represent skewness and kurtosis in the response variable data. For this reason, the form of the distribution assumed for the response variable y, $f(y_i|\ \mu_i, \sigma_i, \upsilon_i, \tau_i)$, can be very general.

To create mixture models with GAMLSS distributions the package *gamlss.mx* uses the expectation minimization (EM) algorithm (Rigby & Stasinopoulos, 2008). A mixture model of GAMLSS distributions has the form

$$f_Y(y \mid \psi) = \sum_{k=1}^{K} \pi_k f_k(y \mid \theta_k) \qquad [5.1]$$

where f_Y depends on parameters $\psi = (\theta, \pi)$ where $\theta = (\theta_1, \theta_2, \ldots, \theta_K)$ and $\pi^T = (\pi_1, \pi_2, \ldots, \pi_K)$; $f_k(y|\theta_k)$ is the probability function of y for component k; and $0 \leq \pi_k \leq 1$ is the prior probability of component k, for $k = 1,2,\ldots, K$ (Rigby & Stasinopoulos, 2008). In the present study, the K value is set at two, because the vegetation's vertical profile above 3 m was predominantly well represented with a bimodal distribution function.

The Akaike Information Criterion (AIC) value was used as a goodness of fit measure to identify the most suitable distributions in the bimodal density estimates (Akaike, 1974). The AIC value offers a relative measure of the information that is lost when a distribution function is used to describe the data, and has the form $AIC = 2p - 2\ln(L)$, where p is the number of parameters and L is the maximised value of the likelihood function for the estimated model.

The GAMLSS mixture models can use any combination of distribution functions, so it was necessary to reduce the 1936 combinations of possible bimodal distributions to a manageable amount. Emphasis was placed on exhausting likely candidate distributions of the dominant vegetation layer in the second component of the mixture model to result in the evaluation of 390 bimodal distributions on each plot in the study.

The procedure began by using the normal distribution function in the first component (understorey) as it had proven reliable at converging, whilst evaluating each of the 44 available GAMLSS distributions in the second component (overstorey). The five second component (overstorey) distribution functions that proved most successful at converging with the lowest AIC value were then used to represent the first component (understorey), whilst evaluating each of the 44 available GAMLSS distributions in the second component (overstorey). Using the same performance criteria, the seven most successful second component (overstorey) distribution functions not yet assigned in the first component (understorey) were assigned as the first component (understorey) and coupled with 18 second component (overstory) distributions most successful at addressing the performance criteria.

To reduce computational time in extrapolating 390 bimodal distributions over each catchment, four catchment specific mixture models were selected with the highest convergence rate and lowest 90^{th} percentile in AIC values. The mixture model with the lowest plot-specific AIC value out of the four catchment specific mixture models was used to identify the optimal plot-specific bimodal distribution for generating LiDAR indices in the predictive models.

Allowing each plot's LiDAR data to determine the distribution function of each vegetation layer addresses the: (a) variation in each layer's canopy profile structure; (b) variation in ratio of LiDAR hits between layers; and (c) variation in the transition area between layers. The interaction of distribution functions influences how well a particular distribution function performs in conjunction with others. For example, figure 5.3 shows the Gumbel (GU) distribution in the first component of a bimodal curve behaves very differently depending on whether an inverse Gaussian (IG) or

logistic (LO) distribution is used in the second component. In this particular example, it is evident the lower tail of the logistic distribution in the over-storey is more compatible with the Gumbel distribution in the understorey and hence provides an overall better fit. In a mixture modelling procedure, the selection of each distribution as well as the interaction of the distributions will affect the final bimodal density estimate. For this reason, the resulting bimodal curves within a particular forest type can be highly variable and may need to be accommodated with a range of candidate distribution functions.

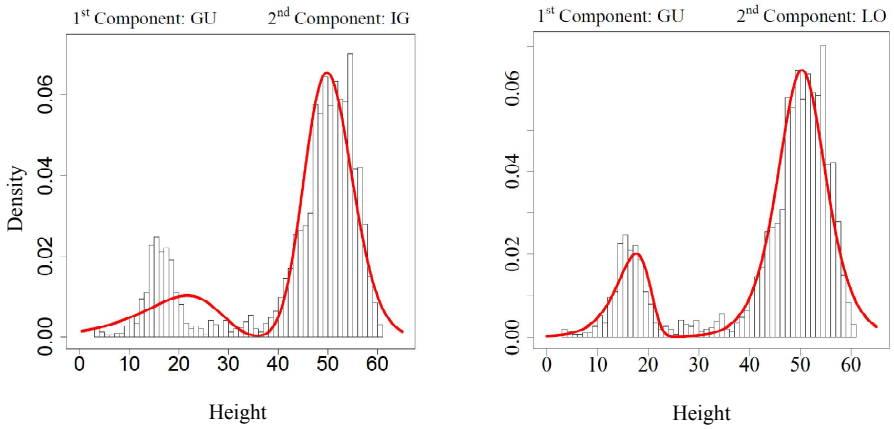

Figure 5.3: Example of how the interaction of distribution functions determines the fit of each component of a mixture model.

5.2.5. Generation of LiDAR indices

Using the GAMLSS package, the different distribution functions have corresponding parameters with identical physical interpretations as they represent the same forest structural attributes. For example, the location parameter, μ, and probability density estimate parameter, ρ, are both comparable between different bimodal distributions as they always represent the canopy mode and proportional density of a particular vegetation layer. As a result, it is not necessary to find one bimodal distribution to represent all sample plots when generating LiDAR indices for a study. On the other hand, the scaling parameter σ, and shape parameters υ and τ, have physical interpretations specific to a distribution function so may not be compared between different mixture models.

Table 5.2 lists plot-level LiDAR indices as generated with the following three methods: indices produced with no stratification of vegetation hits, indices vertically

stratified with a eucalyptus and non-eucalyptus component, and indices horizontally and vertically stratified by calculating plot level vegetation specific averages using subplot grids. All indices have been calculated using all four LiDAR returns and indices with an astricts (*) have also been calculated using only the first return LiDAR hits.

Table 5.2 List of plot level LiDAR indices generate for each plot.

Plot Level LiDAR Indices	**Symbol**
Non stratified indices	No prefix
1. Number of ground points (numeric)	*Gnd*
2. 99th, 95th, 90th, 80th...20th, 10th, 5th, 1st percentile (m)	*P99,..., P1*
3. Standard deviation of hits >3 m (m)	*SD*
Vertically stratified indices (Vegetation specific)	Prefix: *Euc_* or *Non_*
4. Canopy mode using μ parameter (m)	*Mu*
6. Probability density estimate parameter, ρ, using hits >3m (%)	*Den >3*
7.* Number of hits (numeric)	*F1_Hit* or *Hit*
8. Probability density estimate parameter, ρ, corrected with all hits (%)	*Den*
9.* Minimum heigh (m)	*F1_Min* or *Min*
10.* Maximum height (m)	*F1_Max* or *Max*
11.* Height range (m)	*F1_Rg* or *Rg*
12.* Height variance (m)	*F1_Var* or *Var*
13.* Mean height (m)	*F1_Avg* or *Avg*
14.* 99th, 95th, 90th, 80th...20th, 10th, 5th, 1st percentile (m)	*F1_P99,..., P1* or *P99,..., P1*
Vertically and horizontally stratified indices (Vegetation specific)	Prefix: *Euc_* or *Non_*
14. mean of sub-grid minimum height (m)	*Avg_Min*
15. mean of sub-grid maximum height (m)	*Avg_Max*
16. mean of sub-grid range height (m)	*Avg_Rg*
17. mean of sub-grid mean height (m)	*Avg_Avg*

Plot-level indices with no vertical stratification of vegetation layers included height percentiles, the number of ground hits, and standard deviation of hits greater than 3 m. Height percentiles provided a height value for the proportion of data below a given percentile. The 99th percentile defined a measure of the maximum height in the plot, whereas the rest of the percentiles provided an indication of the variation in density across the vegetation profile. The number of ground points was inversely related to the total vegetation density. Standard deviation of all points greater than 3 m provided an indication of the clumpiness of the canopy profile.

Parameters extracted from the bimodal distribution functions include the canopy mode of each vegetation layer, represented by the location parameter, μ. The probability density estimate parameters, ρ, represent the proportion of hits in the eucalyptus and non-eucalyptus layer relative to each other. To vertically stratify the LiDAR hits, the canopy base height of the eucalyptus layer was calculated by determining the height percentile that separates the two strata. For this purpose, the following percentile needed to be solved:

$$(1 - \rho_n) * 100 \qquad [5.2]$$

where ρ_n is the probability density estimate representing the second component of the bimodal distribution function. The number of hits intercepted by the eucalyptus layer reflects the density of the layer and was calculated by determining the total count of LiDAR values greater than the eucalyptus canopy base height. The stratified LiDAR points were used to determine a statistical summary of the minimum, maximum, range, variance, mean, and percentiles for each vegetation layer.

The adjusted probability density estimate index accounted for the number of ground points and non-ground points less than 3 m in height to determine a probability density estimate of each vegetation layer relative to the total count of LiDAR hits within a given plot. The overall proportion of LiDAR points intercepted by each vegetation layer was calculated by dividing the number of hits in the vegetation layer by the sum of ground and all non-ground hits.

Finally, for each vertically stratified vegetation layer, a set of canopy profile indices was adjusted to correct for the within-plot variation in the horizontal heterogeneity of the canopy profile. To produce vertically and horizontally stratified indices, 5 m subplot were used to spatially average for each vegetation layer the mean, minimum, maximum and range statistics over each plot.

5.2.6. Regression analysis of LiDAR indices against field measured forest characteristics

A total of 104 LiDAR indices were used as candidate predictor variables. These indices were derived from a combination of methods using summary statistics, percentile extraction methods, and mixture models. Non-eucalypt basal area, eucalyptus basal area, and eucalyptus stand volume were the response variables.

The large number of candidate predictors and the inherent collinearity between percentiles were of particular concern when developing predictive models with standard regression techniques such as least-squares and stepwise selection. With such datasets, least-squares regressions tend to produce complex over-fitted models. The poor predictive performance of such models was evident in simulation studies that show 95% confidence intervals will only include the true parameter value in roughly 50% of cases, suggesting that prediction errors of ordinary least squares estimates are erroneously small (Adams, 1990; Hurvich & Tsai, 1990; Roecker, 1991). Although stepwise selection addresses the problem of high-dimensionality in data by iteratively testing variable subsets to identify parsimonious models, it ignores the problem of collinearity in predictors. For this reason, Harrell (2000) noted that stepwise model selection yields R^2 values that are biased high and that F-test statistics used for comparing models do not have the correct distribution under the null hypothesis.

For prediction purposes, models generated by shrinkage regression techniques are more accurate than standard regression techniques (e.g. Hastie *et al*. (2001) and citations therein). Shrinkage regression techniques, such as ridge regression, are estimation methods that use penalties or constraints that shrink parameter estimates to avoid over-fitting. Ridge regression minimises the residual sums of squares and imposes a penalty on the sum of the square of the regression coefficient estimates (Hoerl & Kennard, 1970). The coefficients that estimate $\hat{\beta}_j$ are those that minimize the ride regression objective function:

$$O_{RR} = \sum_{i=1}^{n}\left(y_i - \beta_0 - \sum_{j=1}^{p} x_{ij}\beta_j \right)^2 + \lambda \sum_{j=1}^{p} \beta_j^2 \qquad [5.3]$$

where λ controls the amount of shrinkage, and is usually selected by cross-validation, y_i is the response variable, x_{ij} are the p predictor variables, and β_j are the $p+1$ unknown parameters.

Although ridge regression benefits from a lower variance of parameter estimates and increased prediction accuracy, the procedure keeps all parameters in the model, which makes it undesirable for seeking a parsimonious solution that consists only of the most dominant explanatory variables. For this reason a pre-screening step was applied that involved selecting a list of 2, 3, 4, and 5 predictor variables that had the highest absolute conditional correlation with the response variable. That is, after the first variable had been identified, the next chosen variable had maximum absolute correlation with ordinary least-squares fit of the already chosen parameters against the nominated response variable. For each candidate list of predictor variables, a family of competing models with the same number of parameters but different parameter shrinkage levels was generated. To identify the best model from each family of competing models with the same predictor variables, the Generalized Cross Validation (GCV) (Golub *et al*., 1979) procedure was applied, defined as:

$$GCV = \frac{\sum_{i=1}^{n}\left(y_i - \hat{\beta}_0 - \sum_{j=1}^{p} x_{ij}\hat{\beta}_j \right)^2}{n\left(1 - p/n\right)^2} \qquad [5.4]$$

where p is the number of parameters in the model, N is the number of observations, $\hat{\beta}_j$ is the estimate of the j^{th} parameter and the other symbols are as above.

From each family of models with a predetermined number of predictor variables, the models with the most optimal level of shrinkage, based on the GCV values, were compared to find the overall model that offers the best predictive accuracy. For this purpose the Prediction Squared Error (PSE) is a metric of prediction accuracy used to identify the smallest difference between the observed values and those predicted by the model, defined as:

$$PSE = \sum_{i=1}^{n}\left(y_i - \hat{\beta}_0 - \sum_{j=1}^{p} x_{ij}\hat{\beta}_j \right)^2 \qquad [5.5]$$

The quality of any regression model's coefficient estimates are over-optimistic in a procedure that determines the quality of the model's estimate using the same data to fit and then assess the model. To address this concern, the "0.632+" bootstrap method (Efron & Tibshirani, 1997) was adopted to correct for misleading estimates of future observation variances. The 0.632+ bootstrap is comparable to cross-validation but is more efficient, making it desirable when observations are few. The procedure involved randomly selecting 1000 subsets from the original dataset with replacement, with each sample having the same number of observations as the original dataset. The 0.632+ bootstrap mimics cross validation, as for each observation *i*, all bootstrap samples that do not contain observation *i* are used to predict the value of observation *i* and measure the error. Our bootstrap operation included the initial screening of the variables, so any uncertainty created in the model step by that screening was included in the bootstrap estimates of PSE.

5.3. Results

5.3.1. Identifying best fitting mixture models

The first step in identifying the most suitable bimodal distribution function for each plot required an iterative procedure to reduce the dimension of comparisons. The iterations proceeded as follows. The normal distribution function was used in the first component (understorey) of the mixture model whilst testing all available distribution functions in the second component (overstorey). The five best performing second component distribution functions are listed in the first column of table 5.3. In the second step, these five distributions where used in the first component and coupled to each of the available distribution functions assigned to the second component. The second column of table 5.3 provides the seven best performing second component distributions in the second step, based on the criteria outlined in the methodology. In the third step, these seven distributions were represented in the first component and coupled to eighteen best performing second component distribution functions identified in the second step. The eighteen best performing distribution functions were the normal distribution and all the distribution functions listed in table 5.3.

Table 5.3: Best performing distribution functions for plot-based LiDAR evaluated in this study

Best performing distribution functions		
First component in second step	First component in third step	Second component in third step *
Weibull (WEI)	Zero adjusted inverse Gaussian (ZAIG)	Log normal (LogNo)
Gamble (GU)	Weibull (WEI3)	Generalised *t* (GT)
Gamma (GA)	Generalised Gamma (GG)	Generalised Inverse Gaussian (GIG)
Inverse Gaussian (IG)	T Family (TF)	Generalised Beta type 1 (GB1)
Skew T type 4 (ST4)	Logistic (LO)	Box- Cox *t* (BCT)
	Reverse Gumbel (RG)	
	Normal Family (NOF)	

* Distribution functions listed in first and second rows are also evaluated as second component distribution functions in the third step

To identify the best catchment-specific bimodal distributions, all candidate mixture models were evaluated and only those mixture models that converged for all plots in the given catchment were considered. For these mixture models, the 90th percentile of the catchment's plot AIC values was used as a performance criterion to determine the four best performing mixture models. Table 5.4 lists the four most successful mixture models for each plot extent in each catchment to show that bimodal distribution functions vary with both forest age and the sample plot size. A count of the number of plots that performed the best for each of the four most successful mixture models is also provided for both the original plot size and the extended plot size.

Table 5.4: The four best performing distribution functions for each plot extent in each catchment and the number of plots that performed the best for a given mixture model in a given catchment. Empty records imply that the plot size is the same as the original plot size for the given catchment.

Catchment	Original plot size		Extended plot size		15X20 plot size
	Mixture Model	Number of Plots	Mixture Model	Number of Plots	
Black Spur 1	f(GA, GU)	53	f(RG, GU)	60	-
	f(GA, WEI)	16	f(GU, GA)	2	-
	f(GA, IG)	7	f(WEI, IG)	11	-
	f(GA, WEI3)	0	f(WEI, RG)	3	-
Black Spur 2	f(IG, WEI)	7	-	-	f(IG, GU)
	f(GA, TF)	0	-	-	f(ST4, GA)
	f(ST4, IG)	0	-	-	f(RG, ST4)
	f(TF, ST4)	0	-	-	f(WEI, IG)
Black Spur 3	f(LO, ST4)	5	-	-	f(GU, RG)
	f(ST4, IG)	2	-	-	f(IG, GU)
	f(ST4, ZAIG)	0	-	-	f(GU, IG)
	f(ZAIG, WEI)	0	-	-	f(GU, NO)
Ettercon 2	f(ZAIG, ST4)	11	f(GA, GU)	18	f(NO, ST4)
	f(ST4, GU)	9	f(GU, WEI3)	1	f(GA, GU)
	f(ST4, LO)	1	f(TF, IG)	1	f(WEI, IG)
	f(RG, GU)	0	f(IG, NO)	1	f(WEI, WEI)
Ettercon 3	f(WEI, ST4)	20	f(RG, GU)	32	f(ST4, GU)
	f(NO, GU)	17	f(GU, LO)	4	f(WEI, WEI)
	f(GU, NO)	3	f(GU, NO)	2	f(WEI, LO)
	f(ST4, LO)	0	f(WEI, RG)	2	f(GU, GU)
Myrtle 2	f(ZAIG, TF)	13	f(RG, GU)	7	-
	f(WEI, NO)	6	f(IG, WEI)	9	-
	f(WEI, RG)	2	f(WEI, RG)	3	-
	f(NO, NOF)	1	f(GU, GA)	2	-

Table 5.4 shows that none of the distribution functions listed in the third column of table 5.3 are represented in any of the final four mixture models. In Mountain Ash forests, the elimination procedure identified eleven likely candidate distributions for representing the eucalyptus component of the mixture model. The eleven distribution functions included all distributions in first two columns of table 5.3 excluding the Zero adjusted inverse Gaussian (ZAIG) and Generalised Gamma (GG) function. It is worth noting that eight of the eleven distribution functions represent two parameter models, which are a great deal more computationally efficient at converging than the computer intensive distribution functions with three or four parameters.

For each of the plots, mixture model curves were superimposed over frequency histograms of LiDAR hits along the vertical vegetation profile in order to visually

evaluate the effectiveness of the mixture model at representing the distribution of LiDAR hits. Figure 5.4 provides one randomly selected plot for each of the eleven most effective second component distribution functions.

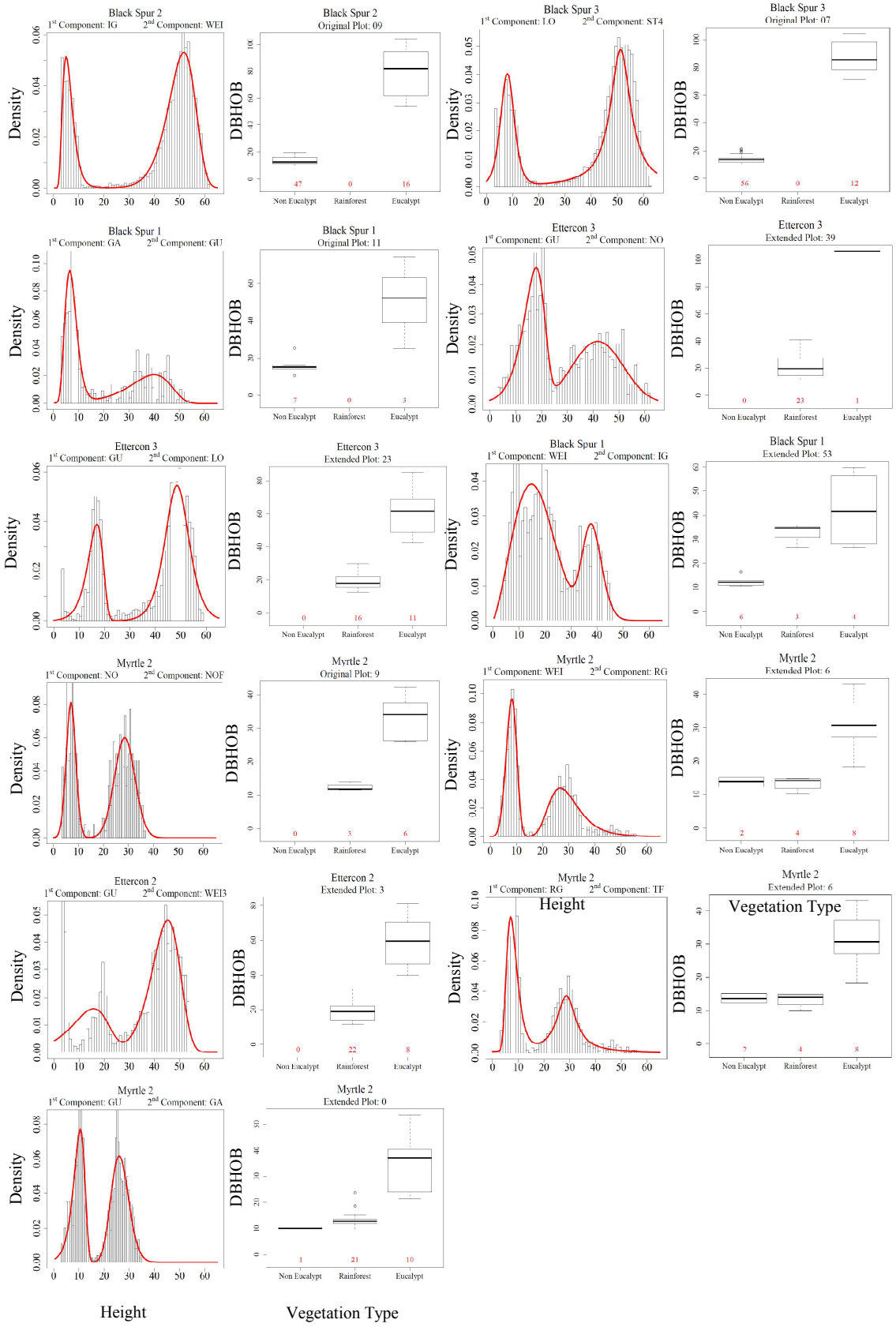

Figure 5.4: Bimodal curves represented with eleven different second component distribution functions fitted to the plot-based LiDAR data. Box plots provide a summary of each plot's forest inventory.

5.3.3. Ridge regression predictions

5.3.3.1. Eucalyptus vegetation layer

Using ridge regression analysis for each of the catchments, figure 5.5 provides scatter plots of predicted versus observed values for eucalyptus; (a) basal area and (b) stand volume. The small number of observations at Black Spur 2 and 3 meant the model was limited to only two parameters to avoid over-fitting noise and erroneous associations between the predictor and response variables. The results for the patch cut treatment catchment, Black Spur 1, show overestimations of predicted basal area in plots with no eucalyptus trees. These plots are mainly located on the edge of cleared patches where eucalyptus regeneration is suppressed due to shading from retained trees. These plots have no eucalyptus trees but have overhanging trees external to the plot, which misrepresent the presence of eucalypts.

In Black Spur 1 there is also a tendency to underestimate basal area in plots with observed basal area greater than 80 m^2/ha. In dense Mountain Ash forest stands the intense competition results in suppressed trees having highly irregular canopy structure. The suppressed trees can contribute a substantial amount of basal area to the plot measurements with a disproportionately reduced crown structure. Such circumstances inevitably result in underestimated basal area predictions using LiDAR data.

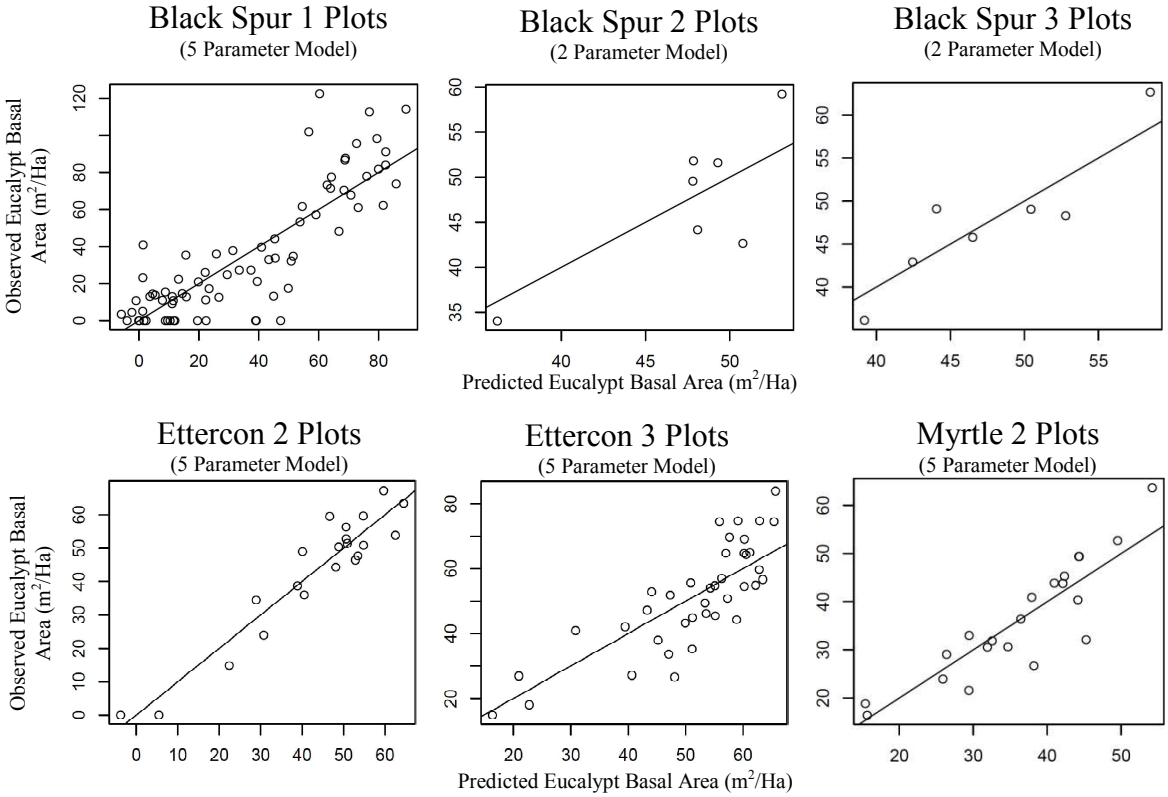

Figure 5.5a: Scatter plots of predicted versus observed eucalyptus basal area values using ridge regression modelling.

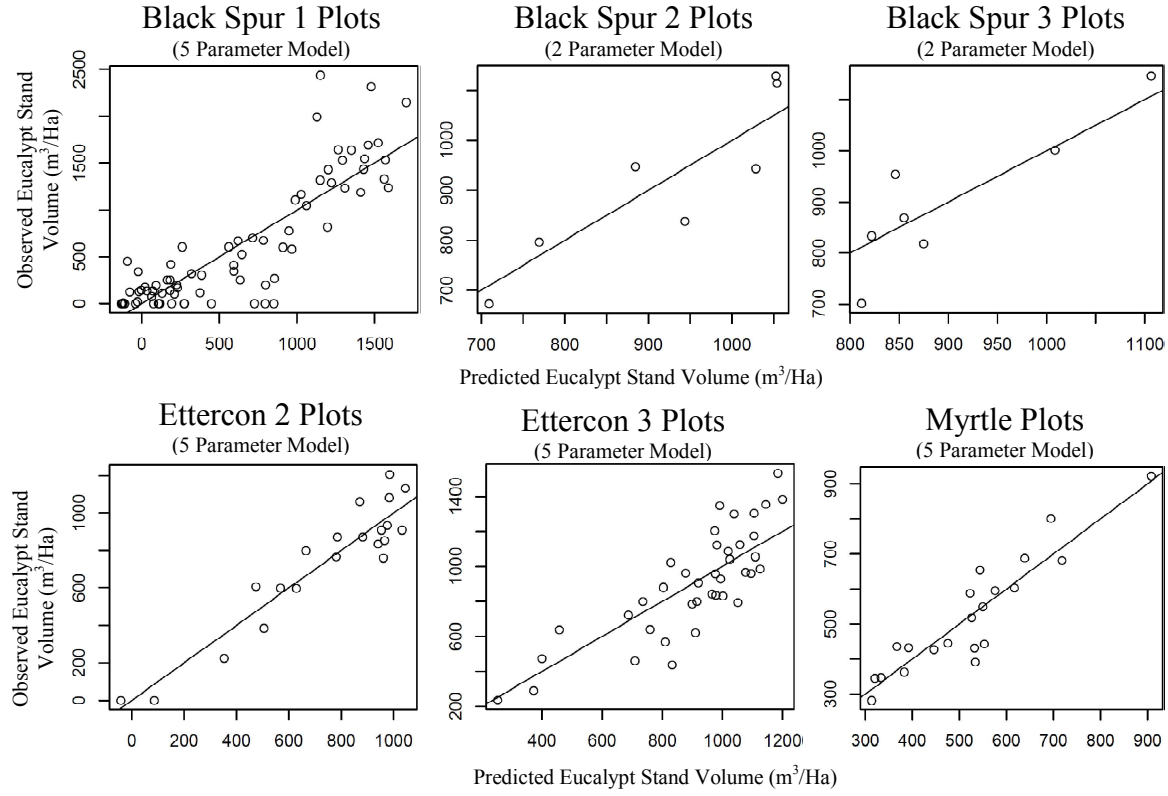

Figure 5.5b: Scatter plots of predicted versus observed eucalyptus stand volume values using ridge regression modelling.

Table 5.5 provides the RMSE and R^2 results of the ridge regression, as well as lists the LiDAR indices used to make predictions of: (a) eucalyptus basal area and (b) stand volume. A significant portion of the predictor variables used in the final models include vegetation specific indices generated with the mixture modelling methodology. The mixture model index, *Euc_Hits*, which represents the total hits intercepted by the eucalyptus layer, and the percentile extraction method index, *P50*, which represents the 50th percentile of all hits, are notably the most consistent predictive LiDAR indices. For comparison with models that use traditional predictor variables, table 5.6 provides the results of predictive models generated using predictor variables that do not require mixture modelling. It is evident that by using mixture model LiDAR indices, basal area and stand volume predictions were respectively improved by 4-20% and 4-16%.

Table 5.5: RMSE and R^2 of the ridge regression model, as well as the list of predictor variables used in the final model to predict eucalyptus: (a) basal area, and (b) stand volume, for each catchment and all catchments lumped together. Predictor variables with an astricts symbol (*) were developed by stratifying the vegetation layers using mixture models.

Catchment	R^2	RMSE (m^2/ha)	Predictor variables used in final Model				
Black Spur 1	0.72	18	P50	F1_Euc_Hits*	SD	F1_Euc_P30*	Non_Euc_P70*
Black Spur 2	0.61	5.1	Den >3*	P50			
Black Spur 3	0.81	3.5	F1_Euc_Hits*	Euc_Max*			
Ettercon 2	0.89	6.2	Euc_Hits*	F1_Euc_P10*	Gnd	SD	Euc_Avg_Avg*
Ettercon 3	0.66	9.6	P50	F1_Euc_Rg*	Euc_Hits*	F1_Euc_Hits*	F1_Euc_P50*
Myrtle 2	0.84	4.7	F1_Euc_P10*	Den >3*	Euc_P99*	SD	F1_Euc_Hits*

(a)

Catchment	R^2	RMSE (m^3/ha)	Predictor variables used in Model				
Black Spur 1	0.76	324.5	P50	Non_Euc_P70*	Euc_Avg_Avg*	SD	Gnd
Black Spur 2	0.81	72.9	P50	Euc_Avg_Rg*			
Black Spur 3	0.78	67.3	F1_Euc_Hits*	Den*			
Ettercon 2	0.88	117.0	F1_Euc_P60*	Euc_Hits*	Gnd	Den >3*	Euc_Avg_Avg*
Ettercon 3	0.67	176.0	P50	F1_Euc_Hits*	Euc_Hits*	F1_Euc_Min*	F1_Euc_P50*
Myrtle 2	0.85	63.7	Euc_Avg_Avg*	F1_Euc_Var*	SD	Non_mu*	Gnd

(b)

Table 5.6: RMSE and R^2 of ridge regression models using only predictor variables that do not require mixture modelling (i.e. rows 1, 2, 3, 10, and 15 in table 5.2)

	Basal Area (m^2/ha)			Stand Volume (m^3/ha)		
Catchment	R^2	RMSE	Number predictor variables	R^2	RMSE	Number predictor variables
Black Spur 1	0.68	19.2	4	0.7	365	4
Black Spur 2	0.53	6.4	2	0.75	91	2
Black Spur 3	0.77	4.2	2	0.74	73.8	2
Ettercon 2	0.69	10.4	4	0.72	179	4
Ettercon 3	0.57	10.7	5	0.59	194	5
Myrtle 2	0.74	6.1	4	0.8	72.3	4

5.3.3.2. Non-eucalyptus vegetation layer

Figure 5.6 provides scatter plots of non-eucalyptus stand basal area predictions for each catchment and table 5.7 provides the RMSE and R^2 results of the ridge regressions, as well as the list of LiDAR indices used to make predictions of non-eucalyptus basal area. Using LiDAR data to model basal area of understorey vegetation is more challenging than modelling overstorey vegetation as the number of hits intercepted by the understorey is a function of the overstorey density. Furthermore, modelling basal area of understorey vegetation is confounded by measured trees leaning out of the plot and unmeasured trees leaning in, as well as unmeasured ferns and non-eucalyptus trees with *DBHOB* less than 10 cm rightfully in the plot and contributing substantially to the understorey profile.

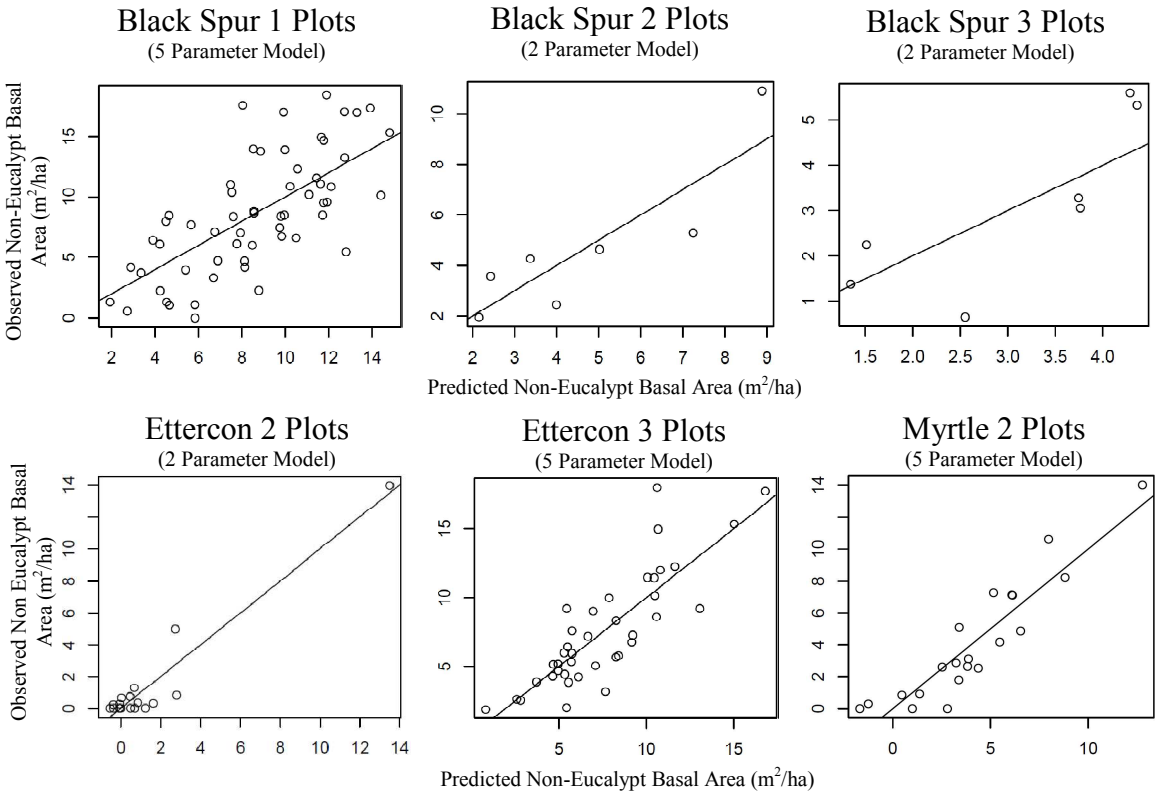

Figure 5.6 Scatter plots of predicted versus observed values of non-eucalyptus basal area using ridge regression modelling.

Table 5.7: RMSE and R^2 of ridge regression used to predict non eucalyptus basal area and the list of predictor variables in the final model.

Catchment	R^2	RMSE (m^2/ha)	Predictor variables used in Model				
Black Spur 1	0.5	3.5	F1_Euc_P1*	SD	F1_Euc_Hits *	Non_Avg*	Euc_Hits *
Black Spur 2	0.9	1.0	Den >3*	F1_Euc_Var*			
Black Spur 3	0.69	1.0	Non_Mu*	Den *			
Ettercon 2	0.91	2.1	P70	Gnd			
Ettercon 3	0.71	2.2	Den >3*	F1_Euc_Var	Gnd	F1_Euc_Hit*	P60
Myrtle 2	0.84	1.5	Den >3*	F1_Euc_Rg*	Non_Mu *	Gnd	Non_P99

5.4. Discussion

A generalised methodology has been presented for representing the vertical forest structure of a broad range of forest types. It was demonstrated that canopy attributes captured by LiDAR data may be summarise into a short list of parameters for empirical analyses against field measured stand characteristics using mixture modelling methods. To evaluate the robustness of the methodology, mixture models of each sample plot were visually assessed to determine how well each component represented the correct vegetation layer. Figure 5.7 illustrates the following four types of erroneous fits identified in the mixture modelling procedure:

(a) Distorted distribution functions in the young regrowth forest of the Myrtle 2 catchment when the plot contained old growth stags unmeasured in the field. It was possible to correct these plots by identifying and removing LiDAR data above an expected maximum young regrowth height across the whole catchment.

(b) Bimodal distribution functions that did not effectively identify the appropriate vegetation layer. This predominantly occurred for plots along streams where overstorey vegetation consisted of rainforest vegetation in the absence of eucalyptus trees. The second component of the mixture model was assigned to represent the eucalyptus layer under such circumstances as no conditions or constraints were applied in the modelling exercise to correct such anomalies. Plots that were within a 20 m buffer of a stream were removed from the regression analysis as it may be assumed that eucalyptus trees are not present along the riparian strip when extrapolating the regression over the catchment. Hill slope plots with no eucalyptus trees were used in the regression and weakened the final results, which was most evident in the patch cut silvicultural treatment catchment Black Spur 1.

(c) Bimodal distribution functions that attempted to represent vegetation profile containing more than two vegetation layers. This error was not corrected and resulted in an underestimate or overestimate of the eucalyptus canopy density depending on how the bimodal distribution captured the three or more vegetation layers.

(d) Distribution functions that integrate vertically overlapping rainforest and eucalyptus trees into the second component. This error was not corrected and resulted in an over-estimated density of the eucalyptus canopy.

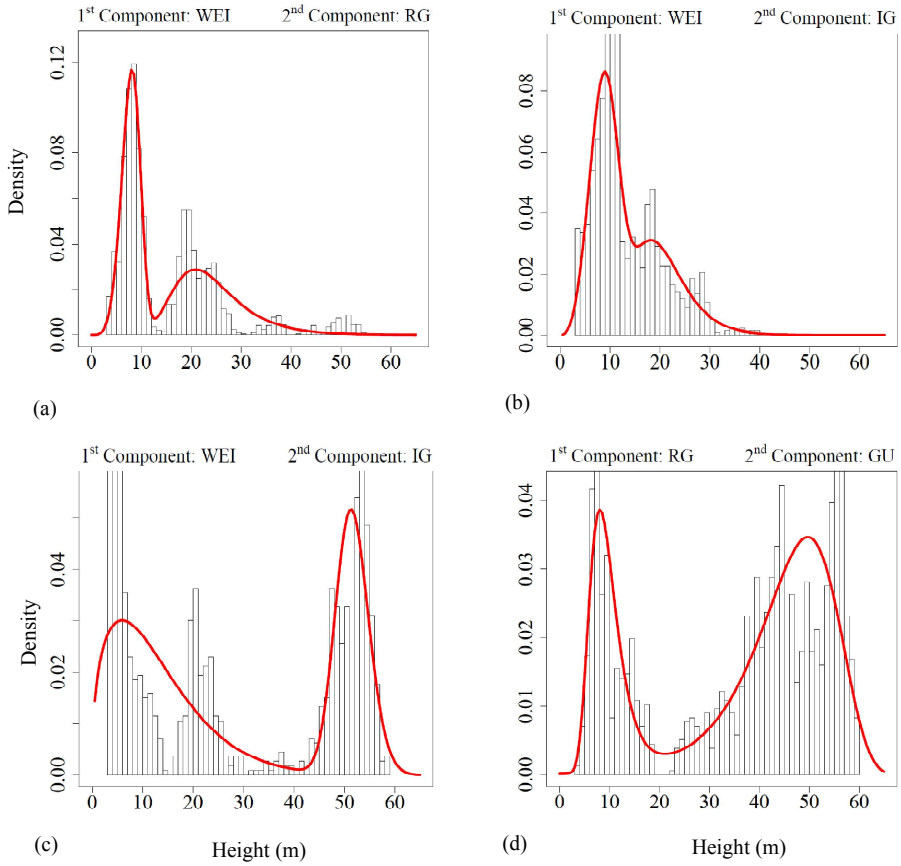

Figure 5.7: Types of erroneous fits identified in the mixture models of the vegetation profile, where: (a) has old growth stags distorting the eucalyptus regrowth distribution, (b) has no eucalyptus trees but the mixture models assumes rainforest layer is eucalyptus layer, (c) has three vegetation layers that are poorly fitted with a bimodal distribution, and (d) has a rainforest layer that has been integrated into the overstorey density estimate.

The complexity in vertical heterogeneity of multilayered forests may be addressed by generalising the mixture modelling procedure with multimodal distributions. Developing distribution curves with variable modes based on the site specific vegetation profile requires a procedure that can determine how many modes best represent the vertical profile, and identify which particular vegetation layer each component of the mixture model represents. To determine how many modes best represent the vegetation profile it may be possible to fit nonparametric kernel smoothing methods through frequency histograms to count the local frequency maxima and use this value to represent the number of components in the mixture model. Identifying which particular vegetation layer each component of the mixture model represents is necessary to successfully identify circumstances where two distributions are more appropriate for representing one vegetation layer in order to

combine them and improve the density estimates. For this purpose, a modelling procedure that uses conditions and constraints for each component of the distribution curve may be used to identify particular vegetation layers in the multimodal mixture model. An understanding of the general forest structure of a particular forest type may allow for mode values and vertical distances between the modes to be used in condition statements to interpret whether two components of a distribution curve represent one or two vegetation layers.

For example, figure 5.8 shows how a Black Spur plot may be more accurately represented with a four modal curve to separate the rainforest middle storey from the eucalyptus layer, which is more effectively represented by the third and fourth component of the mixture model. By establishing conditions based on the mode values or vertical distances that separate them, the density estimates of distributions represented by particular modes may be combined to represent a particular vegetation layer. Such an approach would also recognise when a vegetation layer is missing from the vegetation profile. For example, if it is expected for a eucalyptus layer of a given age to have a canopy mode no smaller than a particular height value and when there are no distributions of this characteristic, then the overstorey layer may be redefined as a rainforest layer. Using such techniques, the predictability of the regression models generated in this study may be improved as erroneous interpretations of mixture models such as those illustrated in figure 5.8 would be corrected. Further research is necessary to determine whether such techniques may identify suppressed trees or overlapping vegetation layers to further improve the predictability of basal area in targeted vegetation layers.

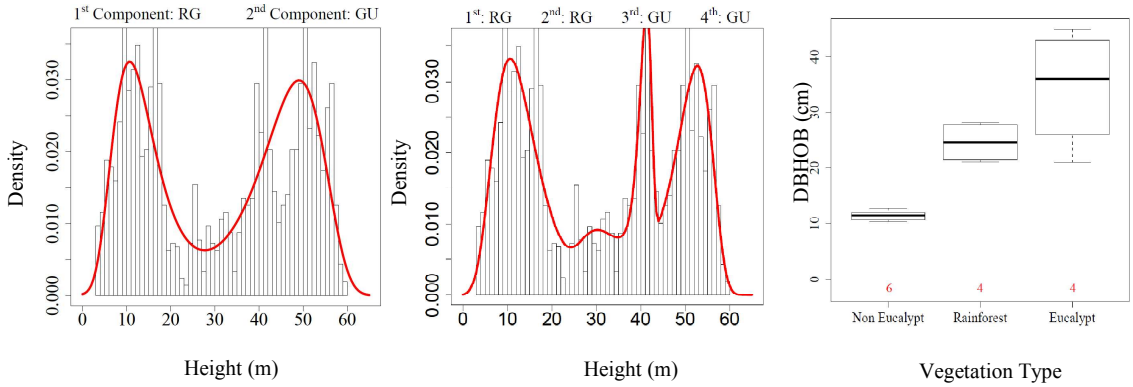

Figure 5.8: An example plot that may be more accurately represented with a four modal curve to capture the density estimate of the eucalyptus vegetation profile.

Fitting mixture models to diameter distribution data has been well developed (Zhang *et al*., 2001b; Liu *et al*., 2002; Zhang & Liu, 2006), and multimodal mixture modelling of LiDAR data may also prove useful in forestry applications that require estimates of diameter frequency distributions. Mixture model parameters characterising the irregular diameter distributions of mixed-species or uneven-aged forest stands may be regressed against multimodal mixture models of LiDAR vegetation height distributions to identify suppressed trees, and different aged cohorts. Further research needs to be undertaken to determine how well such methods may improve timber inventory modelling.

It is speculated that the results in the present study may be further improved by improving the optimisation of the mixture model selection procedure. To reduce computational time during the extrapolation procedure, the present methodology was designed to evaluate only four of the most successful mixture models at each location of a catchment. At the expense of increased computational time, an alternative approach may involve identifying the most successful mixture model for each plot out of all converged mixture models for the given plot. To extrapolate such results all successful plot specific distributions would then need to be tested as candidates and evaluated at each grid over the catchment area. If the sample plots are highly variable with a large range of optimal multimodal distributions then the extrapolation procedure over a large area may prove computationally intensive. The results on the other hand would be more accurate and furthermore, the spatial distribution of the large variety of mixture models may themselves provide useful insight for predicting forest characteristics.

An important advantage in identifying many candidate distributions (eleven in this case) for fitting a range of vegetation profiles is that particular distributions or mixture models may represent specific ecosystems or tree species. For example, overlapping vegetation layers due to a particular species in the middle storey may be recognised with a particular skewed distribution function in a particular component of the mixture model. An empirical analysis relating ecosystem types to particular mixture models was beyond the scope of this study but may prove useful for a very broad range of forest management applications.

The present study has developed LiDAR indices that are highly applicable to forest hydrological studies as these indices directly relate to the vegetation characteristics that influence forest water use. For example, generating mixture model statistics over sub-plots to produce horizontally and vertically stratified vegetation structural attributes provide a measure of the canopies aerodynamic properties. The preserved canopy profile characteristics captured in the mixture models such as canopy density, depth, and closure are strongly related to the transpiring leaf area. Research needs to be undertaken to determine whether spatially represented LiDAR indices relating to forest hydrological systems may be used to explain catchment variations in stream flow.

5.5. Conclusion

Mixture models provide an elegant and robust method for stratifying the vegetation profile into distinct vegetation layers whilst preserving vegetation specific characteristics of the canopy profile. Unlike most previously proposed LiDAR indices in literature that categorise the vertical profile of forest structure into a finite assemblage of statistics (Lefsky *et al*., 1999; Zimble *et al*., 2003; Hall *et al*., 2005; Lefsky *et al*., 2005), mixture models can capture a more complete representation of the continuous point density estimate. Very few studies have explored theoretical distribution functions to represent the vertical profile of vegetation structure in LiDAR data. The most notable examples by Coops *et al.* (2007), Dean *et al.* (2009), and Maltamo *et al*. (2004) all used unimodal Weibull distributions, which are restricted in their application as the vertical and horizontal forest structure around the world is so variable.

The methodology presented in this paper is working towards a generalised approach in representing the vertical forest structure with theoretical distribution functions for a very broad range of forest types. Using the GAMLSS package available with the open source software R (R Development Core Team, 2009), the form of the distributions available is very general and there are no restrictions on the number of modes available in the mixture models. The present study systematically evaluated 44 distribution functions to produce bimodal curves that estimate canopy density of Mountain Ash forests with a range of age and density classes. The results identified eleven likely candidate distributions that were successful at representing the overstorey of Mountain Ash forests and may prove useful for other forest types.

Mixture modelling is a promising method that may summarise complex canopy attributes captured by LiDAR data into a short list of parameters for empirical analyses against field measured stand characteristics. The present study has demonstrated that parameters extracted from bimodal curves are successful at predicting eucalyptus basal area and stand volume as well as basal area of non-eucalypt understorey. Using a ridge regression procedure that accounts for sources of uncertainty ignored in standard regression techniques, the study found that observed versus predicted values of eucalyptus basal area and stand volume was highly correlated with r^2 ranging from 0.61 to 0.89 and 0.67 to 0.88 respectively. Non-eucalyptus basal area r^2 ranged from 0.5 to 0.91. A critical evaluation of the mixture model density estimates for all the study plots identified circumstances under which a more complex multimodal distribution curves may be used to improve the predictive capacity of the mixture modelling methodology.

In chapter six, permanent plot data will be used to develop a temporal model of the regenerating forests, and the LiDAR indices generated in this chapter will be integrated into the model to spatially distribute the forest growth models over the catchments.

Chapter 6: Spatiotemporal modelling of forest growth for forest hydrological studies

6.1. Introduction

Forest growth and stand volume models are generally used to predict temporal changes in the timber inventory for landscape level forest management planning (Hamilton *et al*., 1999). The present study quantifies spatiotemporal forest growth increments over a forested catchment in order to explain a catchment's streamflow response with changes in forest productivity. Using forest growth models to detect trends in streamflow data is complicated by confounding effects of climatic variability, as well as the influence of surface and subsurface flows, and catchment storage on streamflow. For this reason, the present study requires a highly detailed model that captures a small catchment's spatial heterogeneity in a forest's regeneration success, as well as the temporally polymorphic nature in forest growth over a stream gauge's monitoring period.

Traditionally, foresters have used the site index approach to select an appropriate growth curve at a site by fitting a curve through a mean growth response at one point in time. This approach assumes that the variation of growth may be explained by a one-parameter family of curves (Garcia, 1983). The "site-index approach is quite old" (Hall & Bailey, 2001), and fails to differentiate the polymorphic shapes and forms in forest growth curves found in heterogeneous native forest environments. To quantify the polymorphic nature of forest growth, a non-linear mixed effects modelling approach has been adopted for the substantial advantages it provides over the traditional site-index methods.

Permanent plot data, consisting of stand height and DBHOB measurements, are subject to nested sources of variability as a consequence of multiple measurements of the same trees taken from different plots located in different catchments. For this reason, permanent plot data violates the independent randomness of measurements assumption in regression analysis due to serial correlation (West, 1995). Non-linear mixed effects models are able to address the challenges affiliated with the

hierarchical structure of permanent plot data. Using mixed effects models, the nested source of variability may be modelled with an appropriate variance-covariance structure to overcome the limitations present in traditional regression analysis. Furthermore, mixed effects models have the advantage of being applicable to permanent plot data that is neither regularly spaced nor balanced, both of which is the case in this study and common in forestry data (Gregoire *et al*., 1995).

Mixed effects models have recently become popular in forest growth modelling exercises because their flexible variance-covariance structure allows for non-constant correlation between sample plots to be accounted (Lindstrom & Bates, 1990; Gregoire *et al*., 1995; Gregoire & Schabenberger, 1996; Fang & Bailey, 2001; Hall & Bailey, 2001; Calama & Montero, 2004; Hall & Clutter, 2004; Calegario *et al*., 2005; Fortin *et al*., 2006). Mixed effects models estimate both the fixed and random coefficients simultaneously to enable the between plot variability in stand volume to be quantified as a random effect whilst defining a common fixed functional structure. Such a model structure allows for predictive models to be formulated for extrapolation purposes over a catchment if it is possible to predict the value of the random coefficients at unsampled locations.

The aim for this chapter was to use mixed effects models to quantify the spatial heterogeneity and temporally polymorphic nature in forest growth within six forest hydrology experimental catchments. The objective was to create stand volume models with a spatiotemporal resolution appropriate for use in chapter eight to explain streamflow response with vegetation dynamics.

6.2. Methodology

6.2.1. Data description

For each of the six experimental catchments in this study, predictive mixed effects models were developed using permanent growth plots, originally established by Melbourne Water to formulate a relationship between forest productivity and forest water use in Mountain Ash forests. Table 4.1 and 4.2 provide a summary of each catchment's treatment, size, and descriptive statistics of the plots used in the study. Compared to typical forest inventory data used for timber accounting purposes, the

dataset has temporally more regular and spatially denser measurements for a given area. To extrapolate the resulting growth models over the catchments, spatially distributed LiDAR indices that characterise the vegetation's canopy profile (produced in chapter five) were used to explain the variance between the sample plots.

6.2.2. The general forest stand volume growth model

There are several functions available for modelling forest growth rates, some of which include the; Gompertz, Bertalanffy, Weibull, Richards-Chapman, and logistic model (Vanclay, 1995; Fang & Bailey, 2001; Hall & Bailey, 2001; Calegario *et al*., 2005). Generally, these models are represented with non-linear equations and are preferred over linear models as they require fewer coefficients to produce comparable fitted values. Furthermore, linear models such as polynomials are not physically interpretable and do not produce reliable estimates outside the range of observed measurements. On the other hand, non-linear models have a theoretical interpretation that hypothesises growth of an organism as the difference between its anabolic rate (constructive metabolism) and catabolic rate (destructive metabolism) and for this reason remains stable beyond the observed range (Pienaar & Turnbull, 1973).

To determine an appropriate model structure, the *nlme* package in R was used to produce and evaluate the mixed effects model specifications for each of the six catchments in the study (R Development Core Team, 2009). After visually inspecting the fit of some of the non-linear models against the datasets, the following two functions were selected to evaluate their performance at fitting the forest inventory data: the logistic model and the gamma model. The motivations in using the logistic model were based on parameter interpretation, parsimonious characteristics, and the advantage that the logistic model has an *R selfStart* function that can be used to generate initial estimates for the fixed effects coefficients (R Development Core Team, 2009). The logistic equation is:

$$G(t) = \frac{\phi_1}{1 + \exp[(\phi_2 - x)/\phi_3]} \qquad [6.1]$$

where *G(t)* is above ground productivity at year *t*, ϕ_1 is the asymptotic stand volume, ϕ_2 is the time at which the plot reaches half of its asymptotic stand volume, and ϕ_3 is the time elapsed between the plot reaching half and $1/1+e^{-1}) \approx 3/4$ of its asymptotic stand volume.

The gamma model contains very different properties to the logistic model and was produced by deriving the integral of a gamma function, originally used by Kuczera (1987) to explain streamflow trends in similar forest types. The integral of the gamma function produces a curve that contains similar features to the Richards-Chapman equation which is commonly used in Victoria's forest inventory management system (Hamilton *et al*., 1999). The gamma equation may be written as:

$$G(t) = \exp(1) * P\max * T\max_{fg} - P\max * (T\max_{fg} + Age) * \exp^{\left(1-\frac{Age}{T\max_{fg}}\right)} \quad [6.2]$$

where *Pmax* is the maximum forest growth increment, and $Tmax_{fg}$ is the time when forest growth rate is at a maximum. Figure 6.1(a) provides an illustration of the gamma and logistic models, as well as a description of the three logistic parameters; whereas figure 1(b) shows the first derivative of both curves as well as an interpretation of the gamma parameters.

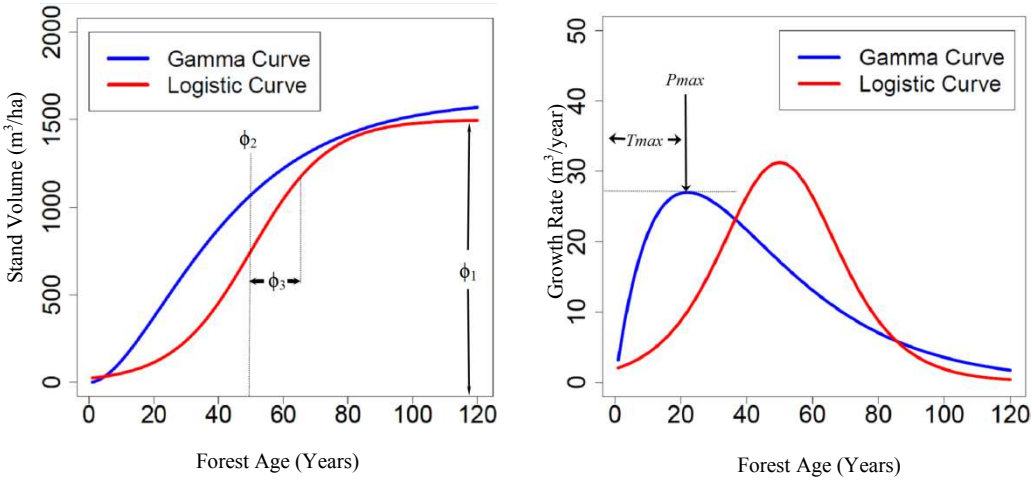

Figure 6.1: An illustration shows: (a) the general shape of the logistic and gamma model, with a description of the logistic parameters; ϕ_1, ϕ_2, and ϕ_3, and (b) first derivative of both curves showing changes in growth rates, with a description of the gamma parameters; *Pmax*, and $Tmax_{fg}$.

6.2.4. The general nonlinear mixed effects model

The non-linear mixed effects model is not restricted to the logistic or gamma model in [6.1] or [6.2] respectively, as it is generally applicable to longitudinal data consisting of repeated measurements within groups. In the case of forest stand volume modelling, [6.1] or [6.2] was assumed to be common to all plots, but the parameter estimates were allowed to vary from plot to plot. To account for inter-catchment variability, the following forest growth modelling procedure was applied to each catchment separately; except Ettercon 2 and 3 were merged as both catchments did not involve a disturbance to the overstorey. As shown in table 4.1, Ettercon 2 involved clearing of the understorey, whereas Ettercon 3 was a control catchment.

Developing a model structure that accounts for the nature of variability in parameter estimates involved a two-level model formulation that represents the within-plot variation and the between plot variation of stand volumes (Fang & Bailey, 2001). The different components of the variation structure for each level will be outlined, followed by an elaborate overview of the considerations required during the model specifications procedure that determined the nature of variability of the different parameters.

6.2.4.1 Within plot variability (first level)

Let y_{ij} denote the j^{th} measurement of the mean stand volume from a total of m_i measurements within the i^{th} plot of a dataset consisting of n plots ($j = 1,....,m_i$; $i= 1, ...,n$). The stand age for plot i at measurement j is t_{ij} and the corresponding residual for y_{ij} is e_{ij}. The non-linear function $y_{ij} = f(\beta_{ij}, \upsilon_{ij}) + e_{ij}$ can be used to represent the relationship between the stand volume and the covariates within the i^{th} plot, where f is a differentiable function of the plot specific parameter vector β_{ij} and covariate vector υ_{ij} (Lindstrom & Bates, 1990). The covariate, also called the predictor vector, consists of stand variables that explain the *between plot variation*, hence will be left out for now to define the general vector form of the *first level within-plot variation* as (Fang & Bailey, 2001):

$$\left.\begin{aligned} & y_i = f(t_i, \beta_i) + e_i \\ & e_i | \beta_i \overset{iid}{\sim} N[0, R_i(\beta_i, \alpha, \theta)] \\ & \mu_i = E[y_i \mid \beta_i] = f(t_i, \beta_i) \\ & f(t_i, \beta_i) = \frac{\phi_1}{1 + \exp[(\phi_2 - x)/\phi_3]} \qquad \text{or} \\ & f(t_i, \beta_i) = \exp(1) * P\max * T\max_{fg} - P\max * (T\max_{fg} + Age) * \exp^{\left(1 - \frac{Age}{T\max_{fg}}\right)} \end{aligned}\right\} \quad [6.3]$$

The formulation in [6.3] is presented in vector form, where $y_i = (y_{i1}, ..., y_{im_i})^T$, $e_i = (e_{i1}, ..., e_{im_i})^T$, $t_i = (t_{i1}, ...t_{im_i})^T$ and $\beta_i = (\beta_{i0}, \beta_{i1}, \beta_{i2})^T$. It should be emphasised that y_i is a continuous response, with the mean vector μ_i functionally independent of the covariance structure (Gregoire *et al*., 1995). Moreover the within-plot error term e_i is assumed to have a mean of zero, and within-plot m_i x m_i covariance matrix of $R_i(\beta_i, \alpha, \theta)$, with a structure of the matrix dependent on fixed effects parameter β_i and covariance parameters, α and θ. The covariance parameters represent the within plot variance due to heteroscedasticity and a correlation pattern of an autocorrelation structure respectively. Fang (2001) has formalised the within-individual variance-covariance as:

$$\begin{aligned} Cov\ (e_i \mid \beta_i) &= R_i(\beta_i, \alpha, \theta) \\ &= \sigma^2 G_i^{1/2}(\beta_i, \alpha) \Gamma_i(\theta) G_i^{1/2}(\beta_i, \alpha) \end{aligned} \quad [6.4]$$

where the m_i x m_i diagonal matrix $G_i^{1/2}(\beta_i, \alpha)$ describes the within plot variance, the m_i x m_i matrix $\Gamma_i(\theta)$ describes the correlation pattern within-plot i, and σ^2 is the scaling factor representing the value of the residual variance of the model (Gregoire *et al*., 1995). The appropriate variance function to adjust for heteroscedasticity and autoregressive error process for the serial correlation structure of the variance-covariance matrix in [6.4] will be determined once the *second level between plot variation* is defined.

6.2.4.2 Between-plot variability (second level)

The greatest benefit mixed effects models offer is their ability to allow the parameter vector β_i to vary between plots by breaking down the regression coefficients into a fixed component common to the population and a random component specific to

each plot (Calama & Montero, 2004). The general form of the nonlinear mixed effects model can therefore be rewritten as $f(A_i\beta + B_i b_i, \upsilon_{ij}) + e_{ij}$ where:

$$\left.\begin{aligned} \beta_i &= A_i\beta + B_i b_i \\ b_i &\sim N(0, D) \end{aligned}\right\} \qquad [6.5]$$

The design matrices A_i for the fixed effects and B_i for the random effects of the i^{th} plot were used to coordinate the model specification. As the logistic model contains three fixed effects, A_i had a *3* x *p* design matrix associated with the i^{th} plot; whereas A_i in the gamma model had a *2* x *p* design matrix.

The B_i is the design matrix corresponding to the *q* x *1* vector of random plot effects b_i. The basic assumption was that the random effects b_i were independently distributed with a mean zero and a variance-covariance matrix (*q* x *q*) defined as *D*. The variance-covariance matrix *D* was common for all plots and defined the variability that exists between plots (Calama & Montero, 2004). The value *q* represented the number of fixed effects parameters that required a random effects component, which varied between catchments.

6.2.5. Model specifications for parameter estimates

With the general formulation of the nonlinear mixed effects model presented, the methodology for specifying the appropriate model structure for the forest stands of interest is outlined below. The modelling exercise was purely data-driven with the variance-covariance structure empirically derived to result in a modelled spatio-temporal response variable that resembles the actual field growth response. To summarise, the procedure for applying [6.3]-[6.5] involved the following:

1. Determine the between-plot variance-covariance structure by specifying whether each of the β_i parameters in [6.1] or [6.2] were mixed (fixed and random) effects or purely fixed effects;
2. Determine the within-plot variance-covariance structure (i.e. $Ri(Bi, \alpha, \theta)$) for each individual plot;

3. Use appropriate LiDAR indices in the design matrix A_i to explain the random effects with covariates.
4. Predict stand volume growth curves with 95% confidence intervals for stands without longitudinal data.

6.2.5.1. Determining the between-plot variance-covariance structure

The variance-covariance matrix for random effects, *D*, defined the structure of variability between plots (Calama & Montero, 2004). The size of the matrix was determined by the number of fixed effects parameters in [6.5] containing a random effects component. This being the case, *D* may be written as (Calama & Montero, 2004):

$$D=\begin{bmatrix} \sigma^2_{b_n} & \dots & \sigma^2_{b_n b_m} \\ \dots & \dots & \dots \\ \sigma^2_{b_n b_m} & \dots & \sigma^2_{b_m} \end{bmatrix} \qquad [6.6]$$

where $\sigma^2_{b_n}$ is the variance for the random effect b_n, and $\sigma^2_{b_n b_m}$ is the covariance among the random effects b_n and b_m.

Three considerations were made for determining which parameters should be mixed (include random effect) and which should be fixed. Firstly separate fits for each plot were obtained to assess whether variability of estimated parameters exists across the plots (Bates and Pinheiro 2000). Variability in the parameter estimate implies that the parameter should have a random component. This approach required each plot to have an adequate number of measurements for the parameter estimates to be stable (Fang & Bailey, 2001). Although this is often not the case with forestry longitudinal data, the present study contains an adequate number of measurements for the parameter estimates to be stable in most instances. In cases where a plot had very wide confidence intervals, the plot was omitted to allow for trend observation in the retained plots. Omitted plots were later reinstated for the rest of the model building exercise.

The second consideration involved running all model parameters as mixed to analyse the standard deviation for each random effect in the covariance matrix, *D,* and identify any random effects close to zero by evaluating the 95% confidence intervals.

As it was possible for small standard deviations to arise due to the scale of the parameter estimate, the variance-covariance matrix was normalised to result in a coefficient of variation that improved the ability to identify any parameters that should be set as fixed (Pinheiro & Bates, 1998). The coefficient of variation matrix D_{CV} was calculated as (Pinheiro & Bates, 1998):

$$\left[D_{cv}\right]_{nm} = \frac{\left[D\right]_{nm}}{\left|\beta_{i(n)}\beta_{i(m)}\right|} \qquad [6.7]$$

where β_i is the i^{th} fixed effect and $i(n)$ and $i(m)$ are fixed effects associated with the n^{th} and m^{th} random effect respectively.

Thirdly, the likelihood ratio test (LRT) and the Akaike Information Criterion (AIC) were used as goodness of fit statistics, to evaluate a reduced model (i.e. model with some parameters only fixed) against a full model that had all parameters mixed. The LRT can only compare two models if one is a nested component of the other (i.e. both models can not have an alternative set of fixed effects and covariance parameters). The LRT, often denoted by □, tests a null hypothesis against an alternative hypothesis using the following statistic:

$$\Lambda(x) = \frac{L(\theta_0 \mid x)}{L(\theta_1 \mid x)} \qquad [6.8]$$

where $L(\theta_0|x)$ and $L(\theta_1|x)$ are likelihood functions for the two hypotheses. If the reduction in parameters significantly reduced the LRT value, then all parameters were left as mixed. When comparing non-nested models the AIC statistic was used (Gregoire *et al*., 1995).

The procedure thus far results in a random coefficient model where β and b_i from [6.5] are vectors of fixed and random effects, and both design matrices A_i and B_i are identity matrices (Fang & Bailey, 2001). The development of the within-plot variance-covariance structure $R_i(B_i, \alpha, \theta)$ is presented next, followed by the procedure for incorporating covariates (i.e. stand variables) to explain the spatio-temporal variability in stand volume. As these additions to the model structure affect the model performance, and hence the goodness of fit criteria LRT and AIC; it was

necessary to evaluate changes in LRT and AIC at every step of the model development and select those models where AIC and LRT values were favourable.

6.2.5.2. Determine the within-plot variance-covariance structure

There are two basic distributional assumptions that need to be tested when using non-linear equations in mixed effects modelling (Bates and Pinheiro, 2000):

- The within plot errors are independent and normally distributed, with a mean of zero and variance σ^2, and they are independent of the random effects.
- The random effects are normally distributed with mean zero and independent for different sample plots, and the covariance matrix is not dependent on the plots.

When these assumptions are violated in mixed effects modelling, the within-plot variance-covariance structure, $Ri(Bi,\alpha,\theta)$, needs to account for;

- heteroscedasticity using a *variance function*; and
- autocorrelation by implementing a *serial correlation structure*.

Heteroscedasticity is the term used to express a non-consistent variance during regression analysis, whereas autocorrelation is the correlation of a variable with itself over successive time intervals.

Variance Function

A variance function for forest growth data adjusts for the variance of error that increases with the age of the forest (i.e. heteroscedasticity). It is common to observe that the variance of error is often related to the mean of a plot's measurements as a larger mean in an older forest usually results in larger variance (Huang *et al*., 2000; Calama & Montero, 2004). According to Davidian and Giltinan (1995), the two most common weighting factors to model the variance are the power function model,

$$\mathrm{Var}(\mu_{ij}, \alpha) = g(\mu_{ij}\ \alpha)\mu_{ij}^{\alpha} \qquad [6.9]$$

and the exponential function model,

$$\mathrm{Var}(\mu_{ij},\alpha) = \exp(\alpha\mu_{ij}), \qquad [6.10]$$

where μ_{ij} is the mean function defined in (6.3). Fitting the functions into the mixed effects model improved the LRT when the variances were not homogenous but changed in the form of the function. Both functions where only tested when the plots of standardised residuals versus the fitted values showed any departure from the model assumptions and the random effects did not account for heterogeneity adequately.

Serial correlation structure

As longitudinal data tends to be serially correlated it may be necessary to modify the model to describe the error structure among measurements from the same plot. In forest inventory data this is not always the case as the correlation structure is often entirely accounted for through the random effects (Hall and Bailey, 2001). To assess the need for adjustments to the autocorrelation structure, plots of the empirical autocorrelation function and the sample semi-variogram were produced. When the error structure suggested within-plot autocorrelation needed adjusting, the first order autoregressive model, AR(1), and the moving average correlation (MA) model were tested. Both models assume a positive correlation decreasing as the distance increases between the observations (Pinheiro and Bates, 2000). In circumstances where the serial correlation structure was not adjusted, Γ_i in (4) was an identity matrix m_i x m_i.

6.2.5.3. Covariate modelling to account for between-plot variation

The random effects component b_i was approximated by the value of the *empirical best linear unbiased predictor* (EBLUP) (Bates and Pinheiro 2000). As the random effects reflect the individual plot's departure from the population mean, plotting the estimated random effects against candidate covariates determined which covariates were able to explain inter-plot variation in stand volume. To have the b_i varying with a particular covariate implied that the random effect also varied from plot to plot due to heterogeneity in the covariate over the catchment. In order to extrapolate the

model over the catchment, the EBLUP of b_i was replaced with a regression that explained b_i with covariates (Calama & Montero, 2004).

For this purpose, LiDAR indices relating to canopy profile attributes such as crown height, density, depth, and closure of both under-storey and over-storey vegetation layers were generated over the catchments to empirically evaluate their capacity in predicting forest growth. LiDAR indices were developed using a wide range of theoretical distribution functions in a mixture modelling procedure that characterised the vegetation structure of the multilayered forests. Refer to chapter five for the procedure undertaken to derive these covariates for each permanent plot in this study.

In using the LiDAR indices, the aim was to reduce the variance of the fixed effects β_i and random effects b_i by explaining some of the heterogeneity in growth response within each catchment. As the number of additional parameters to be estimated increased considerably with inclusion of covariates in mixed-effects models, a forward stepwise approach was adopted that includes covariate coefficient pairs one at a time. The procedure involved starting with a model with no covariates and plotting the estimated random effects against a set of LiDAR indices to identify any strong correlation or systematic patterns (Bates and Pinheiro 2000). The potential importance of the remaining covariates was graphically assessed at each step against random effects generated in the model from the previous step to determine whether the model may be improved with further covariate coefficient pairs. Including covariates in the model to explain inter-plot variation provided a better understanding of the mechanisms producing the growth response.

The regressions that explain how covariates vary for each random effect were incorporated into the design matrix A_i and B_i. Incorporating design matrices A_i and B_i affected the within plot variance function and correlation structure in [6.3] since the within-plot m_i x m_i covariance matrix of $R_i(\beta_i, \alpha, \theta)$, was dependent on the fixed effects parameter β_i. For this reason, the within plot covariance matrix $R_i(\beta_i, \alpha, \theta)$ had to be readdressed, and reapplied iteratively until a satisfactory model was obtained. The variance values for the model components associated with b_i needed to decrease

in the improved model, and the goodness of fit measures (AIC and LRT) needed to improve.

Using the forward stepwise method may result in a model that depends on covariates in a complex manner. However, there are statistical and practical reasons to have a parsimonious model. Statistically, the inclusion of complex parametric functions will typically result in non-identifiability and ill-conditioning of the model (Hall & Bailey, 2001). This was detected when the parameter estimation procedure did not converge or when the solution had an estimated variance-covariance matrix that was almost singular or nearly perfectly correlated. These problems were resolved by simplifying the model's dependence on covariates or removing some of the random effects.

6.2.5.4. Predicting stand volume in unmeasured sites

Given that within-plot errors in [6.4] were assumed to be independent and normally distributed, an appropriate covariance matrix $R_i(\beta_i, \alpha, \theta)$ needed to result in standardised residuals randomly scattered against the fitted value with no trend, and the Q-Q plots needed to be approximately linear (Fang & Bailey, 2001). To successfully explain the stand volume estimates in unmeasured sites the residuals also needed to be small.

Once satisfied with the basic distribution assumptions, stand volumes at age t were predicted for all forested areas that had no prior measurements using the spatially distributed covariates within the design matrices. However, as there were no observations of stand growth outside the permanent plots, the random effects parameters, b_i, were not known and hence given the value zero (Fang & Bailey, 2001). For this reason, it was important to develop a model that had most of the random effects explained with covariates in order to make the model as predictive as possible.

6.3. Results

As the present study evaluated six catchments with two very distinct non-linear equations, the diagnostic plots and results associated with the step-by-step model evaluation procedure was much too extensive to provide in the chapter. For this

reason, only Myrtle 2 and Ettercon 2 & 3 are used to illustrate the model building procedure, whereas summary tables provide final model outcomes for the other catchments. The more extensive results for the Black Spur catchments are included in Appendix A.

6.3.1. Fitting a logistic growth model

Figure 6.2 shows the variation in stand volume for all plots in the following catchments: Myrtle 2 and Ettercon 2 & 3. It is evident there is large variation in forest growth both between and within the catchments, as may be observed for the other catchments in Appendix A1. Tree mortality in the native forest environment resulted with some plots having an abrupt reduction in forest growth and in some cases decline in stand volume.

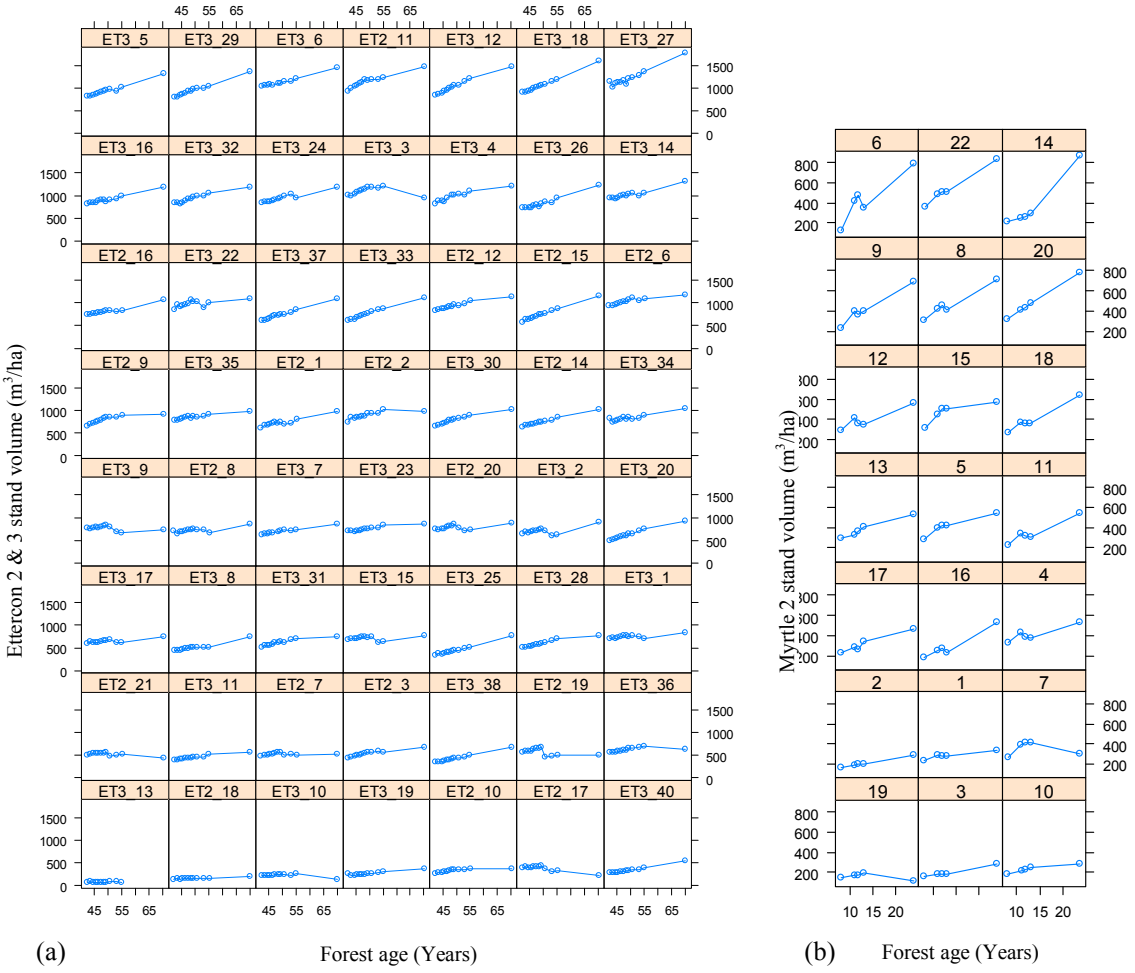

Figure 6.2: Changes in stand volume over time for each plot in; (a) Ettercon 2 & 3, and (b) Myrtle 2.

Figure 6.3 shows that when a simple logistic or gamma model without any random effects was fitted to Myrtle 2 dataset (using *nls*), the residuals were mostly negative for some of the plots and mostly positive for others. Comparing the two models, there was little difference in each plot's residuals, as may be observed for all catchments in Appendix A2. For both models, the individual plot differences observed in figure 6.2 were incorporated in the residuals thus inflating the residual standard error. Fitting separate logistic or gamma models through each plot (using *nlsList*) reduced the residual standard error at the expense of a large number of coefficients being required to represent the individual plots without taking account of the obvious similarity amongst the individual curves in figure 6.2.

To address these problems, a non-linear mixed effects model provided a compromise between the rigid *nls* model and the over parameterised *nlsList* model. To develop a mixed effects model for each catchment it was first necessary to fit a simple non-linear model through each plot to analyse the variation in coefficients within a catchment, and adjust the between-plot variance-covariance structure accordingly.

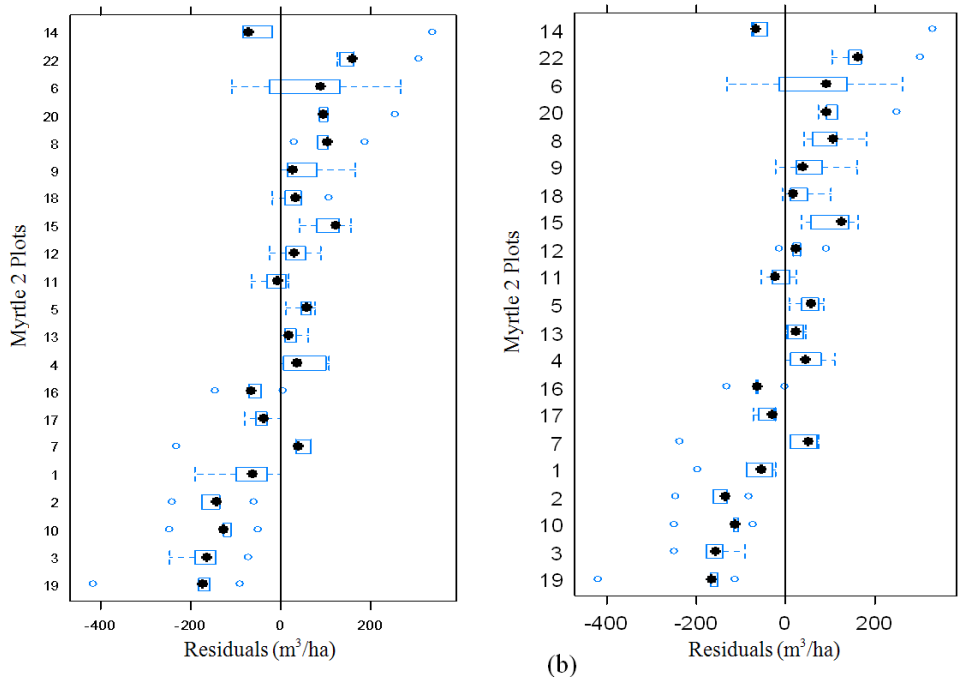

Figure 6.3 Residual standard error of a simple; (a) logistic, and (b) gamma model for Myrtle 2 (using *nls*).

6.3.2. Modelling the variance-covariance structure

Determining the variance-covariance structure involved a highly iterative procedure that involved adjusting the between-plot variance-covariance structure, checking the

within-plot variance-covariance structure, followed by moving backwards and forwards between the two-levels as demonstrated below.

To adjust the between-plot variance-covariance structure, the variation in confidence intervals for the coefficients in *nlsList* were used to determine which parameters are likely to be represented with a random component and which are most appropriately fixed across the plots of a catchment. Using the *nlsList* models, figure 6.4 shows the variation in the coefficient confidence intervals for Myrtle 2 and Ettercon 2 & 3 (Appendix A3 for other catchments). To visually assess the coefficient estimates, plots with very wide confidence intervals needed to be omitted (more often the case for logistic model) to allow for trend observation in the retained plots. Omitted plots were later reinstated for the rest of the model building exercise. Figure 6.4 demonstrates that all coefficient estimates had some level of variation between the plots; except the *scal* and *xmid* parameter in Myrtle 2.

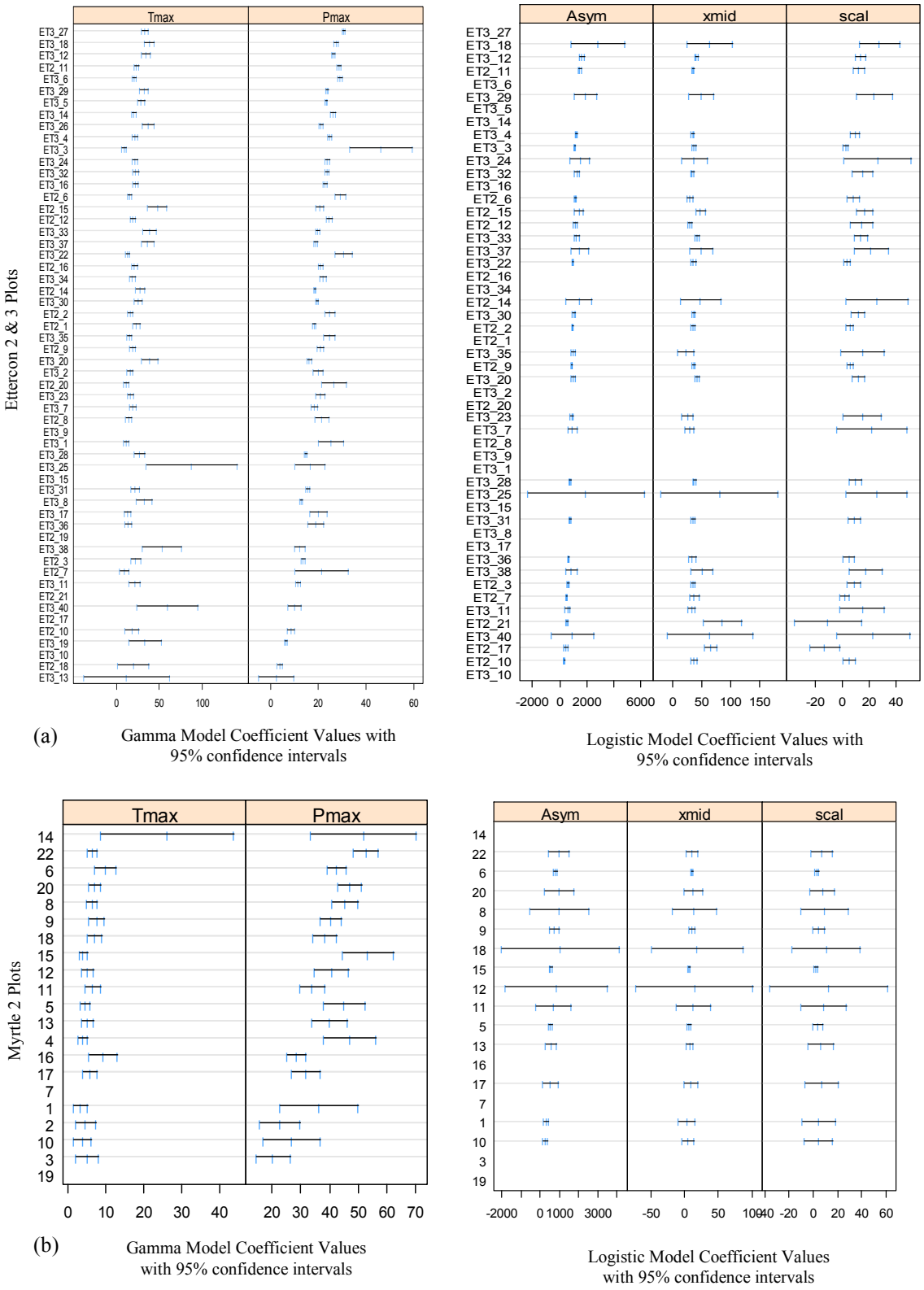

Figure 6.4: Ninety-five percent confidence interval for coefficients in the gamma and logistic model using datasets; (a) Ettercon 2 & 3, and (b) Myrtle 2. Plots with very uncertain confidence intervals were removed and are not shown.

With consideration for the *nlsList* analysis in figure 6.4, the mixed effects modelling procedure started off by assigning a random component to all coefficients except the *xmid* and *scal* parameter in Myrtle 2. The results of the fitted models were compared to converged models with all parameter values fitted with a random component. A model comparison (using ANOVA) found that reinstating the *xmid* random component for Myrtle 2 resulted in a significantly better model (p-value <0.0001) with improved AIC and LRT values. For Ettercon 2 & 3, the gamma model failed to converge with both parameters mixed; despite the *nlsList* analysis in figure 6.4 suggesting such a model structure, meaning the $Tmax_{fg}$ parameter needed to be reduced to a fixed state.

The resulting mixed effects models had fixed effects parameter estimates similar to parameter estimates in *nls* but the residual standard errors were reduced greatly as the random effects successfully explained the variation between the plots. To determine whether the within-plot variance structure needed correcting with a variance model, figure 6.5 (also Appendix A4) shows plots of standardised residuals versus fitted values. The scatter plots visually assessed whether variance of error increased with stand volume, and hence failed to meet the model assumptions relating to heteroscedasticity. Excluding the outlying tagged observations, there is evidence with both models applied to Ettercon 2 & 3 that within-group variability increased with stand volume. The variance of error in Myrtle 2 suggests a variance model is not required to address the within-plot variance structure.

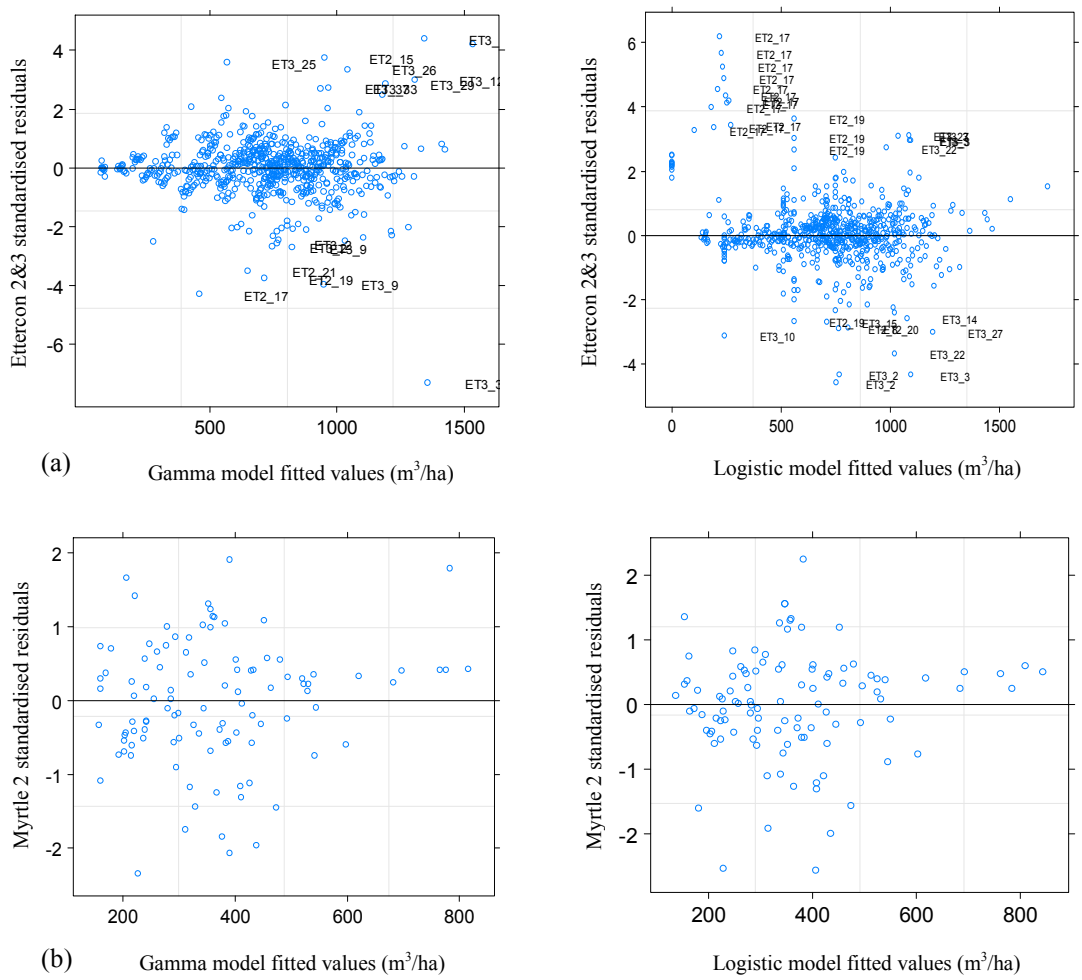

Figure 6.5: Scatter plot of standardised residuals versus fitted values before correcting for heteroscedasticity for: (a) Ettercon 2 & 3, and (b) Myrtle 2.

In figure 6.6 (also Appendix A5) the normal probability plots of the standardised residuals evaluate the assumption of normality for the within group error. The results show that for Ettercon 2 & 3 the distributions of the within group errors had heavier tails than expected under normality but seem reasonably symmetric around zero. It is evident in Ettercon 2 & 3 that the gamma model results in standardised residuals that are slightly more normal than those observed using the logistic model. The normality assumption seems plausible in the Myrtle 2 observations for both models.

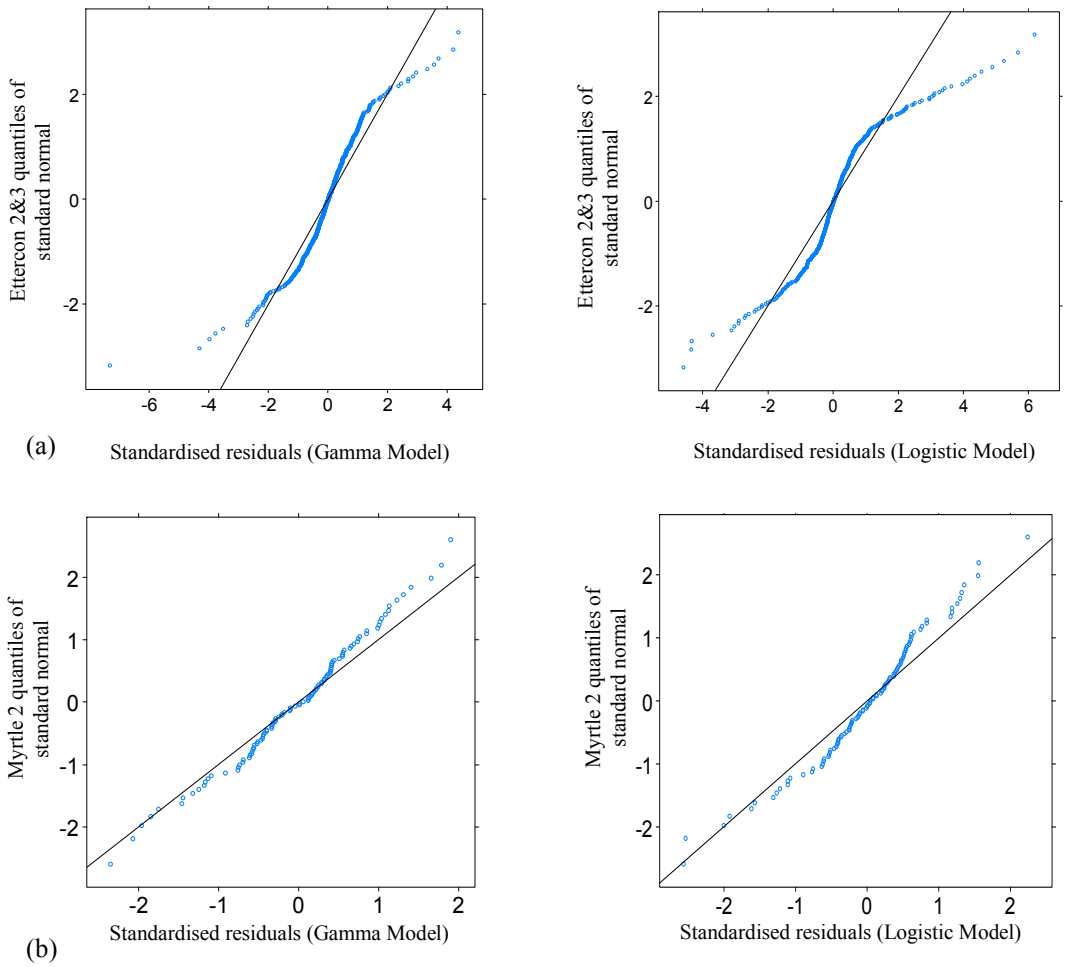

Figure 6.6: Normal probability plot of the within-plot standardised residuals before correcting within-plot variance structure for: (a) Ettercon 2 & 3, and (b) Myrtle 2.

Figure 6.7 (also Appendix A6) shows correlations between the random effect coefficients used in the final model up to this stage. The diagnostic plots for the logistic model suggest; *Asym* is partially correlated to the *scal* parameter in Ettercon 2 & 3, whereas *Asym* is partially correlated to *xmid* in Myrtle 2. To determine whether the logistic models are over-parameterised with unnecessary random effects, it was necessary to evaluate the 95% confidence intervals of the correlation coefficients.

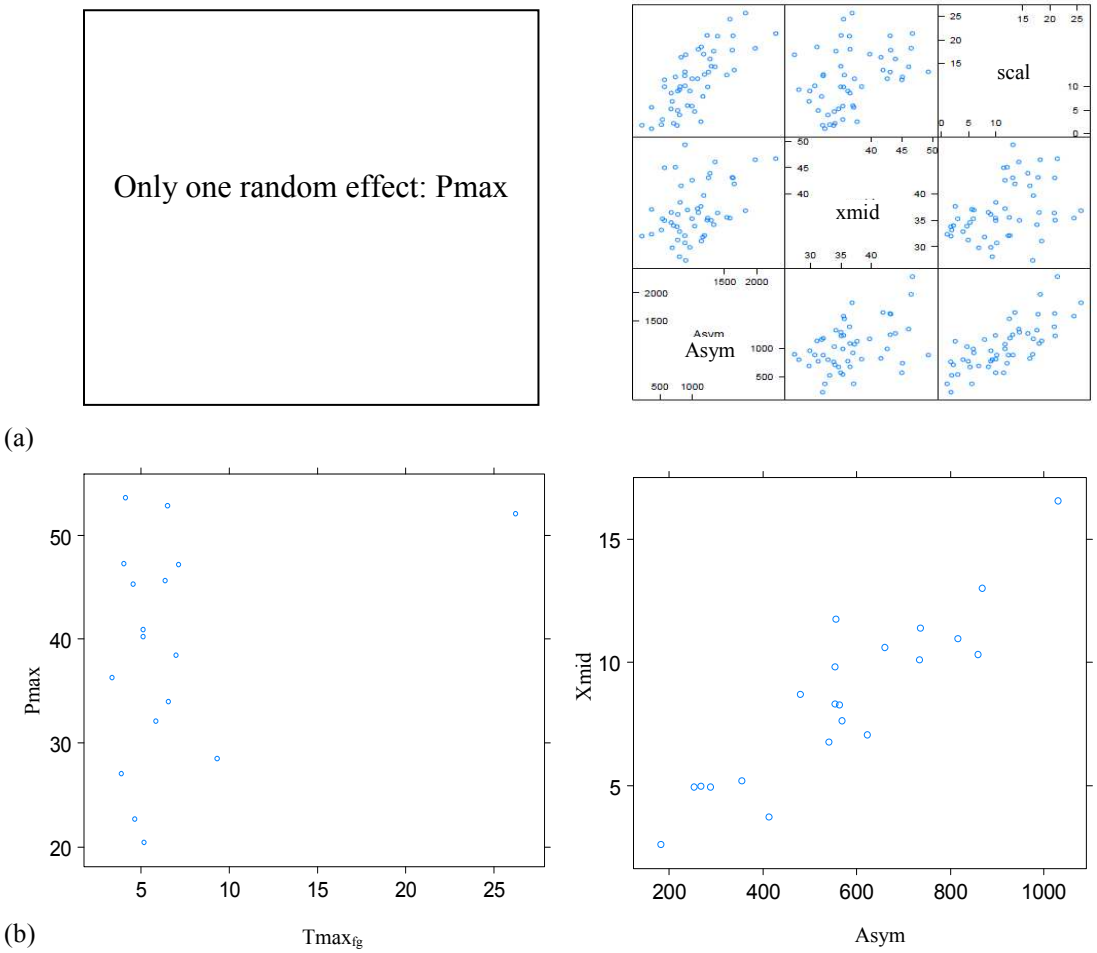

Figure 6.7: Pairs plots for random effect estimates for: (a) Ettercon 2 & 3 and (b) Myrtle 2.

For all six catchments in this study, table 6.1 provides the 95% confidence intervals for the variance-covariance structure, and variance function used to correct for heteroscedasticity. In table 6.1, when the upper limit of the correlation between coefficients is below one, the random effects are not completely correlated and hence should be preserved to explain the between plot variation (Bates and Pinheiro 2000). Also, if the lower limit of the 95% confidence intervals of the standard deviation for each random effect is significantly greater than zero, the random effect should be retained. As the standard deviation may be small due to the scale of the parameter estimates, normalising the variance-covariance matrix with a coefficient of variation (CV) was used to identify which coefficients should be made fixed (Bates and Pinheiro 2000). The CV determined the relative inter-group variability of the coefficients and was defined as the ratio of the standard deviation of the random effects and the absolute value of the corresponding fixed effects. Only the *Asym*

coefficient in Ettercon 2 & 3 had a low CV but was not reduced, by removing the random component, as it was not strongly correlated to the other random effects.

Table 6.1: Summary of the random effects for the final model structure, with 95% confidence intervals of the variance-covariance structure for each catchment in the study

Catchment	Model	coefficient	Lower (5%)	Estimate	Upper (95%)	Coefficient of Variation
Black Spur 1	Gamma	sd(*Pmax*)	7.98	10.11	12.79	0.49
		power	1.03	1.13	1.22	-
	Logistic	sd(*Asym*)	495.32	639.71	826.19	0.65
		sd(*xmid*)	6.62	9.47	13.54	0.20
		cor(*Asym, xmid*)	0.09	0.44	0.70	-
		power	0.72	0.84	0.96	
Black Spur 2	Gamma	sd(*Pmax*)	0.78	1.36	2.37	0.14
		power	1.70	2.21	2.71	-
	Logistic	sd(*Asym*)	100.26	172.11	295.46	0.16
		power	1.39	1.91	2.42	-
Black Spur 3	Gamma	sd(*Pmax*)	0.66	1.15	2.00	0.12
	Logistic	sd(*Asym*)	6.75	15.81	37.00	0.30
Ettercon 2 & 3	Gamma	sd(*Pmax*)	4.03	4.86	5.86	0.31
		power	0.59	0.71	0.84	-
	Logistic	sd(*Asym*)	257.94	329.34	420.51	0.06
		sd(*scal*)	3.81	5.72	8.59	0.13
		sd(*xmid*)	3.86	5.60	8.14	0.21
		cor(*Asym, scal*)	0.47	0.69	0.83	-
		cor(*Asym, xmid*)	0.05	0.42	0.68	-
		cor(*scal,xmidI*)	-0.17	0.36	0.73	-
		power	0.34	0.48	0.63	-
Myrtle 2	Gamma	sd(*Pmax*)	2.88	4.58	7.29	0.11
		sd($Tmax_{fg}$)	1.07	1.64	2.53	0.3
		Cor($Tmax_{fg}$,*Pmax*)	-0.76	-0.29	0.39	-
	Logistic	sd(*Asym*)	158.10	224.55	318.92	0.40
		sd(*xmid*)	2.19	3.58	5.83	0.42
		cor(*Asym,xmid*)	0.65	0.88	0.96	-

6.3.3. Covariate modelling of between-plot variation

Once the improved model structure was evaluated using both diagnostic plots and parameter estimates of the variance-covariance structure, predictive models were developed by explaining random effects with LiDAR indices. LiDAR indices that explain the functional characteristics and biophysical properties of forest growth were considered likely candidates in the model building procedure. For this reason, the biological interpretation of the model parameters was important. The logistic model included: the asymptote parameter, ϕ_1, as the maximum height; inflection parameter, ϕ_2, as the age at which ½ of the maximum height occurs; and the scale parameter, ϕ_3, as the time from the inflection point to the point where the height is ≈ 3/4. For the gamma model, the biological interpretation of the parameters included: the *Pmax* parameter as the maximum growth rate, and $Tmax_{fg}$ parameter as the time when the maximum growth rate is reached.

Starting with the model with no covariates, a forward stepwise procedure involved plotting the estimated random effects against a set of LiDAR indices. The LiDAR index with the strongest correlation with the estimated random effect was integrated into the model through the corresponding fixed effect. Incorporating a covariate into the model structure was followed by an evaluation of the diagnostic plots and parameter estimates of the variance-covariance structure, as outlined above. Once satisfied with the model assumptions, the model was re-run to identify the next covariate with the greatest explanatory capacity. Figure 6.8 (also Appendix A7) shows the correlations of the covariates used in the final models with a locally weighted scatter plot smoother (LOWESS) to visualise potential trends.

The LiDAR data was collected in 2007 and therefore captures the vegetation structure at the time of the permanent plot's last field measurements. For this reason, in the logistic model, the covariates were most effective at characterising the asymptote parameter (*Asym*). As shown in figure 6.8(a), for Ettercon 2 & 3, *Asym* is positively correlated with; the number of hits in the Eucalyptus layer *(EucPoints),* and the canopy mode of the eucalyptus layer *(K2mu)*. Figure 6.8(b) shows that for Myrtle 2, *Asym* is positively correlated with; the 40th percentile of the eucalyptus layer *(Euc_P40)* and *K2mu*.

For the gamma model, in the case of Ettercon 2 & 3, parameter *Pmax* is well correlated with the proportion of hits in the eucalyptus layer *(Final_P2)* and the 50th percentile of the eucalyptus layer (*Euc_P50)*. For Myrtle 2, parameter $Tmax_{fg}$ is well correlated with the average plot height of the eucalyptus layer using 5X5 metre sub-plots averages (*Mean_Euc_Mean*), whereas the *Pmax* parameter is negatively correlated with the number of ground hits (*Gnd_Points*).

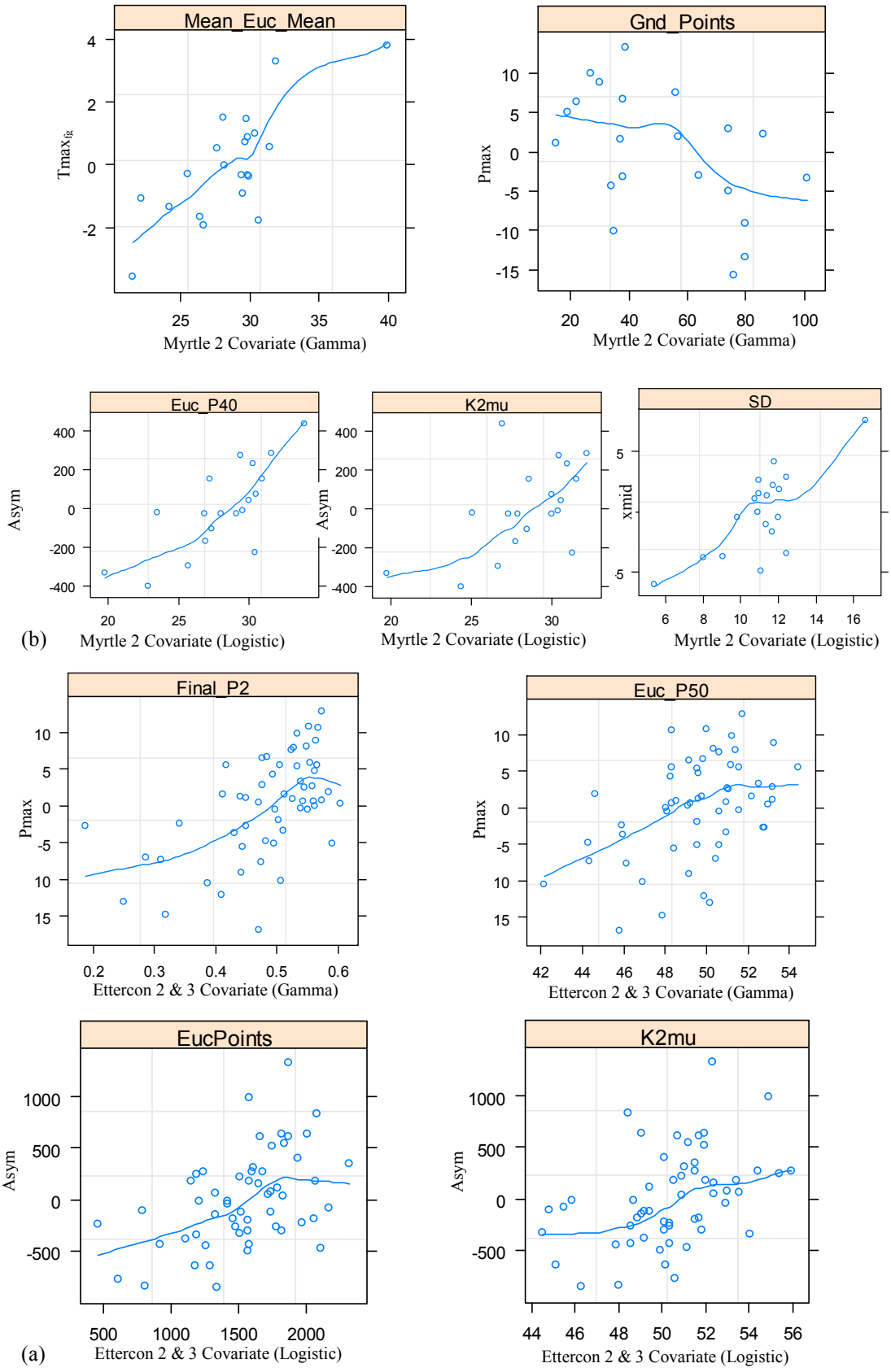

Figure 6.8: Applied LiDAR indices using the forward stepwise procedure to explain the random effects and develop a predictive model for: (a) Ettercon 2 & 3 and (b) Myrtle 2.

During the forward stepwise procedure, the ANOVA method was used to compare results. For both the gamma and logistic models, table 6.3 provides results for the following three models generated for each of the catchments:

- Model (L or G)1 with the simplest mixed effects model containing the random component: *Asym* (logistic) or *Pmax* (gamma);
- Model (L or G)2 with the final variance-covariance structure and no covariates;
- Model (L or G)3 with covariates incorporated into the final variance-covariance structure.

Table 6.2 shows that for each catchment, model 2 was consistently better than Model 1, as increasing the number of random effects always reduced AIC values. It was evident that integrating covariates into the model structure also reduced the AIC values. The degrees of freedom for each model structure show that the logistic model used more covariates to explain the random effects, although the logistic model's larger degree of freedom is also a result of one extra fixed effects parameter. Caution should be noted for Black Spur 2 and 3, as the model structure resulted in a large degree of freedom considering both catchments had seven sample plots. The sample size for the other catchments is provided in table 4.2.

Table 6.2: Summary of the ANOVA results for each catchment provides an assessment of how much the model improved over different stages of development.

Catchment	Model Type	Model	df	AIC	L. Ratio Test	P<value
Black Spur 1	Logistic	L1	5	5779.55		
		L2	7	5338.90	1 vs 2: 444.6	<.0001
		L3	13	5107.96	2 vs 3: 211.8	<.0001
	Gamma	G1	4	5809.46		
		G2	5	5390.46	1 vs 2: 421.0	<.0001
		G3	6	5377.56	2 vs 3: 14.90	<.0001
Black Spur 2	Logistic	L1	5	921.77		
		L2	6	878.57	1 vs 2: 45.2	<.0001
		L3	8	872.87	2 vs 3: 9.7	0.0078
	Gamma	G1	4	940.10		
		G2	5	882.03	1 vs 2: 60.1	<.0001
		G3	6	872.42	2 vs 3: 11.6	<.0007
Black Spur 3	Logistic	L1	5	851.46		
		L3	7	817.72	1 vs 3: 37.7	<.0001
	Gamma	G1	4	860.75		
		G3	5	842.95	1 vs 3: 19.8	<.0001
Ettercon 2&3	Logistic	L1	5	7607.03		
		L2	11	7137.43	1 vs 2: 425.5	<.0001
		L3	13	7109.04	2 vs 3: 32.8	<.0001
	Gamma	G1	4	7602.63		
		G2	5	7498.05	1 vs 2: 106.6	<.0001
		G3	7	7466.39	2 vs 3: 35.6	<.0001
Myrtle 2	Logistic	L1	5	1244.54		
		L2	7	1202.51	1 vs 2: 46.0	<.0001
		L3	10	1181.00	2 vs 3: 27.5	<.0001
	Gamma	G1	4	1244.03		
		G2	7	1205.14	1 vs 2: 35.2	<.0001
		G3	9	1181.54	2 vs 3: 29.2	<.0001

Note: Models L and G stand for logistic and gamma.

To determine whether the final model (model 3) had any departure from the model assumptions on normality and heteroscedasticity, figure 6.9 (also Appendix A8) shows normal probability plots of the standardised residuals, and figure 6.10 (also Appendix A9) shows plots of standardised residuals versus fitted values. It is evident, when comparing figure 6.9 and 6.10 to figure 6.5 and 6.6, that the

standardised residuals of final model have a much more homoscedastic variance, and the quantiles show an improvement in the distribution of the within group errors, but Ettercon 2 & 3 still has slightly heavier tails than expected under normality.

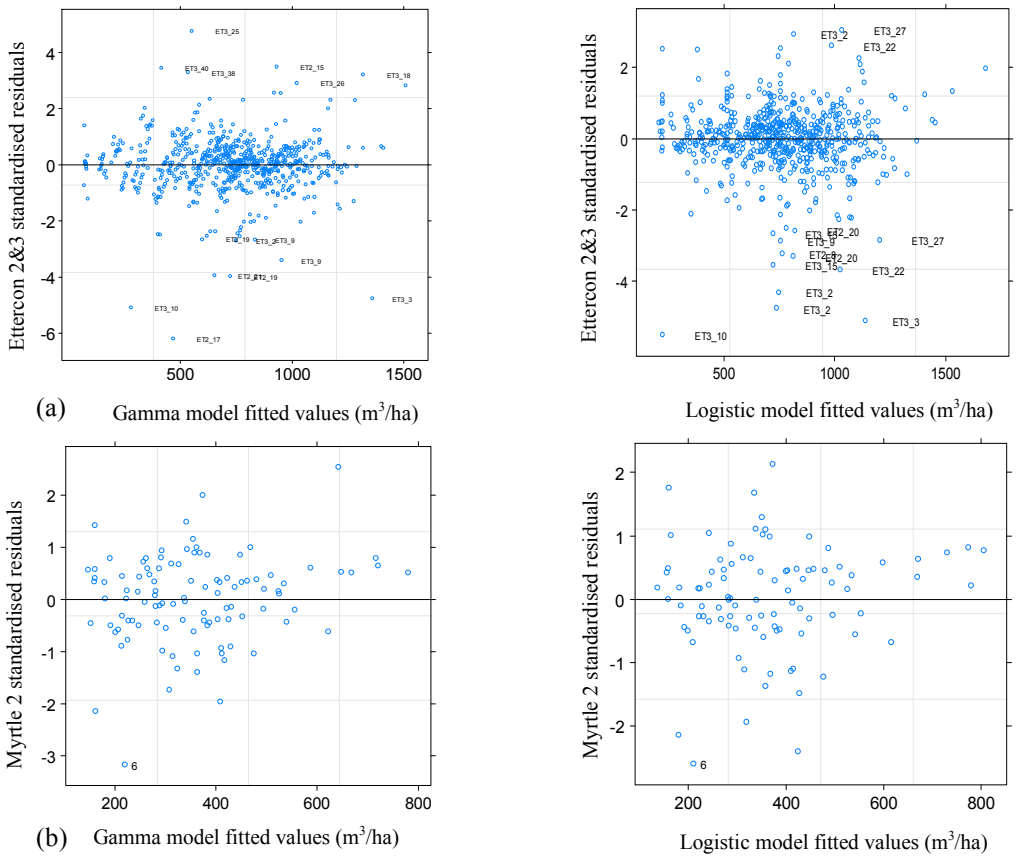

Figure 6.9: Scatter plots of standardised residuals versus fitted values using the final logistic and gamma model for: (a) Ettercon 2 & 3, and (b) Myrtle 2.

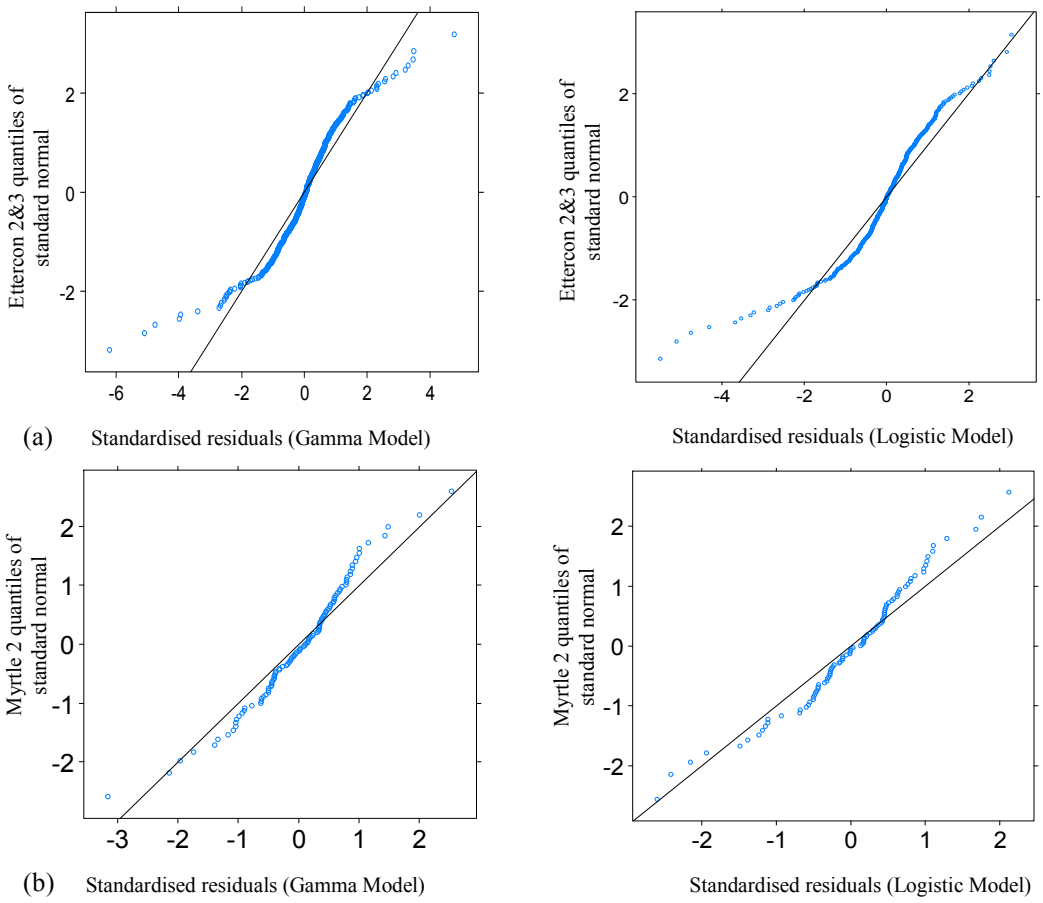

Figure 6.10: Normal probability plots of the within-group standardised residuals using the final logistic and gamma model for: (a) Ettercon 2 & 3, and (b) Myrtle 2.

The quality of fit for the predictive models is provided in figure 6.11 (also Appendix A10), which shows how well the individual plots are predicted using; (1) mixed effects models with estimated random effects (pink curves) and, (2) fixed effects models with random effects equalling zero and the covariates attempting to explain the between-plot variance (blue curves). The blue curves provide an indication of how well the final model predicts stand volumes at unsampled locations; where the accuracy was largely attributed to the strength of the relationship between the covariate and the random effects.

For both models, the random effects (pink line) explained changes in stand volume very well, although, the fifteen year gap between the second last and last field measurement resulted in the gamma model sometimes failing to accurately estimate the last observation. This was particularly the case under circumstances when plot changes in stand volume over the fifteen year data collection gap were not reflective

of the rest of the datasets trend. Under such circumstances the gamma model was not flexible enough to account for such changes.

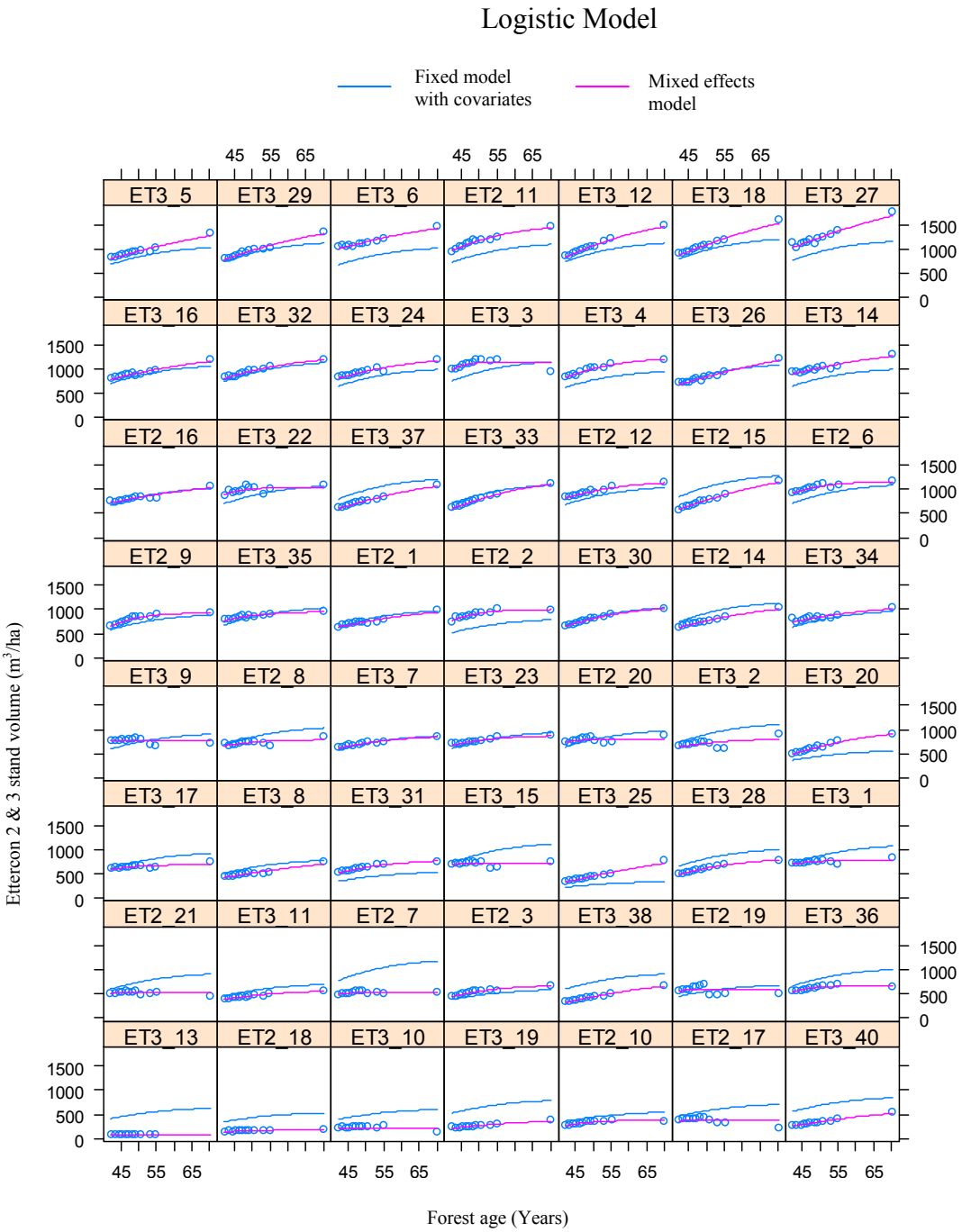

(a)

Figure 6.11: Plot specific predictions that use random effects (Mixed Effects Model); and population average predictions with random effects equalling zero and covariates explaining between plot variations (Fixed Model) for: (a) Ettercon 2 & 3, and (b) Myrtle 2.

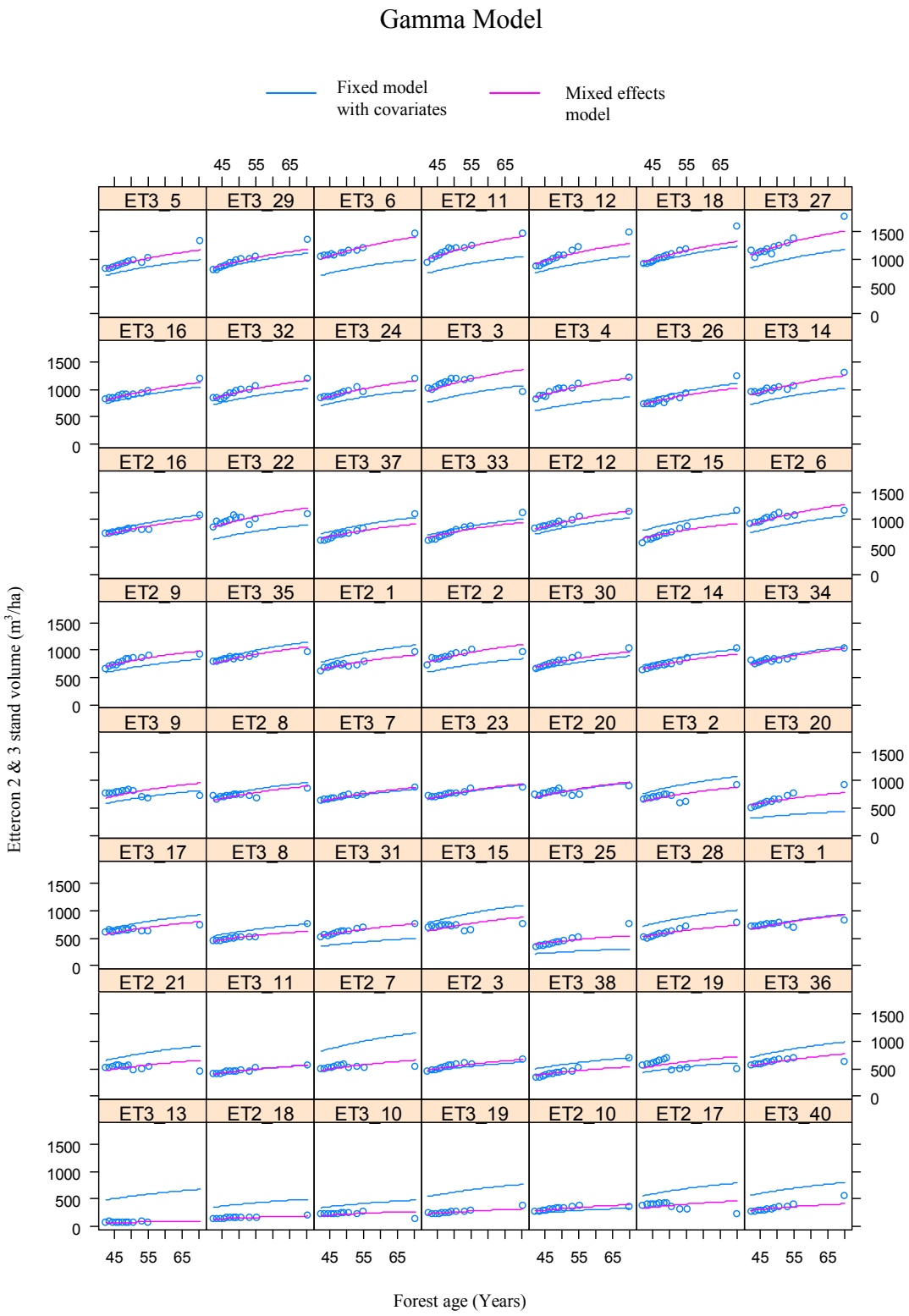

(a)

Figure 6.11: Plot specific predictions that use random effects (Mixed Effects Model); and population average predictions with random effects equalling zero and covariates explaining between plot variations (Fixed Model) for: (a) Ettercon 2 & 3, and (b) Myrtle 2.

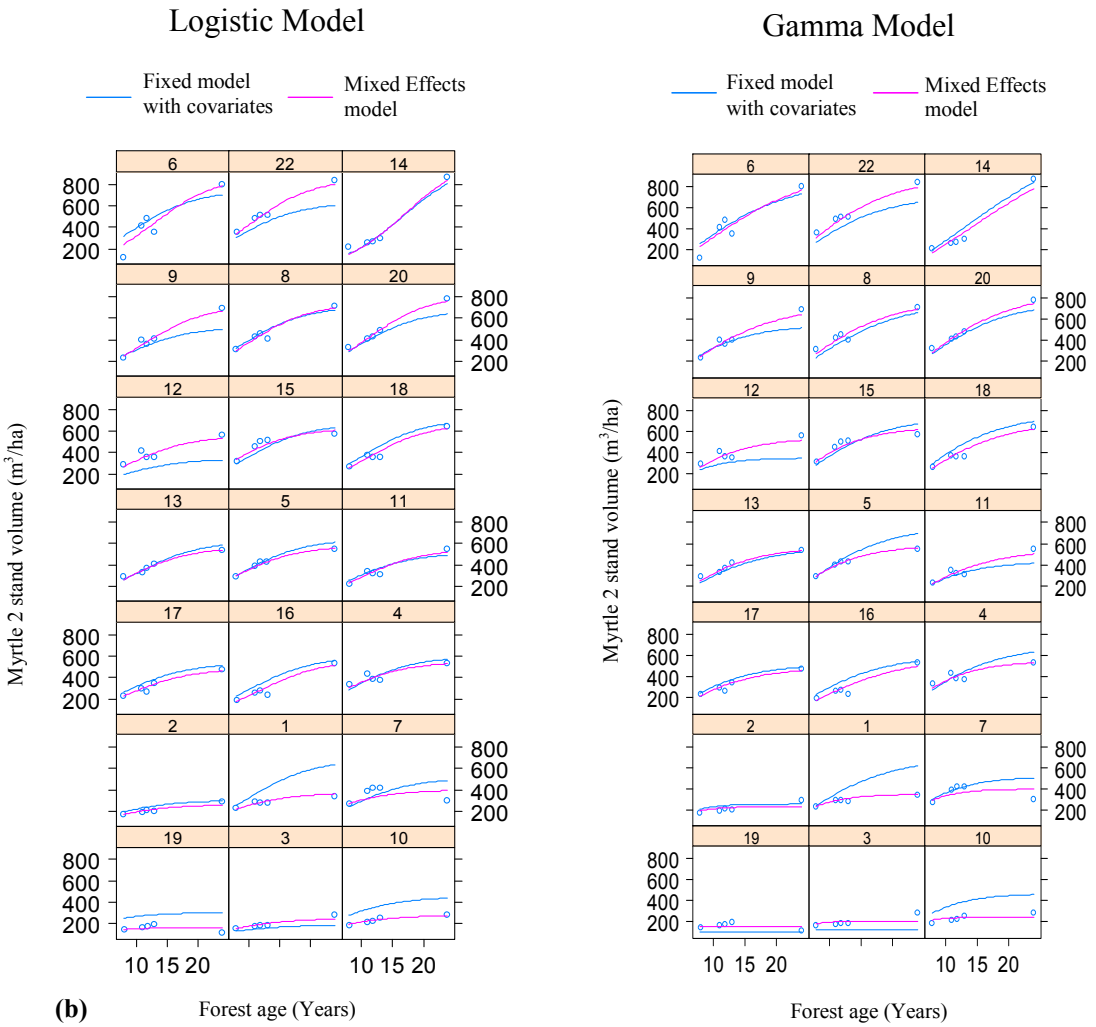

Figure 6.11: Plot specific predictions that use random effects (Mixed Effects Model); and population average predictions with random effects equalling zero and covariates explaining between plot variations (Fixed Model) for: (a) Ettercon 2 & 3, and (b) Myrtle 2.

The final predictability of the model may be evaluated with figure 6.12 (also Appendix A11), which provides a scatter plot of the predicted versus observed values for all observations using the fixed effects model with covariates explaining between-plot variance for; (a) Ettercon 2&3 and (b) Myrtle 2. Figure 6.13 provides a scatter plot of the predicted versus observed values for all observations using the random effects to explain between-plot variance for; (a) Ettercon 2&3 and (b) Myrtle 2. Comparing figure 6.12 and 6.13 clearly shows that the mixed effects model was very effective at explaining between-plot variation, but the predictive capacity of the model at unsampled sites was much poorer due to the explanatory power of the covariates. To improve these predictive estimates it is necessary to; produce LiDAR indices that more accurately capture the functional characteristics and biophysical

properties of forest growth, and formulate a stronger relationship between the LiDAR indices and random effects.

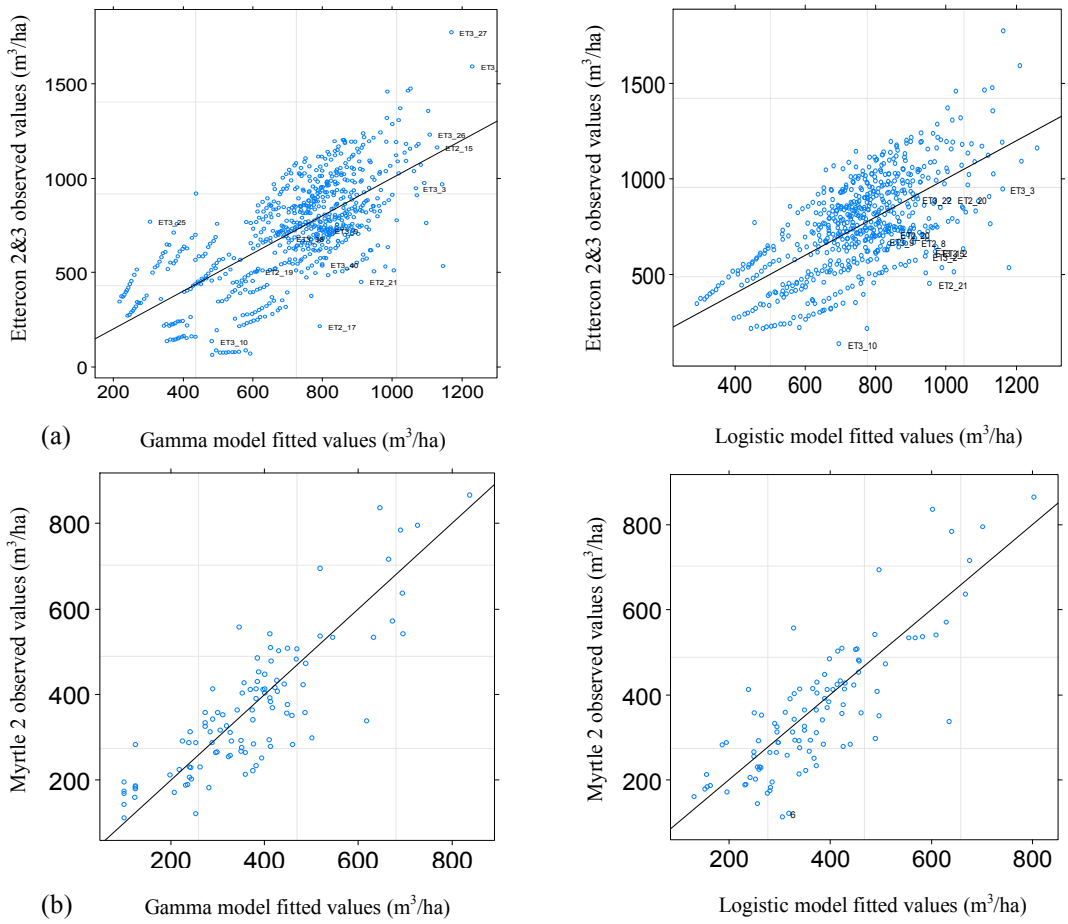

Figure 6.12: Scatter plot of predicted versus observed values for the logistic and gamma models using covariates to explain between-plot variation for: (a) Ettercon 2 & 3, and (b) Myrtle 2.

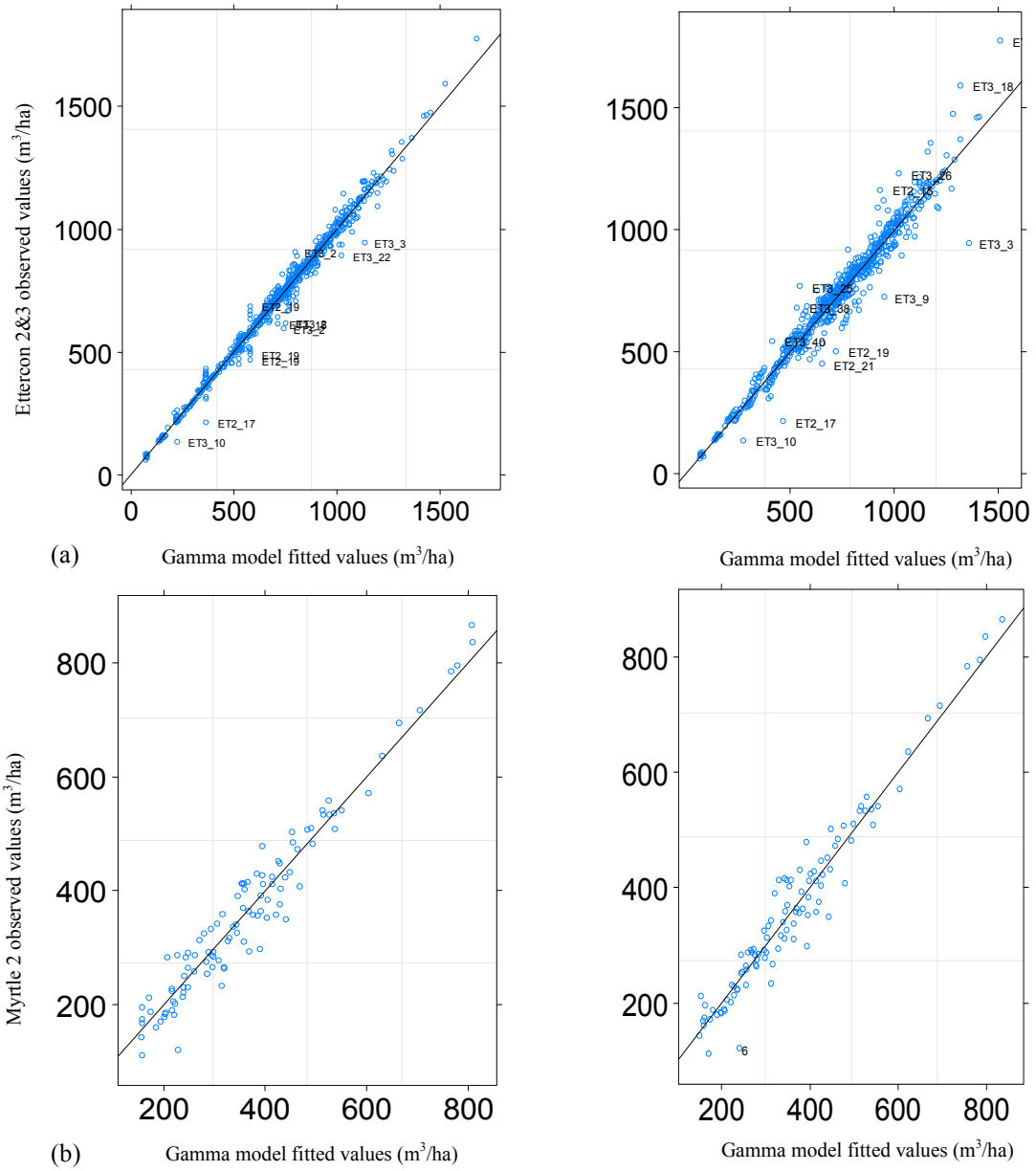

Figure 6.13: Scatter plot of predicted versus observed values for the logistic and gamma models using a mixed effects model to explain between-plot variation for: (a) Ettercon 2 & 3, and (b) Myrtle 2.

6.4. Discussion

Mixed effects models were used to quantify the spatial heterogeneity and temporally polymorphic nature in forest growth. It is important to recognise that an inappropriate variance-covariance structure due to violation of the basic distributional assumptions results in erroneous predictions. Fang and Bailey (2001) found that random effects may relieve problems associated with heteroscedasticity and within-plot correlation, but when this is not the case the variance-covariance structure needs adjusting. In this study, after introducing random effects to both the

logistic and gamma models, the power variance function needed to be applied to correct the variance structure in Black Spur 1 and 2, and Ettercon 2 & 3. The adjustments to the variance-covariance structure resulted in a reduction in the prediction error. Although heteroscedasticity was easy to correct for with a weight that represents the inverse of the trend of the variance, within-plot autocorrelation posed much greater challenges.

Within-plot autocorrelation is affected by a range of factors relating to both the data and model structure and it is often not evident what adjustments to the model structure are appropriate (Fang and Bailey, 2001). For example, longitudinal data with observations within the same plot are correlated with the same plot effect and in a mixed effects model this correlated plot effect is to some degree accounted for with random effects. Although the presence of the random effect implies a correlation structure for the data, precisely what that structure is within a particular plot is difficult to determine. For this reason, Hall and Baily (2001), recognise that there is no closed-form solution for the within-plot correlation matrix when the random effect enters the model in a non-linear fashion. For this reason, the present study opted to model the autocorrelation structure indirectly through the random effects structure without any direct adjustments to the variance-covariance matrix. This approach was further justified as the autoregressive AR(1) and moving average correlation (MA) models contributed little to reduce the predictive error. As has been noted by Jones (1990) and Gregoire and Schabenberger (196b), additional within-subject correlation is often negligible in the presence of random effects (Hall and Bailey, 2001). Several authors in the forestry literature also concluded that modelling the within-plot autocorrelation produced no improvements in the forest growth models (Fang & Bailey, 2001; Calama & Montero, 2004).

The present study used data collected from catchments with differing plot sizes and treatment effects (excluding Ettercon 2&3), and as a result the modelling procedure was undertaken on each catchment separately. For a robust predictive model outcome, this raised concerns relating to the adequacy of each catchment's sample size. Once the present modelling exercise addressed the variance-covariance structure and incorporated covariates, the model structure resulted in approximately 5 to 13 degrees of freedom. As Black Spur 2 and 3 only consisted of seven plots each,

the gamma model's degrees of freedom of six and five respectively was much too high. The small sample size also meant the relationship between the covariates and random effects was highly unstable, introducing a great deal of uncertainty when extrapolating the predictions. The other catchments had an adequate sample size given the complexity of their corresponding model structure.

To improve predictions of the forest growth models, it is necessary to address the limitations and shortcomings of the LiDAR indices used as covariates. When integrating covariates into the model structure with the forward stepwise procedure, the prediction error of each individual plot varied depending on which covariate was used to explain the random effects. It was evident that when alternating between covariates, plots with LiDAR indices that misrepresented the vegetation structure resulted in unstable and highly sporadic prediction errors. Potentially the predictive capacity of the model illustrated in figure 6.12 can be improved to reflect the predictive capacity of figure 6.13 if the random components between the plots are explained with more robust covariates.

Although the resulting predictions using the gamma equation were comparable with the logistic equation that required one extra parameter; the gamma model failed to accurately estimate the last observation that had a fifteen year gap between the second last and last field measurement. This is a concern considering the last observation provides important information on the nature of the vegetation change over the last fifteen years of the dataset. To improve the predictive capacity of the model, it may be necessary to replace the logistic or gamma equation in [6.1] and [6.2] with an alternative equation such as the Chapmen-Richards equation. The gamma equation was chosen for this study as it complements the forest hydrology model described in Chapter four but an alternative forest hydrology model with a first derivative of the Chapman-Richards equation may be used to represent the decadal streamflow trend. The three parameter Chapman-Richards equation may be more effective at fitting the last observation accurately as it is commonly used in forest inventory modelling in Australia, and as the first derivative has a similar shaped to the gamma equation it may also prove useful in forest hydrology modelling.

6.4. Conclusion

Mixed effects models with their flexible variance-covariance structure have shown to be appealing for the analysis of permanent plot data of forest stand attributes. For each catchment, the random effects estimated the between plot variability in stand volume whilst the fixed coefficients defined a common fixed functional structure. The methodology overcame limitations present in traditional regression analysis by modelling the nested source of variability in permanent plot data with a variance-covariance structure. To address the basic distributional assumptions within the modelling framework, a power variance function adjusted the variance-covariance structure whereas autocorrelation was accounted for indirectly with random effects coefficients.

Using both the logistic and gamma equations, mixed effects models provided a far more superior fit of stand volumes than their fixed-effects counterpart. The fitted values in the mixed effects models and the large variation among the random coefficients confirm the adequacy of random effects at representing the highly polymorphic nature of the heterogeneous native forest environment. Although most catchments had an adequate plot sample size relative to the complexity of the corresponding model structure, the small sample size at Black Spur 2 and 3 raise uncertainty.

The predictive models are extrapolated over the catchments in chapter eight by using LiDAR indices to predict the value of the random coefficients at unsampled locations. It is evident in this chapter that the predictive capacity of the mixed effects model is much greater than that of a fixed effects model with LiDAR indices explaining the random component. This suggests the need to improve the spatial characterisation of LiDAR indices in chapter five to improve the predictive capacity of the forest growth models.

The next chapter will use hydrological time series to formulate a climate filter that removes climatic variance from the streamflow data in order to identify the trend due to forest regeneration processes. Chapter eight will then use the models developed in

this chapter to produce lumped catchment-scale forest growth curves to explain the decadal streamflow trends identified by the hydrology model.

Chapter 7: Evaluation of the climate filter and model structure

7.1. Introduction

For the forest growth models of the previous chapter to identify decadal streamflow trends, a climate filter needs to distinguish random climatic fluctuations that lie within the natural variability range of streamflow from decadal trends due to forest growth. Using the climate filter model structure presented in section 4.3.1, the formulation of the optimal climate filter using aggregated rainfall data is undertaken. The aim is to reduce the overall residual standard error of the climate filter in order to extract the magnitude and duration of streamflow trend with the greatest level of confidence, as this improves the forest growth models ability to explain the decadal streamflow trend. To determine how effective the climate filter is at removing climate variation in streamflow, a simulation exercise is undertaken to determine:

- how the climate filter parameter inference is affected by data availability of the hydrological time series, and;
- how substantial a post-disturbance decadal streamflow trend needs to be for the model structure to accurately identify it.

7.2. Methods

7.2.1. Climate filter

Section 4.5.1 provides a detailed overview of the methodology undertaken to generate a climate filter. In summary, a large array of independent variables derived from aggregated rainfall data are used to identify the most effective linear regression for explaining the rainfall induced streamflow variance using the equation:

$$Q_T = a + \sum_{i=1}^{m} B_i P_{i,T} + \sum_{j=1}^{n} Ant_j P_{j,T} + \varepsilon_T \qquad [7.1]$$

where all symbols are the same as equation 4.2.

7.2.2. Simulation experiments

Following Kuczera (1987), the model structure simultaneously estimates the climate and forest water use trend parameters, and with this approach the only assumption

necessary for the model to detect a trend in streamflow data is that the treatment effect under investigation needs to be "substantial enough" for it to represent the predominant post-disturbance decadal trend. To determine how substantial a trend needs to be for it to be detected, a set of experiments using synthetic data were undertaken that varied; the nature of the gamma function trend, the amount of unexplained climatic variation, and data length. The following exercises aim to determine the methodological limitations of the modelling procedure considering the nature of the available hydrological time series described in section 4.5.

7.2.2.1. Synthetic data analysis (experiment 1)

Generating synthetic data using rainfall data

To assess the model's ability at identifying a decadal streamflow trend, it was necessary to generate synthetic data with the following three steps. Firstly, the most optimal climate filter, generated using the methodology in section 4.3.1, and corresponding parameter estimates were used with the corresponding model's original rainfall data to generate synthetic streamflow for each catchment. As the resulting streamflow dataset was perfectly explained with the climate filter, the second step involved adding synthetic noise generated using a normal distribution with a known standard deviation, defined as:

$$\frac{1}{\sqrt{2\pi\sigma^2}} e \frac{-(x-\mu)^2}{2\sigma^2} \qquad [7.2]$$

where μ is the mean and σ is the standard deviation. White noise with σ of 40 mm, 70 mm, and 100 mm was used in the simulation exercise. Finally, to evaluate how well the model structure can recover a known trend based on a given residual standard error, a gamma function with known parameter values was subtracted from the synthetic streamflow dataset. Once the synthetic data was generated, the objective of the exercise was to evaluate how well a generalised nonlinear model structure is able to distinguish rainfall induced climatic fluctuations in the streamflow data from a decadal trend due to regenerating forests. The parameter values were extracted using a Maximum Likelihood (ML) method, which infers the best parameter estimate by identifying the value most likely to have given rise to the particular set of observations.

A range of synthetic gamma function trends were applied to determine how substantial a trend needs to be for the modelling procedure to correctly recover the parameter values. Figure 7.1(a) illustrates how the parameter values for the gamma function in equation 4.4 have been varied with; the extent to which streamflow was reduced (*Lmax*), and the age at which forest water use peaked (*1/K*). Figure 7.1(a) shows that the magnitude in streamflow reduction, *Lmax*, was reduced by 22 different amounts ranging from 60 mm to 500 mm at 20 mm increments. The parameter $Tmax_{sf}$ varied at 5 year increments from 10 years through to 60 years after trend onset, but only $Tmax_{sf}$ of 10, 30 and 60 is illustrated.

As shown in figure 7.1(b), the length of the dataset was also varied to determine the limitations of the model structure when data is only available during periods when the streamflow trend is at a particular phase. Varying the dataset's length involved limiting the length of the data as well as the time when data collection began in relation to the onset of the Gamma trend. The data length varied from 10 years through to 100 years at 10 year increments. For each of these data lengths the time when data collection began relative to trend onset varied from 0 years through to 50 years at 5 year increments. Figure 7.1(b) illustrates an example where for the same set of trends presented in figure 7.1(a) there is only 40 years of data used in the simulation and the dataset begins 20 years after trend onset. Finally, synthetic data was also generated with a calibration period of 10 years prior to trend onset to compare parameter inference with and without a calibration phase.

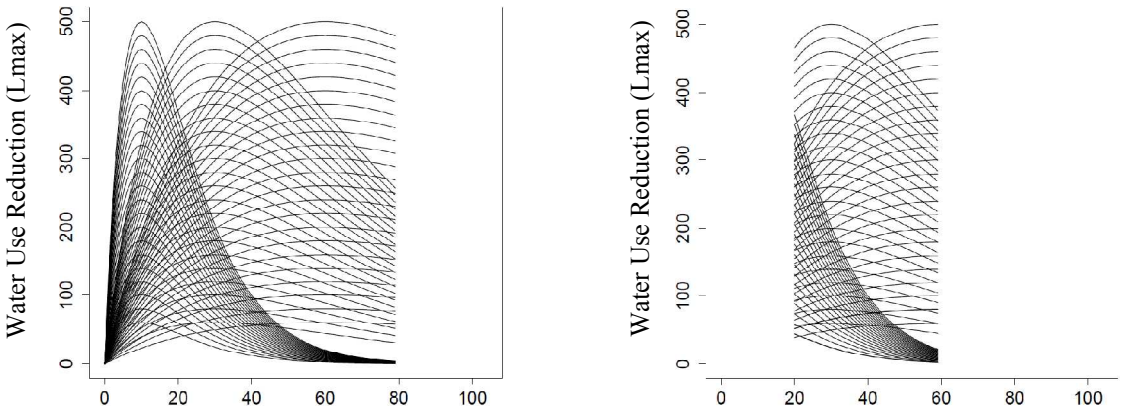

Figure 7.1: (a) Illustration of a set of simulated gamma functions with the timing of the forest water use peak ($Tmax_{sf}$) consisting of three different parameter values and the magnitude of the peak (*Lmax*)

consisting of the whole array of parameter values tested, whereas **(b)** uses the same gamma function but the length of the dataset is reduced to 40 years of data and begins 20 years after trend onset.

Generating synthetic data using control catchment data

Synthetic data was also generated by subtracting a whole array of gamma functions from control catchment streamflow datasets, Myrtle 1 and Slip, and then reducing the dataset extent to reflect the age of the following Maroondah regenerating catchments: Picaninny, Myrtle 2, Ettercon 3 and Black Spur 2. The optimal climate filter was then used on the synthetic streamflow data to evaluate how much decadal trend needs to exist at the treated catchments for the climate filter and overall model structure to accurately recover the *Lmax* and $Tmax_{sf}$ parameter values.

To address the fact that the treated catchments in this study generally consisted of a very short data length, two assumptions were added to the model structure to determine how much they improve parameter inference; an estimate of pre-trend streamflow at the time of trend onset was made, and an estimate of post-recovery streamflow 250 year after trend onset was made. In effect, the assumptions assumed a rainfall-runoff relationship is known when streamflow is at a quasi-hydrological equilibrium and the catchment consists of old-growth forest. Picaninny and Myrtle 2 already included pre-trend streamflow data, which was used to estimate post-recovery streamflow. In cases when the treated catchments did not contain pre-trend and post-recovery streamflow, estimates were derived from control catchment datasets. Parameter inference was compared with and without the added model assumptions.

7.2.2.2. Monte Carlo simulation (experiment 2)

In generating synthetic streamflow data from rainfall data (i.e. first part of experiment 1), only one realisation out of the myriad of possible random samples of white noise was used for each of the three σ parameters; 40 mm, 70 mm, and 100 mm. It needs to be recognised that the resulting parameter estimates would behave differently with a new realisation of white noise drawn from a normal distribution of the same σ value. For this reason, a Monte Carlo (MC) experiment with a sample distribution of 1000 simulations containing varied white noise with the same σ value was applied to one gamma curve containing *Lmax* and $Tmax_{sf}$ values of 500 mm and 30 years respectively. In the results, the *Lmax* and $Tmax_{sf}$ parameter estimates of the

1000 simulations were presented in a form of a histogram. The parameter estimates generated in experiment 1 where identified in the histogram to determine how representative the random sample of white noise in experiment 1 was when compared to the overall sample distribution. Presenting experiment 2 results in such a way helped interpret experiment 1 results.

As a result of the central limit theorem, it would be expected that with a "sufficiently" large number of observations in the dataset, the sample distribution should be normal with the mean located at the actual *Lmax* or $Tmax_{sf}$ parameter value. On the other hand, an insufficient number of observations may result in a biased estimate and for this reason the sample distribution provides insight into how many observations are necessary for an unbiased maximum likelihood (ML) estimate.

7.2.2.3. Markov Chain Monte Carlo simulation (experiment 3)

The final exercise in this chapter involves a Markov Chain Monte Carlo (MCMC) simulation to estimate posterior distributions of both *Lmax* and $Tmax_{sf}$ using synthetic data with white noise identical to that used to evaluate the whole array of gamma curves in experiment 1. The purpose of this exercise is to produce the true posterior distribution using MCMC, which is contrary to the ML procedure that produces a linear approximation of the posterior distribution in experiments 1 and 2. The underlying theory of MCMC is based on the fact that it is possible to express complex integrals as an expectation of some distribution, and an estimate of this expectation may be made by drawing samples from that distribution. MCMC provides parameter estimates of marginal distributions by drawing samples from the high-dimensional parameter space of the model's joint distribution. Gibbs Sampling, one of several available MCMC methods, was applied using the open source software Winbugs (Lunn *et al*., 2000). A desirable feature of Gibbs sampling is that it can be applied automatically as it has no free parameters.

The procedure initialises a random walk with a crude parameter estimate from a range of possible parameter values within a state space. The first section of the random walk, called the burn-in period, is discarded as initialisation involves an arbitrary value not representative of the target distribution, $p(\theta|y)$. Beginning from

the initial state, a Markov chain is generated with a correlated sequence of states using a transition operator to move between sample values by only considering the previous sample values, θ^{t-1}, when randomly generating the next sample value, θ^{t}. Gibbs sample uses a combined transition operator to sample from the parameter space by calculating a multivariate distribution and successively drawing each dimension from the conditional distribution of that variable conditioned on all other variables (Murray, 2007). In effect, the procedure undertakes Bayesian inference as it uses probability theory to address uncertainty when calculating the marginal likelihoods.

As the Markov chain grows, the approximate distribution is improved at each step in the simulation and an equilibrium distribution is reached when the consecutive states are assumed to be drawn from $p(\theta|y)$. Just as finding a fair sample from a population is important in field surveys, the Markov chain needs to sample correctly from a potentially high-dimensional parameter space. For this to be possible the transition operator that influences the Markov chain dynamics needs to satisfy an invariant distribution, which holds if the Markov chain is irreducible, aperiodic and not transient (Murray, 2007). The chain sequence is irreducible if it is possible to visit any part of the target distribution from any other part of the target distribution in a finite number of steps. Aperiodicity holds if no states are only accessible at certain regularly spaced time intervals. Finally, the transition operator, T, is not transient if all subsequent steps of the chain will have the same marginal distribution, in which chase T is said to leave $p(\theta|y)$ stationary.

To provide supporting evidence that the model has converged at $p(\theta|y)$, three runs of the Markov chain were undertaken with initialisation values arbitrarily varying. Each chain is represented with 50,000 iterations and only the last 10,000 iterations were used for inference. Once all three traces of the chains were visually inspected to make sure the last 10,000 iterations represented the same target space, the Bayesian inference was presented in the form of posterior density estimates.

7.3. Results

7.3.1. Climate filter

Compared to most forest hydrological studies, the present study sites consist of an unusually dense collection of rain gauges within a very close proximity to the small catchments. The density of rain gauges was such that no interpolation was necessary. The climate filter was formulated using streamflow data from two old-growth control catchments, Slip and Myrtle 1, as both catchments had no decadal streamflow trend due to forest regeneration. Given the proximity of the 13 Coranderrk rain stations and 18 North Maroondah rain stations to the control catchments Slip and Myrtle 1 respectively (figure 4.4), all rain stations were evaluated to determine how well each station regressed against the corresponding streamflow data.

For each of the corresponding streamflow and rainfall gauges, monthly data values were aggregated using equation 4.2. By coupling the explanatory variables from water year *T* with those of the antecedent water year *T-1*, a total of 2,035 models were constructed each of which had between 3 and 5 explanatory variables. As there were 12 possible months that the water year may begin with, a total of 24,420 models were tested using the standard error of residuals to identify the optimal model. The computational procedure was automated in R (R Development Core Team, 2009).

Tables 7.1 and 7.2 contain results for the modelled coefficient values and residual standard errors for Myrtle 1 and Slip catchments respectively, using;

- the water year and aggregated rainfall data used by Kuczera (1987)
- equation 4.2 with *m* and *n* equalling 2 and 1 respectively to apply a model structure comparable with Kuczera (1987)
- equation 4.2 with a model structure consisting of a maximum of five parameters

It is evident for both catchments, equation 4.2 with the optimal three parameter climate filter reduced the residual standard error when compared to the original model used by Kuczera (1987), and equation 4.2 with the optimal five parameter model structure explained climatic variation most effectively. Considering each rain

station tested 24,420 models, it is worth noting for both catchments, different rain stations resulted in similar data aggregation methods to formulate the optimal model structure. For example, the optimal five parameter model structure for rain stations 7 and 14 at Myrtle 1 have very similar independent variables, as is the case for rain stations 4 and 5 but to a lesser extent. At Slip catchment, an identical model structure was identified for rain stations 9 and 10. These similarities could be attributed to the similar rainfall time series resulting from the close geographic proximity of the rain stations to the stream gauges; which supports the use of using point location rainfall data without the need to create spatiotemporal rainfall maps for the region.

At Slip catchment, a comparison of the five parameter models for the five listed rain stations provides evidence that the aggregation of the antecedent water year is consistent with; independent variable *Ant1* always ending in January or February, and *Ant2* always ending in September or August. This indicates that Slip catchment's water storage due to the previous year's winter and spring rainfall (largely represented in *Ant1*) will influence streamflow.

Table 7.3 provides the percentage by which the optimal models for both Myrtle 1 and Slip catchment improved the climate filter used by Kuczera (1985). The most optimal climate filter explained 23% and 45% of the climatic component of the streamflow variance that the original model failed to account for in Myrtle 1 and Slip catchments respectively.

Table 7.1: Climate Filter Models for Myrtle 1 Catchment

	Water Year	Rain Station [Elevation]	Residual Std Err (mm)	df	Intercept	Independent Variables				
						B1	B2	B3	Ant1	Ant2
Original Model	MAY-APR	7 [749 m]	92.32	35	(-122.42 ± 86.56)	MAY-DEC (0.42 ± 0.07)	JAN-APR (-0.04 ± 0.15)		APR-DEC (0.59 ± 0.12)	
Optimal 3 parameter model	SEP-AUG	7 [749 m]	84.23	35	(-110.21 ± 93.95)	SEP-APR (0.47 ± 0.08)	MAY-AUG (-0.03 ± 0.1)		AUG-OCT (0.26 ± 0.06)	
Optimal models for 5 rain gauges with the longest time series	JUL-JUN	5 [765 m]	71.34	35	(-265.27 ± 92.91)	JUL-OCT (0.57 ± 0.07)	NOV-FEB (0.25 ± 0.08)	MAR-JUN (-0.1 ± 0.1)	JUN-DEC (0.46 ± 0.07)	NOV-SEP (0.16 ± 0.1)
	JUN-MAY	4 [805 m]	72.02	35	(-384.2 ± 100.39)	JUN-OCT (0.58 ± 0.07)	NOV-FEB (0.18 ± 0.08)	MAR-MAY (-0.19 ± 0.12)	MAY-JAN (0.58 ± 0.09)	DEC-JUL (0.16 ± 0.05)
	OCT-SEP	10 [526 m]	77.39	33	(-83.89 ± 103.76)	OCT-FEB (0.6 ± 0.1)	MAR-MAY (0.08 ± 0.14)	JUN-SEP (0.26 ± 0.09)	SEP-MAY (0.07 ± 0.1)	APR-DEC (0.34 ± 0.11)
	SEP-AUG	7 [749 m]	81.97	35	(-111.53 ± 93.07)	SEP-OCT (0.69 ± 0.16)	NOV-APR (0.37 ± 0.09)	MAY-AUG (-0.02 ± 0.1)	AUG-SEP (0.22 ± 0.06)	
	SEP-AUG	14 [467 m]	82.68	33	(-242.39 ± 117.7)	SEP-OCT (0.72 ± 0.16)	NOV-APR (0.4 ± 0.09)	MAY-AUG (0.12 ± 0.11)	AUG-OCT (0.27 ± 0.07)	

Note: The coefficient values for each of the parameters in the final models are associated with the standard error of the residuals within the brackets.

Table 7.2: Climate Filter Models for Slip Catchment

	Water Year	Rain Station [Elevation]	Residual Std Err (mm)	df	Intercept	Independent Variables				
						B1	B2	B3	Ant1	Ant2
Original Model	MAY-APR	9 [443 m]	63.72	27	(-603.07 ± 105.9)	MAY-DEC (0.54 ± 0.06)	JAN-APR (0.08 ± 0.12)	APR-DEC (0.68 ± 0.1)		
Optimal 3 parameter model	JUN-MAY	9 [443 m]	52.72	28	(-384.44 ± 85.74)	JUN-FEB (0.49 ± 0.05)	MAR-MAY (-0.29 ± 0.1)	MAY-JAN (0.58 ± 0.08)		
Optimal models for 5 rain gauges with the longest time series	AUG-JUL	11 [658 m]	35.33	32	(-559.54 ± 55.13)	AUG-FEB (0.52 ± 0.03)	MAR-MAY (-0.05 ± 0.06)	JUN-JUL (0.33 ± 0.07)	JUL-JAN (0.41 ± 0.04)	DEC_SEP (0.12 ± 0.04)
	AUG-JUL	5 [611 m]	39.73	33	(-505.65 ± 59.91)	AUG-SEP (0.74 ± 0.1)	OCT-FEB (0.49 ± 0.05)	MAR-JUL (0.09 ± 0.05)	JUL-FEB (0.41 ± 0.04)	JAN_AUG (0.1 ± 0.04)
	JUN-MAY	10 [240 m]	44.69	38	(-502.51 ± 57.94)	JUN-JUL (0.87 ± 0.1)	AUG-FEB (0.47 ± 0.04)	MAR-MAY (-0.22 ± 0.09)	MAY-JAN (0.61 ± 0.07)	DEC_AUG (0.17 ± 0.05)
	JUN-MAY	9 [443 m]	45.11	27	(-558.03 ± 101.8)	JUN-JUL (0.7 ± 0.09)	AUG-FEB (0.48 ± 0.04)	MAR-MAY (-0.24 ± 0.09)	MAY-JAN (0.6 ± 0.07)	DEC_AUG (0.13 ± 0.05)
	MAY-APR	13 [410 m]	50.53	28	(-501.59 ± 65.99)	MAY-FEB (0.55 ± 0.04)	MAR-APR (-0.37 ± 0.16)		APR-JAN (0.74 ± 0.1)	DEC_SEP (0.23 ± 0.07)

Note: The coefficient values for each of the parameters in the final models are associated with the standard error of the residuals within the brackets.

Table 7.3: Improvements in the standard error of residuals when compared to the climate filter used by Kuczera (1987)

	Optimal Three Parameter Model	Same Rain Station Optimal 5 Parameter Model	Overall Optimal Model (not same rain station)
Myrtle 1 Original Model (92.32 mm)	9 % reduction (84.23 mm)	11 % reduction (81.97 mm)	23 % reduction (71.34 mm)
Slip Original Model (63.72 mm)	17% reduction (52.72 mm)	29 % reduction (45.11 mm)	45 % reduction (35.33 mm)

Note: The standard error of the model is provided in the brackets

7.3.2. Simulation experiments

The following results illustrate the model's ability at identifying a decadal trend in streamflow when; magnitude of the peak (*Lmax*), timing of the peak ($Tmax_{sf}$), data length, data range, pre-trend calibration period, and climate standard deviation (σ) are synthetically altered. To help interpret figures, the following is an explanation:

- Experiment 1: Grey scaled line/point plots (e.g. top row of figure 7.2) provide a relative assessment of how the gamma curve parameter estimates vary for the whole array of *Lmax* and $Tmax_{sf}$ values tested using one realisation of white noise with a known σ. The plots include three rows of values aligned with the $Tmax_{sf}$ axis (in a box above the figure) and provide information on the minimum, maximum, and total number of *Lmax* values converged for each $Tmax_{sf}$ value.
- Experiment 2: Frequency histograms of a sample distribution (e.g. middle row of figure 7.3) represent 1000 datasets, each with a unique white noise and the same gamma curve containing *Lmax* and $Tmax_{sf}$ values of 500 mm and 30 years respectively. The blue line in the histograms locates the actual parameter value used in the datasets, whereas a red line locates the parameter estimate for the dataset with white noise identical to experiment 1.
- Experiment 3: Posterior distribution curves from the MCMC simulation (e.g. bottom row of figure 7.2) are colour coded and provide an accurate inference of the parameter estimates for datasets with $Tmax_{sf}$ of 10, 30 or 60 years, and *Lmax* of 100, 200, 300, 400, and 500 mm. Only posterior distributions with a standard error half of the datasets actual parameter values are presented to improve interpretability of the results; otherwise the figures were too

cluttered for interpretation. The white noise used in experiment 3 is identical to datasets used to experiment 1.

7.3.2.1. Influence of unexplained climatic variation on parameter inference

Figure 7.2, 7.3 and 7.4 evaluate the model's ability at extracting gamma curve parameter estimates when σ is set as; 40, 70 and 100 mm. The data extent represents 80 years of data that begins at trend onset and is illustrated in Figure 7.1(a). In generating datasets with pre-determined σ, random noise was sampled using a normal distribution on 80 observations (i.e. data length) so the dataset's σ is not exactly the assigned σ value. The point/line plots (from here in referred to as point plots) in figure 7.2 demonstrate there is very little variation in the residual standard errors between the different gamma curves simulated as the ML estimates are consistently reflective the dataset's σ value, which is approximately; 40.4, 64, and 110.7 mm. For each sigma value in the point plots, the different behaviour in the residual standard errors is due to the nature of the random sample for each σ value and should not be interpreted otherwise. The posterior distributions in figure 7.2 illustrate that with an increase in σ, the distribution range of the residual standard errors widens.

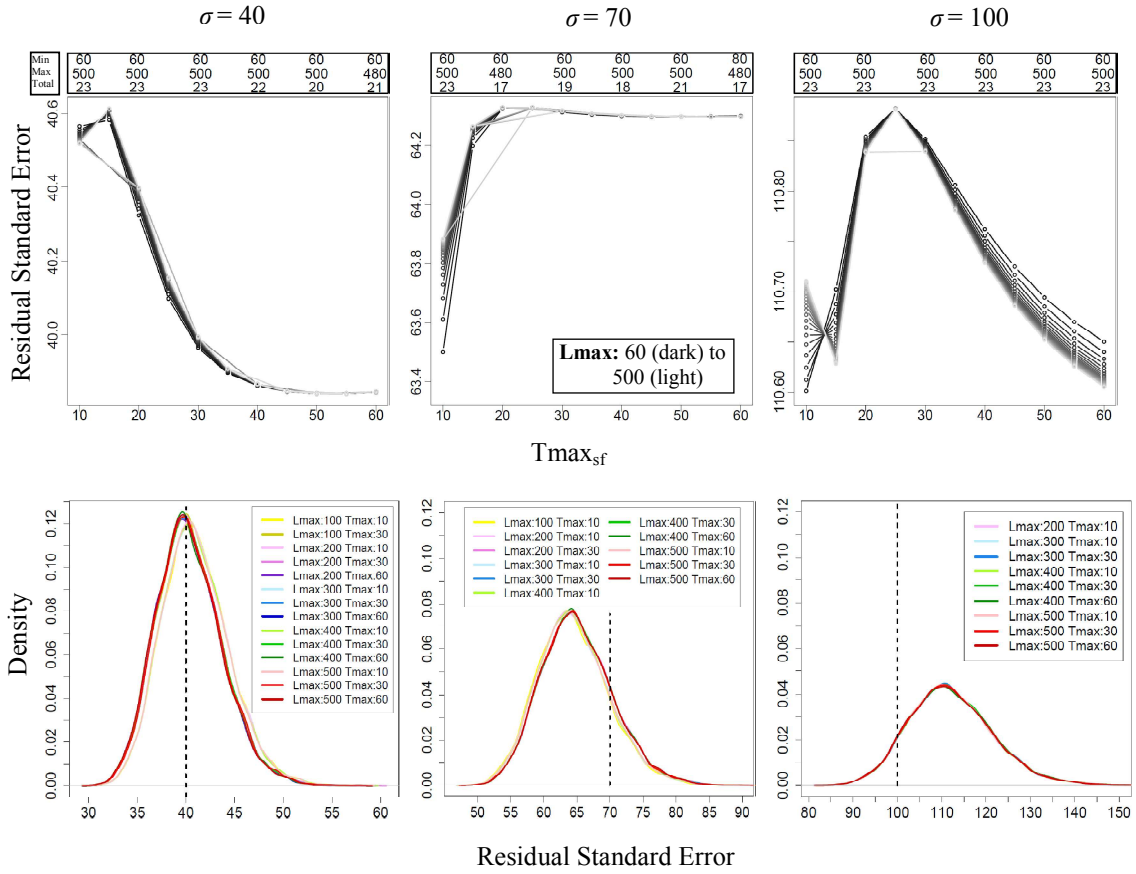

Figure 7.2: Residual standard errors using 80 years of synthetic data with varying *Lmax*, $Tmax_{sf}$, and σ values. The shades of grey in the plotted points represent the range of *Lmax* values tested, whereas the x-axis represents the range of $Tmax_{sf}$ values tested. MCMC posterior distributions of the residual standard error are also provided.

Figure 7.3 shows that reducing the dataset's σ value improves the predictive accuracy of $Tmax_{sf}$. This is evident as the distribution range of the frequency histograms and the standard error in the posterior distribution curves both increase with σ. The posterior distribution curves show that the standard error for $Tmax_{sf}$ estimates increase as the streamflow trend become more subtle with a lower *Lmax* and a higher $Tmax_{sf}$ value. It is evident that as the ratio of *Lmax* and σ decreases the noise makes it harder to infer the trend.

The posterior distributions also show that as *Lmax* decreases, the ML estimate (mean) becomes less accurate and this is a result of the nature of the random sample. As the frequency histograms resemble a normal distribution, the error is not a result of bias due to sample size in the streamflow observations. The histograms suggest

that 80 observations provide an adequate data length for an unbiased ML estimate for a dataset with *Lmax* of 500 and $Tmax_{sf}$ of 30.

For any given σ, the point plots include a purple line to represent a perfect fit and show that increasing the datasets *Lmax* value improves $Tmax_{sf}$ predictions. This result is consistent for all gamma curves throughout the chapter. $Tmax_{sf}$ estimates are relatively similar and accurate when *Lmax* is approximately greater than two times the σ value, whereas results deteriorate rapidly once *Lmax* approaches the magnitude of σ. Increasing the $Tmax_{sf}$ value of the dataset in effect reduces the dataset's recovery period after year $Tmax_{sf}$, which may explain why $Tmax_{sf}$ predictions and standard errors deteriorate with increased $Tmax_{sf}$.

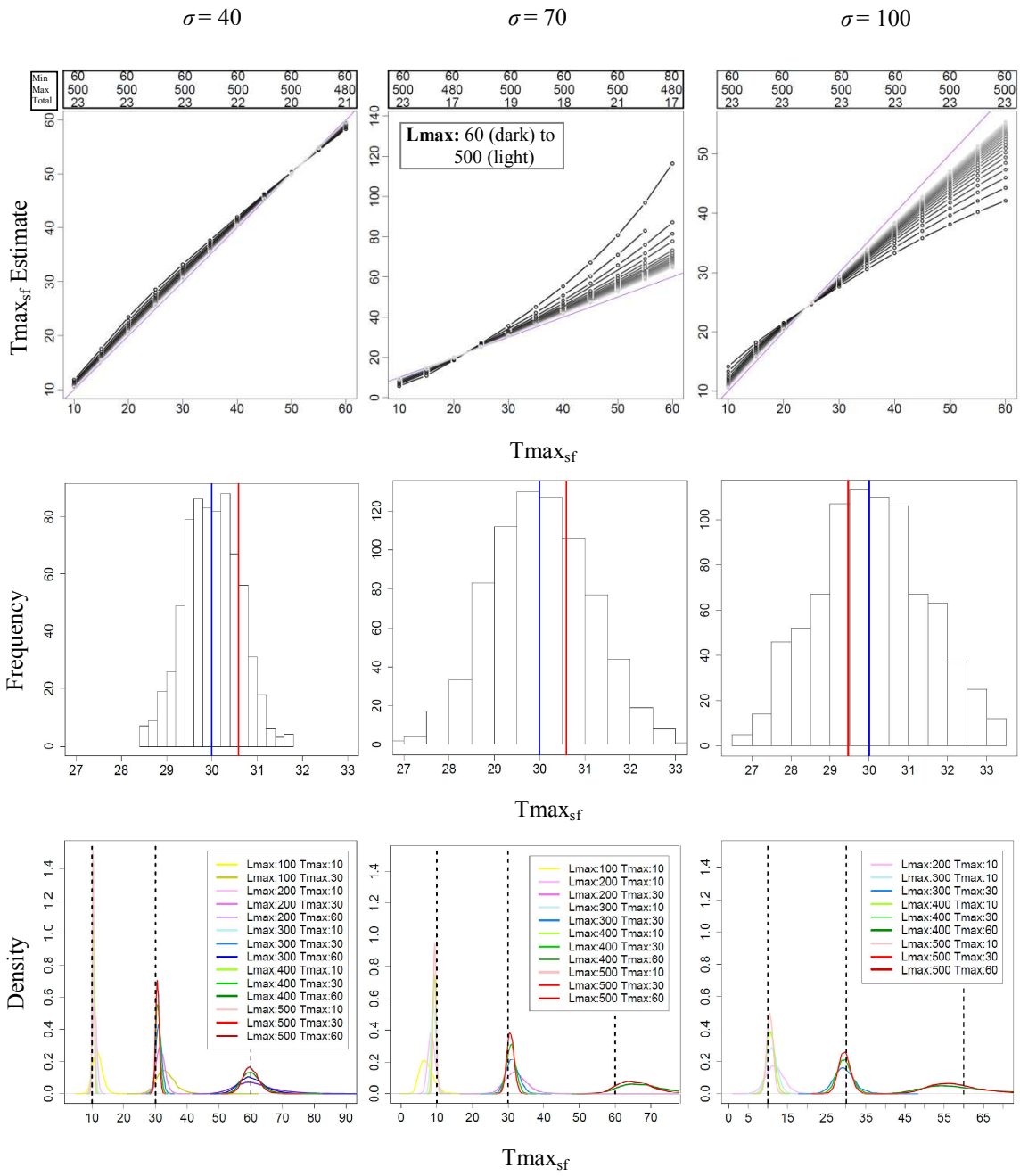

Figure 7.3: Point plots of *Tmax$_{sf}$* estimates for the whole array of gamma curves using 80 years of data that begin at trend onset (Experiment 1). Histograms represent *Tmax$_{sf}$* estimates for 1000 datasets, all of which were generated with unique realisations of white noise and a gamma curve containing *Lmax* and *Tmax$_{sf}$* values of 500 mm and 30 years, respectively (Experiment 2). Posterior distribution curves provide the standard errors associated with the estimates for a range of gamma curves (Experiment 3).

Using the same synthetic data, figure 7.4 provides results for *Lmax* estimates. Although the point plots suggest predictions are just as accurate when σ is 40 or 100 mm, it is evident from the red lines in the histograms that this is due to chance in the random samples. The histogram for σ of 40 mm shows that the white noise used to

represent the point plots (i.e. red line) overestimated *Lmax* significantly considering the distribution range of σ 40 mm, whereas the white noise representing σ of 100 was more conservative within its distribution range.

The posterior distributions suggest that for all *Lmax* values with a $Tmax_{sf}$ of 10 (i.e. lightest shade of each colour), the standard errors are approximately half of the datasets σ values. With an increase in the dataset's $Tmax_{sf}$ value, the *Lmax* standard errors gradually increase, and hence the expected value becomes less certain. This may be due to two reasons; firstly an increase in $Tmax_{sf}$ effectively reduces the dataset's recovery period after year $Tmax_{sf}$, and secondly increasing $Tmax_{sf}$ results in the streamflow trend being less pronounced, and hence more uncertain to identify. Finally, note that the errors in the expected maximum likelihood of *Lmax* (i.e. mean of the posterior distributions) reflects the nature of the white noise used in the datasets (experiment 1).

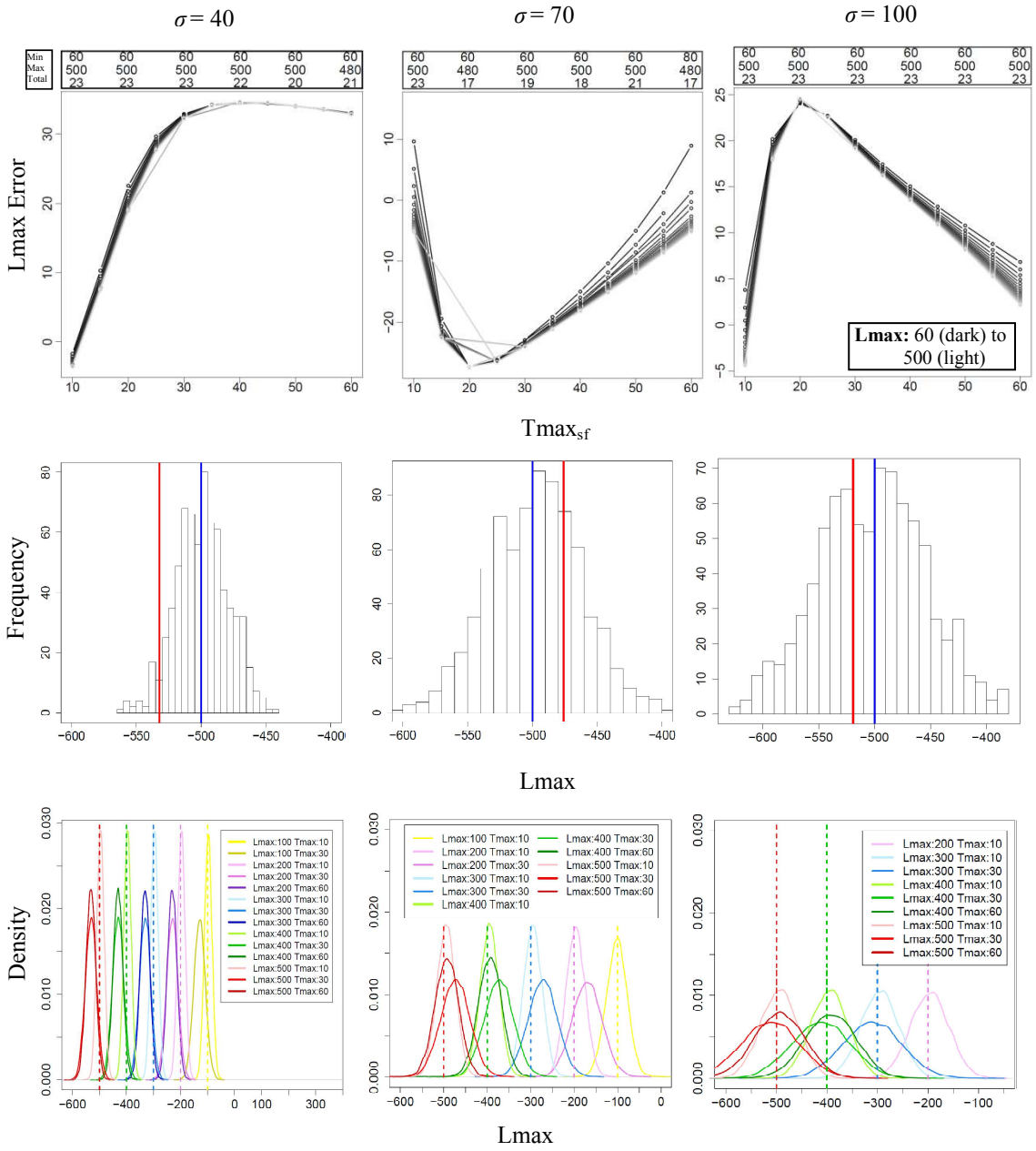

Figure 7.4: Point plots (Experiment 1), histograms (Experiment 2), and posterior distributions (Experiment 3) of *Lmax* estimates using the same datasets illustrated in figure 7.2 and 7.3.

7.3.2.2. Influence of data length on parameter inference

It has been demonstrated in the previous section that with a sufficiently long enough dataset, ML estimates produce asymptotically efficient standard errors. ML maximises the probability that the observed data are the result of a particular set of distributional parameters, and the procedure becomes increasingly difficult when it lacks a sufficient number of observations from which to derive information. Below, the data length is reduced to evaluate the extent to which ML estimates and standard

errors deteriorate as a result of data length. Figure 7.5 provides an illustration of the trends evaluated using 19, 39, and 59 years of data.

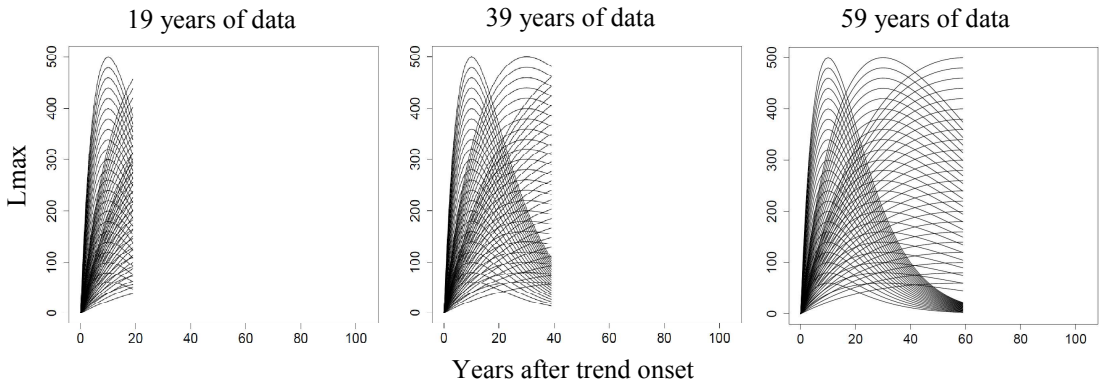

Figure 7.5: An example of trends evaluated using 19, 39, and 59 years of data. In the simulations, the parameter $Tmax_{sf}$ varied at 5 year increments from 10 years through to 60 years after trend onset but for clarity purposes, only three $Tmax_{sf}$ parameter values; 10 years, 30 years and 60 years are illustrated.

Using datasets with σ of 70 mm, results of $Tmax_{sf}$ estimates for each of the three data lengths are provided in figure 7.6. The point plots show that the shorter the dataset the more unstable the ML estimates of $Tmax_{sf}$. Datasets represented with minimal streamflow recovery phase after year $Tmax_{sf}$, or without the $Tmax_{sf}$ year in the data extent, result in convergence failure or erroneous parameter estimates. For this reason, datasets with smaller $Tmax_{sf}$ values require less data for the problem to be well posed, as the recovery phase of the gamma curve becomes established earlier. The posterior distributions and point plots suggest that 40 years of data may be adequate for circumstances when $Tmax_{sf}$ is 10.

The normality and the distribution range of the sample distributions in the histograms determine whether the data length is appropriate for solving the ML estimate efficiently. With the reduced data length, the skewed sample distribution of the $Tmax_{sf}$ parameter estimates suggests the ML problem is ill-posed for a 19 year long dataset with *Lmax* of 500 and $Tmax_{sf}$ of 30. The posterior distributions suggest that the 19 year long datasets with a $Tmax_{sf}$ of 10 are also ill-posed as the distribution range does not include the dataset's actual parameter value. It is evident that increasing the data length reduces the histograms distribution range, improves the

normality of the sample distribution, and the posterior distributions begin to include the actual parameter values.

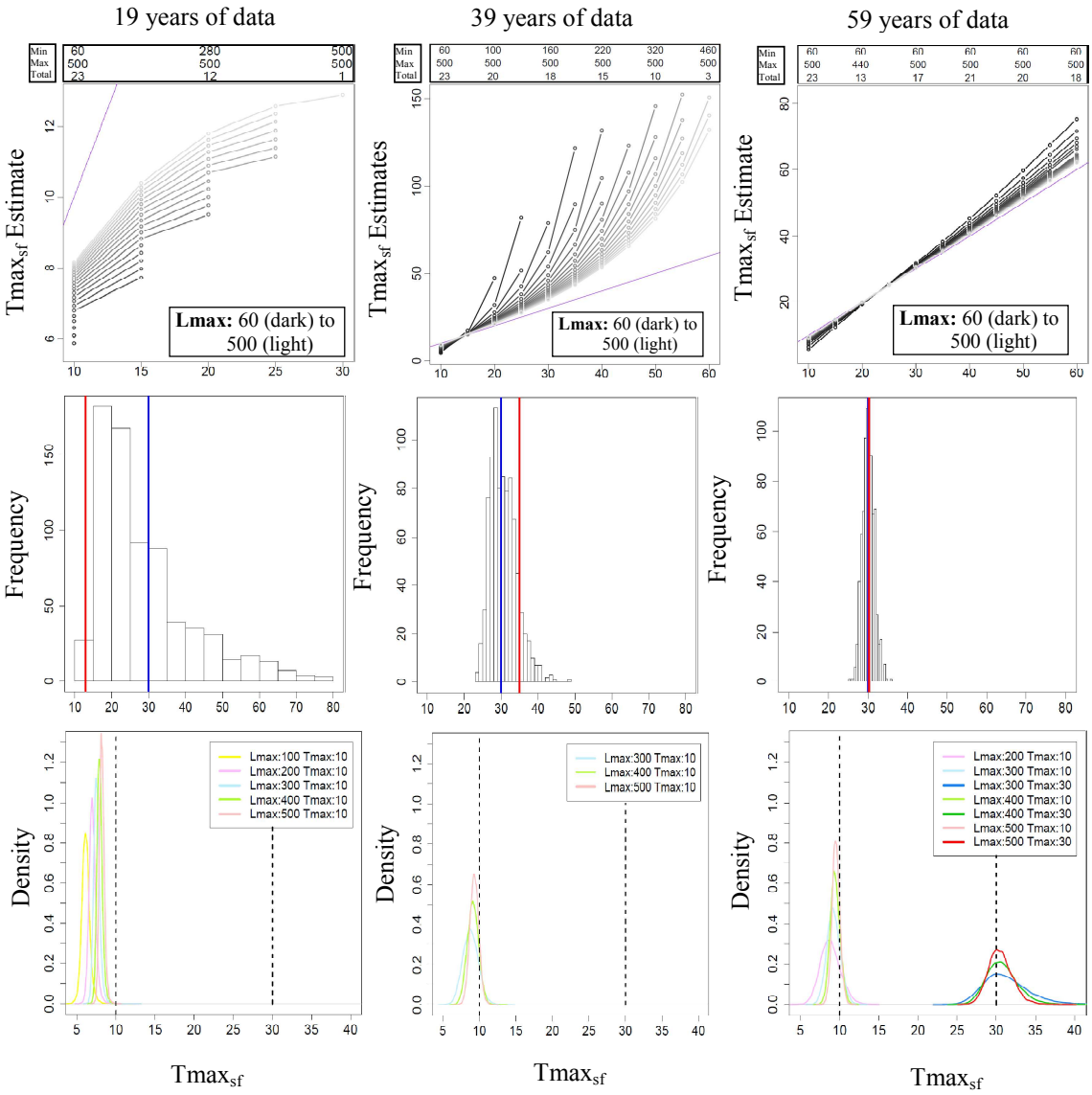

Figure 7.6: *Tmax$_{sf}$* parameter estimates for a 19, 39 and 59 year long dataset that begins at trend onset. All datasets have σ of 70 mm.

The *Lmax* estimates for each of the three data lengths are provided in figure 7.7. It is worth noting that the point plots (experiment 1) suggest the magnitude of *Lmax* error is reduced with an increase in data length; but the patterns in the changing ML estimates over the range of *Tmax$_{sf}$* values are largely driven by the nature of the random sample used to generate the datasets. Caution should be taken when interpreting the over- or under-estimation of *Lmax* in the point plots.

The skewed sample distributions and distribution range in the frequency histograms are similar to those observed in the $Tmax_{sf}$ estimates of Figure 7.6. The posterior distributions show that for a given $Tmax_{sf}$ value, the standard errors in *Lmax* estimates are consistent over the whole range of *Lmax* values evaluated.

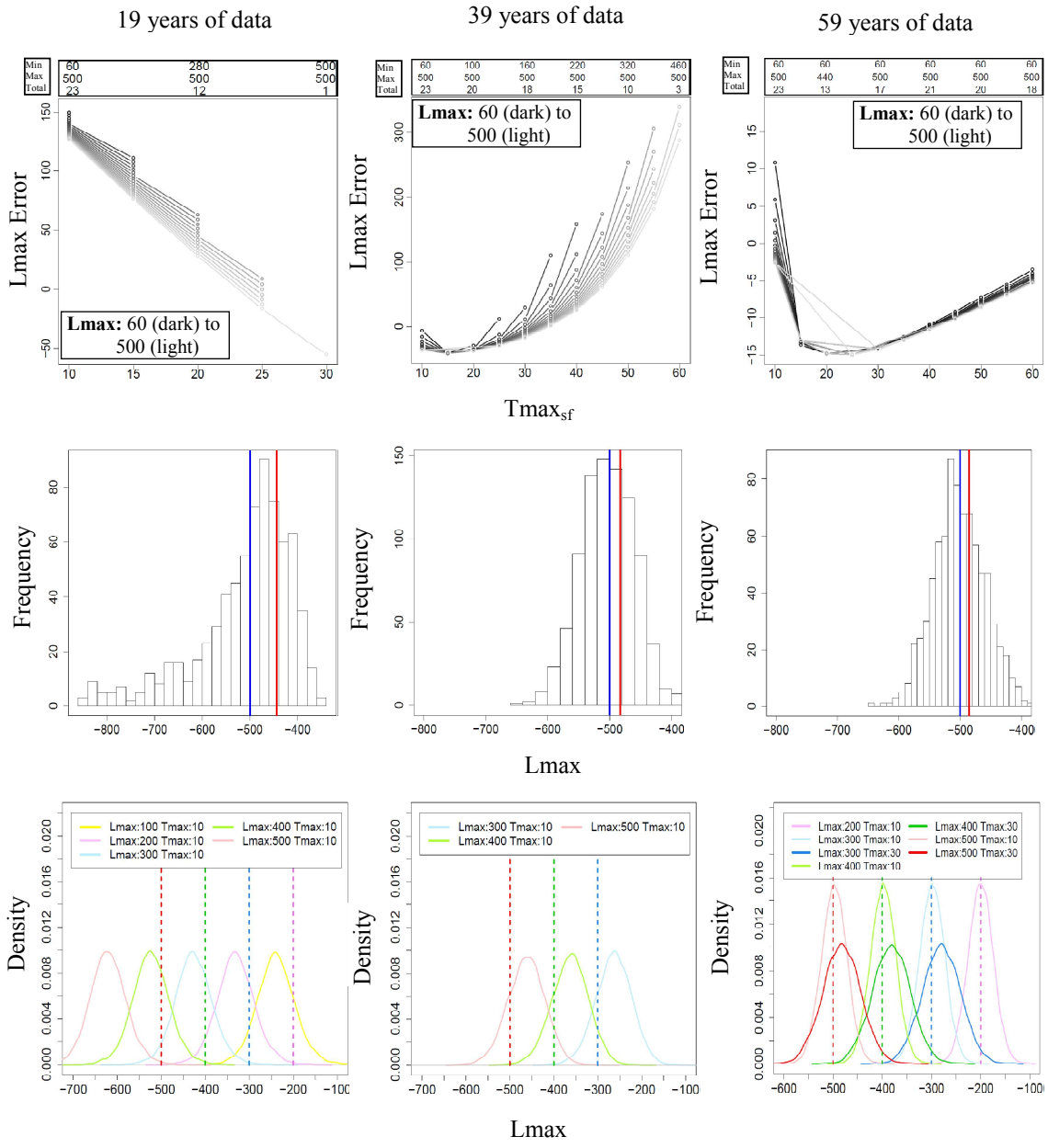

Figure 7.7: *Lmax* parameter estimates for a 19, 39 and 59 year long dataset that begins at trend onset. All datasets have σ of 70 mm.

7.3.2.3. Influence of data range on parameter inference

Figure 7.8 (a) and (b) respectively remove the first 10 and 20 years of data after trend onset from a 39 and 79 year long dataset, to evaluate the influence of data range on

parameter estimates. Figure 7.8 (a) may be compared to the 39 year long dataset in figure 7.6 to show that removing all data between trend onset and year $Tmax_{sf}$ increases the $Tmax_{sf}$ standard error. Datasets represented with $Tmax_{sf}$ of 10 in figure 8(a) begin with and include the year $Tmax_{sf}$ and for this reason, when compared to the same data length in figure 7.7, removing the first 10 years of data after trend onset has a negligible effect on the *Lmax* posterior distributions.

Figure 7.8(b) shows that removing 20 years of data immediately after trend onset from datasets with $Tmax_{sf}$ of 10, results in skewed *Lmax* posterior distributions with the model more likely to over-estimate *Lmax*. To determine whether these skewed results are a result of the Markov chains not converging at the target distribution, figure 7.8(c) traces the three Markov chains for a dataset with *Lmax* 300 and $Tmax_{sf}$ 10. The results show that all three traces have reached their equilibrium distribution to equally represent the skewed tail of the *Lmax* posterior distribution.

Overall, the results suggest datasets with a well represented recovery phase, that includes the "point of inflection" in the skewed tail end of the gamma function, are more likely well posed if the dataset does not include observations immediately after trend onset.

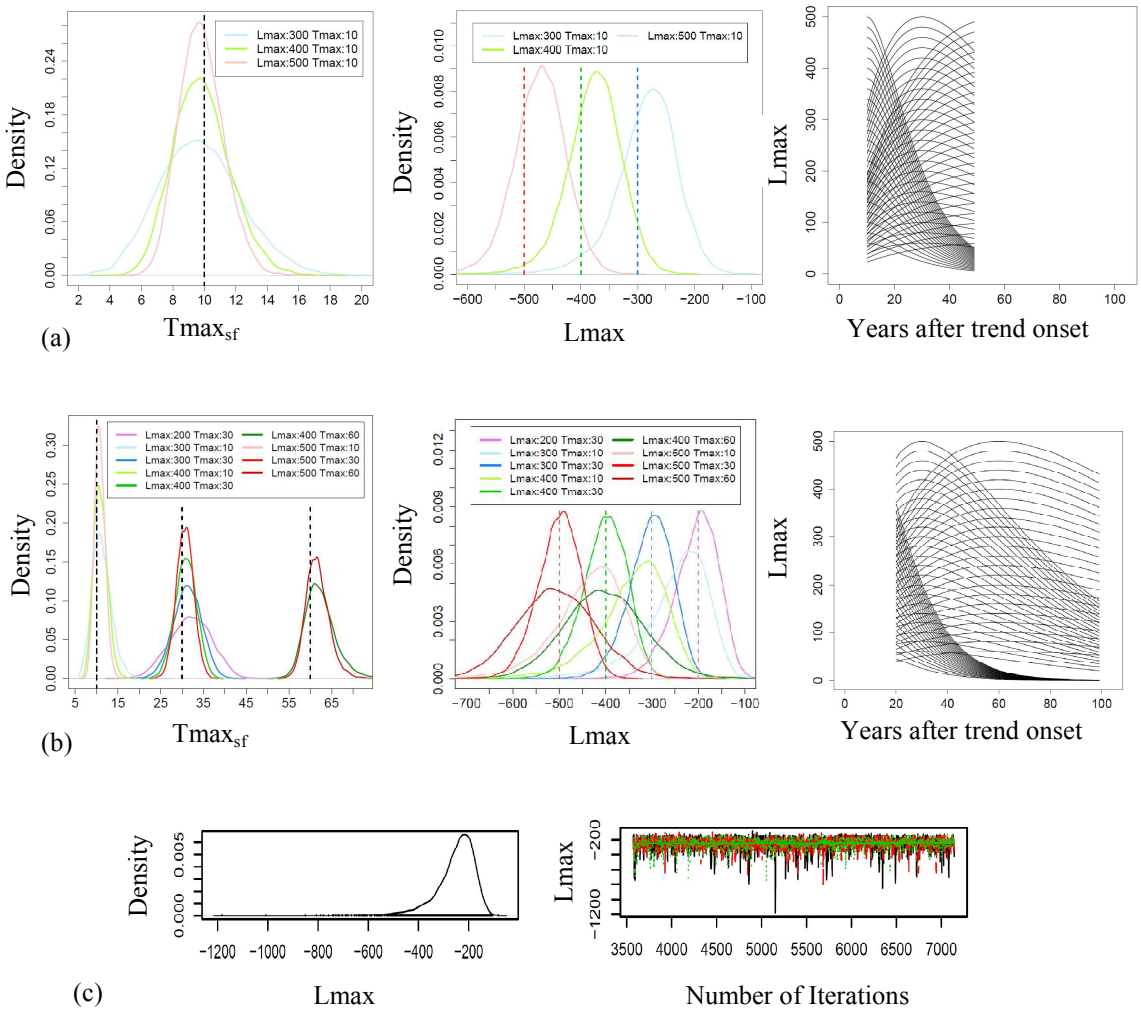

Figure 7.8: Parameter estimates for $Tmax_{sf}$ and *Lmax* when σ is 70 mm for: (a) 39 year long dataset begins 10 years after the trend onset; and (b) 79 year long dataset that begins 20 years after the trend onset; whereas (c) shows three Markov chains used to construct the posterior distribution for the 79 year long dataset with *Lmax* 300 and $Tmax_{sf}$ 10. Both datasets have σ of 70 mm.

7.3.2.4. Influence of calibration phase on parameter inference

To determine how a "calibration period" contributes towards a more accurate parameter inference, figure 7.9(a) and (b) are represented with identical 59 year long post-trend datasets but figure 7.9(b) also includes 10 extra years of data prior to trend onset. It is evident that 10 years of "calibration" data improves the posterior distributions of *Lmax* substantially whereas improvements to $Tmax_{sf}$ are negligible. This is expected as the calibration period provides extra information on the nature of the climatic variation in the dataset, which allows for the magnitude of the trend to become more certain.

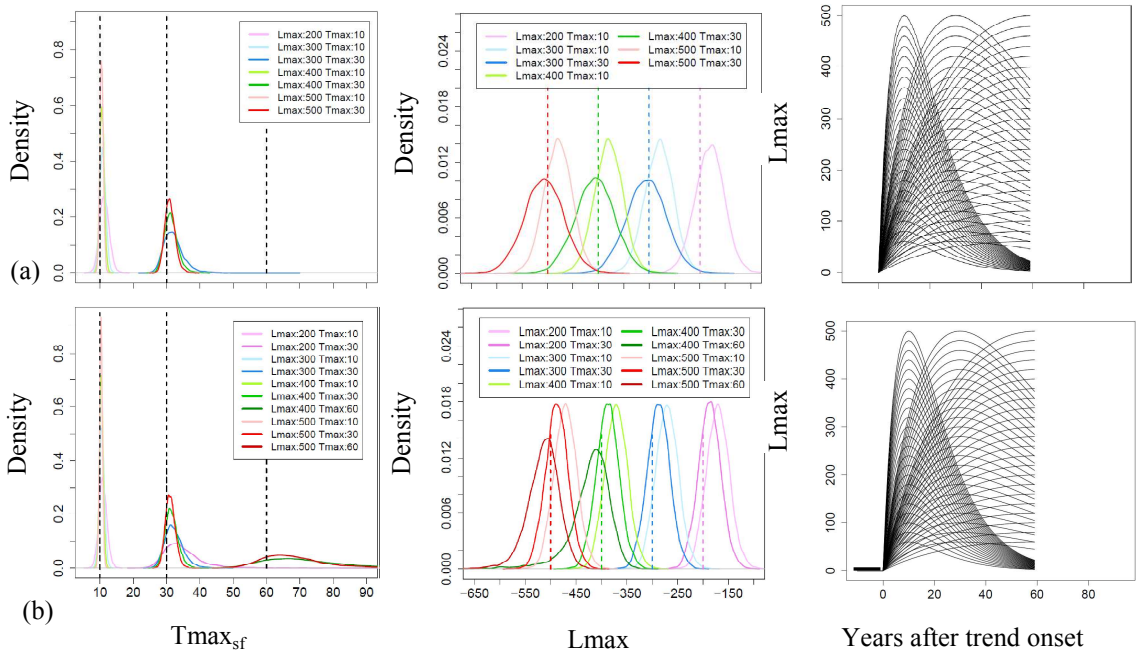

Figure 7.9: The effects of calibration data on the posterior distributions of $Tmax_{sf}$ and $Lmax$ for a 59 year long post-trend dataset. Both datasets have σ of 70 mm.

7.3.2.5. Influence of assumed pre-trend streamflow and post-trend recovery of streamflow on parameter inference

Figure 7.10(a) and (b) use datasets with thirty observations; 20-50 years and 50-80 years after trend onset, respectively, to evaluate the behaviour of the model structure with two added assumptions. The model assumes; one estimate of pre-trend old-growth streamflow at the time of trend onset, and one estimate of post-recovery streamflow 250 year after trend onset. In practice, such estimates are possible as: datasets with pre-trend streamflow observations may be used to assume post-recovery old-growth streamflow; whereas when treated catchments do not contain pre-trend and post-recovery streamflow observations, estimates may be derived from control catchment data. The added assumptions recognise that old-growth catchments are in a quasi-hydrological equilibrium (Kuczera, 1987).

Figure 7.10 provides posterior distributions for both $Lmax$ and $Tmax_{sf}$ to compare results when the model includes; only the pre-trend streamflow estimate and both the pre-trend and post-recovery streamflow estimate. Note that for both data lengths, there is a very broad range of phases in streamflow trend depending on the datasets $Lmax$ and $Tmax_{sf}$ value, and interpretation of the resulting posterior distributions

should consider the phase of the dataset in mind. The red dots in the trend line plots indicate which assumption was used for each row of posterior distribution curves.

It was evident for both sets of data, when neither of the assumptions are made, the problem was ill-posed and results were poor (not shown). Including a pre-trend streamflow estimate improves the inference for datasets containing high *Lmax* values (i.e. 500) if the datas*et al*so represents a substantial recovery phase of the trend, as shown in both figure 7.8(a) with $Tmax_{sf}$ of 10 and (b) with $Tmax_{sf}$ of 30. Incorporating the second assumption into the datasets improves the results much more effectively in both figure 7.8(a) and (b). For datasets with observations 20-50 years after trend onset, it is evident that all datasets with *Lmax* greater than 400 performed very well. For the datasets with observations 50-80 years after trend onset, it is evident that datasets with $Tmax_{sf}$ of 10 were ill-posed even with the two added assumptions, whereas the rest of the datasets improved substantially when *Lmax* was greater than 300 mm. These results provide strong evidence that by providing the model information on the baseline value from which the trend begins and ends from, the inference of the gamma function parameters are significantly improved.

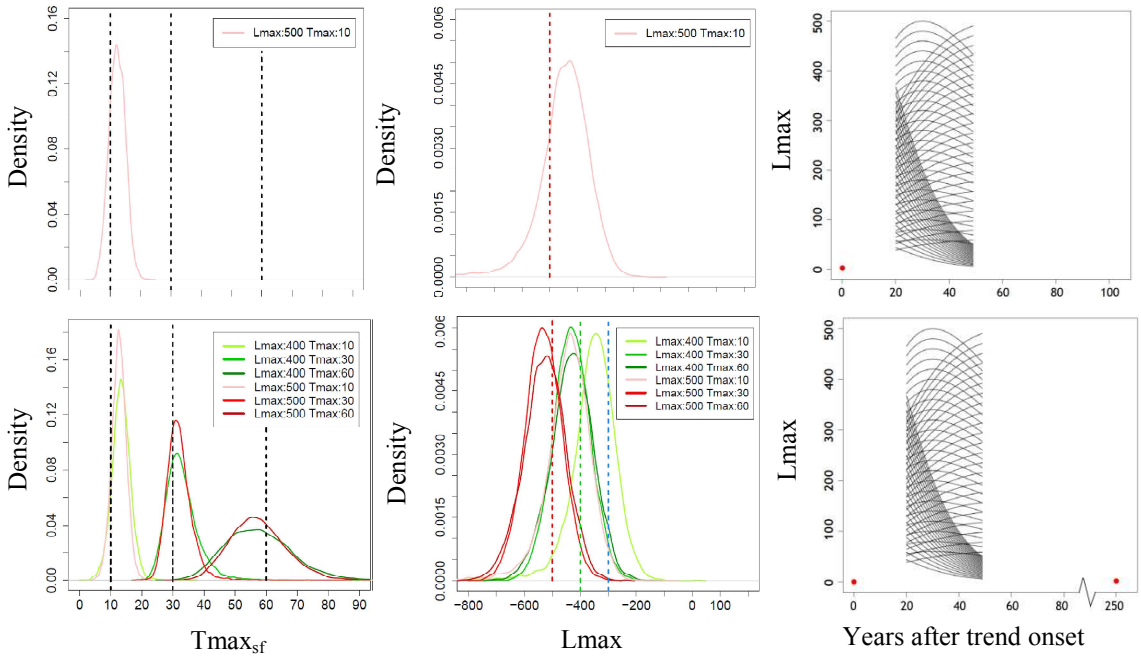

(a)

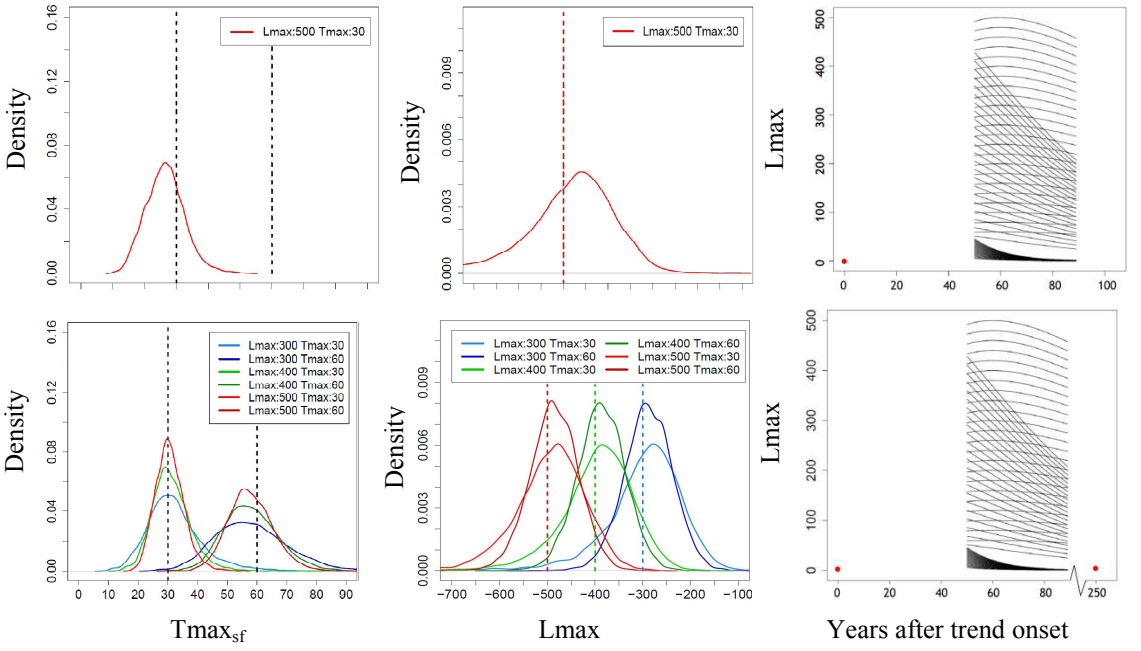

(b)

Figure 7.10: Improvements to parameter estimates when introducing an assumption of known pre-trend and post recovery streamflow for datasets with σ of 70 mm, and two varying extents that begin and end; (a) 20-50 years and (b) 50-80 years after trend onset. Note the red dots in the line plots locate the year when the assumptions were made.

7.3.2.6. Using real streamflow data

The following simulations involve synthetic data produced by extracting a range of gamma curves from control streamflow catchments, Myrtle 1 and Slip. The Slip

catchment's data extent was reduced to reflect the forest age of Picaninny regenerating catchment, whereas Myrtle 1 was reduced to reflect the age of Myrtle 2, and Black Spur 2. The extent of Black Spur 2 represents a similar data extent when compared to Ettercon 2 and 3, and other Black Spur catchments. The parameter estimates were recovered using the most successful five parameter climate filters in table 7.1 and 7.2 to result in a σ of 71.34 and 35.33 mm for Myrtle 1 and Slip catchment, respectively. As in the previous section, simulations were undertaken with and without the two added assumptions on pre-trend and post-recovery streamflow estimates.

Myrtle 2 has a 13 year calibration period followed by 22 years of trend data so only the post-recovery assumption is evaluated against a model with no added assumption. Figure 7.11 (a) shows *Lmax* and $Tmax_{sf}$ point plots and posterior distributions for simulations without the added assumption whereas figure 7.11(b) shows *Lmax* and $Tmax_{sf}$ results for data with a post-recovery assumption. It is evident that including the assumption improved estimates for datasets without observations at year $Tmax_{sf}$ (i.e. $Tmax_{sf}$ of 30 and 60), whereas little improvement took place for datasets that already had well established observations on either side of the $Tmax_{sf}$ year (i.e. $Tmax_{sf}$ of 10). The point plots illustrate how the ML estimates are forced to be closer to the true value for datasets without observations on both sides of year $Tmax_{sf}$, as the assumption forces the trend to recover within an assumed time frame (i.e. when forest reaches old-growth). For datasets where ML estimates are improved the posterior distributions suggest the standard errors are still wide.

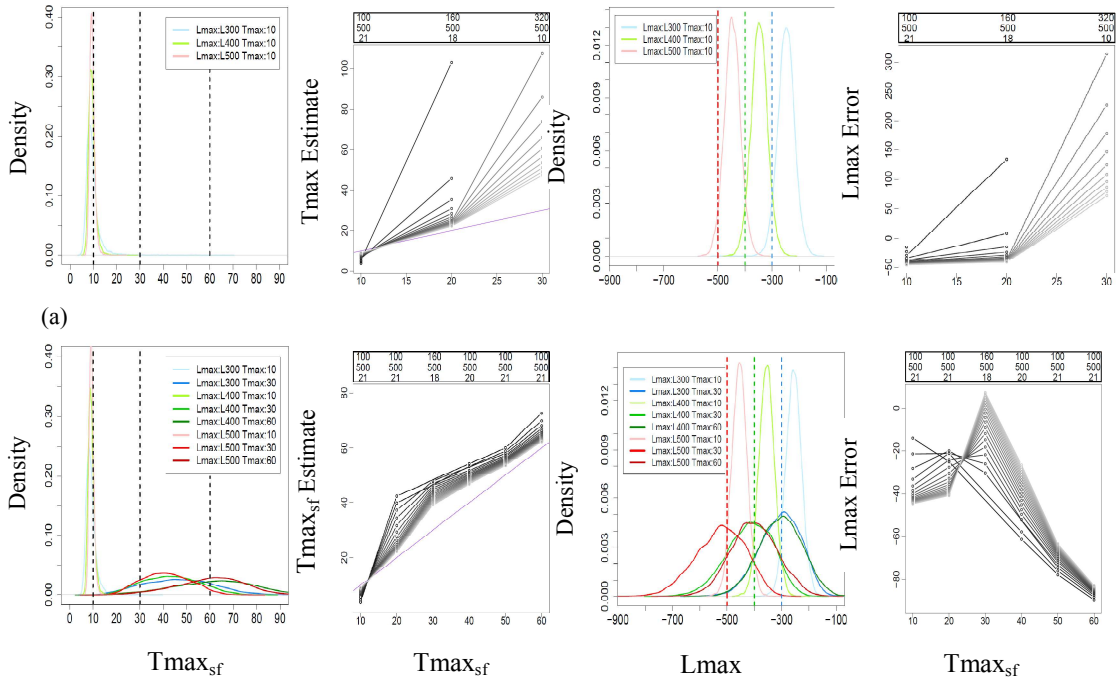

Figure 7.11: Parameter estimates using real streamflow data with; **(a)** the data extent identical to the Myrtle 2 dataset, and **(b)** improvements to the same dataset with an added post-recovery streamflow assumption.

Figure 7.12 shows that similar improvements are evident in the posterior distributions of Picaninny catchment which includes 15 year of calibration data and 35 years of trend data. The very efficient standard errors are a result of a climate filter with a standard error of 35.33 mm.

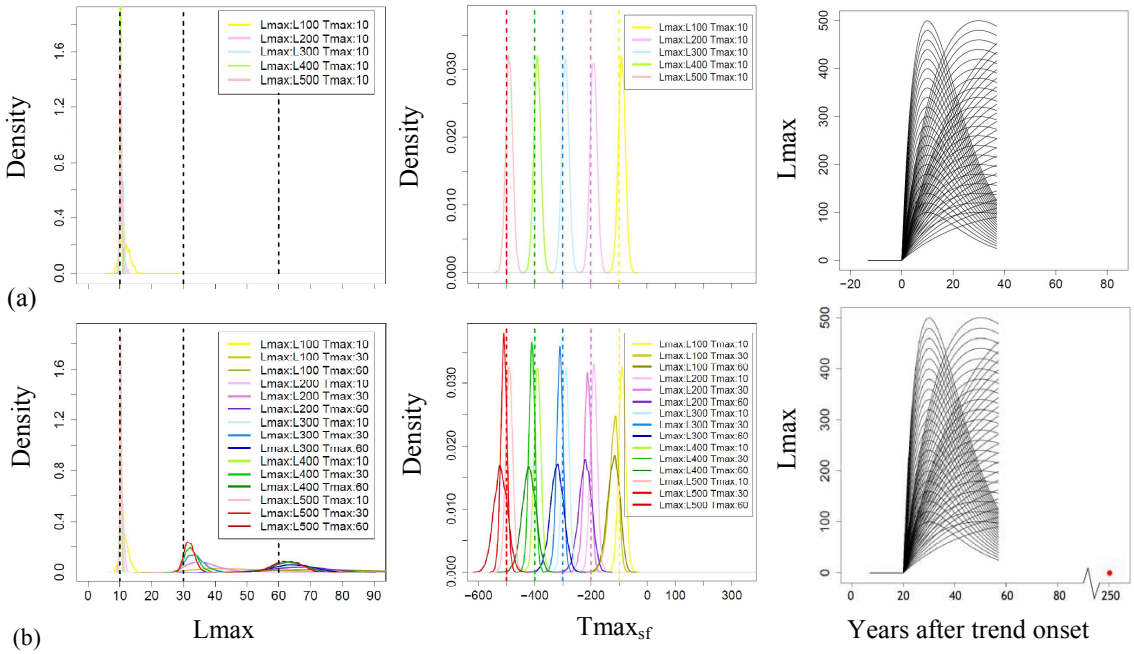

Figure 7.12: Parameter estimates using real streamflow data with; **(a)** the data extent identical to the Picaninny dataset; and **(b)** improvements to the same dataset with an added post-recovery streamflow assumption.

Figure 7.13 uses the Black Spur 2 data extent with 29 years of data ranging from the age of 33 till 62 to provide the posterior distributions for models with an assumed, (a) pre-trend streamflow estimate, and (b) pre-trend and post-recovery streamflow estimate. It is evident in figure 7.13 that datasets with $Tmax_{sf}$ of 10 performed poorly, even with the added assumptions. The line plot may explain this outcome as the datasets with $Tmax_{sf}$ of 10 only represent the tail end of recovery phase in streamflow, making the problem ill-posed. The line plots also illustrate how datasets with $Tmax_{sf}$ of 30 and 60 have very contrasting streamflow trend phases, as datasets with $Tmax_{sf}$ of 30 are recovering in streamflow, whereas datasets with $Tmax_{sf}$ 60 are progressively trending towards year $Tmax_{sf}$. For both datasets, it is evident that the model performs very poorly when only implementing the pre-trend streamflow assumption, whereas with both assumptions the posterior distributions improve quite substantially for all *Lmax* values greater than 300 mm. This simulation results provides evidence that the hydrological time-series for the Ettercon and Black Spur catchments will fail to indentify the streamflow trend without the added assumptions.

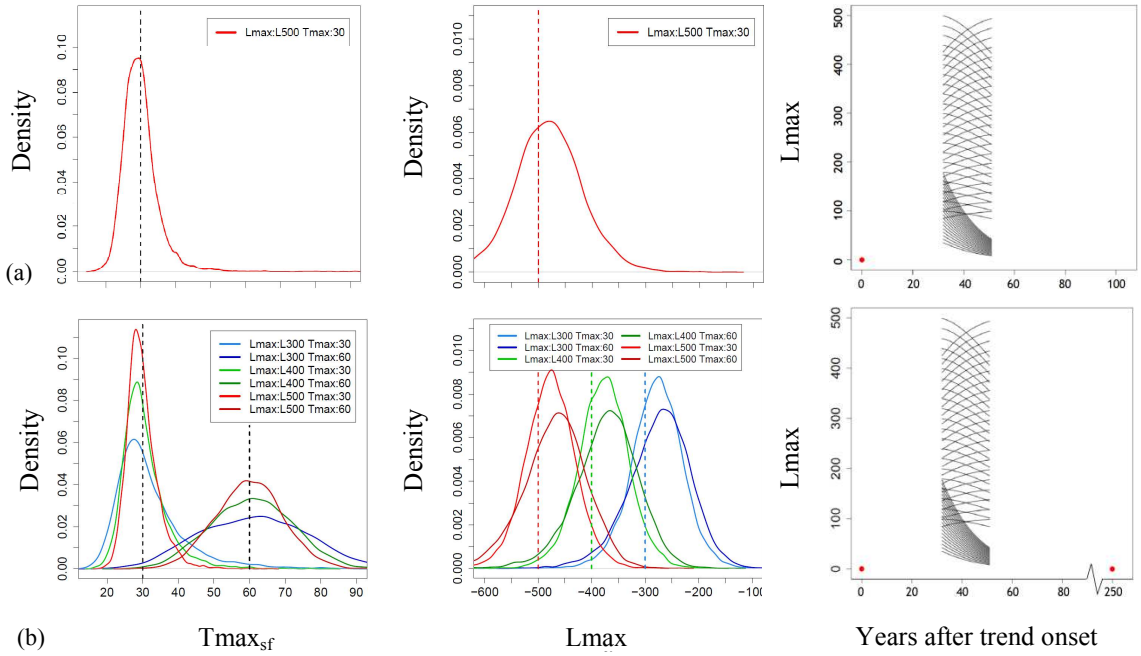

Figure 7.13: Parameter estimates using real streamflow data with the data extent identical to the Black Spur 2 dataset, and; **(a)** an added pre-trend streamflow assumption; and **(b)** an added pre-trend and post-recovery streamflow assumption.

7.4. Discussion

7.4.1. Climate filter

Conceptual hydrological models are always represented with some form of a transfer function that relates a series of inputs such as rainfall and transpiration to a series of outputs such as streamflow. To formulate a transfer function that estimates streamflow at ungauged catchments, the input data needs to be readily available and capable of emulating the ungauged catchment's predominant runoff generating processes. As there are a large number of variables that often govern a catchment's hydrological phenomena, the challenge is to answer the research question by formulating a model structure that emulates the governing set of laws at the spatiotemporal scale of interest. For the purpose of this study, the changes in vegetation dynamics is the physical law that governs the decadal changes in ET, which may be emulated with changes in forest growth rates using an annual time scale.

The model structure evaluated in this study was chosen in its simple form as data requirements are met with rainfall and forest inventory data over vast regional areas

that require ungauged streamflow estimates. To make estimates in ungauged catchments, a climate filter needs to be formulated by relating rainfall data to gauged streamflow data as a means to define the transfer rate of seasonal rainfall from the source area to the outlet. It has been demonstrated that such a climate filter may be coupled to a non-linear forest growth function to isolate a decadal streamflow trend from random climatic fluctuation in a synthetic dataset.

As velocity of surface and subsurface flows, as well as storage, influence the transfer rates of seasonal rainfall into annual streamflow volumes, the climate filter implicitly represent the rainfall-runoff transformation. The formulation of the climate filter applies the principle of superposition as the linear response model represents the total response that is non-linear in its complex form. Rainfall-runoff processes are non-linear primarily due to a catchment's antecedent conditions, hydraulic conductivity, and effect of the rainstorm's intensity, and duration on the nature of the flow velocity (Beven, 2001). In effect the climate filter scales the base flow discharge, which may be stochastic in nature.

Figure 7.14 provides a log transformed time series of the Slip and Myrtle 1 streamflow catchments with a kernel filter superimposed in red to illustrate how the oscillation in the recharging and discharging phases of base flow vary from year to year. Figure 7.15 summarises the whole datasets by showing the number of times each month of the year was represented with a maximum and minimum in base flow discharge based on the kernel filter. The climate filter presently aggregates rainfall data in a consistent fashion for all the years without accounting for the influence of shorter temporal-scale climatic variations on annual streamflow volumes shown in figure 7.14 and 7.15.

The scale dependency of the hydrological processes encapsulated in the climate filter is a critical issue. It is well recognised that rainfall statistics are sensitive to scale and vary in time (Seed, 2000). The climate filter needs to be further developed so that the governing equation implicitly encapsulates the physical laws involved in runoff generation processes more effectively, with the overarching objective to reduce unexplained white noise. Identifying how rainfall statistics such as rainstorm intensity and duration correspond to streamflow processes may explain more of the

climatic variations in streamflow. To improve the climate filter it may be necessary to account for the shorter temporal-scale climatic variation on annual streamflow volumes. This would improve the residual standard errors in the climate filter.

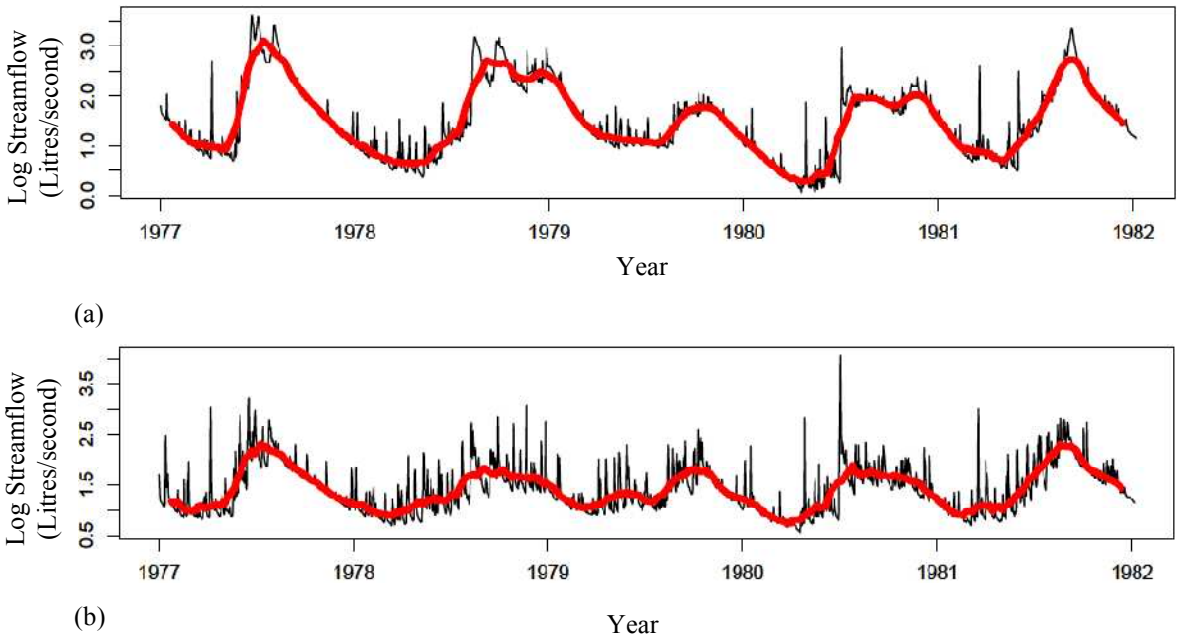

Figure 7.14: Log transformed streamflow with a kernel filter to illustrate the base flow process for (a) Slip and (b) Myrtle 1 control catchments.

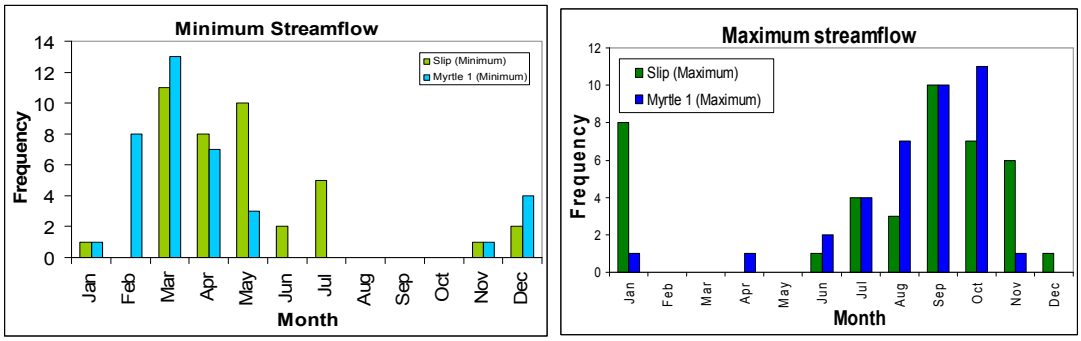

Figure 7.15: Histograms show how frequently the base flow reached its maximum and minimum discharge level for each month at both the Slip and Myrtle 1 control catchments.

7.4.2. Simulation experiments

Generalised non-linear modelling of streamflow data provides a robust method for distinguishing random climatic fluctuations in streamflow from decadal trends in streamflow due to vegetation dynamics. The simulation exercise provided an evaluation of the behaviour in the model structure for a range of scenario cases in order to improve the model structure under circumstances when conditions of data

availability as well as treatment effects are limited. The illustrated results provide both a quantitative measure of inference accuracy for relatively comparable datasets, as well as a qualitative measure that demonstrates the behaviour of the model structure with changing dataset circumstances. For example, the following properties of the model structure were illustrated in the form of quantified measurements in the figures provided in the results:

- two dataset with a same σ, $Tmax_{sf}$, $Lmax$, and data extent could result in different $Tmax_{sf}$ and $Lmax$ ML estimates purely due to the random nature of the climatic variance in the dataset,
- biased ML estimates occur when an insufficient number of observations are used in the streamflow time series dataset,
- reducing the datasets σ value improves the predictive accuracy of $Tmax_{sf}$ and $Lmax$,
- increasing the $Lmax$ value improves $Tmax_{sf}$ predictions,
- as the trend becomes more subtle with an increase in $Tmax_{sf}$ and decrease in $Lmax$, the success rate of the model convergence decreases, and the standard errors for models that do converge increase,
- for any given $Tmax_{sf}$ value, $Lmax$ estimates deteriorate once $Lmax$ is less than twice the magnitude of σ as the ratio $Lmax{:}\sigma$ strongly influences inference accuracy,
- posterior distributions of $Lmax$ become more dispersed without observations that include year $Tmax_{sf}$,
- if a dataset does not include observations immediately after trend onset, the dataset needs to be well represented with observations at the recovery phase of the gamma function, and in particular at the "point of inflection" in the skewed tail end of the gamma function to make the problem well posed, and
- pre-trend observations ("calibration data") improve the posterior distributions of $Lmax$ substantially whereas improvements to $Tmax_{sf}$ are negligible.

Improvements to results have also been demonstrated with an inclusion of a well founded physical property in vegetation dynamics that states: when a forest reaches maturity and forest growth rate is negligible streamflow reaches a hydrological equilibrium (Kuczera, 1987). By including an estimate of streamflow when the forest

is old-growth, the inference is much more accurate. An assumption that pre-treatment streamflow and post-recovery streamflow is of a particular magnitude improves streamflow estimates over the rest of the regeneration process in the following manner:

- for datasets beginning after year $Tmax_{sf}$, an assumption that estimates streamflow at trend onset improves parameter inference,
- for dataset with few or no observations after year $Tmax_{sf}$, an assumption that estimates post-trend recovery of streamflow improves parameter inference,
- both pre-trend and post-trend estimates of streamflow may be used in the model structure to improve parameter inference when data length is limited and observations only exist around year $Tmax_{sf}$.

7.5. Conclusion

It has been demonstrated that a model structure based on a multiple non-linear regression equation provides an effective way of isolating a decadal streamflow trend in synthetic hydrological time series. To improve parameter inference in the proposed model structure it is necessary to increase the $Lmax{:}\sigma$ ratio, and as $Lmax$ is pre-defined in the catchment's condition, an accurate climate filter that decreases σ in the model structure is a crucial objective. A methodology was presented that uses rainfall series data to produce explanatory variables that explain the climatic variance in streamflow. In doing so, the climate filter reduces the overall residual standard error in the model structure in order to extract the magnitude and duration of streamflow trend with the greatest level of confidence.

It has been demonstrated that to infer a streamflow trend in a well posed problem, it is necessary for the data length to capture the predominant features in the gamma function by having an adequate representation of observations; before and after year $Tmax_{sf}$, around the "point of inflection" in the skewed tail end of the gamma function, and during the time when the catchment is old growth. As most streamflow datasets do not contain observations during all of these periods, it has been demonstrated that parameter inferences significantly improve if the model structure includes information on the baseline value from which the trend begins and ends (i.e. assumed streamflow at old growth). The simulation exercise demonstrates that the six study catchments consist of short hydrological time-series, which may be ill-

posed without assumptions on streamflow conditions when the hydrological system is at equilibrium and the forest is old-growth.

The next chapter applies the forest growth models to the LiDAR data to extrapolate the models and generate lumped catchment-scale forest growth models in order to explain the identified trends in the streamflow data.

Chapter 8: Relationship between forest growth and streamflow trends

8.1. Introduction

As the conceptual model outlined in chapter four consists of parameters that are not directly measurable, model calibration is required to estimate these parameters by fitting simulated model output to observed data. The measure of fit between the simulated and observed values is called the objective function, and the goal of the calibration procedure is to find model parameter values that minimise the objective function. Chapter seven undertook a simulation exercise that integrated a range of scenarios into synthetic hydrological time series to analyse the behaviour of the objective function and uncertainty associated with the predictions. It was found that uncertainty in parameter inference of streamflow trends is affected by: the level of disturbance within a catchment; the ability of the climate filter to explain climatic variance; and both the period and duration of the hydrological time series in relation to the disturbance.

To recognise that real hydrological time series may have an initial increase in streamflow after a disturbance, the model structure complicates the parameter inference problem by integrating an ellipse function. For this reason, the model structure in this chapter includes a greater number of parameters, and the degree of difficulty in solving global optimisation problems increases with the dimensionality of the problem. As the *nlme* optimisation algorithm used in chapter seven was not able to fit the more complex model structure to the streamflow data, parameter inference in this chapter required an optimisation algorithm that was more advanced than the gradient based optimiser used by the *nlme* function of chapter seven. For this reason, the shuffle complex evolution (SCE) method (Duan *et al*., 1993) was used to infer the parameter estimates.

The SCE method inferred parameter estimates, *Lmax* and $Tmax_{sf,}$ which represent the magnitude and duration of the streamflow trends. These parameters were compared to the lumped catchment-scale forest growth model parameters, *Pmax* and $Tmax_{fg,}$

which represent the magnitude and duration of growth. The aim of this chapter was to identify whether the *Tmax* values for growth and streamflow trend coincide, and whether the magnitude of *Pmax* and *Lmax* values are complimentary for corresponding catchments. The overall objective is to determine whether these parameter values may be explained by the different treatment effects. To achieve this, the chapter undertook and evaluated the following tasks:

1. Spatial maps of forest characteristics were produced for each catchment using the relationship between measured plot-level stand characteristics and LiDAR indices generated in chapter five.
2. Spatiotemporal stand volume estimates were generated using; the LiDAR indices generated in chapter five, and the predictive growth models generated in chapter six. The resulting spatiotemporal maps were used to calculate lumped catchment-scale forest growth curves by amalgamating the stand volume curves of each grid over each catchment.
3. The multiple non-linear regression outlined in chapter four was fitted through the streamflow data using the SCE optimisation algorithm in order to make simultaneous parameter estimates of the climate filter and decadal streamflow trends.
4. The resulting outputs from points two and three were used to compare parameter estimates of streamflow trends with parameter estimates of forest growth curves to explain streamflow trends with forest growth models.

A further objective was to review all relevant hydrological research undertaken in the catchments for comparison with results generated in this study to determine whether; the multiple non-linear regression provides similar results, and forest growth models provide supporting evidence of the streamflow trends.

8.2. Methodology

8.2.1. Spatial forest productivity over catchment

Using GIS, LiDAR data was segregated into grid cells the size of the extended permanent plots used in each corresponding catchment. With the mixture modelling procedure outlined in section 5.2.5, LiDAR indices were generated for each grid cell over the whole catchment. The following three models where then applied to

generate spatial maps of stand characteristics using the LiDAR indices: ridge regression model, gamma model, and logistic model. The ridge regression model generated in section 5.3.3 estimated eucalyptus stand volumes and *BA*, as well as non-eucalyptus *BA*, whereas the gamma and logistic models generated in section 6.3.3 estimated eucalyptus stand volume for comparison with the ridge regression model.

Comparisons in stand volume estimates are made using the three models to evaluate the sensitivity in the heterogeneous pattern of the predicted values. In evaluating the different models the gamma and logistic model generate temporal maps and only the 2009 spatial maps are compared with the ridge regression model.

8.2.2. Lumped catchment-scale forest growth curves

Using both the logistic and gamma models generated in section 6.3.3, the spatiotemporal models of forest growth were made and lumped to the catchment-scale by calculating for each growth year the average stand volume per hectare for each catchment. This simply involved summing for each year the total stand volume estimates over the catchment and dividing the sum by the catchment area to determine stand volumes per hectare. Using the *nlme* function in R, both the logistic and gamma models where fitted through the modelled outputs of stand volumes per hectare to derive catchment-scale forest growth model parameter values.

8.2.3. Parameterising the decadal streamflow trends

Given the short data length of the hydrological time series (table 4.4 & 4.5) and complications related to North Maroondah catchments having two successive disturbances (i.e. 1939 bushfire and experimental treatment), the optimisation algorithm available with the *nlme* library failed to fit the multiple non-linear regression models. This meant a more efficient and effective optimiser was necessary to make simultaneous parameter estimates of the climate filter and decadal streamflow trends. For this purpose, the SCE method is applied and an explanation of the underlying concepts used by the algorithms is provided below.

8.2.3.1. Shuffle complex evolution (SCE) method

The SCE method treats the global search as a process of natural evolution (Duan *et al*., 1993). A random sample of points in the parameter space are used to constitute a population, which are partitioned into several communities (complexes), each of which evolves independently by searching the space for optimal parameters in different directions. After a certain number of generations, the complexes are shuffled (mixed) and new complexes are formed to enhance survivability by sharing of information gained independently by each complex. Each member (sample) of a community (complex) is a potential parent that may reproduce a new sample (offspring) by; grouping parents within the community into sub-complexes, and then applying the triangular probability distribution procedure presented by Nelder and Mead (1965) to each sub-complex. To ensure the evolution process is competitive, the sub-complexes with better objective function values have a higher probability of generating offspring. Each new offspring replaces the worst member of the sub-complex it belongs too, which ensures every parent has at least one chance of reproducing, and no information contained in the sample is ignored. In addition, offspring may be introduced in a random location, which is analogous to mutation in biological evolution; to ensure optimisation does not get trapped in unpromising parameter spaces.

The SCE method brings together four concepts that have proven successful for global optimisation, which include (Duan *et al*., 1993):

- combination of probabilistic and deterministic approaches as the deterministic strategy makes effective use of the response surface information whilst the random element help make the algorithm flexible and robust;
- clustering helps concentrate the search in the most promising regions identified by the initial complex;
- systematic evolution of a complex of points towards global improvement. This ensures the search is relatively robust and guided by the structure of the objective function; and
- competitive evolution to improve global convergence efficiency by guiding the search towards a direction with improved objective function values.

Duan *et al* (1994) demonstrate that the SCE method is an effective and efficient optimisation technique for calibrating conceptual forest hydrology models, and they provide recommended parameter values for the algorithm available as part of the R software.

8.2.4. Comparing streamflow trends with forest growth models

In the above sections, the forest growth models were extrapolated over the catchments to produce lumped catchment-scale growth curves, and the multiple non-linear regression identified trends in streamflow data. For each corresponding catchment the parameter estimates, *Pmax* and $Tmax_{fg,}$ which represent the magnitude and duration of growth are compared to *Lmax* and the sum of *TInc* and $Tmax_{sf,}$ which represent the magnitude and duration of the streamflow trends. For corresponding catchments, comparisons in parameter values are made to determine whether $Tmax_{fg}$ and the sum of *TInc* and $Tmax_{sf}$ values coincide, and whether the magnitude of *Pmax* and *Lmax* values are complimentary. The aim is to identify whether streamflow trend parameter values may be explained by the different treatment effects. The results are compared to published literature representing the study catchments to determine whether multiple non-linear regression results are comparable to paired catchment studies, and whether forest growth models may provide further insight into published results.

8.3. Results and Discussion

8.3.1. Spatial forest characteristics over each catchment

For each of the three models, Figure 8.1(a) provides estimates of eucalyptus stand volumes for Ettercon 2 (refer to Appendix B for all other catchments) with all maps representing the growing season 2008/09 to allow for comparison. Figure 8.1(b) provides spatial estimates of eucalyptus and non-eucalyptus *BA* using the ridge regression model. For each map, a stream buffer has been delineated by hand using a canopy height map generated from LiDAR data to visually identify the riparian strip and help interpret the maps.

It is evident that within the delineated stream buffer area, eucalyptus stand volumes are relatively low and non-eucalyptus BA are relatively high compared to hillslope

grids. This suggests the mixture modelling procedure of chapter five performed well at identifying areas with a reduced eucalyptus canopy cover. Eucalyptus stand volumes within the stream buffers are not zero as the grids along the stream intersect the buffer and are therefore partially located outside the buffer where eucalypts are found. As intersected grids are partially represented by eucalyptus trees, they were included in the catchment-scale eucalyptus growth rate calculations of section 8.3.2.

Stand volume maps of figure 8.1(a) show that the spatial pattern over the catchment is reasonably similar for all three models but the actual stand volume predictions are higher in the logistic model. The ridge regression model is expected to be the most accurate map in figure 8.1 (a) as the stand volume estimates were based on the relationship between LiDAR data collected in 2007 and field measurements in 2009, whereas the other two models are based on a relationship between 2007 LiDAR data and permanent plot data predominantly collected prior to 1993. As the permanent plots were decommissioned between 1993 and 2008, the growth models were strongly influenced by stand characteristics prior to 1993; hence the resulting growth curve over- or under-estimated the 2009 field measurements when coupled to the 2007 LiDAR data.

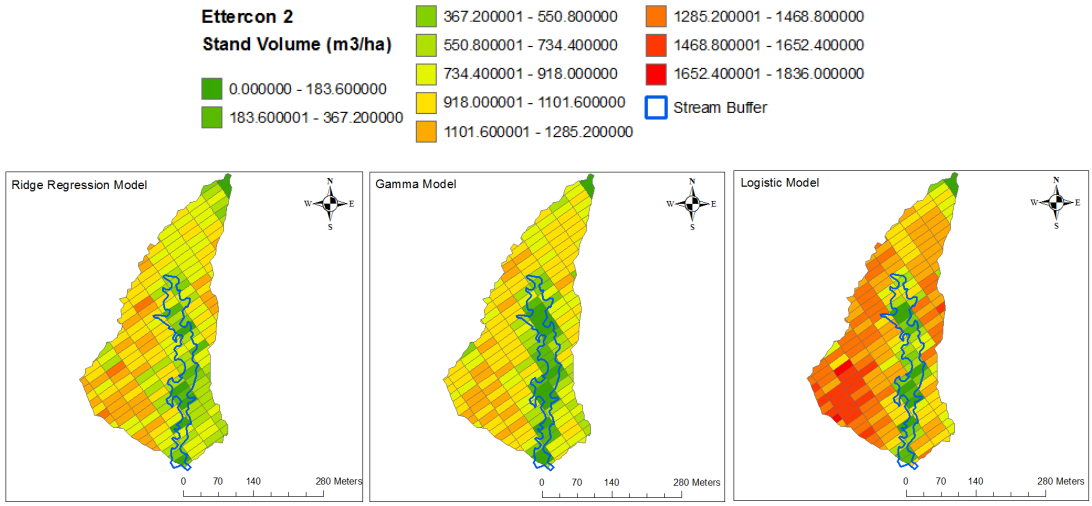

(a)

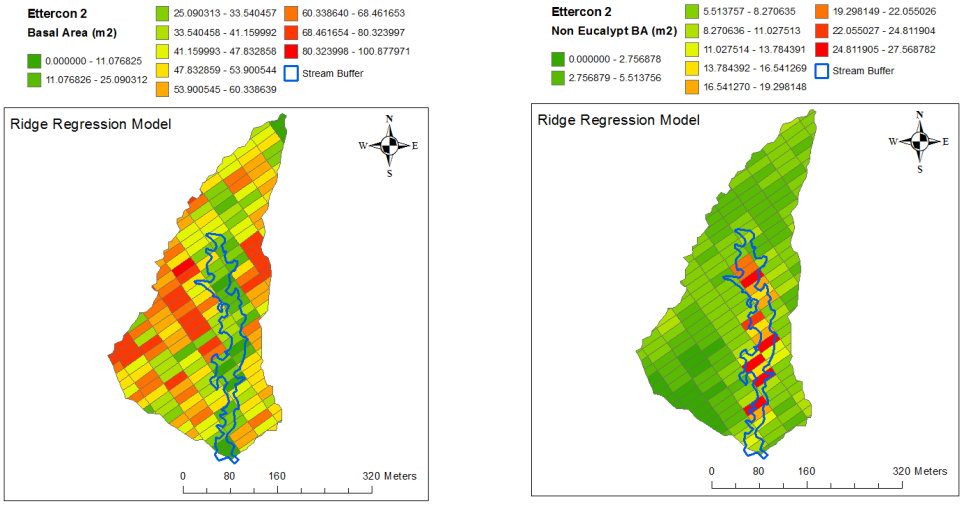

(b)

Figure 8.1: (a) Spatial estimates of eucalyptus stand volumes for Ettercon 2 using the ridge regression, gamma, and logistic model, and to allow for comparison all maps represent the growing season 2008/09; and **(b)** eucalyptus and non-eucalyptus basal area for Ettercon 2 using the ridge regression models.

It is worth noting that all maps in figure 8.1(a) have a similar spatial pattern of stand volumes over the catchment grids. This suggests the different set of LiDAR indices used as independent variables in each of the models captured the spatial heterogeneity in forest growth well. From a process-based modelling perspective, the spatial representation of forest characteristics used to explain *ET* rates will have a flow on effect on the runoff routing procedure in the overall water balance. For example, as hydraulic conductivity often diminishes down the soil profile (Beven, 2001), lateral flow rates of the saturated subsurface zone are strongly influenced by

groundwater levels. As a result, accurate *ET* pattern across a catchment will influence spatial ground water recharge rates, hence lateral flow rates and streamflow estimates. For this reason, the forest growth modelling exercises undertaken in this dissertation would provide valuable spatiotemporal input for a modelling framework that aims to capture the lateral flow processes using daily time steps.

8.3.2. Lumped catchment-scale forest growth

8.3.2.1. Ridge regression (Spatial)

Table 8.1 provides a summary of 2008/09 stand volumes and *BA* estimates for each catchment using ridge regression models. Estimates of stand characteristics were generated by summing over the following catchment areas; the whole catchment, stream buffer, hillslope, and treatment effects in Black Spur 1 (patch and non-patch) and Myrtle 2 (regeneration). Table 4.1 shows that Black Spur 2 and 3 used seven plots to generate the relationship between LiDAR indices and field measurements so interpretation of Table 8.1 should be made with caution for these two catchments.

Wang and Hamilton (2002) modelled ash eucalypt *BA* over the Central Highlands of Victoria, to find that *E.regnans BA* varies between 35-60 m^2 ha^{-1}, 40- 70 m^2 ha^{-1}, and 45-80 m^2 ha^{-1} for 23, 37, and 69 year-old forest respectively. Results for hillslope areas in table 8.1 are consistent with these results, except for the 37 year-old Black Spur 1 patch cut area, which had stunted growth after treatment due to shading from retained trees. There is some evidence that regeneration at Myrtle 2 represents the higher end of the expected *BA* range, as is possibly the case for Black Spur 3.

The summary statistics for the stream buffer areas are also plausible for all catchments, even though Black Spur 3 has a high eucalyptus *BA* of 57.19 m^2 ha^{-1}. Figure 8.2 shows Black Spur 3 consists of large 40X40 m grids over a small catchment area of 7.4 ha, and the high *BA* along the stream is a result of grids along the stream also including dense eucalypt stands along the hillslope. Furthermore, as Black Spur 3 represents the headwater of a small catchment, the stream buffer is fragmented with eucalypts shading the stream and increasing the eucalypt *BA*.

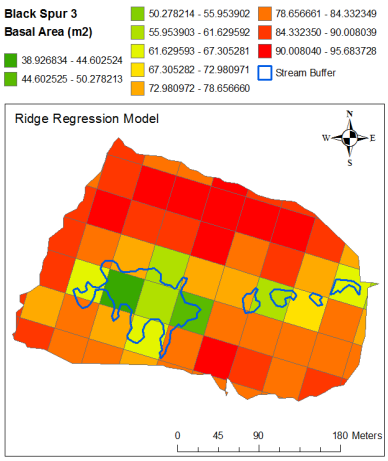

Figure 8.2: Basal area of Black Spur 3 showing the size of the catchment relative to 40X40 m grids, and the fragmented stream buffer due to eucalypts shading the stream.

For each catchment in table 8.1, non-eucalypt *BA* is much higher for stream buffers compared to hillslopes, which is an expected result considering rainforest species are found along the riparian strips. Ettercon 2 had its Acacia understorey removed in 1972 followed by regeneration of scrub species *Correa lawrenciana* and *Pomaderris aspera*; whereas control catchment Ettercon 3 consisted predominantly of *Acacia melanoxylon* and *A.dealbata* species. Modelling non-eucalypt understorey did not explicitly distinguish canopy structure of specific species in order to recognise variations in species-specific *BA* relative to LiDAR canopy profile. This was not necessary as most of the variation in the understorey structure was between catchments, and the catchments were modelled separately with catchment-specific field data. As a result, non-eucalypt *BA* estimates for Ettercon 2 and 3 reflected the treatment effects well with hillslope *BA* of 1.83 and 2.6 $m^2 ha^{-1}$ respectively.

Table 8.1: Summary statistics of stand characteristics using ridge regression models. Catchments are stratified into stream buffer, hillslope, and treated areas. Coded stand characteristics in table include: Non (non-eucalypt), Euc (eucalypt), BA (basal area), and Vol (stand volume)

Catchment	Area (type)	Area (ha)	Euc Age	Euc_BA (m^2 ha^{-1})	Euc_Vol (m^3 ha^{-1})	Non_BA (m^2 ha^{-1})
Black Spur 1	Catchment	17.66	69 &37	45.84	838.73	10.85
	Hillslope	17.36	69 &37	46.34	842.09	10.91
	Stream	0.30	69	17.15	643.09	7.18
	Patch	6.82	37	24.27	414.06	7.08
	Non Patch	10.84	69	59.40	1105.67	13.21
Black Spur 2	Catchment	9.60	69	45.06	793.46	4.49
	Hillslope	8.98	69	47.31	823.32	3.20
	Stream	0.62	69	12.25	358.97	23.20
Black Spur 3	Catchment	7.42	69	79.13	1320.64	5.66
	Hillslope	6.75	69	81.28	1335.99	5.27
	Stream	0.66	69	57.19	1164.04	9.71
Ettercon 2	Catchment	9.50	69	47.10	848.56	3.11
	Hillslope	8.43	69	49.99	890.35	1.83
	Stream	1.07	69	24.25	518.40	13.28
Ettercon 3	Catchment	14.84	69	62.57	1148.86	3.45
	Hillslope	13.42	69	66.68	1229.60	2.60
	Stream	1.42	69	23.61	383.70	11.55
Myrtle 2	Catchment	33.47	185 & 23	-	-	-
	Regeneration	20.88	23	55.81	422.07	3.46
	Old-growth	11.31	185	-	-	-
	No LiDAR	1.28	23	-	-	-

8.3.2.2. Logistic and gamma models (Spatiotemporal)

For each catchment, table 8.2(a) provides a summary of the logistic and gamma model parameter estimates for the lumped catchment-scale forest growth curves. Table 4.1 provides a summary of treatments for each catchment to help interpret table 8.2. Note, Black Spur 1 only includes permanent plot data for the non-patch cut area and growth curves were not constructed for cleared patches consisting only of 2008/09 measurements. As permanent plots for Ettercon 2 and 3 were of the same size and both catchments did not involve disturbance to eucalyptus trees, the catchments were merged to improve eucalypt stand volume estimates. When comparing Black Spur 1 to Ettercon 2 & 3, results show the Ettercon stands were less productive with smaller parameter values for *Pmax*, $Tmax_{fg}$, and *Asym*. The larger stand volumes at Black Spur 1 may be a result of the retained trees having an increase in resource capture due to stunted growth in the other 60% of the catchment (cleared patches). For this reason, the Black Spur 1 $Tmax_{fg}$ at 37.7 years of age may

have been earlier if no treatment took place, which suggests the 32 year old Black Spur forest was treated around the time of $Tmax_{fg}$.

Results also show that thinning Black Spur 2 and 3 increased $Tmax_{fg}$ as the reduced competition after thinning prolonged the increase in post-treatment growth rates. La Sala (2007) supports these findings in Tasmania by showing stand *BA* increments increased for a longer period of time after stand *BA* reductions of 65%, 50%, and 33% in 24 year old *E.regnans* forest. La Sala (2007) also found that even when stocking density was intensely reduced after thinning (i.e. 65% *BA* removal) there was no drop in stand growth increments in the first post-treatment year, which was supported by Connell *et al.* (1997) and Brown (1997). Table 8.2 show that with increased thinning intensity, the maximum stand growth increment (*Pmax*) decreases, as the reduced number of retained trees result in a reduced maximum resource capture.

Streamflow data for the Black Spur catchments commenced 5-6 years prior to treatment when the forest was 32 years old, and continued for 15-20 years after treatment. It is evident that the growth phase during stream gauging (i.e. when the forest was 32-56 years old) had relatively small changes to incremental growth from year to year as the measurements were taken around the time of $Tmax_{fg}$. This coupled with the effects that treatment had on growth rate changes (i.e. slower growth with reduced *Pmax* and increased $Tmax_{fg}$) raises challenges in identifying a trend in the hydrological time series already complicated by climatic variability in rainfall. It is likely that climatic variability in streamflow data is of similar magnitude to the streamflow trend due to changes in regeneration processes over the stream gauging period.

In table 8.2, the Myrtle 2 growth rate peaked at 5.3 years, which is much earlier than would be expected. Figure 6.2 provides Myrtle 2 permanent plot data to show that in many plots, death of trees results in reduced stand volumes; and given the short data length, the mixed effects model interpreted this to represent the beginning of reduced growth rates (i.e. $Tmax_{fg}$). Watson (2001) documented that in 1996 there was a major psyllid insect attack causing tree death at Myrtle 2, which reduced growth rates and caused early streamflow recovery. To complicate matters, the permanent plots were

decommissioned between 1998 and 2008/09, which coincided with a significant drought period in the region that would have further reduced *BA* growth increments measured in 2008/09.

The regeneration phase and duration of growth measurements in the permanent plot data, coupled with the psyllid attack and timing of the drought between the second last and last observation, raises uncertainty in the Myrtle 2 parameter estimates. To address some of these limitations, the Myrtle 2 dataset was merged with other catchments to construct growth curves representing a broader range of forest age classes. Although table 4.1 shows the catchments have different permanent plot sizes and treatment effects, merging catchment data provides a fuller representation of *E.regnans* growth trends using data for 5 to 22 and 32 to 52 year-old forest.

Table 8.2(b) provides parameter estimates generated using merged permanent plot data, and results show that only the gamma model converged. This provides supporting evidence that the gamma model is more appropriate than the logistic model at representing changes in forest productivity over the lifetime of an *E.regnans* forest. Interestingly, when the gamma model was applied to all six merged catchments, results suggest with 95% confidence that peak in growth ($Tmax_{fg}$) occurs when the forest was between 24.4 and 27 years of age. This supports the hypothesis that forest productivity is inversely related to vegetation induced streamflow trends, considering Kuczera (1987) applied the gamma curve to streamflow data of mountain ash catchments from the same region to show maximum forest water use was approximately 27 years after forest disturbance.

Table 8.2: Logistic and Gamma model parameter estimates for the lumped to catchment-scale forest growth curves. The 95% confidence intervals are provided in parentheses.

	Catchment	Gamma Model		Logistic Model		
		Pmax	***Tmax$_{fg}$***	***Asym***	***Xmid***	***Scal***
(a)	Black Spur 1	20.48	37.7	1285.16	39.68	13.39
		(16.3-24.7)	(34.1-41.3)	(1003.5-1566.8)	(35.9-43.4)	(12.1-14.6)
	Black Spur 2	19.6	64.80	1086.97	45.4	13.5
		(16.5-22.7)	(53-76.6)	(913.7-1260.3)	(42.4-48.4)	(11.7-15.3)
	Black Spur 3	16.12	74.02	984	50.26	14.4
		(12.4-19.9)	(65.5-82.6)	(750.5-1217.5)	(47.8-52.7)	(12.8-16.1)
	Ettercon 2&3	18.84	20.47	973.27	36.35	10.49
		(17.1-20.6)	(19.4-21.5)	(856.9-1089.7)	(34.5-38.2)	(8.5-12.5)
	Myrtle 2	38.43	5.31	567.32	8.45	4.92
		(34.4-42.5)	(4.3-6.3)	(463.4-671.2)	(6.7-10.2)	(3.9-6)
	Merged catchment data					
(b)	Myrtle 2 & Black Spur 1,2 & 3	33.65 (26.6-40.7)	45.89 (41.7-50.1)	-	-	-
	Myrtle 2 & Ettercon 2&3	22.9 (20.6-25.1)	19.7 (18.8-20.6)	-	-	-
	All	22.44 (20.0-24.8)	25.69 (24.4-27)	-	-	-

Figure 8.3 shows gamma and logistic growth curves, and current annual increments (CAI) using; (a) Black Spur 1, (b) Ettercon 2 & 3, and (c) Myrtle 2 data to highlight the limitations with the catchment specific datasets. The black circles in figure 8.3 represent the duration period over which data was available to construct the curves. It is evident that although fitting the logistic and gamma model generates visually similar forest growth curves over the period represented by data, the first derivatives (i.e. CAI) have very contrasting features. This should be expected, considering the datasets represent a period in growth when incremental changes are very subtle and different equations capture those subtle changes differently. The results show that the type of non-linear model used to construct the growth curve will influence the resulting maximum growth rate and timing of the growth peak; which are the predictive forest growth characteristics that are important at explaining the nature of the decadal streamflow trends using a Kuczera type curve.

Considering the limitations in the modelled results of figure 8.3, they show that for Ettercon 2&3 and Black Spur 1 the permanent growth data was collected after the

time when forest growth rates peaked. It is evident that Ettercon 2 & 3 has a more rapidly declining growth rate than Black Spur 1, which may be explained by the increase in resource availability of retained trees at Black Spur 1 after the patch cut. The rate of decline in both catchments may have also been exacerbated by drought conditions that reduced growth prior to the 2008/09 measurements. The drought would have affected the growth rate of all catchments, but this was most evident at Myrtle 2 already subject to the psyllid attack. Although non-linear models have a theoretical interpretation that remains stable beyond the observed range, if the model fit projects the shape of the equation incorrectly then the future estimates will also be incorrect. This was found to be the case for the Myrtle 2 dataset, which represented a very different part of the growth curve when coupled with other catchments in figure 8.4. Comparing Myrtle 2 growth rates in figure 8.3 and 8.4 demonstrates the importance of using permanent plot data from a range of age classes for constructing regional growth models.

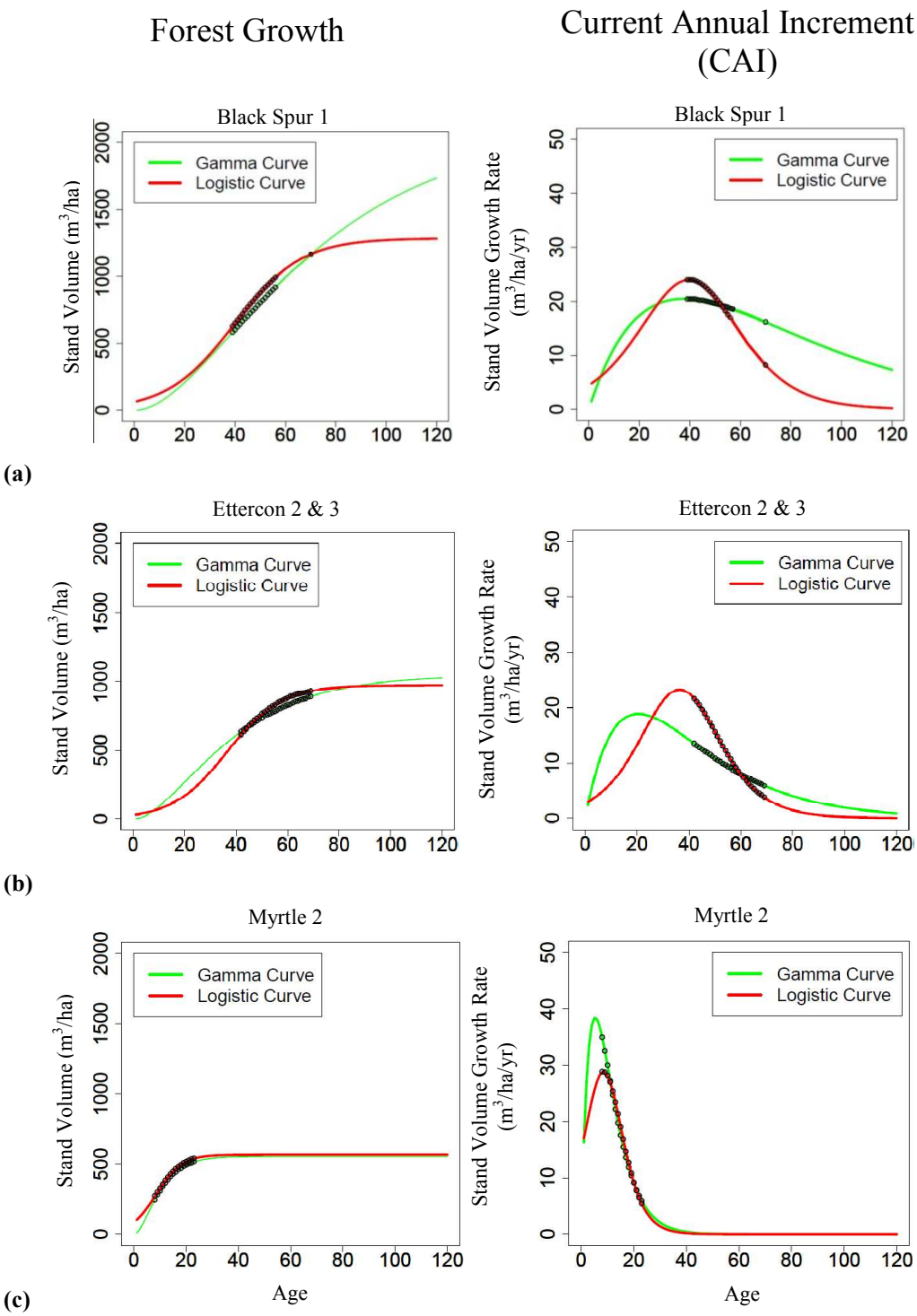

Figure 8.3: Catchment level forest growth and current annual increments for (a) Black Spur 1, (b) Ettercon 2 & 3, and (c) Myrtle 2. The dots represent the forest age when permanent plots were measured.

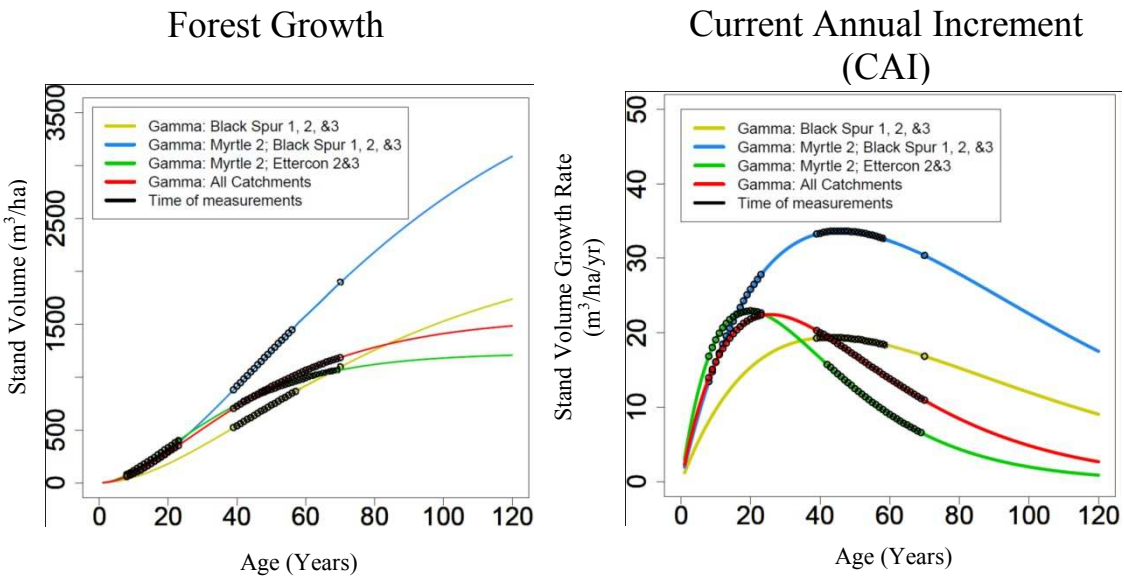

Figure 8.4: Catchment level forest growth and current annual increments for a set of catchments merged together.

8.3.3. Evaluating decadal streamflow trends with forest growth curves

A large body of literature has quantified the effects of land-cover disturbance on streamflow for the experimental catchments (Langford & O'Shaughnessy, 1977; Langford & O'Shaughnessy, 1979; Jayasuriya *et al*., 1993; Vertessy *et al*., 1996; Vertessy *et al*., 1997; Watson *et al*., 2001; Bren *et al*., 2010). The present study, however, is the first to quantify the spatiotemporal forest growth over the catchments to help explain observed streamflow. In this section, published results will be evaluated against quantified forest growth and streamflow trends in the present study.

8.3.3.1. Selective logging of Black Spur catchments

Silvicultural practices in regrowth eucalypt forests of Tasmania and Victoria are increasingly focused on using thinning practices to reduce rotation lengths (Connell *et al*., 1999; Whiteley, 1999). When the growth rate of a forest begins to decline (i.e at $Tmax_{fg}$), thinning is known to boost stand productivity (Brown, 1997; Smith *et al*., 1997). In Tasmania, commercial thinning takes place for forests aged 25-40, with a 50% *BA* reduction prescribed for forests with a minimum *BA* of 32 m^2 ha^{-1} (Forestry Tasmania, 2001). In Victoria, stands aged 20-40 with at least 30 m^2 ha^{-1} *BA* are thinned using 50% *BA* reductions (Department of Natural Resources and Environment, 1997). Using the Kuczera curve as a reference, thinning occurs around

the time when the regenerating forest, after clearfell harvesting, uses the most amount of water. Below, the evaluations of streamflow changes due to thinning are relative to regrowth levels and not pre-disturbance mature forest conditions.

Jayasuriya *et al* (1993) undertook a paired catchment study using Ettercon 3 as a control catchment to evaluate Black Spur treatments on streamflow. Five years of pre-treatment data were calibrated against Ettercon 3 using a simple linear regression model:

$$Q_{treat} = a + bQ_{cont} \qquad [8.1]$$

where Q_{treat} and Q_{cont} are annual runoff for treated and control catchments respectively, and a and b are regression coefficients. The calibrated model was applied to post-treatment data to extract the residuals, which were assumed to represent the treatment effect. In assuming the residuals represent the treatment effect, the calibration period needed to consist of the same vegetation driven streamflow trends for both the treated and control catchments. This assumption may be plausible for forest consisting of old-growth as the vegetation dynamics result in minimal streamflow trend, but for regrowth the pre-treatment conditions are likely to be different for the control and treated catchments.

By assuming the paired catchments had similar pre-treatment streamflow trends, Jayasuriya *et al* (1993) found streamflow increases of 25-30% (130-150 mm year^{-1}) for Black Spur 1 & 3 over eleven post-treatment years. Using the non-patch cut area of Black Spur 1 to represent natural growth rates of Black Spur catchments, table 8.2 shows growth rates began to drop ($Tmax_{fg}$) at age 37, around the time when treatments took place. In comparison, Ettercon 2&3 had $Tmax_{fg}$ at 20.47 years of age, which suggests the same aged control and treated catchments were at different stages of development during calibration. During the calibration period, Ettercon consisted of a progressively declining growth rate between 32-38 years of age, whereas Black Spur was approaching a maximum growth rate. Given the shape of the Kuczera curve reflects the inverse of forest growth rates, the variability in pre-treatment growth rates may have resulted in variable streamflow trends between control and treated catchments. As a result, streamflow trends after the 1939 fire may have

confounded the streamflow changes attributed to the treatment effects. This example demonstrates the importance of forest growth models for evaluating the suitability of control catchments in paired catchment studies.

With streamflow changes due to 1939 fires confounding the treatment effects, identifying both trends simultaneously using the streamflow modelling procedure developed in this study was challenging. The simulation exercise of chapter seven demonstrated in section 7.3.2.2 (figure 7.8) that data length at Black Spur and Ettercon catchments are very short and cause problems with parameter inference. Section 7.3.2.3 (figure 7.10a) showed that when the data range consists of the 1939 growth phase at Ettercon and Black Spur catchments, parameter inference is highly uncertain. Section 7.3.2.6 used a synthetic data extent reflective of the hydrological time series to show that the parameter inference problem was ill posed using the existing climate filter. Figure 7.15 shows the model requires a baseline value from which the 1939 trend begins and ends from (i.e. streamflow at old-growth), and this information was not available as stream gauging began in the 1970's. For this reason, this section places emphasis on understanding how forest growth responses correspond to published streamflow trends that use paired catchment studies, whereas section 8.3.2.2 evaluates the hydrological model structure on clearfelled old-growth forest catchments.

Without recognising the pre-treatment regeneration processes over the stream gauging period, Jayasuriya *et al* (1993) concluded that streamflow increases can be achieved by artificially reducing forest density with thinning practices. Such conclusions are contrary to findings by Fife *et al.* (2002) and Jarvis (1975) who found there is no significant increase in ET between thinned and unthinned sites. The discrepancy between results are likely attributed to a combination of the following reasons; the simple regression in [8.1] not capturing the climatic variance over the short calibration period, the 1939 regeneration dynamics confounding the results as discussed above, or the differences in forest ages between the studies.

Fife *et al.* (2002) thinned 5 year old plantations that where still expanding in resource capture and rapidly increasing in growth rates, whereas the Black Spur catchments were thinned at around $Tmax_{fg}$ when the catchment was already fully utilising the

site's water resource. With consideration for forest regeneration processes, Goodwin (1990) suggests larger trees tend to respond more slowly to the increase in available resources after thinning, but the response is of a longer duration. The duration of growth response to thinning is determined by the thinning intensity and rate at which the removed *BA* is replaced (Brown, 1997). Interpreting this process from a hydrological perspective, Jayasuriya *et al* (1993) and Fife *et al.* (2002) collectively found that thinning larger trees results in a slower and prolonged streamflow increase compared to a rapid recovery to pre-treatment conditions for young forests, as larger gap sizes in older forests required a longer time to be filled in by a smaller number of trees. It is also evident that the magnitude of increase depends on the degree of resource capture at the time of treatment, with higher streamflow increases if treatment occurs when the forest regeneration phase is closer to *Pmax*. For these reasons, it is plausible for Jayasuriya *et al* (1993) to observe streamflow increases after thinning 60% of a 38 year old forest considered to be limited by energy rather than water. Similar results were also observed after thinning Blue Jacket catchment, which consists of vegetation similar to that found at Black Spur (Bren *et al*, 2010).

It is evident that when thinning occurs, the water resource becomes available for the retained trees, which increases growth rates and water use of retained trees. Figure 8.5(a) shows how *BA* of a 24 year of stand of *E.regnans* responds to different levels of thinning (La Sala, 2007), whereas Figure 8.5(b) provides cumulative stand volumes of Black Spur and Ettercon catchments using the parameter estimates generated in table 8.2. The contrasting growth rates between control and thinned forest in figure 8.5 reflect the differences in development of water conducting *SA*, and hence differences in the changing rates of *T* (Dunn & Connor, 1993). It is evident that when the control catchments begin to decrease in growth, the thinned catchments increase resource capture for growth until the forest reach the site's growth capacity.

Brown (1997) suggests that as *BA* of thinned stands approach that of unthinned stands, the rate of increase will decline and *BA* should not exceed that of the unthinned stand. However, if the thinned and unthinned stands have different growth potentials due to site quality then a thinned stand can potentially exceed that of an unthinned stand. For this reason, figure 8.5 suggests Black Spur 2 has a higher

growth potential than Ettercon 2&3; keeping in mind Black Spur 2 and 3 growth models are uncertain with only 7 sample plots used in each. It is also evident in figure 8.5 that for the highly thinned sites, the retained trees did not reach the site's growth capacity. The heavily thinned stand in figure 8.5(a) and heavily thinned Black Spur 3 catchment in figure 8.5(b) both decreased in growth rates before the reduced number of retained trees reached the catchment resource capacity. This would potentially result in streamflow increases until a complete harvest rotation stimulates regrowth as selectively logged forests suppressed new regeneration due to shading and at the same time were not able to use the whole catchment's resources.

Table 8.2 also shows that Black Spur 3 has a significantly reduced maximum growth rate (*Pmax*) compared to Black Spur 1, and it is evident that as the intensity of the thinning increases, *Pmax* decreases, as available water and other resources are not used by the reduced number of retained trees. Also note in figure 8.5 that the non-patch cut area of Black Spur 1 has a sustained growth trend around the time when the Ettercon catchments began to decrease. This suggests the suppressed growth in the patch cut area increased radiation for retained trees due to edge effect and increased water availability due to lateral subsurface flow processes from the patches, resulting in increase growth of the retained trees (Bassett & White, 2000). Considering Jayasuriya *et al* (1993) found streamflow increases at Black Spur 1, not all available water was utilised by the retained trees; keeping in mind the calibration phase had confounding factors due to the 1939 fires.

From a forest hydrology management perspective, it is important to recognise that prescribed thinning aims to reduce the overall logging rotation of the final harvest from approximately 90 to 65 years (Whiteley, 1999). As streamflow progressively increases towards old-growth conditions between ages 65 and 90, shorter rotations result in younger forest on average. Although more intensive thinning may result in initial increases in streamflow, this leads to shorter rotations rates of faster growing trees to counteract the water gains. For this reason, integrated catchment management principles are required to determine an appropriate balance of the counteracting harvest management strategies.

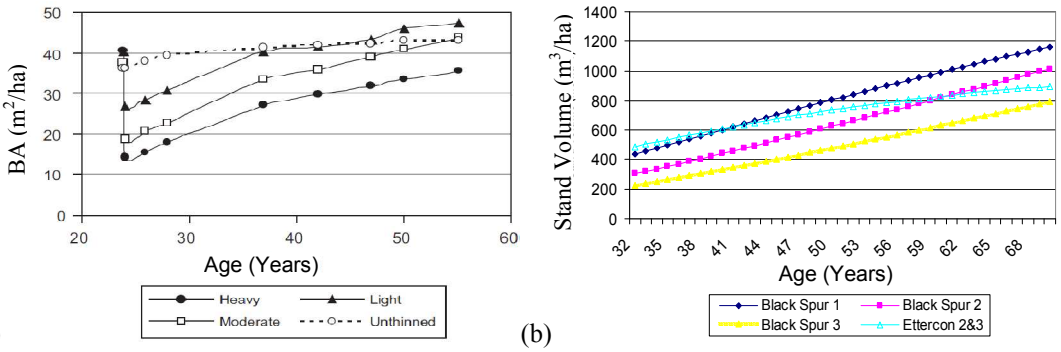

(a) (b)

Figure 8.5: (a) Mean stand basal area (BA) for heavy (65%), Moderate (50%) and Light (33%) treatments over time (from La Sala, 2007), and **(b)** Stand volume for Black Spur 1, 2, and 3 and Ettercon 2&3 using the parameter values in table 8.2.

8.3.3.2. Clearfell logging of Myrtle 2 and Picaninny catchments

Watson *et al* (2001) undertook a paired catchment study on treated catchments, Myrtle 2 and Picaninny, and applied a multiple regression model using monthly rainfall data to address limitations with the short pre-treatment datasets. In order to place confidence intervals around the predictions, statistical assumptions associated with the model were accounted for by; log-transforming the streamflow data to address heteroscedasticity, using a sinusoidal trigonometric term as an independent variable to addressed seasonality, and AR1 model to address serial correlation. The model found that for the 12 years of post-treatment data at Myrtle 2; an increase in streamflow of almost 400 mm peaked about 2-3 years after treatment, fell to pre-treatment levels after 5 years and continued to fall to a minimum of approximately 200 mm about 10 years after treatment. Near the end of the experiment period, a psyllid infestation occurred, which lead to crown dieback and partial streamflow recovery in the last two years.

The present study extended the streamflow dataset for an extra decade and found very similar results using the ellipse function and gamma function to identify the streamflow trend. Results found that streamflow increased to a maximum of 397 mm before streamflow dropped to pre-treatment levels after 4.3 years, and continued to drop until the end of the dataset. The model predicts maximum streamflow losses of 188 mm approximately 80 years after treatment. The delayed recovery in streamflow may be a result of the psyllid infestations and drought conditions over the last decade reducing growth rates and prolonging the time for the forests to reach maximum growth rates, a time when streamflow is thought to begin the recovery phase.

For the Picaninny catchment, Watson *et al* (2001) used 22 years of data and found an almost immediate peak in increased streamflow, which fell to pre-treatment levels after 9 years and continued to stay below pre-treatment levels for the rest of the data duration. The differences in initial streamflow increase trends between Myrtle 2 and Picaninny have been attributed to regeneration failure at Picaninny in the first five years after treatment (Watson *et al*., 2001). Comparing variability in streamflow trend between Myrtle 2 and Picaninny suggests the ellipse function may be too rigid for capturing the plethora of "natural" regeneration processes. The variable rates of resource capture during early regeneration require a two parameter non-linear function to provide more flexibility at addressing differences in streamflow trends.

Recently, Bren *et al* (2010) revisited Picaninny using the same methodology introduced by Watson (2001) on an extended dataset, to find the 1997-2007 drought resulted in marked changes in the behaviour of Picaninny with respect to the Slip control catchment. Both studies found annual flow reached a peak of approximately 300 mm relative to the Slip control catchment before declining to pre-logging levels after approximately 8 years and continuing to decline with a maximum reduction of around 200 mm per annum. As the streamflow has become ephemeral in the most recent years, whereas the control catchment continues to flow, the data suggests that 34 years after treatment there is no sign of recovery. Figure 8.6 provides the results for the Picaninny streamflow trend using the gamma and ellipse function to show an increase in streamflow of 319 mm for the first 5.7 years followed by a maximum decrease in streamflow of 111 mm, 15.8 years after the treatment.

In figure 8.6, the streamflow data superimposed over the trend shows there were signs of streamflow recovery during the very wet period around 1996, followed by streamflow reductions over the drought period between 1998 and 2010. It is evident that the gamma function attempted to accommodate for these contrasting climatic conditions pre- and post- drought, but in doing so under- and over-estimated streamflow conditions pre- and post-drought respectively. The model structure was unable to recognise the complex streamflow trend as the climate filter was calibrated under conditions very different to the climatic variation observed post-treatment, which raises limitations with the climate filter and the model structure that uses a

non-linear function to represent the dynamic changes in streamflow. It is evident the gamma function and climate filter are not able to account for decadal climatic variations due to drought periods.

Addressing the climate filter limitations may involve the recommendations already discussed in section 7.4.1, whereas the non-linear curve may be improved with a trend that reflects the inverse of the regeneration processes considering streamflow and forest growth are negatively correlated. This may involve predicting multivariate responses (i.e. streamflow trend and forest growth trend) instantaneously from the same set of explanatory variables using an approach involving multiple response non-linear regression (Breiman & Friedman, 1997). Rather than undertaking separate regressions on each response variable as undertaken in this study, the objective would involve finding a correlation between the response variables (i.e. streamflow and forest growth) to improve predictive accuracy of the streamflow modelling procedure. As both response variables are strongly correlated and respond to the same environmental conditions, the highly developed forest growth models generated in the present dissertation would provide a useful representation of the regeneration processes for a multiple response non-linear regression model. Other important research recommendations are discussed in the conclusion chapter.

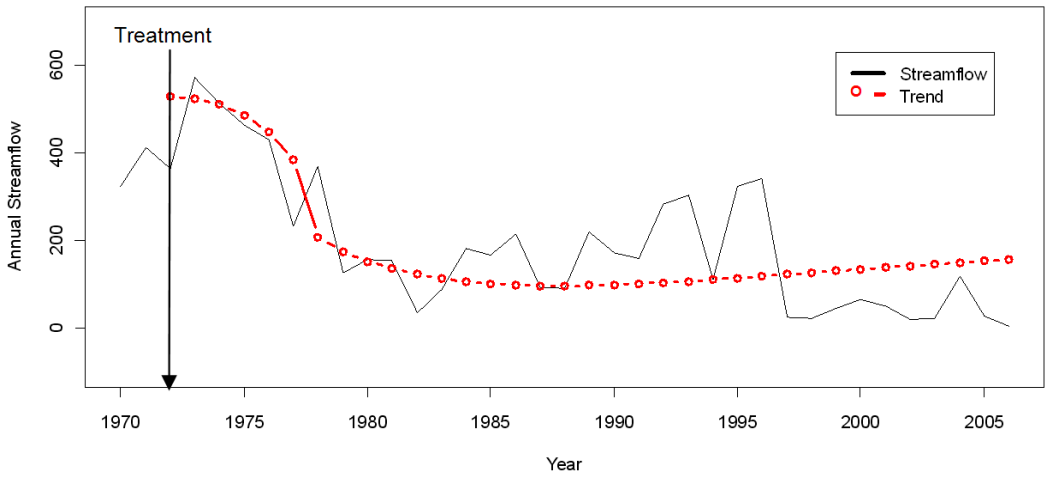

Figure 8.6: Annual streamflow at Picaninny and the predicted trend using the ellipse and gamma function.

8.4. Conclusion

The present chapter brought together a very broad range of statistical modelling techniques developed in the previous chapters to demonstrate how modelling forest growth may be used to explain vegetation-induced streamflow trends. The procedure involved extrapolating mixture models and mixed effects models to predict vegetation layer specific stand characteristics. The resulting spatial heterogeneity was detailed enough to distinguish different ecosystems and differentiate the stand productivity across each catchment. The ridge regression, logistic and gamma models all showed similar spatial heterogeneity in stand productivity. Actual estimates differed between mixed effects models as the temporal dataset was decommissioned for 15 years and predominantly collected prior to 1993. For this reason, the growth models responded strongly to stand characteristics prior to 1993 whilst coupled to the spatial distributed 2007 LiDAR data.

Catchment-scale forest growth curves demonstrated that stand productivity could be explained by changes in resource availability after treatment effects. The non-linear functions in figure 8.3 were sensitive to short data lengths, which meant catchment data needed to be merged in figure 8.4 to capture a general growth trend of *E.regnans* over a broad age-class range. Results found only the gamma function converged for merged data, suggesting *E.regnans* growth is the inverse of streamflow trends modelled using the Kuczera curve. To further support this hypothesis, a generalised growth response of all merged data resulted in the $Tmax_{fg}$ value corresponding well with $Tmax_{sf}$ modelled in streamflow by Kuczera (1987).

Due to study limitations relating to length of the datasets, timing of treatment effects, and confounding drought effects, the hydrology model failed to simultaneously identify streamflow trends attributed to the 1939 fire and treatment effects in selectively logged catchments. Instead, forest growth models were evaluated against published paired catchment studies to demonstrate how post-treatment effects in such studies may be confounded by different growth processes in control and treated catchments over the calibration period. A hypothesis was also presented to explain contrasting catchment responses to thinning reported in literature, suggesting; (a) thinning at later ages results in slower and prolonged forest growth and streamflow

responses compared to younger forests, and (b) the magnitude of streamflow increase depends on the difference in the degree of resource capture (i.e. water) by the forest immediately pre- and post-treatment.

In evaluating clearfelled catchments, the hydrology model results agreed reasonably well with published literature. To improve results, the ellipse function may be replaced with a non-linear function to account for the effects of variable post-treatment regeneration success on streamflow. In addition, to address the confounding effects of prolonged drought conditions, a multiple response non-linear regression procedure may replace the gamma function that has only one general form not malleable with complex climatic conditions. As response variables streamflow and forest growth are correlated in their response to drought, a multiple response regression may improve streamflow predictions using forest inventory data and explanatory variables common to both response variables.

The present study distinguishes itself from previous forest hydrology research by using forest growth models to explain streamflow trends attributed to forest regeneration processes. A parsimonious hydrology model framework was intentionally designed to allow for integration of a complex representation of hydrologically relevant forest regeneration processes using forest inventory data. In rigorously quantifying forest regeneration processes, a forest growth modelling methodology was developed that may prove useful for a very broad range of forest management applications, particularly for timber inventory evaluation. From a forest hydrology perspective, the most valuable outcome of this dissertation is the compilation of evidence demonstrating the inverse relationship between forest growth and long-term changes in streamflow. In doing so, the study draws attention on the importance of utilising forest inventory databases for managing forested water resources.

Chapter 9: Conclusion

9.1. Summary of dissertation

A review of Tasmania's and Victoria's forest hydrology models, Macaque and TasLUCaS, was undertaken to determine how well their estimates inform policy makers of the potential impacts of land cover disturbance on the water resource. It was found that the most significant limitation with the present Tasmanian and Victorian forest hydrology management system is that the model applications are not data-driven with a crucial spatiotemporal representation of hydrologically relevant vegetation dynamics that influence forest water use.

To address this limitation, a review of forest regeneration processes related to forest water use was undertaken to provide supporting evidence for the development of a model that quantifies forest growth for explaining decadal streamflow trends. The review supported the argument that forest hydrology models underutilise existing forest inventory and forest mensuration databases for managing the forested water resource. Detailed forest inventory data exist for most forested catchments in south eastern Australia and this valuable information should be used to generate hydrologically relevant forest growth models for managing changes in streamflow conditions.

Building on existing forest hydrology models that only use catchment-specific forest age and broad forest type information to estimate an ungauged catchment's forest water use, the present study explicitly quantifies spatiotemporal forest growth to explain streamflow trends. This new approach builds on the work undertaken by Kuczera (1985) who implicitly explained decadal streamflow trends with expected forest growth rates. Although the Kuczera curve is arguably the most regarded empirical equation in Australian forest hydrology research, no research to date has explicitly demonstrated how forest growth models may be used to identify the Kuczera curve in streamflow data. For this purpose, the proposed model structure evaluated changes in forest water use after a land-cover disturbance with a detailed account of hydrologically relevant vegetation dynamics extracted from regionally available forest inventory data.

The model structure runs on an annual time step and largely builds on the climate-bushfire yield response model produced by Kuczera (1985); as the Kuczera curve has favourable properties that reflect the inverse of how forest growth rates change over the regeneration period. The present study extends this work by formulating an improved climate filter to explain climatic variability in streamflow. The climate filter reduces the overall residual standard error of the model as a means to extract the streamflow trend with the greatest level of confidence. As the Kuczera curve does not accommodate for the potential increase in streamflow immediately after a land-cover disturbance, the proposed model structure integrates an ellipse function to quantify the extent and duration of the streamflow increase under circumstance where the data suggests an increase exists. To allow for the forest growth model to be integrated into the Kuczera model framework, the forest growth rates were modelled using the same gamma function Kuczera (1985) used to explain streamflow trends.

In order to produce a spatiotemporal representation of forest growth over a forested catchment, LiDAR data was used to stratify a multilayered eucalyptus forest and characterise the structure of specific vegetation layers. The novel methodology used mixture models with a wide range of theoretical distribution functions to produce canopy profile indices that may prove useful for a whole range of forest management applications. In the present study, the LiDAR indices were used on permanent plot data to predict overstorey stand volumes and basal area, and understorey basal area of 18-, 37-, and 70-year old Mountain Ash forest with variable density classes. Mixed effects models were used to capture the spatial heterogeneity and temporally polymorphic nature in forest growth over each catchment's stream-gauge monitoring period. Mixed effects models were applied to allow for growth curves to vary between plots by breaking down the regression coefficients into a fixed component common to the population and a random component specific to each plot. As the random effects reflect the departure of individual plots from the population mean, plotting the estimated random effects against the LiDAR indices determined which indices explain inter-plot variation, hence predicting spatiotemporal variability in stand volume.

Using the spatially distributed LiDAR indices and forest growth models, spatiotemporal models of forest growth were lumped to the catchment-scale by calculating for each growth year the average stand volume per hectare for each catchment. The catchment specific forest growth model parameter values were then used to explain the decadal streamflow trends published in previous studies and compared to the modelled trends in the present study.

9.2 Limitations of the present study

The present study was based on long-term experiments, established to investigate impacts of forest harvesting on Melbourne's water supply. The most significant problem with the experiment design is the small size of the six catchments, ranging between 7.4 and 33.5 ha. The region's complex subsurface zone consists of 15 m deep soils with high permeability and water-holding capacity, which raises uncertainty in delineating boundary conditions with ground surface models using DEM data (pers. comm. Kuczera, 2010). The extremely deep soils coupled with the large ratio of catchment circumference to catchment area makes it difficult to estimate rainfall area contributing to streamflow yields. It is highly probable that some of the measured streamflow was sourced from rainfall external to 'catchments' due to complex subsurface flow processes, and some of the rainfall over the 'catchments' leaked across ridgelines into adjacent catchments. Considering DEM data is the only option for delineating catchment boundaries, the relative proportion of water moving between adjacent catchments may be significantly reduced using gauged catchments larger than 10,000 ha as this would reduce the catchment circumference to catchment area ratio.

The experiment design is also limited by the temporal extent of the hydrological time series, corresponding timing of treatments, drought, and growth phase of the 1939 regenerating forests. Considering mountain ash forest growth rates at Black Spur and Ettercon were expected to peak approximately around the time when stream gauging commenced, stream gauging began when changes in growth rates were minimal and about to decline. The treatment effect counteracted the declining growth rates by increasing resources for retained trees, resulting in changes in forest growth rates being subdued over the stream gauging period. This was not the case for Picaninny

and Myrtle 2, where old growth was clear-felled and replaced with forest that had rapidly changing growth rates.

The conditions at all the catchments was complicated by prolonged drought conditions between 1998 and 2008, which coincided with the period when permanent growth plots and stream gauges were decommissioned at Black Spur and Ettercon. The gap in available data was followed by one observation in 2008 strongly affected by drought conditions that depleted the catchment groundwater store and affected the rainfall-runoff relationship (Bren *et al*., 2010). This limited the extent to which the multiple regression models where able to accurately account for changes in climatic variance and identify streamflow trends.

It should be emphasised that these limitations are common to experiments in Australia focused on the hydrology of eucalypt forests. Despite these limitations, the stream gauged study site consists of a rare forest inventory with a wide variety of assemblages of forest density and structural types. The area over which the forest inventory encompasses is suitably sized for a PhD research project primarily aimed at developing hydrologically relevant forest growth models to advance the field of forest hydrology.

9.3. Specific conclusions

9.3.1. Limitations of existing forest hydrology models.

Although Macaque has a very detailed representation of the forest hydrological system, the complexity of the model does not reflect the data availability over the regions that the model was designed to undertake predictions for. For this reason, Macaque is a useful model for improving our understanding of hydrological processes within experimental sites but is unsuitable for regional management applications. Macaque contains over 70 parameters, many of which are sensitive to *ET* estimates, and yet past applications of the model have only involved forest age data to reflect the spatiotemporal changes in forest characteristics that influence *ET* (Peel *et al*., 2002a).

Macaque hypothesises that streamflow trends after a land cover disturbance are a result of changes in *LAI* and g_s with age. It is evident that Macaque's forest water use predictions are not data-driven as regional *LA* measurements are often non-existent due to; the laborious nature of destructive sampling of *LA*, and complications that exist with field estimates due to vertical orientation of *E.regnans* leaves and line-of-site obstruction by understorey vegetation. For these reasons, the empirical equations that underpin the *ET* estimates are based on *LA* measurements collected at one point in time in four *E.regnans* stands. As it is known that *LA* is highly variable for a given forest age due to site-specific water deficit conditions, there is a great deal of uncertainty as to how the seasonal and inter-annual variability of *LA* affected the measurements used to represent decadal changes in *LA* over vast regions.

TasLUCaS is a forest hydrology management tool that erroneously assumes forests converted into plantation or regenerating forest will have the same hydrological impact on the water resource for a given age. The model simply fits the Macaque *LAI:Age* curve through 8 paired catchments, five forest and three pine plantations, to formulate a generalised equation that is meant to represent changes in streamflow for any catchment in Tasmania. The model structure uses annual average rainfall data to determine expected streamflow levels when the forest is old-growth and then applies the calibrated *LAI:Age* curve to forest or plantation age data to estimate forest water use relative to the old-growth streamflow levels. It has been shown that this simplified model structure produces highly erroneous results as the model is not data-driven with site-specific information on vegetation dynamics.

9.3.2. Relationship between forest productivity and forest water use

A review of plant physiological processes related to forest water use was undertaken to outline the physical and physiological characteristics that regulate the water flow pathway of timber yielding forest types and plantations. The overall objective was to determine how water use efficiency (*WUE*) over a life time of a timber stand influences the relationship between forest productivity and forest water use. It is evident that forests regulate productivity and water use with mechanisms that function over a range of time scales with: short-term diurnal responses to climate involving stomatal regulation; medium-term responses to seasonal climatic

variability and available soil water involving shifts of resource allocation from leaf to root development; and long-term responses imposed by competition for finite resources involving structural changes to a stand's leaf area, sapwood area, and root biomass for regulating the hydrological equilibrium of a catchment.

The review found that forest growth models may be used to quantify catchment level forest water use once considerations are made for the causal plant physiological processes and environmental variables that influence *WUE*. To generate a parsimonious regional relationship between forest productivity and water use, a separate relationship needs to be generated for broadly uniform climatic conditions to account for the negative linear relationship between vapour pressure deficit and *WUE*. Also, a separate relationship may be required for soil types with very contrasting soil moisture holding capacity and soil penetrability conditions; as such conditions affect energy distribution between root and above-ground biomass development, which affect *WUE*. Differences in inter-specific root system architecture between *Symphyomyrtus* and *Monocalyptus* species will also affect *WUE* for the same reasons. Finally, the extent of the limitation of water resource due to competition and environmental pressures affect *WUE,* which is the reason why pre-canopy closure forests, understocked forests without water limitations, and higher quality sites are less *WUE*, whereas intensive systems such as plantations and water limited forests are more *WUE*.

Considering the close proximity of the small catchments, the study site consists of relatively uniform climatic and soil conditions and is dominated by vegetation consisting of *Monocalyptus* species (Langford & O'Shaughnessy, 1977). This suggests that the environmental conditions for all sites will have the same pressures on *WUE*. The different treatment effects between catchments resulted in different aged forests and vegetation densities post-treatments. As all sites represent high quality and well stocked sites without water limitations, it is likely that WUE may only be slightly variable when comparing pre- and post- canopy closure forests. For these reasons, the relationship between forest productivity and forest water use would be very similar for all the study sites, allowing for the use of forest growth models to explain changes in streamflow trends.

9.3.3. Hydrologically significant spatial characteristics of forest growth

Discrete Light Detection and Ranging (LiDAR) data were used to stratify a multilayered eucalyptus forest and characterise the structure of the vertical profile. A novel methodology was presented that may prove useful for a very broad range of forest management applications, particularly for timber inventory evaluation and forest growth modelling. In this study, LiDAR data were used to stratify a multilayered eucalyptus forest and characterise the structure of specific vegetation layers for forest hydrology research. A methodology was presented that produces canopy profile indices of understorey and overstorey vegetation using mixture models with a wide range of theoretical distribution functions. Mixture models provide a mechanism to summarise complex canopy attributes into a short list of parameters that can be empirically analysed against stand characteristics. The LiDAR indices prove useful for forest hydrology research as a stand's crown height, density, depth, and closure, influence aerodynamic properties of the forest structure and the amount of transpiring leaf area, which in turn determine *ET* rates.

Few studies have explored theoretical distribution functions to represent the vertical profile of vegetation structure in LiDAR data. All prior studies have focused on a Weibull distribution function, which is unimodal. In a complex native forest ecosystem, the form of the distribution of LiDAR points may be highly variable between forest types and age classes. The present study compared 44 probability distributions within a two component mixture model to determine the most suitable bimodal distributions for representing LiDAR density estimates of Mountain Ash forests in south-eastern Australia. An elimination procedure identified eleven candidate distributions for representing the eucalyptus component of the mixture model.

The methodology was demonstrated on a sample of plots to predict overstorey stand volumes and basal area, and understorey basal area of 18-, 37-, and 70-year old Mountain Ash forest with variable density classes. The 70-year old forest has been subjected to a range of treatments including: thinning of the eucalyptus layer with two distinct retention rates, removal of the understorey, and clear felling of patches

that have 37 year old regenerating forest. It was demonstrate that the methodology has clear potential, as observed versus predicted values of eucalyptus basal area and stand volume were highly correlated, with bootstrap based r^2 ranging from 0.61 to 0.89 and 0.67 to 0.88 respectively. Non-eucalyptus basal area r^2 ranged from 0.5 to 0.91.

9.3.4. Hydrologically significant spatiotemporal forest growth models

Mixed effects models were used to quantify the spatial heterogeneity and temporally polymorphic nature in forest growth. Applying both the logistic and gamma equation, non-linear mixed effects models were generated for each catchment using permanent plot data consisting of differing plot sizes and treatment effects. It was demonstrated that mixed effects models with their flexible variance-covariance structure are appealing for the analysis of permanent plot data of forest stand attributes. The mixed effects models estimated both the fixed and random coefficients simultaneously to enable the between plot variability in stand volume to be quantified as a random effect whilst defining a common fixed functional structure. Such a modelling approach allowed for predictive models to be formulated for extrapolation over a catchment by predicting the value of the random coefficients at unsampled locations. Considering the highly variable fixed coefficients between the catchments and the large variation among the random coefficients, it was evident in the results that the models captured the highly polymorphic nature of the growth curves over the heterogeneous native forest environment.

It was demonstrated that the mixed effects models addressed the challenges affiliated with the hierarchical structure of permanent plot data by modelling the nested source of variability with a variance-covariance structure to allow for the non-constant correlation between sample plots to be accounted. Adjustments to the variance-covariance structure were necessary using a power variance function to avoid an inappropriate variance-covariance structure that would otherwise result in erroneous predictions due to violation of the basic distributional assumptions. Although the presence of random effects in the model also implies a correlation structure for the data, precisely what that structure was within a particular plot was difficult to determine as there is no closed-form solution for the within-plot correlation matrix

when the random effect enters the model in a non-linear fashion. For this reason, the present study opted to model the autocorrelation structure indirectly through the random effects structure without any direct adjustments to the variance-covariance matrix; which was further justified as the autoregressive (AR) and moving average correlation (MA) models contributed little to reducing the predictive error.

The need to separately model each catchment's forest growth raised concerns relating to the adequacy of each catchment's sample size. Once the present modelling exercise addressed the variance-covariance structure and incorporated covariates (i.e. LiDAR indices), the model structure resulted in approximately 5 to 13 degrees of freedom. As Black Spur 2 and 3 only consisted of 7 plots each, the degree of freedom of the gamma model of 6 and 5 respectively was too high. The small sample size also meant the relationship between the LiDAR indices and random effects was highly unstable, introducing uncertainty when extrapolating the predictions. The other catchments had an adequate sample size given the complexity of their corresponding model structure.

For predicting stand volumes at sites with no prior field measurements using spatially distributed LiDAR indices, it was necessary to assign a value of zero to the random effects parameters and make predictions using covariates within a fixed effects model. For this reason, it was important to develop a model that had most of the random effects explained with LiDAR indices in order to make the fixed effects model as predictive as possible. It was demonstrated that the model's predictive capacity was much greater for a mixed effects model with random components compared to a fixed model with LiDAR indices. For this reason, to improve predictions of the forest growth models, it would be necessary to address the limitations and shortcomings of the LiDAR indices used as covariates.

9.3.5. Climate filter and simulation exercise to evaluate the model structure

A methodology was presented that uses rainfall time series to produce explanatory variables that capture the climatic variance in streamflow. By aggregating monthly rainfall data using a large array of combinations, a total of 24420 models were compared using the standard error of residuals to identify the optimal model. In

doing so, the climate filter reduced the overall residual standard error in the model structure in order to extract the magnitude and duration of streamflow trend with the greatest level of confidence. Compared to the original model proposed by Kuczera (1987), the results showed that the most optimal climate filter explained 23% and 45% more of the climatic component of the streamflow variance in Myrtle 1 and Slip catchments respectively.

With consideration for the climate filter's ability to account for climatic variance, a simulation exercise was undertaken to demonstrate how the model structure provides an effective way in isolating a decadal streamflow trend in synthetic hydrological time series. It was found that to improve parameter inference in the proposed model structure it is necessary to increase the $Lmax{:}\sigma$ ratio, and as $Lmax$ is pre-defined in the catchment's condition due to the developmental stage of the forest, an accurate climate filter that decreases σ in the model structure is a crucial objective. For this reason, future research needs to focus on developing a methodology that improves the climate filter.

It was also shown that for a given σ (due to limitations in the climate filter), to infer a streamflow trend in a well posed problem it is necessary for the data length to capture the predominant features in the gamma function. The parameter inference problem is improved when the data length includes an adequate representation of observations; before and after year $Tmax_{sf}$, around the "point of inflection" in the skewed tail end of the gamma function, and during the time when the catchment is old growth. As most streamflow datasets do not contain observations during all of these periods, it has been demonstrated that parameter inferences significantly improve if the model structure includes an assumption on the baseline value from which the trend begins and ends (i.e. assumed streamflow at old growth). The simulation exercise demonstrates that the treated catchments consist of short hydrological time-series, which may be ill-posed without knowledge on streamflow conditions when the hydrological system was at equilibrium and the forest was old-growth.

9.3.6. Explaining streamflow trends with forest growth models

To explain streamflow trends with forest growth models it was necessary to spatially extrapolate the mixture models and mixed effects models across each catchment. Results showed that by stratifying the canopy profile using mixture models, it was possible to predict stand characteristics specific to each vegetation layer and distinguish rainforest along the riparian strips from eucalypt forests on hillslopes. The ridge regression, logistic and gamma model were all able to differentiate low and high yielding eucalypt stands. The models showed similar spatial heterogeneity in stand characteristics, but the actual estimates differed between models. The ridge regression model was considered to be most accurate at estimating stand characteristics as the procedure involved relating 2007 LiDAR data to 2009 field measurements, whereas the mixed effects models were complicated by a temporal component that applied a dataset decommissioned for 15 years and predominantly collected prior to 1993.

Catchment-scale forest growth curves were produced to show different treatment effects resulted in differences in stand productivity. It was found that the patch cut area at Black Spur 1 had suppressed growth due to shade effects, resulting in the surrounding non-patch cut areas having enhanced growth due to increased radiation and available water. Black Spur 2 and 3 demonstrated a typical response of forest growth to reduced stocking densities with increased $Tmax_{fg}$ and decreased *Pmax* corresponding to thinning intensity. The Myrtle 2 growth models were erroneous due to the short datasets being confounded with tree mortality caused by psyllid infestations, and drought conditions.

Short data lengths meant the results were sensitive to the non-linear function used to quantify maximum growth rates and timing of the growth peak; parameters considered important for explaining the nature of the decadal streamflow trend. To address this problem, catchment data was merged to capture the general growth trend of *E.regnans* aged 5 to 52. The results found that only the gamma function converged with the merged dataset, suggesting the gamma function was more appropriate at representing changes in forest productivity over the lifetime of an *E.regnans* forest. Considering the gamma function is the same function representing

streamflow trends in the "Kuczera curve", the result provides supporting evidence that forest productivity is inversely related to the vegetation induced streamflow trend. In generalising the forest growth process over the catchments, results showed that $Tmax_{fg}$ was estimated between 24.4 and 27 years of age, which coincides with the timing of minimum streamflow levels ($Tmax_{sf}$) Kuczera (1987) found for the same forest types. This provides further evidence that forest water use is related to forest productivity.

The evaluation of streamflow trends against forest growth curves was undertaken separately for the selectively logged (Black Spur), and clearfelled catchments (Myrtle 2 and Picaninny). For the selectively logged catchments, simultaneously identifying streamflow trends attributed to the 1939 fires and treatment effects was not possible considering; the length of the dataset, the timing of the treatment effects, and confounding drought effects in the most recent decade. For this reason, forest growth responses in thinned catchments were evaluated against published literature that used paired-catchment studies to identified streamflow trends. This lead to an evaluation of a crucial paired catchment assumption that; post-treatment residuals of a calibrated model are attributed to the treatment effect. It was demonstrated that the 1939 streamflow trends may have confounded the streamflow changes attributed to the treatment effects as the control catchment consisted of a progressively declining growth rate during calibration, whereas the treated catchments were approaching a maximum growth rate over the same period. Differences in regeneration phase suggests differences in streamflow trend during calibration

Contrasting results in literature on catchment response to thinning was also evaluated using forest growth models. It was found that the duration of streamflow response to thinning is determined by the thinning intensity and rate at which the removed *BA* is replaced. Thinning at a later age results in slower and prolonged forest growth and streamflow response compared to thinning of rapidly recovering younger forests. Also the magnitude of streamflow increase depends on the degree of resource capture by the forest at the time of treatment, and is greatest when the regeneration phase is close to *Pmax*. It was also shown that for heavily thinned stands with too few retained trees, forest growth reaches an asymptote below a catchment's resource

capacity and under such conditions streamflow increases will not retreat to pre-treatment conditions.

The gamma and ellipse model were used to identify streamflow trends in the clearfelled catchments and results agreed reasonably well with published studies for these catchments. Considering initial streamflow responses of Myrtle 2 and Picaninny varied due to contrasting regeneration success rates, it is evident that the ellipse function is too rigid at capturing the variable streamflow trends immediately after harvesting, and future research should consider a non-linear function. The gamma function is also not able to capture change in the behaviour of a catchment's hydrology when prolonged drought conditions affect climatic variability. As forest growth and streamflow trend are affected by drought conditions simultaneously, the gamma function may be replaced with a multiple response non-linear regression procedure. This would involve determining the correlation between the response variables (i.e. streamflow and forest growth) to improve the predictive accuracy of streamflow with forest inventory data and explanatory variables common to both response variables (Breiman & Friedman, 1997).

To conclude, the present study provides a highly novel approach in forest hydrology research as it is the first study to use forest inventory data to generate spatiotemporal forest growth models to explain vegetation-induced streamflow trends. In rigorously quantifying forest regeneration processes, a methodology was developed that may prove useful for a very broad range of forest management applications, particularly for timber inventory evaluation. The dissertation also provides a valuable contribution to forest hydrology research by compiling strong evidence that demonstrates an inverse relationship between forest growth and long-term changes in streamflow. In Australia, important water supply catchments are often forested, particularly in the mountainous terrain of the high yielding catchments supplying our large cities and the Murray Darling Basin. The research provides compelling evidence to utilise forest inventory data readily available over these vast regions for managing the forested water resource. Below are recommendations that provide for a future research direction.

9.4. Recommendation for future research

The advantage of the methodology presented in this study is that it draws heavily on forest inventory data to explain streamflow trends. The Department of Sustainability and Environment (DSE) has over 700 permanent growth plots across Victoria, with approximately 25% of these plots in ash forests of the Central Highlands and Central Gippsland Forest Management Areas (Department of Sustainability and Environment website, 2010). Many of these plots have been monitored since the 1960s, and some since the 1930s. Melbourne Water also has approximately 300 permanent plots in mountain ash, alpine ash and mixed species forests established in the 1970s and revisited on a 10 year cycle until the 1990s. Presently, Melbourne Water's forest inventory datasets are only archived in the form of original field sheets, and would provide a rich source of information in electronic form for forest hydrological studies as the plots are located in the following stream gauged water supply catchments: Wallaby creek (9,965 ha), Maroondah (10,400 ha), O'Shannassy (11,900 ha), and Upper Yarra (33,670 ha). Importantly, these catchments contain hydrological time series that spans several decades.

To complement the permanent plot data available for forest hydrology research, Melbourne Water and DSE recently collected LiDAR data over much of the Central Highlands forests of Victoria. In effect, 18.5 billion data points across Melbourne water catchments have been collected for an accurate representation of vegetation structure and stand characteristics. With the use of this data, the forest growth modelling procedure presented in this dissertation has great potential for forest hydrology research in these catchments.

To advance the present study, the methodology that generated spatiotemporal maps of stand *BA* may be enhanced to produce spatiotemporal maps of sapwood area (*SA*), a very strong surrogate for *T* rates (Dunn & Connor, 1993; Roberts *et al*., 2001; Macfarlane *et al*., 2010). Roberts (2001) undertook research into the allometric relationship between *BA* and *SA* for *E.sieberi* forest, a common species in Melbourne's water catchments, to result in an R^2 of 0.94. Vertessy (1997) collected data for 15 and 62 year old *E.regnans* forest and resulted in a *BA:SA* relationship with an R^2 of 0.95 and 0.69 respectively. As there is a strong relationship between

BA and *SA*, the spatiotemporal modelling procedure presented in this dissertation can be enhanced to estimate *SA* in the following way.

9.4.1 Producing spatiotemporal sap wood area maps with forest growth models

Sap flow through trees is often used to estimate instantaneous *T* and may be determined with a measure of sap velocity (v_s) through *SA* of a tree (Pfautsch *et al*., 2010). For tall eucalypt forests, differences in *T* with age is a result of differences in *SA,* as it has been found that mean daily v_s is relatively constant for different aged classes of *E.seiberi* (Roberts *et al*., 2001), *E.marginata* (Macfarlane *et al*., 2010), and *E.regnans* (Dunn & Connor, 1993; Vertessy *et al*., 1995). As a result, spatiotemporal *T* predictions may be developed by scaling up tree-level *T* measurements to a catchment-level using forest growth models that estimate spatiotemporal changes in *SA*.

To produce spatiotemporal maps of *SA*, the aim would be to develop a mathematical representation of the catchments regeneration process and determine how *SA* changes over this period. The present dissertation has demonstrated how a catchment's regeneration process may be effectively represented in mathematical form with mixture models and non-linear mixed effects models using LiDAR and permanent plot data. To estimate how *SA* changes with a regenerating forest, the methodology could be improved by addressing the fact that historically permanent plot data has not involved measurements of *SA* but temporal changes in *SA* may be estimated using a *BA*:*SA* relationship.

A tree-level *BA*:*SA* relationship may be formulated with extensive wood core sample measurements of *SA* and *BA* at one point in time over a range of forest age classes. A tree's *SA* may vary for a tree with a given *BA* depending on whether the tree represents a stand's dominant or suppressed tree. For this reason, to estimate tree-level *SA,* the *BA:SA* relationship needs to integrate explanatory variables that recognise each tree's position in the stand's forest structure. To scale up the *BA*:*SA* relationship to a catchment scale, spatially distributed *BA* estimates need to be made whilst preserving the tree-level *BA* distributions, as a stand's *SA* will vary for a stand with a given *BA* depending on the *BA* distribution of the trees.

To generate spatial maps of tree *BA* distributions, parameters from multi-modal mixture models of LiDAR vegetation hits may be regressed against parameters of multi-modal mixture models that characterise the *BA* distributions of trees (Zhang *et al*., 2001b; Liu *et al*., 2002; Zhang & Liu, 2006; Jaskierniak *et al*., 2010;). The regression relationship between parameters of the two mixture models may be used to extrapolate field measured *BA* distributions using LiDAR data, and the *BA:SA* relationship may be used to spatially estimate *SA* from the *BA* distributions.

The above section has described how to create a spatial map of *SA* distributions. The next stage would involve permanent plot data to extrapolate these results over time. Using the same methodology used in the dissertation, the permanent plot data would generate temporal changes in stand *BA* over the catchments, and a non-parametric approach would need to be developed to estimate likely changes in *BA* distributions over time given the vegetation structure and *BA* distribution at the time of data collection. The non-parametric approach would recognise that young forests have a *BA* distribution of trees that is unimodal and as the forest develops with suppressed and dominant trees, bimodal and multi-model distributions form. The overall objective would be to generate spatiotemporal *BA* distribution maps for the tree-level *BA:SA* relationship to convert these estimates into spatiotemporal *SA* maps.

Using the spatiotemporal *SA* maps, forest water use may be scaled up from tree- to stand-level by calculating stand-level sapwood-area-weighted mean sap velocity of trees, and multiplying this by the sapwood area of the stand (Vertessy *et al*., 1995). The research undertaken in the present study has provided a significant contribution towards the development of such a forest hydrology model. The novel approach demonstrated in the present study allows for the development of a range of data-driven hydrology models aimed at explicitly quantifying vegetation dynamics that influence vegetation-induced streamflow trends. The motivation behind the proposed modelling approach is to provide the forest hydrology community scientific reason to access the highly rich source of information embedded in forest inventory data presently underutilised for the management of the forested water resource

References

Adams, J., 1990. A computer experiment to evaluate regression strategies. *Proceedings of the Statistical Computing Section, American Statistical Association.*

Akaike, H., 1974. New look at statistical-model identification. *IEEE Transactions on Automatic Control* AC19: 716-723.

Albrektson, A., 1984 Sapwood basal area and needle mass of Scots pine (Pinus sylvestris L.) trees in central Sweden. *Forestry*, 57: 35-43.

Armstrong Agricultural Services & National Strategic Services, 2001. Executive Summary of Project Report.

Arnold, R., Bush, D. & Stackpole, D., 2005. Genetic variation and tree improvement. In: Nambier, S., Ferguson, I. (Eds.), *New forests. Wood production and environmental services.* CSIRO publishing, Melbourne.

Axelsson, P., 1999. Processing of laser scanner data—algorithms and applications. *ISPRS Journal of Photogrammetry and Remote Sensing*, 54: 138–147.

Barilotti, A., Sepic, F. & Abramo, E., 2008. Automatic detection of dominated vegetation under canopy using Airborne Laser Scanning data. SilviLaser, Edinburgh, UK.

Bassett, O.D. & White, G., 2000. Review of the impact of retained overwood trees on stand productivity *Australian Forestry*, 64: 57-63.

Battaglia, M., Sands, P., White, D. & Mummery, D., 2004. CABALA: A linked carbon, water and nitrogen model of forest growth for silvicultural decision support. *Forest Ecology and Management*, 193: 251-282.

Beadle, C.L. & Inions, G., 1990. Limits to growth of eucalypts and their biology of production. In: Dargavel, J., Semple, N. (Eds.), *Prospects for Australian forest plantations.* Centre for Resource and Environmental Studies, ANU, Canberra, pp. 183-193.

Beadle, C.L. & Mummery, D., 1989. Stand growth and development of leaf area index in young plantations of *Eucalyptus nitens* at 2X2 m spacings. *N Z For Res Inst Bull*, 151: 254–258.

Benyon, R.G., Marcar, N.E., Crawford, D.F. & Nicholson, A.T., 1999. Growth and water use of *Eucalyptus camaldulensis* and *E.occidentalis* on a saline discharge site near Wellington, NSW, Australian. *Agricultural Water Management*, 39: 229-244.

Beven, K.J., 2001. *Rainfall-Runoff Modelling. The Primer.* John Wiley & Sons Ltd, Chicester.

Connell, M.J., Raison, R.J. & Brown, A.G., 1999. Intensive Management of Regrowth Forest for Wood Production in Australia. A Review of Current Practice and Future Potential, Orbost, Victoria. CSIRO Forestry and Forest Products. 91 pp.

Coops, N., Hilker, T., Wulder, M., St-Onge, B., Newnham, G., Siggins, A. & Trofymow, T., 2007. Estimating Canopy Structure of Douglas-fir forest stands from discrete-return LiDAR *Trees- Structure and Function*, 21: 295-310.

Cornish, P.M., 1993. The effects of logging and forest regeneration on water yields in a moist eucalypt forest in New South Wales. *Journal of Hydrology*, 150: 301-322.

Cornish, P.M. & Vertessy, R.A., 2001. Forest age-induced changes in evapotranspiration and water yield in a eucalypt forest. *Journal of Hydrology*, 242: 43–63.

Cowan, I.R., 1981. Coping with water stress. In: Pate, J.S., McComb, A.J. (Eds.), *The biology of Australian plants*. University of Western Australia Press, Nedland.

Coyea, M.R. & Margolis, H.A., 1992. Factors affecting the relationship between sapwood area and leaf area of balsam fir. *Canadian Journal of Forest Research*, 22: 1684-1693.

Cromer, R.N., Tompkins, D., Barr, N.J., Williams, E.R. & Stewart, H.T.L., 1984. Litter-fall in *Pinus radiata* forest, The effect of irrigation and fertilizer treatments. *Journal of Applied Ecology*, 21: 313-326.

Cromer, R.N. & Williams, E.R., 1982. Biomass and nutrient accumulation in a planted *E.globulus* (Labill.) Fertiliser trial. *Australian Journal of Botany*, 30: 265-278.

Cruiziat, P., Cochard, H. & Ameglio, T., 2002. Hydraulic architecture of trees: main concepts and results. *Annual Forest Science*, 59: 723-752.

Davidian, M. & Giltinan, D.M., 1995. *Nonlinear models for repeated measurement data*. Chapman and Hall, London.

Davidson, N.J. & Reid, J.B., 1980. Comparison of early growth characteristics of the Eucalyptus subgenera Monocalyptus and Symphyomyrtus. *Aust. J. Bot.* , 28: 453-61.

Dean, T.J., Cao, Q.V., Roberts, S.D. & Evans, D.L., 2009. Measuring heights to crown base and crown median with LiDAR in a mature, even-aged loblolly pine stand. *Forest Ecology and Management*, 257: 126-133.

DeLucia, E.H., Maherali, H. & Carey, E.V., 2000. Climate-driven changes in biomass allocation in pines. *Global Change Biology*, 6: 587-593.

Eagleson, P.S., 1982. Ecological optimality in water-limited natural soil-vegetation systems. 1 Theory and hypothesis. *Water Resources Research*, 18: 325-240.

Eagleson, P.S. & Segarra, R.I., 1985. Water-limited equilibrium of savanna vegetation systems. *Water Resources Research*, 21: 1483-1493.

Eagleson, P.S. & Tellers, T.E., 1982. Ecological optimality in water-limited natural soil-vegetation systems 2. Test and application. *Water Resources Research*, 18: 341-354.

Efron, B. & Tibshirani, R., 1997. Improvements on cross-validation. the 0.632+ bootstrap method. *Journal of the American Statistical Association*, 2: 548-560.

Ellis, T.W., Hatton, T.J. & Nuberg, I.K., 1999. A simple method for estimating recharge from low rainfall agroforestry systems. In Envirowater99. 2nd Inter-Regional Conference on Environment-Water, (Ed.),^(Eds.), Musey, A., Santos Pereira, L., Fritsch, M., Polytechnique et Universitaires Romandses. Laussane, Switzerland.

England, J.R. & Attiwill, P.M., 2006. Changes in leaf morphology and anatomy with tree age and height in the broadleaved evergreen species Eucalyptus regnans F.Muell. *Trees-Struct. Funct.* , 20: 79–90.

Espinosa-Bancalari M.A., D.A., P. & J.D., M., 1987. Leaf area - sapwood area relationships in adjacent young Douglas-fir stands with different early growth rates. . *Canadian Journal of Forest Research* 17: 174-180.

Falkiner, R.A., Nambier, E.K.S., Polglase, P.J., Theivaeyanathan, S. & Stewart, L.G., 2006. Root distribution of *Eucalyptuse grandis* and *Corymbia maculata* in degraded saline soils of south-eastern Australia. *Agroforestry Systems*, 67: 279-291.

Fang, Z. & Bailey, R.L., 2001. Nonlinear Mixed Effects Modeling for Slash Pine Dominant Height Growth Following Intensive Silvicultural Treatments. *Forest Science*, 47: 287-300.

Farquhar, G.D. & Sharkey, T.D., 1982. Stomatal conductance and photosynthesis. *Annual Review of Plant Physiology*, 33: 317-345.

Feikema, P., Lane, P., Peel, M., Sherwin, C., Freebairn, A. & Salkin, O., 2006. Hydrological studies into the impact of timber harvesting on water yield in state forests supplying water to Melbourne – Part 1 of Hydrological studies. The University of Melbourne, Melbourne.

Fife, D., Benyon, R.G., Washusen, R. & Yang, J.L., 2002. High value products from blue gums on farms at low rainfall. Final report for National Heritage Trust project No. 990199, (CSIRO: Mount Gambier, South Australia).

Florence, R.G., 1996. *Ecology and Silviculture of Eucalypt Forests*. CSIRO Publishing Melbourne.

Hamilton, F., Penny, R., Black, P., Cumming, F. & Irvine, M., 1999. Victoria's Statewide Forest Resource Industry- an outline of methods. *Australian Forestry*, 62: 353-359.

Harrell, F.E., 2000. *Regression Modeling Strategies: With Applications to Linear Models*.

Hastie, T., Tibshirani, R. & Friedman, J., 2001. *The elements of statistical learning: data mining, inference, and prediction.*

Hatton, T., Reece, P., Taylor, P. & McEwan, K., 1998. Does leaf water efficiency vary among eucalypts in water-limited environments? *Tree Physiology*, 18: 529-536.

Haydon, S.R., Benyon, R.G. & Lewis, R., 1996. Variation in sapwood area and throughfall with forest age in Mountain Ash (*Eucalyptus regnans*, F.Muell.). *Journal of Hydrology*, 187: 351-366.

Hellmuth, E.O., 1968. Eco-physiological studies on plant in arid and semi-arid regions in Western Australia. III. Comparative studies on photosynthesis, respiration, and water relation of ten arid and two semi-arid zone plants under winter and late summer climatic conditions. *Journal of Ecology*, 59: 225-260.

Hickel, K. & Zhang, L., 2006. Estimating the impact of rainfall seasonality on mean annual water balance using a top-down approach. *Journal of Hydrology*, 331: 409-424.

Hoerl, A. & Kennard, R., 1970. Ridge regression - applications to non-orthogonal problems. *Technometrics*, 12: 69-82.

Holmgren, J. & Persson, A., 2004. Identifying species of individual trees using airborne laser scanner. *Remote Sensing and Environment*, 90: 415-423.

Honeysett, J.L., Beadle, C.L. & Tunbull, C., R.A., 1992. Evapotranspiration and growth of two contrasting species of eucalypts under non-limiting and limiting water availability. *Forest Ecology and Management*, 50: 203-216.

Honeysett, J.L., White, D., Worledge, D. & Beadle, C.L., 1996. Growth and water use of *Eucalyptus globulus* and *E.nitens* in irrigated and rainfed plantations. *Australian Forestry* 59: 64-73.

Howard, N. & O'Shaughnessy, P.J., 1971. Coranderrj Experiment Area: First progress report, pretreatment calibration. Melbourne Metropolitan Boards of Works, Rep No. MMBW-W-0001

Huang, S., Price, D. & Titus, S.J., 2000. Development of ecoregion-based height–diameter models for white spruce in boreal forests. *For. Ecol. Manage*, 129: 125-141.

Hubbard, R., M. , Stape, J., M.G., R., Almeida, A., C. & Rojas, J., 2010. Effects of irrigation on water use and water use efficiency in two fast growing Eucalyptus plantations. *Forest Ecology and Management*, 259: 1714-1721.

La Sala, A., 2007. Long-term response of *Eucalyptus regnans* F.Muell. to commercial thinning in a regrowth eucalypt forest in Tasmania. *Australian Forestry*, 70: 167-172.

Lane, P.N.J. & Mackay, S.M., 2001. Streamflow response of mixed-species eucalypt forests to patch cutting and thinning treatments. *Forest Ecology and Management*, 143: 131-142.

Langford, K.J., 1976. Changes in yield of water following a bushfire in a forest of *Eucalyptus regnans*. *Journal of Hydrology*, 29: 87-114.

Langford, K.J. & O'Shaughnessy, 1977. First progress report, North Maroondah.

Langford, K.J. & O'Shaughnessy, P.J., 1979. Second Progress Report: North Maroondah. Water Supply Catchment Hydrology Research

Lefsky, M.A., Cohen, W.B., Acker, S.A., Parker, G.G., Spies, T.A. & Harding, D.J., 1999. LiDAR remote sensing of the canopy structure and biophysical properties of Douglas-Fir Western Hemlock forests. *Remote Sensing and Environment*, 70: 339-361.

Lefsky, M.A., Hudak, A.T., Cohen, W.B. & Acker, S.A., 2005. Geographic variability in LiDAR predictions of forest stand structure in the Pacific Northwest. *Remote Sensing and Environment*, 95: 532-548.

Lindser, S., 1984. Potential and actual production in Australian forest stands. In: Landsberg, J.J., Parsons, W. (Eds.), *Research for forest management*. CSIRO, Melbourne, pp. 11-35.

Lindstrom, M. & Bates, D., 1990. Nonlinear Mixed Effects Models for Repeated Measures Data. *Biomatrics*, 46: 673-687.

Liu, C., Zhang, L., Davis, C.J., Solomon, D.S. & Gove, J.H., 2002. A Finite Mixture Model for Characterizing the Diameter Distributions of Mixed-Species Forest Stands *Forest Science*, 48: 653-661.

Lloyd, S.P., 1982. Least Squares Quantization in PCM. *IEEE Transactions on Inference Theory*, 28: 129-137.

Lunn, D.J., Thomas, A., Best, N. & Spiegelhalter, D., 2000. WinBUGS -- a Bayesian modelling framework: concepts, structure, and extensibility *Statistics and Computing* 10: 325-337.

Macfarlane, C., Bonda, C., White, D., Grigg, A., Ogdena, G. & Silberstein, R., 2010. Transpiration and hydraulic traits of old and regrowth eucalypt forest in southwestern Australia. *Forest Ecology and Management*, 260: 96-105.

Magnani, F., Grace, J. & Boroghetti, M., 2002. Adjustment of tree structure in response to the environment under hydraulic constraints. *Functional Ecology*, 16: 385-393.

Morris, D.M. & Benyon, R.G., 2005. Plantation water use. In: Nambier, S., Ferguson, I. (Eds.), *New Forests. Wood production and environmental serives*. CSIRO, Melbourne.

Morris, D.M. & Collopy, J., 1999. Water use and salt accumulation by *Eucalyptus camaldulensis* and *Casuarina cunninghamiana* on a site with shallow saline groundwater. *Agricultural Water Management*, 39: 205-227.

Morris, D.M. & Collopy, J., 2000. Effects of thinning on water use and soil conditions in a groundwater-dependent eucalypt plantation. CFTT Report No. 2000/037. (Department of Natural Resources and Environment: Melbourne)

Murray, I., 2007. Advances in Markov chain Monte Carlo methods. Thesis. Gatsby Computational Neuroscience Unit, University College London, London.

Naesset, E., 1997a. Determination of mean tree heights of forest stands using airborne laser scanner data. *Remote Sensing and Environment*, 29: 547-553.

Naesset, E., 1997b. Estimating timber volume of forest stands using airborne laser scanner data. *Remote Sensing and Environment*, 61: 547-553.

Naesset, E., Gobakken, T., Holmgren, J., Hyyppa, J., Hyyppa, H., Maltamo, M., Nilsson, M., Olsson, H., Persson, A. & Soderman, U., 2004. Laser Scanning of Forest Resources: The Nordic Experience. *Scandinavian Journal of Forest Research*, 19: 482-499.

Nambiar, S. & Ferguson, I., 2005. *New Forest: Wood production and environmental services*. CSIRO Publishing, Sydney.

Nelder, J.A. & Mead, R., 1965. A simplex method for function minimization. *Computer Journal*, 7: 308-313.

Nemani, R.R. & Running, S.W., 1989. Testing a theoretical climate soil-leaf area hydrologic equilibrium of forests using satellite data and ecosystem simulation. *Agricultural and Forest Meteorology*, 44: 245-260.

Noble, I.R., 1989. Ecological Traits of the Eucalyptus: Subgenera Monocalyptus and Symphyomyrtus *Aust. J. Bot.*, 37: 207-24.

North East Catchment Management Authority, 2004. North East Regional Catchment Strategy. North East CMA, Wodonga Victoria.

O'Grady, A.P., Eamus, D. & Hutley, L.B., 1999. Transpiration increases during the dry season: patterns of tree water use in eucalypt open-forests of Northern Australia. *Tree Physiology*, 19: 591-597.

Peel, M.C., Watson, F.G.R. & Vertessy, R., 2002a. Modelling of Low Flows in the North Esk River using the Macaque model. Launceston City Council & CRC for Catchment Hydrology

Raison, R.J., Brown, A. & Flinn, D., 2001. *Criteria and Indicators for Sustainable Forest Management*. CABI Publishing.

Raison, R.J., Khanna, P.K. & Crane, W.J.B., 1982. Effects of intensified harvesting on rates of nitrogen and phosphorus removal from *Pinus radiata* and *Eucalyptus* forests in Australia and New Zealand. *New Zealand Journal of Forest Science*, 12: 392-403.

Riano, D., Meier, E., Allgower, B., Chuvieco, E. & Ustin, S., 2003. Modeling airborne laser scanning data for the spatial generation of critical forest parameters in fire behavior modeling. *Remote Sensing and Environment*, 86: 177-186.

Rigby, R.A. & Stasinopoulos, D.M., 2008. A flexible regression approach using GAMLSS in R. STORM Research Centre, London Metropolitan University, London.

Roberts, S., Vertessy, R.A. & Grayson, R.G., 2001. Transpiration from Eucalyptus sieberi (L. Johnson) forests of different age. *For. Ecol. Manag.*, 143: 153-161.

Roecker, E., 1991. Prediction error and its estimation for subset-selection models. *Technometrics* 33: 459-468.

Rogers, R. & T.M., H., 1979. Foliar weight and area related to current sapwood area in oak. . *Forest Science*, 25: 298-303.

Schiecz, G. & Long, I.F., 1969. Surface resistance of crop canopies. *Water Resources Research*, 5: 622-633.

Sinclair, R., 1980. Water potential and stomatal conductance of three Eucalyptus species in the Mount Lofty Range, South Australia: Response to summer drought. *Australian Journal of Botany* 28: 499-510.

Sivapalan, M., 2009. The secret to 'doing better hydrological science': change the question! *Hydrol. Process.*, 23.

Smith, D.M., Larson, B.C., Kelty, M.J. & Ashton, P.M.S., 1997. *The Practice of Silviculture: Applied Forest Ecology*. John Wiley &Sons, New York, USA

Specht, R.L., 1972. Water use in perennial evergreen plant communities in Australia and Papua New Guinea. *Australian Journal of Botany*, 20: 273-299.

Talsma, T. & Gardner, E., 1986. Soil water extraction by a mixed eucalypt forest during a drought period. *Australian Journal of Soil Research*, 24: 25-32.

Theivaeyanathan, S., Benyon, R.G., Plglase, P., KFalkiner, R.A. & Myer, B.J., 2001. Tree plantations for controlling water tables in irrigation districts of the southern Murray-Darling Basin. Proceedings of the 7th national PURSL conference on productive use and rehabilitation of saline lands, , Launceston, Australia. National PURSL Committee. 81-87.

application to the Maroondah catchments. *Forest Ecology and Management*, 143: 189-204.

West, P.W., 1981. Comparative growth rates of several eucalypts in mixed-species stands in Southern Tasmania. *Ne Zealand Journal of Forestry Science*, 11: 45-52.

West, P.W., 1995. Application of Regression Analysis to Inventory Data with Measurements on Successive Occasions. *Forest Ecology and Management*, 71: 227-234.

West, P.W. & Mattay, J.P., 1993. Yield prediction models and comparative growth rates for six eucalypt species. *Australian Forestry*, 56: 211-225.

White, D.A., 1996. Physiological responses to drought of *Eucalyptus globulus* and *Eucalyptus nitens* in plantations. PhD Thesis. University of Tasmania, Hobart.

White, D.A., Beadle, C.L., Honeysett, J.L. & Worledge, D., 1986. Stomatal conductance of *Euclaypt globulus* and *E.nitens* in irrigated and rainfed plantations. In: Brown, A.G. (Ed.), *Australian tree species research in China*. ACIER Proceedings No. 48.

White, D.A., Beadle, C.L., Sands, P.J., Worledge, D. & Honeysett, J.L., 1999. Quantifying the effect of cumulative water stress on stomatal conductance of *Eucalyptus globulus* and *E.nitens*: A phenomenological approach. *Australian Journal of Plant Physiology*, 26: 17-27.

White, D.A., Dunin, F.X., Turner, N.C., Ward, B.H. & Galbraith, J.H., 2002. Water use by contour-planted belts of trees comprised of four Eucalyptus species. *Agricultural Water Management*, 53: 133-152.

Whitehead, D., 1978. The estimation of foliage area from sapwood basal area in Scots pine. *Forestry* 51: 137-149.

Whitehead, D., 1985. A review of processes in the water relations of forests. In: Landsberg, J.J., Parsons, J. (Eds.), *Research for forest management*. CSIRO, Melbourne.

Whitehead, D. & Beadle, C.L., 2004. Physiological regulation of productivity and water use in Eucalyptus: A review. *Forest Ecology and Management*, 193: 113-140.

Whitehead, D., Edwards, W.R.N. & Jarvis, P.G., 1984. Conducting sapwood area, foliage area, and permeability in mature trees of *Picea sitchensis* and *Pinus contorta Canadian Journal of Forest Research*, 14: 940-947.

Whiteley, S.B., 1999. Calculating the sustainable yield of Tasmania's state forests. . *Tasforests* 11: 23–34.

Appendix A

Appendix A1: Changes in stand volume over time

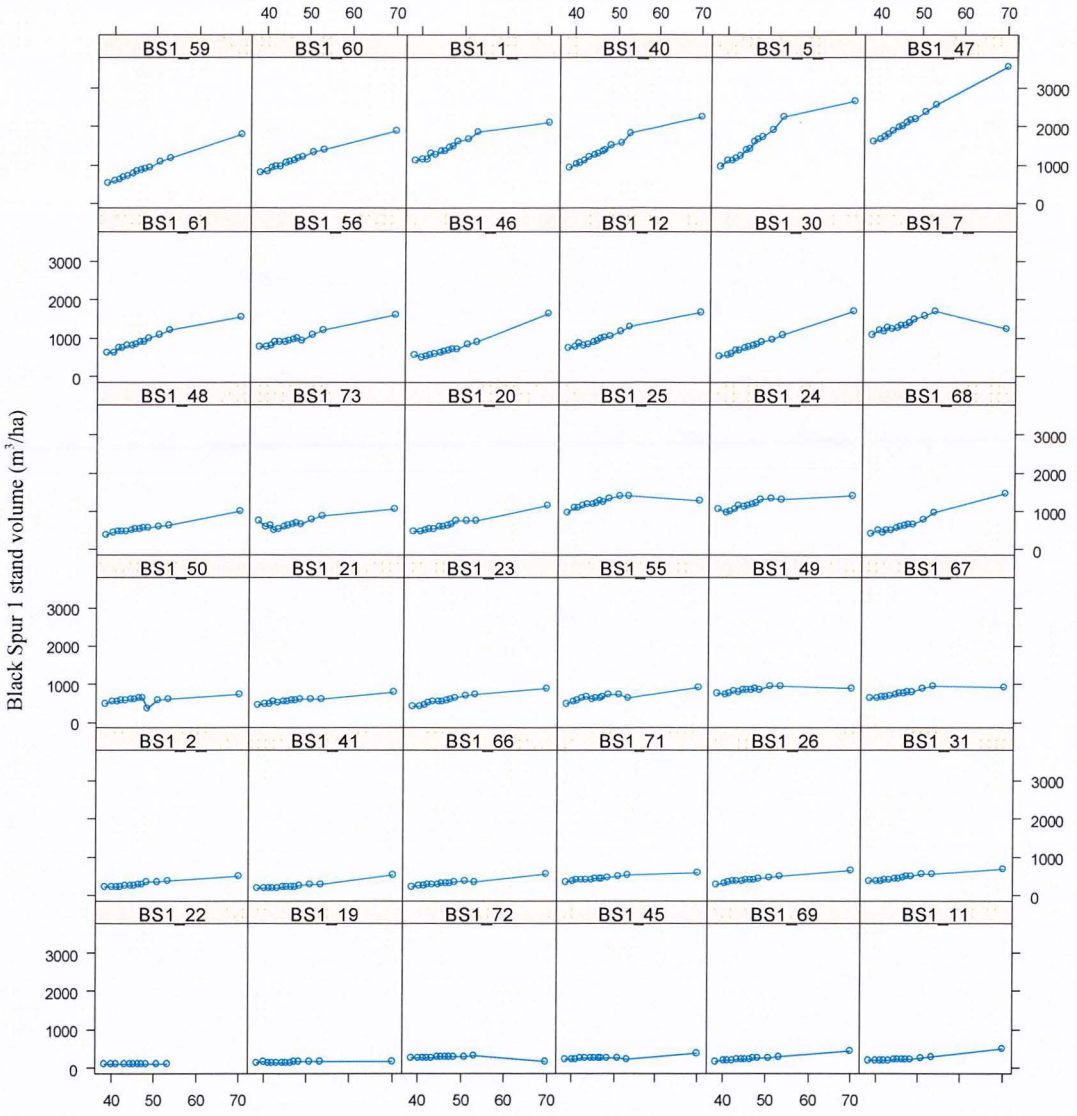

Figure B1: Changes in stand volume over time for each plot in; (a-c) Black Spur 1, 2 and 3.

Appendix A2 Residual standard error of a simple Logistic, and Gamma model

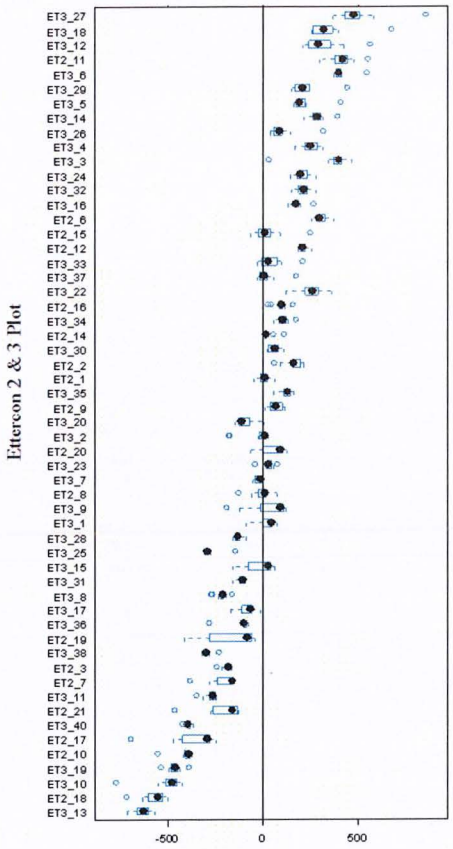

(a) Gamma model residuals (m^3/ha)

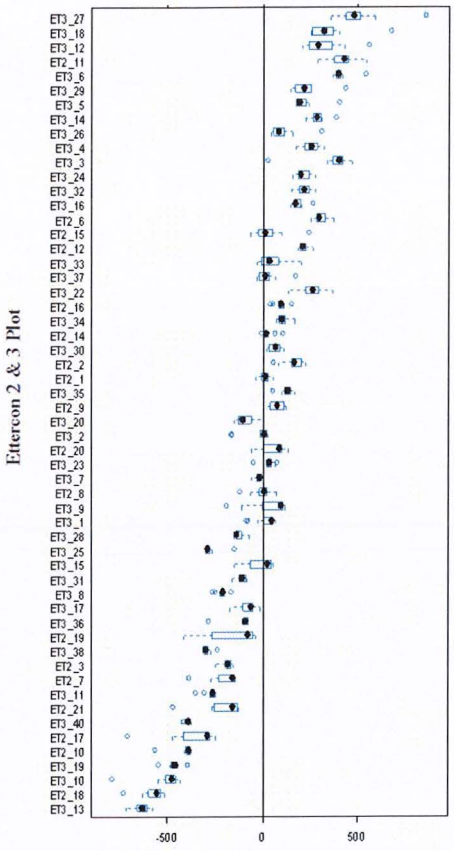

Logistic model residuals (m^3/ha)

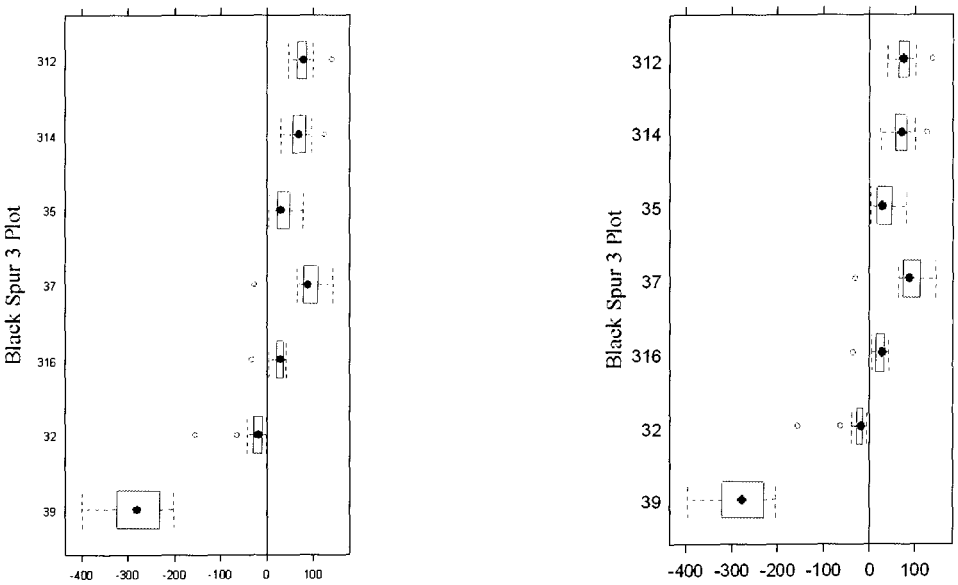

(d) Gamma model residuals (m^3/ha) Logistic model residuals (m^3/ha)

Figure B2 continued: Residual standard error of a simple Logistic and Gamma model for: (a) Ettercon 2&3, (b-d) Black Spur 1, 2 and 3 (using *nls*).

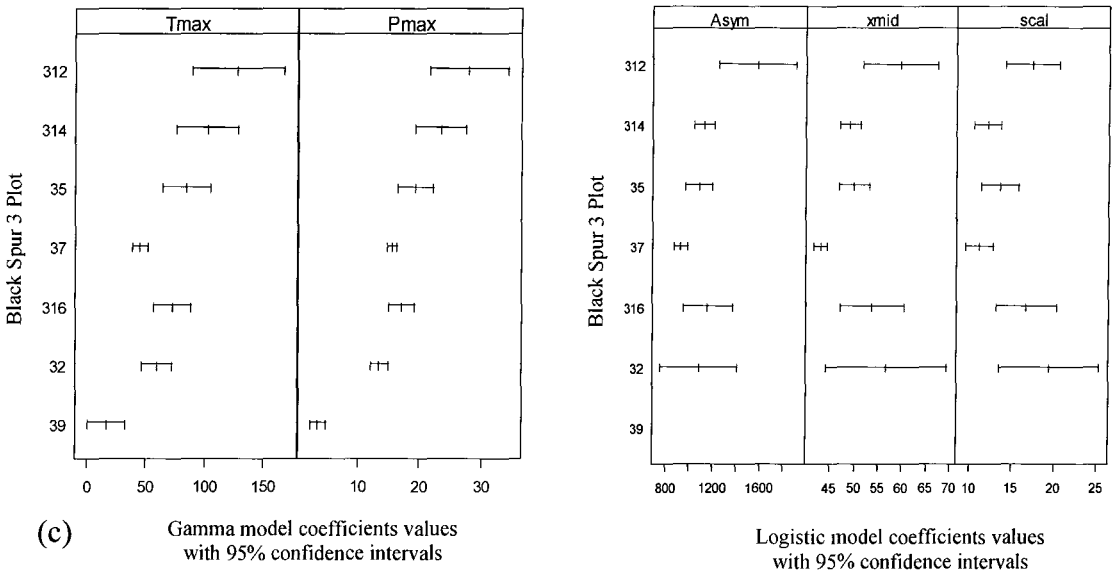

Figure B3 continued: Ninety-five percent confidence interval for coefficients in the Logistic and Gamma model using datasets; (a-c) Blackspur 1, 2, and 3. Plots with very uncertain confidence intervals were removed and are not shown.

Appendix A5: Normal probability plot of the within-group standardised residuals before correcting within-plot variance structure

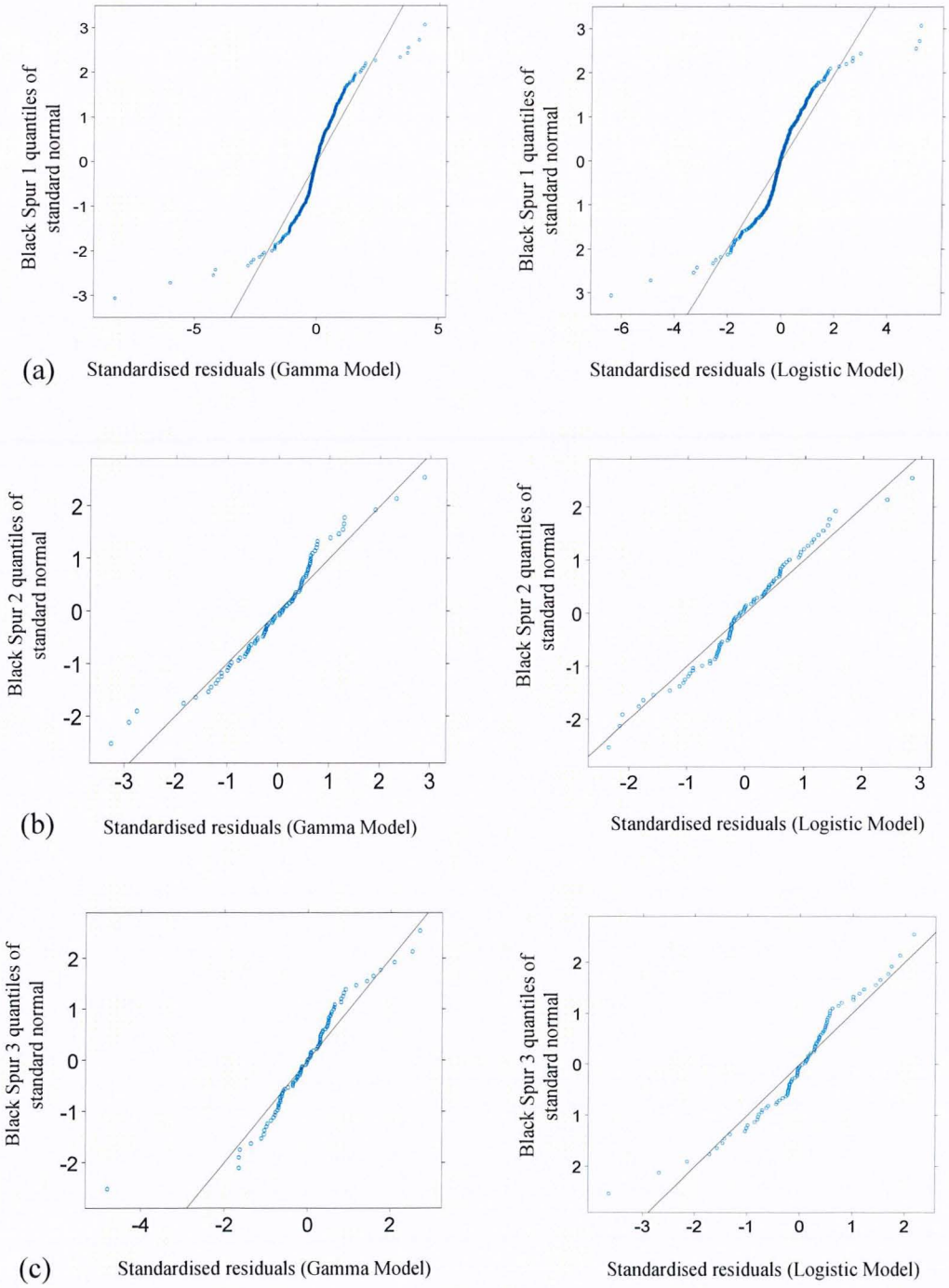

Figure B5: Normal probability plot of the within-group standardised residuals before correcting within-plot variance structure for: (a) Ettercon 2 & 3, and (b) Myrtle 2.

Appendix A7: LiDAR indices applied using the forward stepwise procedure to explain the random effects and develop a predictive model

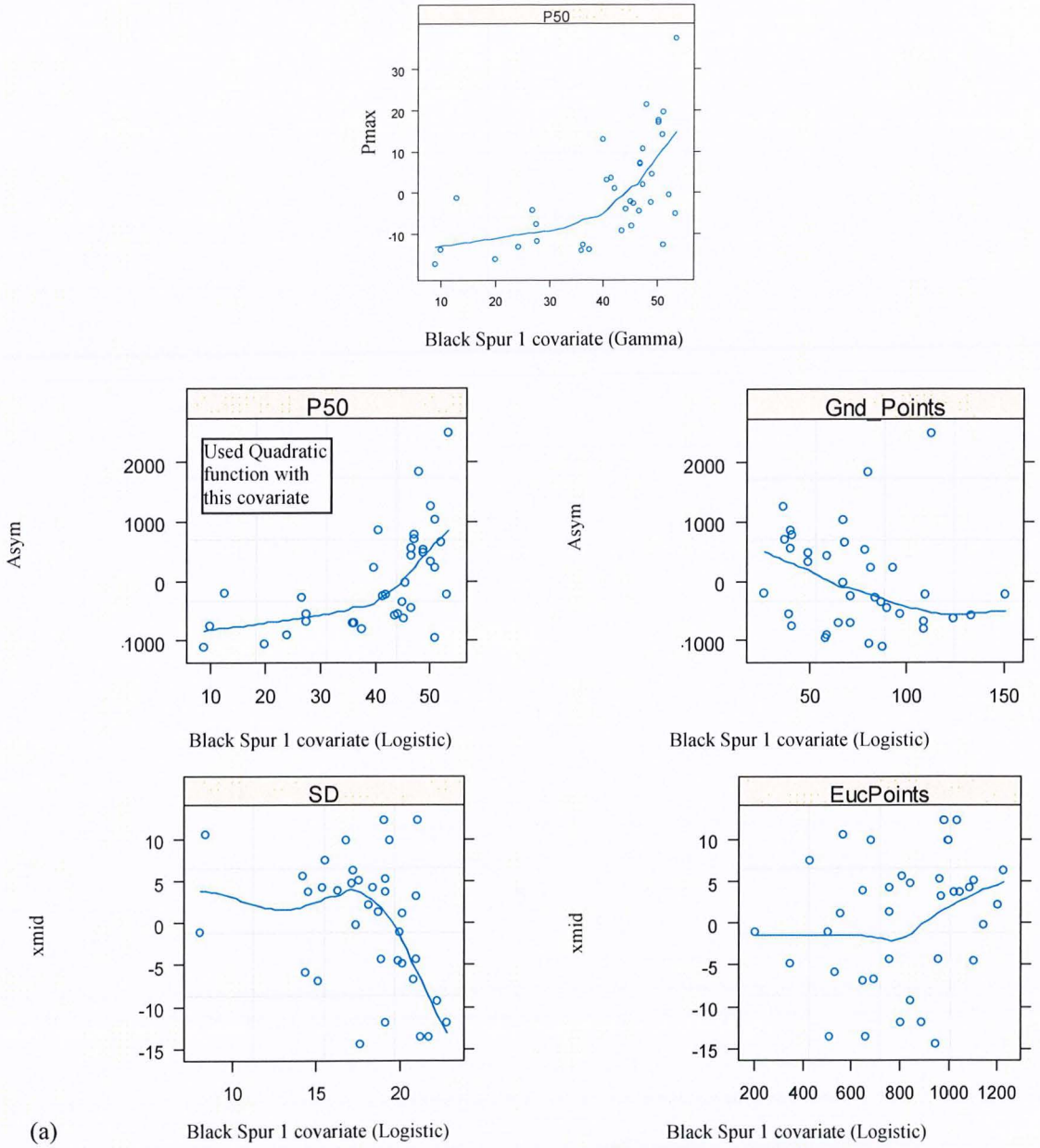

Figure B7: Applied LiDAR indices using the forward stepwise procedure to explain the random effects and develop a predictive model for: (a-c) Black Spur 1, 2, and 3.

Appendix A8: Final scatter plot of standardised residuals versus fitted values

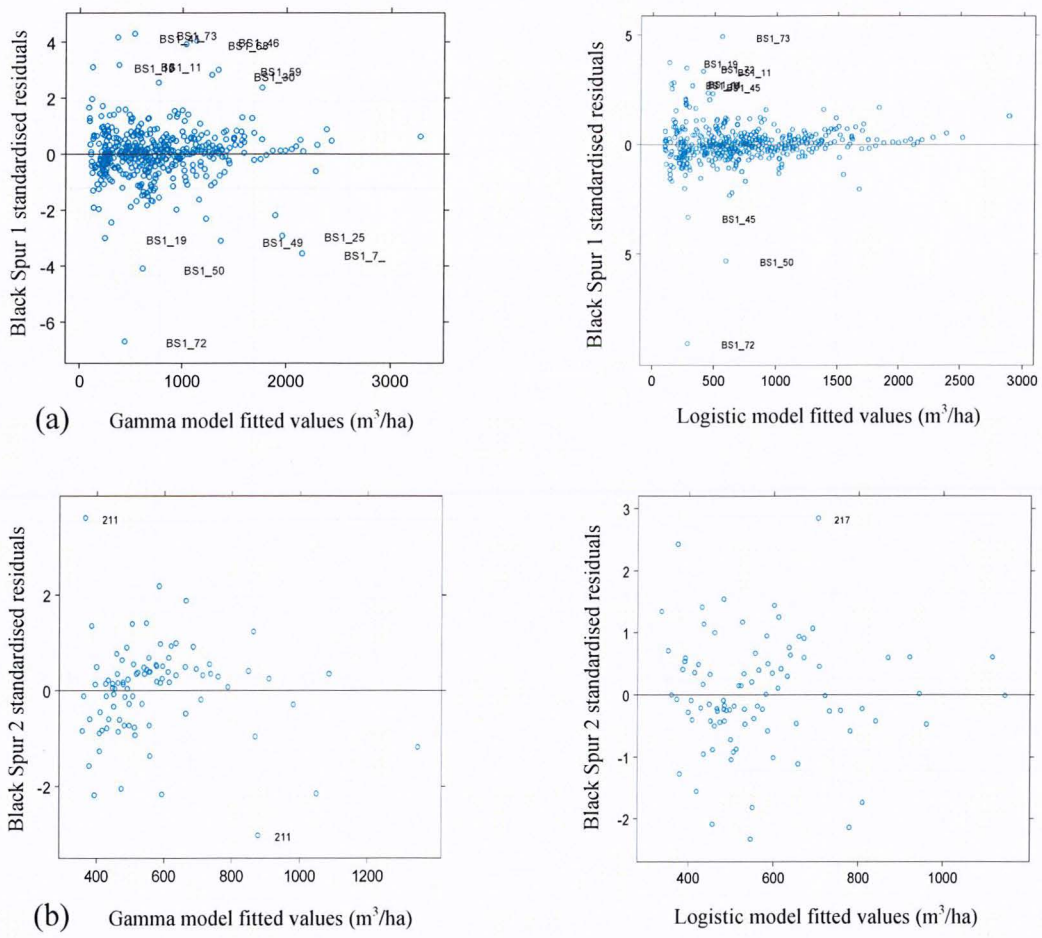

Figure B8: Scatter plots of standardised residuals versus fitted values using the final Logistic and Gamma model for: Black Spur 1 and 2 (Black Spur 3 is same as Figure B4).

Appendix A10: Plot specific predictions using Mixed Effects models and Fixed models

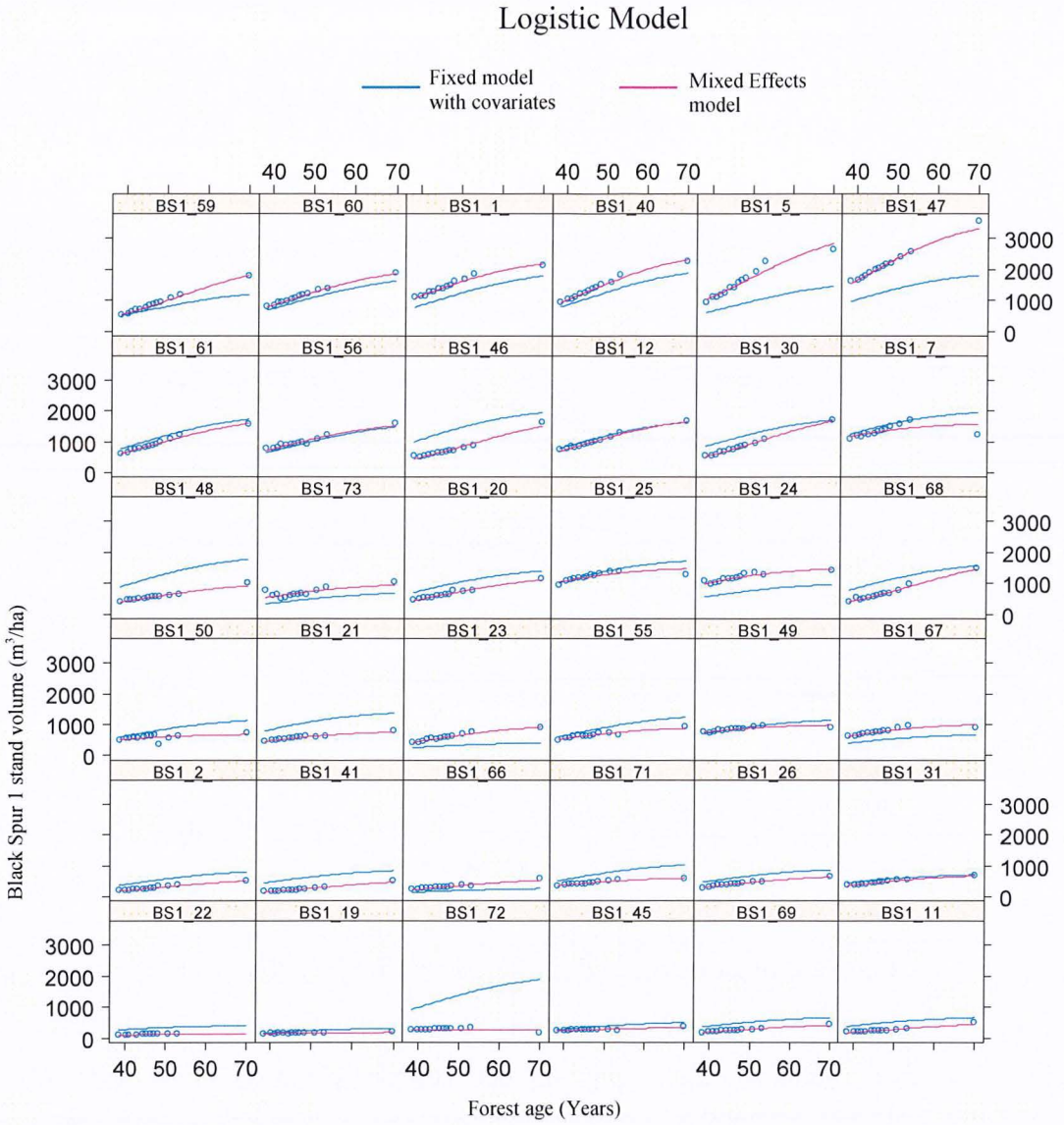

Figure B10: Plot specific predictions that use random effects (Mixed Effects Model); and population average predictions with random effects equalling zero and covariates explaining between plot variations (Fixed model) for: (a-c) Black Spur 1, 2, and 3.

Gamma Model

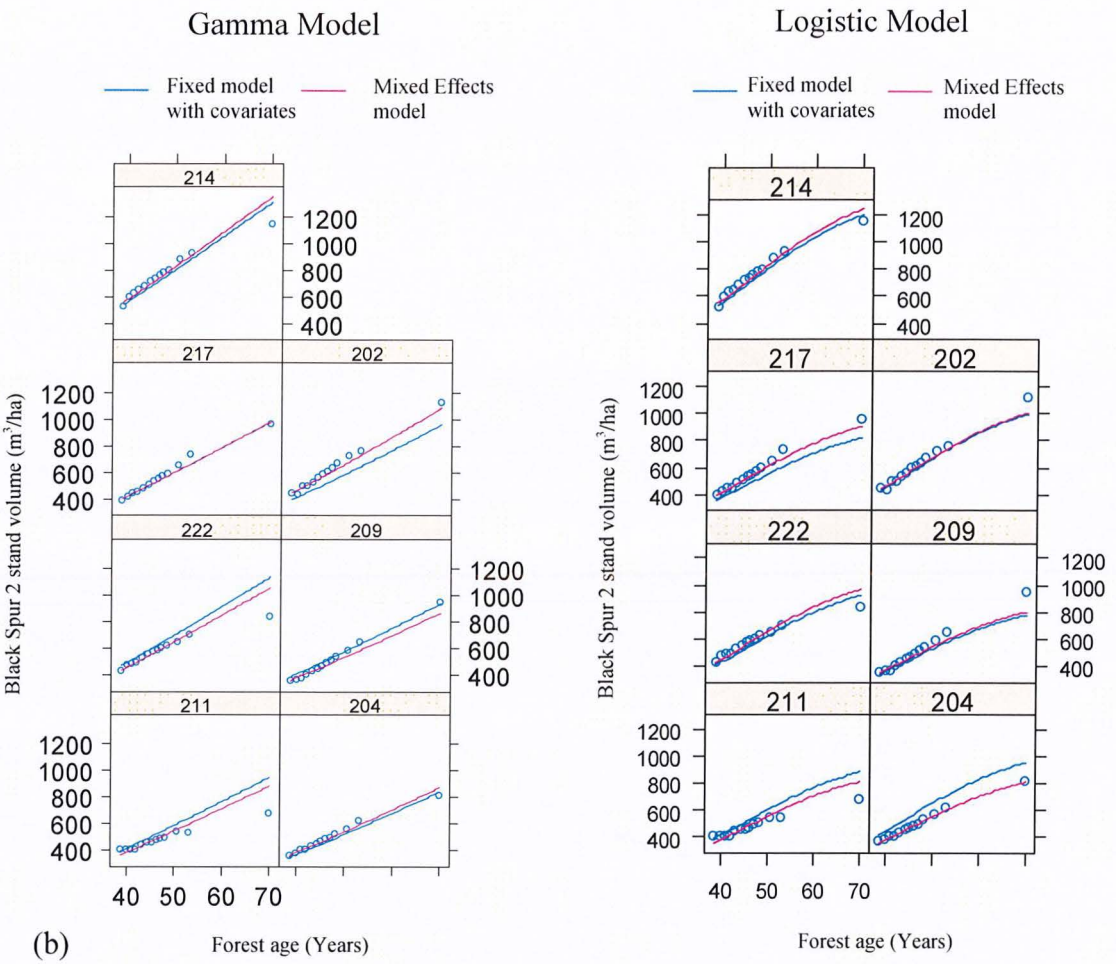

Figure B10 continued: Plot specific predictions that use random effects (Mixed Effects Model); and population average predictions with random effects equalling zero and covariates explaining between plot variations (Fixed model) for: (a-c) Black Spur 1, 2, and 3.

Logistic Model Logistic Model

Appendix A11: Final model's scatter plot of the predicted versus observed values

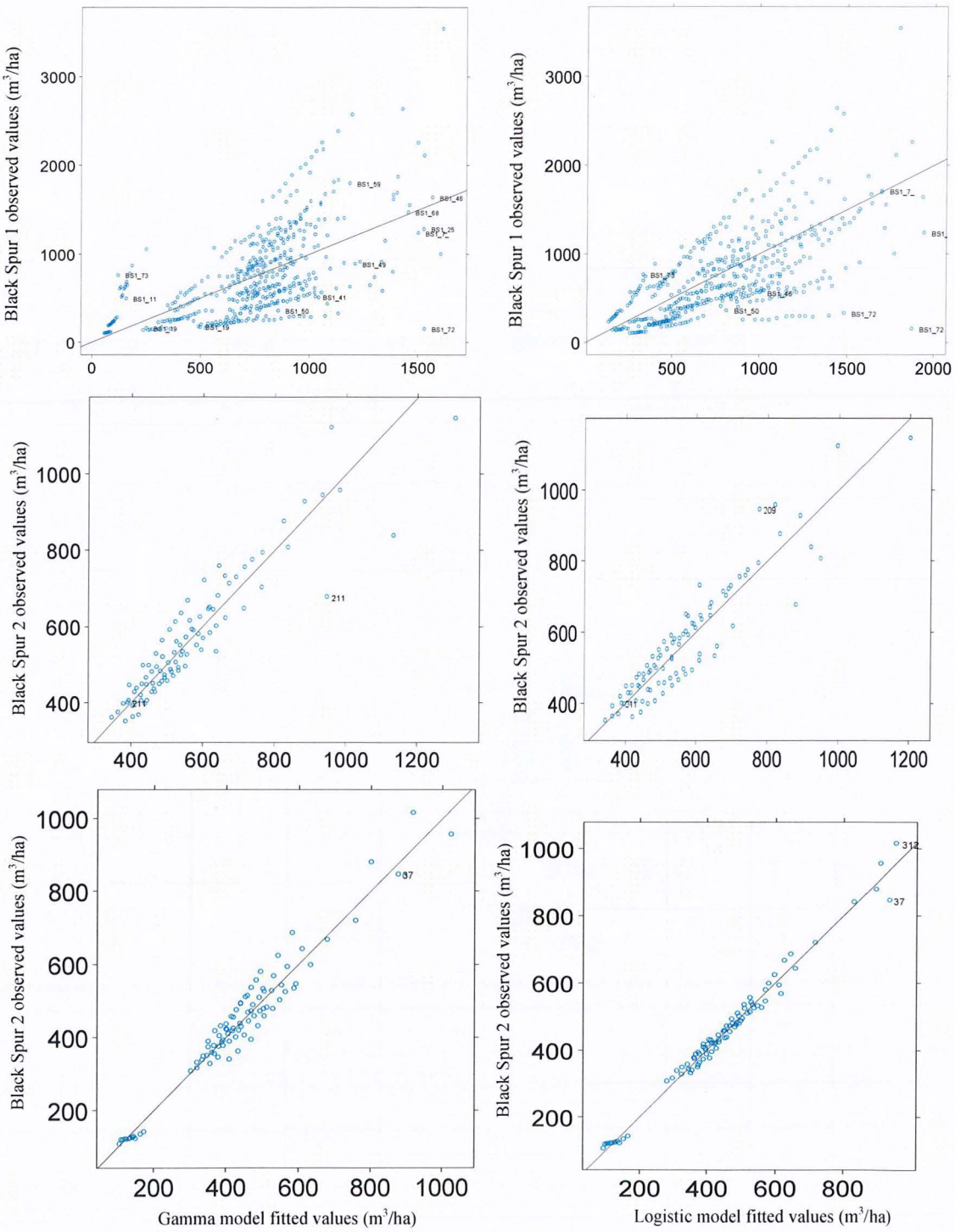

Figure B11: Scatter plot of predicted versus observed values for the Logistic and Gamma models using covariates to explain between-plot variation for: (a-c) Black Spur 1, 2, and 3.

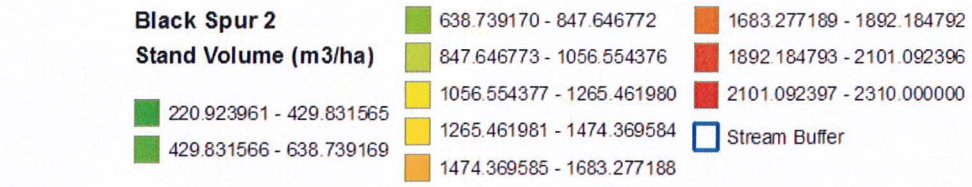
Black Spur 2
Stand Volume (m3/ha)
220.923961 - 429.831565
429.831566 - 638.739169
638.739170 - 847.646772
847.646773 - 1056.554376
1056.554377 - 1265.461980
1265.461981 - 1474.369584
1474.369585 - 1683.277188
1683.277189 - 1892.184792
1892.184793 - 2101.092396
2101.092397 - 2310.000000
Stream Buffer

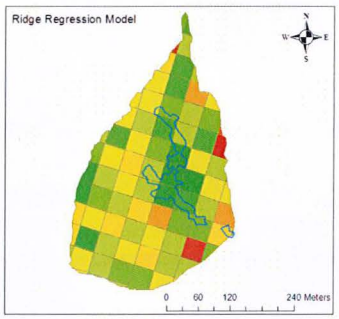
Ridge Regression Model
N
W
E
S
0 60 120 240 Meters

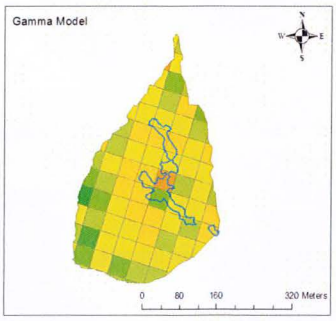
Gamma Model
N
W
E
S
0 80 160 320 Meters

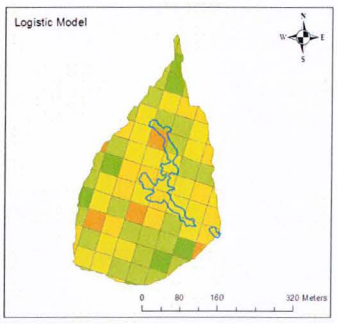
Logistic Model
N
W
E
S
0 80 160 320 Meters

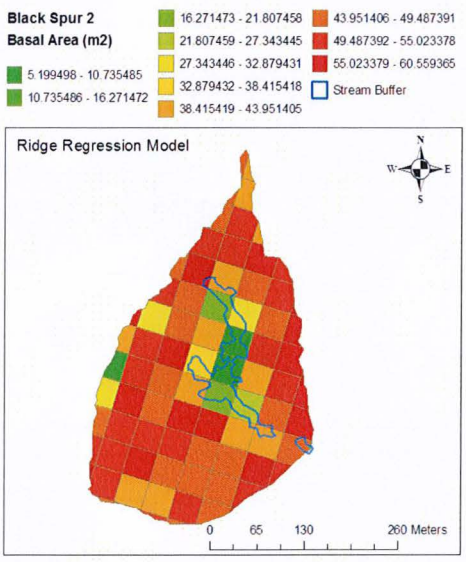
Black Spur 2
Basal Area (m2)
5.199498 - 10.735485
10.735486 - 16.271472
16.271473 - 21.807458
21.807459 - 27.343445
27.343446 - 32.879431
32.879432 - 38.415418
38.415419 - 43.951405
43.951406 - 49.487391
49.487392 - 55.023378
55.023379 - 60.559365
Stream Buffer
Ridge Regression Model
N
W
E
S
0 65 130 260 Meters

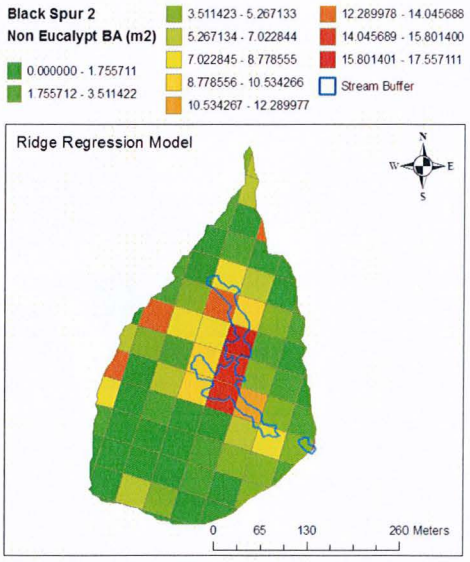
Black Spur 2
Non Eucalypt BA (m2)
0.000000 - 1.755711
1.755712 - 3.511422
3.511423 - 5.267133
5.267134 - 7.022844
7.022845 - 8.778555
8.778556 - 10.534266
10.534267 - 12.289977
12.289978 - 14.045688
14.045689 - 15.801400
15.801401 - 17.557111
Stream Buffer
Ridge Regression Model
N
W
E
S
0 65 130 260 Meters

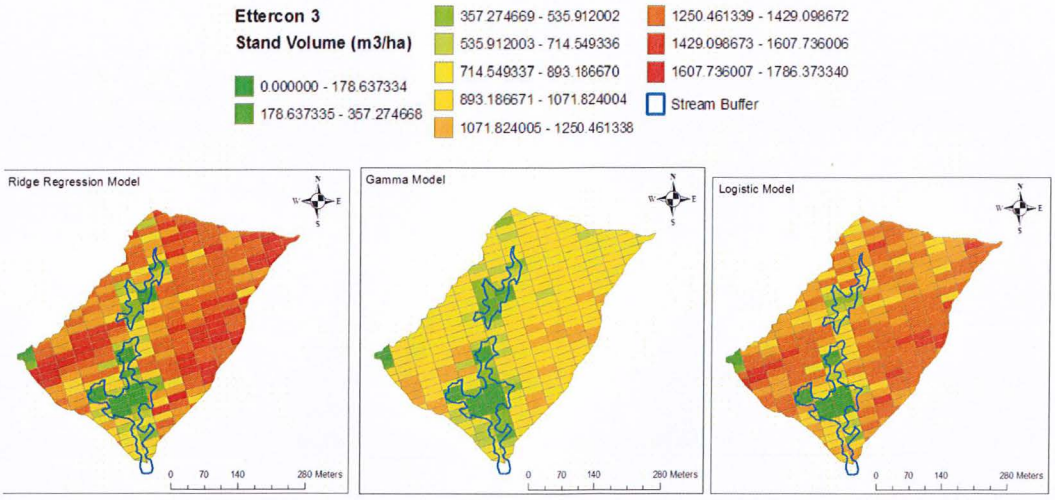
Ettercon 3
Stand Volume (m3/ha)
0.000000 - 178.637334
178.637335 - 357.274668
357.274669 - 535.912002
535.912003 - 714.549336
714.549337 - 893.186670
893.186671 - 1071.824004
1071.824005 - 1250.461338
1250.461339 - 1429.098672
1429.098673 - 1607.736006
1607.736007 - 1786.373340
Stream Buffer
Ridge Regression Model
Gamma Model
Logistic Model
0 70 140 280 Meters

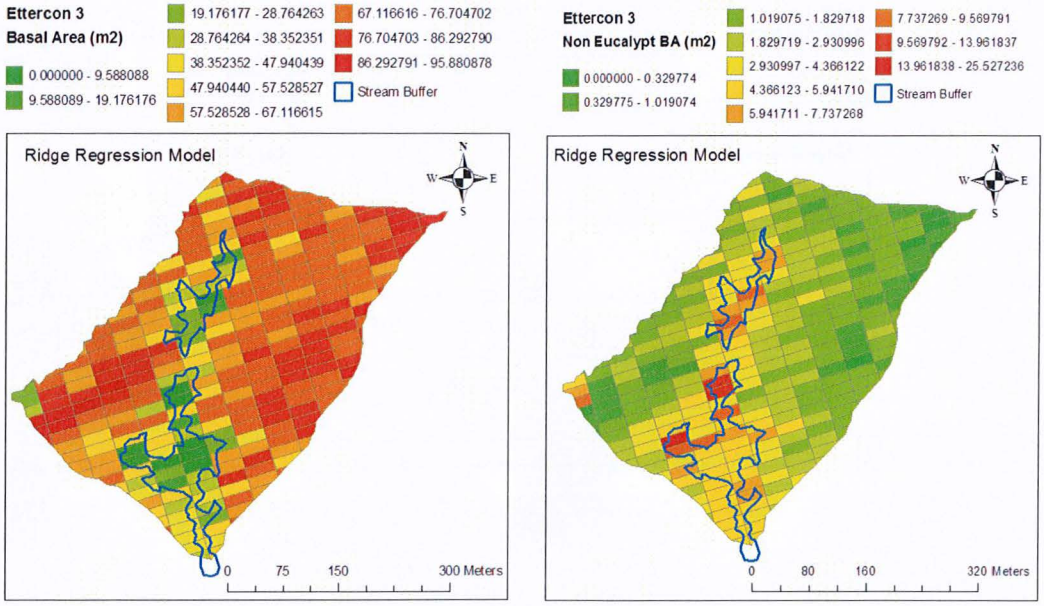
Ettercon 3
Basal Area (m2)
0.000000 - 9.588088
9.588089 - 19.176176
19.176177 - 28.764263
28.764264 - 38.352351
38.352352 - 47.940439
47.940440 - 57.528527
57.528528 - 67.116615
67.116616 - 76.704702
76.704703 - 86.292790
86.292791 - 95.880878
Stream Buffer
Ridge Regression Model
0 75 150 300 Meters
Ettercon 3
Non Eucalypt BA (m2)
0.000000 - 0.329774
0.329775 - 1.019074
1.019075 - 1.829718
1.829719 - 2.930996
2.930997 - 4.366122
4.366123 - 5.941710
5.941711 - 7.737268
7.737269 - 9.569791
9.569792 - 13.961837
13.961838 - 25.527236
Stream Buffer
Ridge Regression Model
0 80 160 320 Meters